

# **NON-PHYSICAL ENTHALPY METHOD FOR PHASE CHANGE MODELLING IN THE SOLIDIFICATION PROCESS**

**A thesis submitted to the University of Manchester for the degree  
of Doctor of Philosophy in the Faculty of Engineering and  
Physical Sciences**

**2010**

**by**

**Ricardo Mondragon Camacho**

**School of Mechanical, Aerospace and Civil Engineering**

# CONTENTS

<b>NON-PHYSICAL ENTHALPY METHOD FOR PHASE CHANGE MODELLING IN THE SOLIDIFICATION PROCESS .....</b>	<b>1</b>
<b>CONTENTS .....</b>	<b>2</b>
<b><i>TABLES</i> .....</b>	<b>6</b>
<b><i>FIGURES</i> .....</b>	<b>6</b>
<b>ABSTRACT .....</b>	<b>12</b>
<b>DECLARATION.....</b>	<b>13</b>
<b>COPYRIGHT STATEMENT.....</b>	<b>14</b>
<b>PREFACE.....</b>	<b>15</b>
<b>ACKNOWLEDGEMENTS .....</b>	<b>16</b>
<b>NOMENCLATURE .....</b>	<b>18</b>
<b>1 CASTING .....</b>	<b>22</b>
<b><i>1.1 Introduction .....</i></b>	<b><i>22</i></b>
<b><i>1.2 Solidification Process.....</i></b>	<b><i>24</i></b>
<b><i>1.3 Conventional solidification processes.....</i></b>	<b><i>25</i></b>
<b><i>Terminology.....</i></b>	<b><i>25</i></b>
<b>1.3.1 Expendable mould casting .....</b>	<b>26</b>
<b>1.3.2 Non-expendable mould casting .....</b>	<b>29</b>
<b><i>1.4 Special solidification processes.....</i></b>	<b><i>31</i></b>
<b>1.4.1 Squeeze casting.....</b>	<b>32</b>
<b>1.4.2 Indirect squeeze casting .....</b>	<b>33</b>
<b>1.4.3 Metal compression forming (MCF).....</b>	<b>33</b>
<b>1.4.4 Different processes to produce a billets in a semisolid state .....</b>	<b>33</b>

<b>1.5</b>	<b><i>Mathematical modelling</i></b>	<b>35</b>
1.5.1	Introduction	35
1.5.2	Simulation or modelling	36
1.5.3	Modelling types	36
1.5.4	Brief history for solidification modelling	37
<b>2</b>	<b>SOLIDIFICATION MODELLING METHODS</b>	<b>51</b>
2.1	<i>Introduction</i>	51
2.2	<i>Analytical methods</i>	53
2.2.1	Neumann's method	53
2.2.2	Heat balance integral method	56
2.3	<i>Numerical methods</i>	56
2.3.1	Strong numerical methods for solving a phase-change problem	57
2.3.2	Weak numerical methods for solving a phase-change problem	60
2.3.3	Numerical methods for solving convection/diffusion phase-change problems	66
2.4	<i>Methods for microstructure simulation</i>	70
2.4.1	Modelling of microstructure	71
2.4.2	Modelling of processes and average microstructural features	71
2.4.3	Modelling of grain structures using stochastic methods	71
2.5	<i>Conclusion</i>	72
<b>3</b>	<b>A NON-PHYSICAL ENTHALPY METHOD FOR THE NUMERICAL SOLUTION OF ISOTHERMAL SOLIDIFICATION</b>	<b>75</b>
3.1	<i>Introduction</i>	75
3.2	<i>Conservation law for a moving CV</i>	78
3.2.1	Relationships between temporal derivatives	79
3.2.2	Proposition	80

3.3	<i>Equivalent governing equations</i>	82
3.4	<i>Discontinuities for non-physical equations</i>	83
3.5	<i>Moving CV in a moving CV</i>	85
3.5.1	Proposition	86
3.6	<i>Finite elements equations</i>	88
3.7	<i>Matching transport derivatives</i>	90
3.7.1	Proposition	90
3.8	<i>Matching on an element domain</i>	91
3.8.1	Proposition	92
3.9	<i>Details of FEM for transport</i>	94
3.10	<i>Isothermal solidification in an Eulerian frame</i>	97
3.11	<i>System assembly and solution</i>	99
3.12	<i>Integral evaluation</i>	100
3.13	<i>Numerical experiments</i>	103
3.13.1	Isothermal solidification for 1-D element	103
3.13.2	1-D semi-infinite domain with phase-change	104
3.13.3	2-D semi-infinite domain with phase-change	105
3.13.4	3-D cube domain with phase-change	106
3.14	<i>Conclusions</i>	107
4	<b>WEAK DISCONTINUITY ANNIHILATION IN SOLIDIFICATION MODELLING</b>	122
4.1	<i>Introduction</i>	122
4.2	<i>Basic concepts</i>	124
4.3	<i>Definition of non-physical enthalpy and density</i>	126
4.4	<i>A single discontinuity in the domain</i>	129
4.5	<i>Multiple discontinuities</i>	131
4.6	<i>Finite Element Equations</i>	133
4.7	<i>Simplified finite element equations</i>	136
4.8	<i>Solidification in an Eulerian frame</i>	139
4.9	<i>System assembly and solution</i>	141

<b>4.10</b>	<b><i>Integral evaluation</i></b>	<b>142</b>
4.10.1	<i>Jump term evaluation</i>	144
<b>4.11</b>	<b><i>Numerical experiments</i></b>	<b>145</b>
4.11.1	<i>Isothermal solidification for 1-D element</i>	146
4.11.2	<i>1-D semi-infinite domain with phase-change</i>	147
4.11.3	<i>3-D cube domain with various type of solidification</i>	148
<b>4.12</b>	<b><i>Conclusions</i></b>	<b>149</b>
<b>5</b>	<b>RESULTS</b>	<b>164</b>
5.1	<i>Introduction</i>	164
5.2	<i>Solidification with single discontinuity</i>	165
5.2.1	<i>Results using a fine mesh density</i>	165
5.2.2	<i>Results using a medium mesh density</i>	166
5.2.3	<i>Results using a coarse mesh density</i>	166
5.3	<i>Solidification with multiple-discontinuities</i>	167
5.3.1	<i>Results using a fine mesh</i>	167
5.3.2	<i>Results using a medium mesh</i>	168
5.3.3	<i>Results using a coarse mesh</i>	168
5.4	<i>Solidification involving two discontinuities with narrow and wide mushy zone</i>	168
5.4.1	<i>Two discontinuities with narrow and wide mushy solidification for 1-D element</i>	169
5.4.2	<i>1-D semi-infinite slab domain with two discontinuities and linear mushy solidification, narrow and wide</i>	170
5.4.3	<i>3-D cube domain with linear mushy solidification, narrow and wide, and two discontinuities present</i>	170
5.5	<i>Conclusions</i>	173
<b>6</b>	<b>CONCLUSIONS</b>	<b>202</b>
6.1	<i>Solidification processes and modelling techniques</i>	203
6.2	<i>Reflexions about NEM</i>	204
6.3	<i>Future work</i>	205
	<b>REFERENCE</b>	<b>206</b>

<b>APPENDIX A .....</b>	<b>213</b>
<b>APPENDIX B .....</b>	<b>215</b>
<i>Integral evaluation.....</i>	<i>215</i>
<i>Jump term evaluation .....</i>	<i>216</i>

Number of words: 41,597

## **TABLES**

Table 3.1 Material properties for numerical test.....	108
Table 3.2 Performance data for various time-steps using a constant mesh density of $\Delta x = \Delta y = \Delta z = 1.00$ mm equivalent to 750 elements .....	109
Table 3.3 Performance data for various mesh densities using time-step $\Delta t = 0.005$ s .....	110
Table 4.1 Material properties for numerical test.....	151
Table 4.2 Performance data for various mesh densities.....	152
Table 4.3 Performance data for various time-steps.....	153
Table 5.1 Performance data for Isothermal solidification.....	174
Table 5.2 Performance data for Isothermal, Multi-discontinuous and Mushy solidification .....	181
Table 5.3 Material properties for numerical test.....	185
Table 5.4 Performance data for various mesh densities.....	186
Table 5.5 Performance data for various time-steps.....	187

## **FIGURES**

Figure 1-1 The oldest existing copper casting [58].....	40
Figure 1-2 Dendritic solidification at different physical scales [59].....	40
Figure 1-3 Equiaxed solidification process.....	41
Figure 1-4 Columnar and equiaxed solidification.....	41
Figure 1-5 Typical two part sand mould [9] .....	42
Figure 1-6 Shell moulding process [10].....	42
Figure 1-7 Lost foam casting process [10].....	43
Figure 1-8 Vacuum process [5].....	43
Figure 1-9 High pressure die-casting process (cold chamber) [5] .....	44

Figure 1-10 Low pressure die-casting process (hot chamber) [5].....	44
Figure 1-11 Continuous casting process typical scheme [60].....	45
Figure 1-12 Particle evolution during solidification in combination with agitation.....	45
Figure 1-13 Thixocasting process; (a) heating the billet into the semisolid state, (b) charge in the casting machine, (c) die-casting process and (d) finished model [21].....	46
Figure 1-14 Thixoforging process; (a) heating the billet into the semisolid state, (b) charge in the forging machine, (c) forging process and (d) finished model [21] .....	46
Figure 1-15 Squeeze casting [23].....	47
Figure 1-16 Indirect squeeze casting; (a) Metal poured into shot sleeve; (b) resulting non-uniform pressure profile in the die cavity [23].....	47
Figure 1-17 Metal compression forming; (a) Shut-off pin is withdrawn for filling; (b) shut-off pin is engaged and the male die pressurizes the cavity; (c) resulting uniform pressure profile in the cavity [23].....	48
Figure 1-18 Thixoforming process [23].....	48
Figure 1-19 Thixoforming and rheocasting [23].....	49
Figure 1-20 Different elaboration processes of billets for thixocasting [23].....	49
Figure 1-21 Casting stir ultra-sonic process [24].....	50
Figure 1-22 PID process [23].....	50
Figure 2-1 Representation for two-phase Stefan problem .....	73
Figure 2-2 1-D fixed grid with a moving front .....	73
Figure 2-3 Latent heat release for isothermal and mushy solidification.....	74
Figure 3-1 Velocities in reference domain.....	111
Figure 3-2 Liquid and solid domains in a solidifying body .....	111
Figure 3-3 Non-physical behaviour on 1-D elements .....	112
Figure 3-4 1-D solidification problem on an Eulerian frame.....	112
Figure 3-5 Isothermal solidification and linear elements.....	113
Figure 3-6 Non-physical variable profile for phase-change 1-D element - CVCMM .....	113
Figure 3-7 Non-physical variable profile for phase-change 1-D element - NEM .....	114
Figure 3-8 Mesh for 1-D semi-infinite slab problem.....	114
Figure 3-9 Temperature history for phase-change 1-D semi-infinite slab.....	115
Figure 3-10 Temperature profile comparison for phase-change 1-D semi-infinite slab...	115
Figure 3-11 Non-physical variable history for phase-change 1-D semi-infinite slab.....	116
Figure 3-12 Mesh for 2-D semi-infinite corner.....	116
Figure 3-13 Temperature history for phase-change 2-D semi-infinite corner .....	117
Figure 3-14 Temperature profile comparison for 2-D semi-infinite corner.....	117

Figure 3-15 Solidification Front moving over 2-D semi-infinite corner diagonal.....	118
Figure 3-16 Mesh for 3-D cube problem .....	118
Figure 3-17 Temperature history CVCM - NEM comparison on a 3-D Cube using same mesh density at specific point over diagonal $x=y=z=2$ mm.....	119
Figure 3-18 CVCM - NEM non-physical variable comparison on a 3-D Cube using same mesh density at specific point over diagonal $x=y=z=2$ mm.....	119
Figure 3-19 Temperature history CVCM - NEM comparison on a 3-D Cube using different mesh density at a specific point over the diagonal $x=y=z=2$ mm .....	120
Figure 3-20 CVCM - NEM non-physical variable comparison on a 3-D Cube using different mesh density at a specific point over the diagonal $x=y=z=2$ mm .....	120
Figure 3-21 Temperature history for Isothermal solidification at different points over the cube diagonal using same mesh density .....	121
Figure 3-22 Non-physical variable comparison for Isothermal solidification at different points over the cube diagonal using same mesh density.....	121
Figure 4-1 Velocities in reference domain.....	154
Figure 4-2 Control volume domain containing discontinuities .....	154
Figure 4-3 Solidification with phase discontinuities and associated regions in a linear element.....	155
Figure 4-4 Non-physical (CVCM) variable profile for phase-change in a 1-D element ..	155
Figure 4-5 Non-physical variable (NEM) profile for phase-change 1-D element.....	156
Figure 4-6 1-D solidification problem with two fronts on an Eulerian frame .....	156
Figure 4-7 Mesh for 1-D semi-infinite slab problem.....	157
Figure 4-8 Temperature history for phase-change 1-D semi-infinite slab.....	157
Figure 4-9 Temperature profile comparison for phase-change 1-D semi-infinite slab.....	158
Figure 4-10 Non-physical variable history for phase-change 1-D semi-infinite slab.....	158
Figure 4-11 Mesh for 3-D cube problem .....	159
Figure 4-12 Latent heat release for different cases of solidification.....	159
Figure 4-13 Isothermal Mushy and Multi-discontinuous solidification at $x=y=z=2$ mm for different meshes .....	160
Figure 4-14 Non-physical variable behaviour for Isothermal, Mushy and Multi-discontinuous solidification on a point $x=y=z=2$ mm.....	160
Figure 4-15 Temperature history for Isothermal, Mushy and Multi-discontinuous solidification on a point $x=y=z=2$ mm for different meshes.....	161
Figure 4-16 Non-physical variable comparison for Isothermal, Mushy and Multi-discontinuous solidification on a point $x=y=z=2$ mm for different meshes .....	161



Figure 4-17 Mushy and Multi-discontinuities solidification contrasted with single discontinuity NEM at $x=y=z=2$ mm for different time steps.....	162
Figure 4-18 Non-physical variable comparison at $x=y=z=2$ mm for various time steps..	162
Figure 4-19 Mushy and Multi-discontinuities solidification contrasted with single discontinuity CVCN at $x=y=z=2$ mm for different time steps.....	163
Figure 4-20 Non-physical variable comparison at $x=y=z=2$ mm for different time steps	163
Figure 5-1 Temperature history for isothermal solidification at different points along the diagonal of the cube for a fine mesh .....	175
Figure 5-2 Non-physical variable comparison for isothermal solidification along the diagonal of the cube for a fine mesh .....	175
Figure 5-3 Temperature history for isothermal solidification at different points along the diagonal of the cube for a fine mesh .....	176
Figure 5-4 Non-physical variable comparison for isothermal solidification along the diagonal of the cube for a fine mesh .....	176
Figure 5-5 Temperature history for isothermal solidification at different points along the diagonal of the cube for a medium mesh .....	177
Figure 5-6 Non-physical variable comparison for isothermal solidification along the diagonal of the cube for a medium mesh .....	177
Figure 5-7 Temperature history for isothermal solidification at different points along the diagonal of the cube for a medium mesh .....	178
Figure 5-8 Non-physical variable comparison for isothermal solidification along the diagonal of the cube for a medium mesh .....	178
Figure 5-9 Temperature history for isothermal solidification at different points along the diagonal of the cube for a coarse mesh .....	179
Figure 5-10 Non-physical variable comparison for isothermal solidification along the diagonal of the cube for a coarse mesh .....	179
Figure 5-11 Temperature history for isothermal solidification at different points along the diagonal of the cube for a coarse mesh .....	180
Figure 5-12 Non-physical variable comparison for isothermal solidification along the diagonal of the cube for a coarse mesh .....	180
Figure 5-13 Temperature history for Isothermal, Pure Mushy and Multi-discontinuities solidification along the diagonal of the cube for a fine mesh .....	182
Figure 5-14 Non-physical variable comparison for Isothermal, Pure Mushy and Multi-discontinuities solidification along the diagonal of the cube for a fine mesh.....	182

Figure 5-15 Temperature history for Isothermal, Pure Mushy and Multi-discontinuities solidification along the diagonal of the cube for a medium mesh .....	183
Figure 5-16 Non-physical variable comparison for Isothermal, Pure Mushy and Multi-discontinuities solidification along the diagonal of the cube for a medium mesh .....	183
Figure 5-17 Temperature history for Isothermal, Pure Mushy and Multi-discontinuities solidification along the diagonal of the cube for a coarse mesh .....	184
Figure 5-18 Non-physical variable comparison for Isothermal, Pure Mushy and Multi-discontinuities solidification along the diagonal of the cube for a coarse mesh .....	184
Figure 5-19 Non-physical variable (CVCM) comparison for multi-discontinuous narrow and wide mushy solidification for 1-D element .....	188
Figure 5-20 Non-physical variable (NEM) comparison for multi-discontinuous narrow and wide mushy solidification for 1-D element .....	188
Figure 5-21 Mesh for 1-D semi-infinite slab problem .....	189
Figure 5-22 Temperature history for multi-discontinuous and narrow mushy solidification for 1-D semi-infinite slab .....	189
Figure 5-23 Temperature profile for multi-discontinuous and narrow mushy solidification for 1-D semi-infinite slab .....	190
Figure 5-24 Non-physical variable comparison for multi-discontinuous and narrow mushy solidification for 1-D semi-infinite slab .....	190
Figure 5-25 Temperature history for multi-discontinuous and wide mushy solidification for 1-D semi-infinite slab .....	191
Figure 5-26 Temperature profile for multi-discontinuous and wide mushy solidification for 1-D semi-infinite slab .....	191
Figure 5-27 Non-physical variable comparison for multi-discontinuous and wide mushy solidification for 1-D semi-infinite slab .....	192
Figure 5-28 Mesh for 3-D cube problem .....	192
Figure 5-29 Latent heat release involving multi-discontinuities with narrow and wide mushy solidification .....	193
Figure 5-30 Multi-discontinuous and narrow mushy solidification on a point $x=y=z=2$ mm for different meshes .....	193
Figure 5-31 Non-physical variable behaviour for Multi-discontinuous and narrow mushy solidification on a point $x=y=z=2$ mm .....	194
Figure 5-32 Multi-discontinuous and wide mushy solidification on a point $x=y=z=2$ mm for different meshes .....	194

Figure 5-33 Non-physical variable behaviour for Multi-discontinuous and wide mushy solidification on a point $x=y=z=2$ mm.....	195
Figure 5-34 Temperature history comparison for Multi-discontinuous narrow and wide mushy solidification on a point $x=y=z=2$ mm for different meshes.....	195
Figure 5-35 Non-physical variable comparison for Multi-discontinuous narrow and mushy solidification on a point $x=y=z=2$ mm for different meshes.....	196
Figure 5-36 Multi-discontinuous with narrow mushy solidification for different time steps on a coarse mesh contrasted to a fine mesh at a point $x=y=z=2$ mm.....	196
Figure 5-37 Non-physical variable comparison for Multi-discontinuous and narrow mushy solidification for different time steps on a coarse and fine mesh at a point $x=y=z=2$ mm .....	197
Figure 5-38 Multi-discontinuous with wide mushy solidification for different time steps on a coarse mesh contrasted to a fine mesh at a point $x=y=z=2$ mm.....	197
Figure 5-39 Non-physical variable comparison for Multi-discontinuous and wide mushy solidification for different time steps on a coarse and fine mesh at a point $x=y=z=2$ mm .....	198
Figure 5-40 Temperature history for Multi-discontinuous narrow and wide mushy solidification for different time steps at a point $x=y=z=2$ mm .....	198
Figure 5-41 Non-physical variable comparison for Multi-discontinuous narrow and wide mushy solidification for different time steps at a point $x=y=z=2$ mm.....	199
Figure 5-42 Multi-discontinuous and narrow mushy solidification at different points along the diagonal of the cube for a fine mesh .....	199
Figure 5-43 Non-physical variable comparison for Multi-discontinuous and narrow mushy solidification along the diagonal of the cube for a fine mesh .....	200
Figure 5-44 Multi-discontinuous and wide mushy solidification at different points along the diagonal of the cube for a fine mesh .....	200
Figure 5-45 Non-physical variable comparison for Multi-discontinuous and wide mushy solidification along the diagonal of the cube for a fine mesh .....	201

# ABSTRACT

This research is concerned with the development of a mathematical approach for energy and mass transport in solidification modelling involving a control volume (CV) technique and finite element method (FEM) and incorporating non-physical variables in its solution. The former technique is used to determine an equivalent capacitance to describe energy transport whilst the latter technique provides temperatures over the material domain.

The numerical solution of the transport equations is achieved by the introduction of two concepts, i.e. weighted transport equations and non-physical variables. The main aim is to establish equivalent transport equations that allow exact temporal integration and describe the behaviour of non-physical variables to replace the original governing transport equations.

The variables defined are non-physical in the sense that they are dependent on the velocity of the moving CV. This dependence is a consequence of constructing transport equations that do not include flux integrals. The form of the transport equations facilitate the construction of a FEM formulation that is applicable to heat and mass transport problems and caters for singularities arising from phase-change, which can prove difficult to model. However, applying the non-physical enthalpy method (NEM) any singularity involved in the solidification process is precisely identified and annihilated

# DECLARATION

I declare that no portion of the work referred to in the thesis has been submitted in support of an application for another degree or qualification of this or any other university or other institute of learning

# COPYRIGHT STATEMENT

- i. The author of this thesis (including any appendices and/or schedules to this thesis) owns certain copyright or related rights in it (the “Copyright”) and he has given The University of Manchester certain rights to use such Copyright, including for administrative purposes.
- ii. Copies of this thesis, either in full or in extracts and whether in hard or electronic copy, may be made only in accordance with the Copyright, Designs and Patents Act 1988 (as amended) and regulations issued under it or, where appropriate, in accordance with licensing agreements which the University has from time to time. This page must form part of any such copies made.
- iii. The ownership of certain Copyright, patents, designs, trade marks and other intellectual property (the “Intellectual Property”) and any reproductions of copyright works in the thesis, for example graphs and tables (“Reproductions”), which may be described in this thesis, may not be owned by the author and may be owned by third parties. Such Intellectual Property and Reproductions cannot and must not be made available for use without the prior written permission of the owner(s) of the relevant Intellectual Property and/or Reproductions.
- iv. Further information on the conditions under which disclosure, publication and commercialisation of this thesis, the Copyright and any Intellectual Property and/or Reproductions described in it may take place is available in the University IP Policy (see <http://www.campus.manchester.ac.uk/medialibrary/policies/intellectual-property.pdf>), in any relevant Thesis restriction declarations deposited in the University Library, The University Library’s regulations (see <http://www.manchester.ac.uk/library/aboutus/regulations>) and in The University’s policy on presentation of Theses

# PREFACE

Mechanical engineering has always been my driving force. Through its application, we try to explain and make sense of the world around us. I obtained my previous two degrees in mechanical engineering, (BEng and MSc) in the Polytechnic National Institute in Mexico. It was therefore a natural progression to want to study a PhD in one of the leading institutions in the world.

The University of Manchester, formerly known as UMIST, has not only challenged me intellectually but also tested my patience and self-discipline and has provided me with the opportunity to be in contact with people with exceptional intellectual knowledge and moral conduct. During my period of study I have had first hand experience of working as a teaching assistant in the following Laboratories: notched bars, vibrations one degree of freedom, torsion bars, gyration mass distribution and buckling effect in beams. My research in the non-physical enthalpy method has introduce me to diverse fields that have required my full commitment and focus i.e., partial differential equations, numerical methods, code programming, solidification and casting.

Below are listed the Papers from this research which have been published and/or presented for scrutiny by peers in this specific field.

1. K. Davey and R. Mondragon, *A non-physical enthalpy method for the numerical solution of isothermal solidification*, International Journal for Numerical Methods in Engineering **84** (2010), no. 2, 214-252.
2. ---, *A transport level-set approach for the annihilation of weak discontinuities in solidification modelling*, IV European Conference on Computational Mechanics, "Solid, structures and coupled problems in engineering", 2010, p.^pp.
3. ---, "Non-physical enthalpy method for a Stefan problem," *PGR-MACE 2010, Postgraduate Research Conference*, The University of Manchester, Manchester, UK, 2010, pp. 22-23.
4. ---, *Non-physical enthalpy method for an isothermal problem*, VIII Symposium of Mexican Students in the UK, 2010, p.^pp.
5. ---, *The annihilation of weak discontinuity in solidification modelling*, Seventh International Conference on Engineering Computational Technology, Civil-Comp Press, Stirlingshire, Scotland, 2010, p.^pp. paper 129.
6. ---, *The annihilation of multiple discontinuities in solidification modelling*, Seventh International Conference on Engineering Computational Technology, Civil-Comp Press, Stirlingshire, Scotland, 2010, p.^pp. paper 131.
7. R. Mondragon and K. Davey, *Weak discontinuity annihilation in solidification modelling*, International Journal for Computers and Structures **89** (2011), no. 7-8, 681-701.

# ACKNOWLEDGEMENTS

The author wishes to express his sincere gratitude to Dr. Keith Davey for his valuable advice and guidance throughout the preparation of this work. The author is also grateful to CONACYT for providing support.



To my family in Mexico  
Carmen Camacho, Rogelio Mondragon and Maria Mondragon

Especiallly  
H. Evelia Ortiz Hernandez

and my family here  
Glenys Olalla

# NOMENCLATURE

## ABBREVIATIONS

CRS	Computational reference system
CV	Control Volume
CVCM	Control Volume Capacitance Method
MRS	Material reference system
NEM	Non-physical Enthalpy Method
$n$	Variable at time $t_n$
$n+1$	Variable at time $t_{n+1}$

## OPERATORS

$\nabla_{\Gamma_k}$	Gradient operator on the tangential plane of the discontinuity front
$\langle \cdot, \cdot \rangle$	Inner product
$] \cdot [$	Outward brackets denoting jump condition or subtraction
$x^* \equiv x(\chi^*, t) = x(X, t) \equiv x$	e.g. diffeomorphisms
$\emptyset$	Null set

## SYMBOLS

$c$	Heat capacitance
$\hat{c}$	Non-physical capacitance
$\hat{c}^e$	Capacitance element

---

$c_s^e$	Source capacitance element
$d\mathbf{x}^*$	Infinitesimal change on $\mathbf{x}^*$
$(D\mathbf{v}^+)_{\ell m}$	Directional derivative
$\text{div}_{\Gamma_i}$	Divergence defined locally at $\Gamma_i$
$dV_i$	Measure of the element volume sweep by the movement of phase boundary
$f$	Element volume fraction
$g$	Mass fraction
$\Gamma$	Boundary for the domain $\Omega$
$\Gamma_i$	Discontinuity or interface front
$h$	Specific enthalpy
$\hat{h}$	Non-physical enthalpy
$\hat{h}'$	Source-like term
$\hat{h}_k^p$	Specific enthalpy for phase materials
$k$	Thermal conductivity
$\kappa$	Diffusivity
$L$	Latent heat release
$\underline{n}$	Outward unit normal vector
$\Omega/\Gamma_i$	Domain without source terms present
$\Omega^*$	CV transported by a velocity $\underline{v}^*$
$\Omega^+$	CV transported by a velocity $\underline{v}^+$
$\underline{q}$	Heat flux
$\rho$	Density
$\hat{\rho}$	Non-physical density and part of the particular solution for $\hat{h}$ tied to $\underline{v}^*$
$S_e$	Source term element

---

$\Sigma_i$	Boundary for the domain $\Gamma_i$ that is on the tangential plane of the moving front
$T$	Temperature
$t$	Time
$V_e$	Element volume
$V_k^{\text{swept}}$	Swept volume resulting when $\Gamma_k$ sweeps through the element
$\Delta V$	Sweep volume by the boundary $\Gamma_k$
$\underline{v}$	Velocity field for MRS
$\underline{v}^*$	Velocity field for control volume or CRS
$x$	Co-ordinate in the spatial reference system
$X$	Co-ordinate in the material reference system
$\chi^*$	Co-ordinate in the computational reference system

## SUPERSCRIPTS

$e$	Element
$i$	Discontinuity front
$\ell$	Liquid domain
$k$	k-th front phase
$K$	Interfaces
$K_e$	Subset of $\{k : k = 1 : K\}$
$\text{liq}$	Liquidus
$m$	Mass fraction approximation
$N$	Normal component
$s$	Solid domain
$\text{sol}$	solidus
$T$	Tangential component

---

## SUBSCRIPTS

- \*      Related to the reference system or CV
- +      Related to a discontinuity in a moving CV
- ×      Related to a discontinuity in a moving element
- C      Material phase combination

# 1 CASTING

---

## ***1.1 Introduction***

A brief timeline of metal casting and its impact on the development and advancement of human cultures and civilization [1, 2, 3, 4], can be tracked over 6000 years of technological advances where metal casting has played an important role in our everyday lives.

The oldest preserved cast parts, weapons and cult objects made of copper originate from the Middle East and India. They date back to the period around 3000 BC. It is possible that metal casting technology using moulds, originated in the Middle East. However, there are suggestions that this process may have been developed in India and China.

The oldest known casting in existence is a copper frog, 3200 B.C., casted in Mesopotamia, see Figure 1-1; after this Chinese cast iron was produced around 800 – 700 B.C., which has been confirmed with the earliest sand moulding found in China around 645 B.C.

The melting ovens of the early Iron Age can partly be traced back to ceramic burning ovens. The techniques involved in model and mould building were mastered very well from the outset. Lost moulds made of loam and clay, wax models, single piece-work as

well as permanent moulds made of stone and metal for the serial production of casting parts were already being used. Hollow casting parts discovered have similarly proved that their production by using cores was also in use during this era.

Cast iron piping to transport water was first used in Dillenburg Castle, in 1455, in Germany; however the first man to describe the foundry process in writing was Vannoccio Biringuccio (1480 – 1539), in Italy, who is known as the father of the foundry industry. A major step forward to the production of iron as a raw material for the industrial revolution was taken when Abraham Darby (1678 – 1717), in England, developed a method of producing pig iron in a blast furnace fuelled by coke rather than charcoal. The first malleable iron, known as whiteheart, was developed in a cupola furnace, in 1720, in France, by Rene Antoine de Reaumur. Steel production changed when Benjamin Huntsman, in 1750, in England, reintroduced the cast crucible process in which steel for the first time is completely melted producing a uniform composition within the melt. A.G. Eckhardt revealed centrifugal casting basic principles, in 1809, in Soho, England. Finally, in 1825, Aluminium, the most common metal on earth's surface was isolated. The first mass production process to produce steel from molten pig iron was achieved, in 1851, in England, by Sir Henry Bessemer and William Kelly, the process uses blasts of air to eliminate impurities, silicon, manganese and excess of carbon. Metallography was developed in 1863, in Sheffield, England, by Henry C. Sarby; this was the first process to physically examine the surface of castings for quality analysis.

At the beginning of the last century, the first true stainless steel was achieved, in 1913, in Sheffield, England, by Harry Brearley. The spectroscopy for metal analysis was pioneered in 1930 at the University of Michigan. Ductile iron was invented in 1943 by adding magnesium to the widely used grey iron. The shell moulding process was invented during WWII, in 1947, in Germany, by J. Croning. The hot-box process of making and curing cores in one operation was developed in 1953, eliminating the use of dielectric drying ovens. The lost-foam casting process was invented in 1964 by M.C. Fleming, which in the 1980's had an impact on the automobile industry in the production of engine blocks, cylinder heads, crankshafts and transmissions. The scanning electron microscope was invented in 1965 by the Cambridge University Engineering Department in England. The first metal matrix composite casting was poured in 1965, in New York, USA. The cold-box process was developed in 1968. This used sand mixed with a catalyst that cured at room temperature. The semi-solid metalworking (SSM) process was conceived in the early 1970's at the Massachusetts Institute of Technology. This combines casting and forging features. The V-process moulding was developed in 1971, in Japan. This uses

unbonded sand and a vacuum. The first cast metal matrix composite automobile part, a brake rotor, was used in production in 1996 by Lotus. The electromagnetic casting process was developed in 1997; this reduces the cost and energy expenditure in steel production.

In casting's long journey, this began over 6000 years ago between the Tigris and Euphrates Rivers, in a land known as Mesopotamia. Ancient artisans produced idols and ornaments using natural beeswax for patterns, clay for moulds and manually operated bellows for stoking furnaces. Today's precision components for spacecraft and jet engines are produced by investment castings using the latest advances in computer technology, robotics and counter-gravity casting techniques.

Computer aided engineering in the metal forming industry has been an area of intense research activity for the last three decades. In order to remain competitive in today's market, a modern metal forming industry has to take full advantage of the benefits offered by such techniques. Thus, process problems can be analysed in detail, faster and at an earlier stage in the design cycle [5]. The modelling of liquid-solid phase-change phenomena is extremely important in many areas of science and engineering for example in the automotive and aerospace industries this has become increasingly intense. As suppliers and manufacturers of components strive to maintain profit margins whilst reducing cost, it is evident that the manufacturing process involved should be more productive and of higher quality.

## **1.2 Solidification Process**

Solidification involves a wide range of physical phenomena but the most challenging to model is the complexity of interaction among physical phenomena occurring on different length scales ranging from atomic rearrangements over single crystal-melt interaction, to heat release at the system level. Dendritic solidification and physical scales are shown in Figure 1-2 and classified as [6]:

- (a) Macroscopic scale: mass, momentum, heat and species transport phenomena, cooling rate, latent heat evolution, grain patterns, macrosegregation, porosity, volume change
- (b) Grain scale: columnar and equiaxed crystals, local heat and species transfer, interfacial drag, spacing, coarsening
- (c) Interfacial scale: interface instabilities, capillarity, local equilibrium, dendrite tip under cooling and movement
- (d) Atomic scale: nucleation and multiplication of crystals, atomic attachment kinetics and interface structure (faceted, non-faceted)



Solidification during the phase-change involves rearrangements of atoms to form a new crystal structure. Therefore, in terms of energy levels it requires heat flux from the system to the surroundings which changes the free energies and also the relative thermodynamic stability of the phase present. Small grains having random orientations are nucleated in the melt and rapidly progress developing dendritic arms, which is shown in Figure 1-3. An equiaxed zone is formed close to the mould surface and competitive growth is experienced by the random oriented outer equiaxed grains, see Figure 1-4, which have a preferred growth direction (parallel and opposite to the direction of the heat flow) to eliminate the others [7]. Columnar grains (planar interface) are the case for pure materials and equiaxed dendrites (constitutional) are the case for alloys.

The essential feature of solidification is the existence of a moving interface between the liquid and the solid phases at the macroscopic scale as defined in Figure 1-2, where the moving front has to be determined. Heat is released/absorbed within the moving front and thermal properties of the liquid and the solid phases are thus different, which makes this problem complex and highly non-linear.

### ***1.3 Conventional solidification processes***

Recent research has demonstrated that if the liquid velocity exceeds a critical velocity there will be a danger that the surface of the liquid metal may fold over by surface turbulence [8]. Therefore, a surface oxide film may fold into the bulk of the liquid if the speed of advance of the liquid front exceeds this critical velocity. The folded films constitute initiation sites for gas entrapment, shrinkage cavities and hot tears. After being frozen into the casting the folded films become effective cracks, lowering strength and fatigue resistance. Castings, for which velocities throughout the mould never exceed the critical velocity, are consistently strong with a high fatigue resistance. Hence, a formation of defects can occur if the critical velocity is exceeded at the gate entrance. However, the following essential terminology used in the casting process is listed, which facilitates the understanding of casting processes [5]

#### ***Terminology***

- Pattern: An approximate duplicate of the final casting used to form the mould cavity.
- Moulding material: The material that is packed around the pattern and then the pattern is removed to leave the cavity where the casting material will be poured.
- Flask: The rigid wood or metal frame that holds the moulding material.

- Cope: The top half of the pattern, flask, mould or core.
- Drag: The bottom half of the pattern, flask, mould or core.
- Core: An insert in the mould that produces internal features in the casting, such as holes.
- Core print: The region added to the pattern, core or mould used to locate and support the core.
- Mould cavity: The combined open area of the moulding material and core where the metal is poured to produce the casting.
- Riser: An extra space in the mould that fills with molten material to compensate for shrinkage during solidification.
- Gating system: The connected channels that deliver molten material into the mould cavities.
- Pouring cup or pouring basin: The part of the gating system that receives the molten material from the pouring vessel.
- Sprue: The pouring cup attaches to the sprue, which is the vertical part of the gating system. The other end of the sprue attaches to the runners.
- Runners: The horizontal portion of the gating system that connects the sprues to the gates.
- Gates: The controlled entrances from the runners into the mould cavities.
- Vents: Additional channels that provide an escape for gases generated during the pour.
- Parting line or parting surface: The interface between the cope and drag halves of the mould, flask or pattern.
- Draft: The taper on the casting or pattern that allow it to be withdrawn from the mould
- Core box: The mould or die used to produce the cores.

Although many conventional processes suffer from defects, they still form an important part of the casting industry. The following general classification is based on the re-usability of the mould for the solidification process.

### 1.3.1 Expendable mould casting

Expendable mould casting is a generic classification that includes plaster, sand, shell, investment (lost-wax technique) and lost-foam mouldings. This method of mould casting involves the use of temporary, non-reusable moulds.

### **1.3.1.1 Waste moulding of plaster**

A durable plaster intermediate is often used as a stage toward the production of a bronze sculpture or as a pointing guide for the creation of a carved stone. A plaster reproduction of the clay original work is more durable and resistant to cracking due to the fact that it does not need be constantly moist, hence it can be storage. In waste moulding a simple and thin plaster mould, reinforced by sisal or burlap, is cast over the original clay mixture. After, the plaster reproduction is cured and removed from the original clay during which incidentally some fine details can be destroyed in the undercuts present in the clay. However any details have been captured in the plaster mould [2]. The mould may then at any later time be used to cast a plaster positive image, identical to the original clay. The surface of this plaster may be further refined and may be painted and waxed to resemble a finished bronze casting [5].

### **1.3.1.2 Sand casting**

Sand casting is one of the most popular and simplest types of casting that has been used for centuries. Sand casting is ideal for small batches to be produced in comparison to permanent mould casting [9]. A green (moist) sand casting has almost no part weight limit, whereas dry sand has a practical part mass limit of 2300–2700 kg. Minimum part weight ranges from 0.075–0.1 kg. The sand is bonded together using clays, chemical binders or polymerized oils (such as motor oil). Sand can be recycled many times in most operations and requires little maintenance.

The mould is formed in a mould box with two halves that helps in removing the pattern, shown in Figure 1-5. Sand moulds are temporary in nature; a new mould has to be formed each time for an individual casting.

Drag, the bottom half of the mould, is made on a moulding board. Cores require greater strength to hold their form during pouring. Dimensional precision also needs to be greater because interior surfaces are more difficult to machine, hence errors are costly to fix. One of the chemical binding systems is used in forming the cores. Once the core is inserted, the top half of the mould or the cope, is placed on top. The interface between the two mould halves is called a parting line. Sometimes, weights are placed on the cope, which helps in securing the two halves together [10].

### **1.3.1.3 Plaster mould casting**

Plaster casting is similar to sand casting except that plaster of paris is substituted for sand as a mould material.

Generally the form takes less than a week to prepare after which a production rate of 1–10 units/hr-mould can be achieved with items as massive as 45 kg (99 lb) and as small as 30 g (1 oz) with very good surface finish and close tolerances [10]. Plaster casting is an inexpensive alternative to other moulding processes for complex parts due to the low cost of the plaster and its ability to produce near net shape castings. The biggest disadvantage is that it can only be used with low melting point non-ferrous materials such as aluminium, copper, magnesium and zinc [5]

#### **1.3.1.4 Shell moulding**

Shell moulding is similar to sand casting but the moulding cavity is formed by a hardened "shell" of sand instead of flask filled with sand. The sand used in this process is finer than normal casting sand and is mixed with a resin so that it can be heated by the pattern and harden into a shell around the pattern. Because of the resin it gives a much finer surface finish, see Figure 1-6. The process is easily automated and more precise than sand casting [2]. Common metals that are cast include cast iron, aluminium, magnesium and copper alloys. This process is ideal for complex items that are small to medium sized.

#### **1.3.1.5 Investment casting**

Investment casting (known as lost-wax casting) is a process that has been practised for thousands of years with the lost-wax process being one of the oldest known metal forming techniques. From 6000 years ago when beeswax formed the pattern, to today's high technology waxes, refractory materials and specialist alloys, the castings ensure that high-quality components are produced with key benefits of accuracy, repeatability, versatility and integrity [2].

Investment casting derives its name from the fact that the pattern is invested or surrounded with a refractory material. The wax patterns require extreme care for they are not strong enough to withstand forces encountered during the mould making. One advantage of investment casting is that the wax can be re-used [10]

The process is suitable for repeatable production of net shape components from a variety of different metals and high performance alloys. Although generally used for small castings, this process has been used to produce complete aircraft door frames with steel castings of up to 300 kg and aluminium castings of up to 30 kg. Compared to other casting processes such as die casting or sand casting it can be an expensive process. However the components that can be produced using investment casting can incorporate intricate

contours and in most cases the components are cast near net shape thus requiring little or no rework once cast.

#### **1.3.1.6 Lost-foam casting**

Lost-foam casting is a type of evaporative-pattern casting process that is similar to investment casting except that foam is used for the pattern instead of wax, see Figure 1-7. This process takes advantage of the low boiling point of foam to simplify the investment casting process by removing the need to melt the wax out of the mould [5, 10].

#### **1.3.1.7 Full-mould casting**

Full-mould casting is an evaporative-pattern casting process which is a combination of sand casting and lost-foam casting. It uses an expanded polystyrene foam pattern which is then surrounded by sand much like sand casting. The metal is then poured directly into the mould, which vaporizes the foam upon contact [10].

#### **1.3.1.8 Vacuum casting**

In this process a thin preheated sheet of plastic film is placed over a pattern and a vacuum is applied to draw the sheet to the pattern contours. The flask containing the mould is filled with dry unbonded silica sand which is compacted by vibration. A second plastic sheet is placed at the back of the flask and the mould is further compacted under vacuum. Whilst the vacuum process is maintained, the pattern is then removed and the two halves of the mould are joined and secured for pouring, see Figure 1-8. After the metal has solidified, the vacuum is removed and the casting is released [2]. The vacuum process can produce castings of all sizes and shapes which range from thin-sectioned curtain walls in aluminium to cast iron pressure pipe fittings and stainless steel valve bodies to massive 8-tonne ship anchors [9].

### **1.3.2 Non-expendable mould casting**

Non-expendable mould casting differs from expendable processes in that the mould will have a considerably longer production life. This technique includes at least four different methods: permanent, die-casting, semi-solid casting, centrifugal and continuous casting.

#### **1.3.2.1 Permanent mould casting**

Permanent mould casting is a metal casting process that employs reusable moulds ("permanent moulds"), usually made from metal. The most common process uses gravity to fill the mould however gas pressure or a vacuum are also used. Common casting metals

are aluminium, magnesium and copper alloys. Other materials include tin, zinc, lead alloys, iron and steel are also cast in graphite moulds [11, 12]. Permanent moulds while lasting more than one casting still have a limited life before wearing out.

### **1.3.2.2 Die casting**

The die-casting process forces molten metal under high pressure into mould cavities which are later machined into the desirable form. Most die-castings are made from nonferrous metals, specifically zinc, copper and aluminium based alloys but ferrous metal die-castings are possible [5, 12].

High pressure die-casting is the most common process used, where molten non-ferrous metals are injected at high pressure into a metal mould by a hydraulically powered piston, see Figure 1-9. The equipment for the process can be very costly, hence high pressure die-casting is only economically viable when used for high volume production [5].

Low pressure die-casting uses a die that is filled from a pressurised crucible underneath, see Figure 1-10. The process is particularly suited to the production of rotationally symmetrical products such as automobile wheels.

The die-casting method is especially suited for applications where many small to medium sized parts are needed with good detail, a fine surface quality and dimensional consistency.

### **1.3.2.3 Semi-solid metal casting**

Semi-solid metal (SSM) casting is a modified die casting process that reduces or eliminates the residual porosity present in most die castings. Rather than using liquid metal as the feed material, SSM casting uses a higher viscosity feed material that is partially solid and partially liquid. A modified die casting machine is used to inject the semi-solid slurry into re-usable hardened steel dies. The high viscosity of the semi-solid metal, along with the use of controlled die filling conditions, ensures that the semi-solid metal fills the die in a non-turbulent manner so that harmful porosity can be essentially eliminated [13].

The combination of heat treatment, fast cooling rates (from using un-coated steel dies) and minimal porosity provides excellent combinations of strength and ductility. Other advantages of SSM casting include the ability to produce complex shaped parts net shape, pressure tightness, tight dimensional tolerances and the ability to cast thin walls [13]. This process is further explained in section 1.4

### **1.3.2.4 Centrifugal casting**

Centrifugal casting is both gravity and pressure independent which enables the generation of its own force feed, up to 900 N, using a temporary sand mould held in a spinning

chamber. Semi- and true-centrifugal processing permits 30-50 pieces/hr-mould to be produced, with a practical limit for batch processing of approximately 9000 kg total mass with a typical per-item limit of 2.3-4.5 kg.

Small art pieces such as jewellery are often cast by this method using the lost wax process as the forces enable the rather viscous liquid metals to flow through very small passages and into fine details such as leaves and petals [2]. This effect is similar to the benefits from vacuum casting, also applied to jewellery casting.

### **1.3.2.5 Continuous casting**

Continuous casting is a refinement of the casting process for the continuous, high-volume production of metal sections with a constant cross-section. Molten metal is poured into an open-ended, water-cooled copper mould, which allows a 'skin' of solid metal to form over the still-liquid centre. The strand, as it is now called, is withdrawn from the mould and passed into a chamber of rollers and water sprays; the rollers support the thin skin of the strand while the sprays remove heat from the strand, gradually solidifying the strand from the outside in, see Figure 1-11. After solidification, predetermined lengths of the strand are cut off by either mechanical shears or travelling oxyacetylene torches and transferred to further forming processes or to a stockpile [3, 4]. Cast sizes can range from strip (a few millimetres thick by about five metres wide) to billets (90 to 160 mm square) to slabs (1.25 m wide by 230 mm thick). Sometimes the strand may undergo an initial hot rolling process before being cut [5].

Continuous casting is used due to the lower costs associated with continuous production of a standard product and also increases the quality of the final product. Metals such as steel, copper and aluminium are continuously cast, with steel being the metal with the greatest production cast using this method.

## **1.4 Special solidification processes**

The reduction in processing involved by casting parts rather than using forging or other techniques, has encouraged the use of cast parts in applications where previously other techniques were the only way of obtaining the required mechanical properties. In order to achieve the required mechanical specification the casting process should be controlled to ensure that the parts produced are reliably free from defects, rather than use steel or iron-cast parts which are made to fulfil the specific properties and quality by conventional processes. Industries such as automotive and aerospace have shown an interest in the advantages offered from the die-casting process [14, 15, 16]. The process has been

constantly developed over the years and now presents an option, which increases the quality and decreases the cost of the cast products. It is now common to simulate the filling and basic aluminium solidification, allowing the prediction of macro-structural defects such as incomplete filling [14] or hotspots due to restricted flow [15].

Advances in new casting technology have been used in pressure die-casting in particular to obtain mould filling at low speed. This can be achieved by using innovative filling processes with aluminium alloys in the liquid or semisolid state. Different techniques such as high-pressure die-casting (HPDC), low-pressure systems, squeeze casting, indirect squeeze casting, metal compression forming (MCF) and semisolid metal (SSM) processing have been developed. Semisolid forming includes thixoforming and rheoforming. During the semisolid casting process preheating by induction is needed to obtain the same temperature and the same liquid fraction through the billet in a short time. Thixocasting in the semisolid state helps to avoid turbulence during mould filling.

Globular microstructure is required to perform a successful forming of metals in the two-phase stage. This type of morphology is commonly obtained by vigorous agitation during solidification but can also be achieved by sufficiently grain refinement [17, 18], long ripening time [19], continuous rheocasting and vigorous electromagnetic stirring of continuous castings [20].

The physics of primary particle morphology during solidification with vigorous agitation is shown in Figure 1-12. Two methods can be applied to achieve a globular microstructure and these are rheocasting or as-rheocast [20, 21], which are best suited for a forming process. The former utilizes the slurry from vigorous agitation during early stages of solidification whilst the latter uses the slurry that is fully solidified and later partially re-melted without agitation. Thixocasting and thixoforming process heated the metal up between the solidus and liquidus temperature, which allowed the use of less energy on the forming process [22]. Thus working conditions have to be controlled to achieve the required properties, see Figure 1-13 and Figure 1-14.

### **1.4.1 Squeeze casting**

In this process the metal is poured initially into the mould in a liquid state which after solidification initiate the molten metal alloy is under pressure in order to reduce porosity and form a sound part, see Figure 1-15. The pressure reduces the porosity but mould wear and manufacturing costs are higher [10].



### 1.4.2 Indirect squeeze casting

In this process the pressure is applied on the gate area via a plunger and uses pressure during solidification to eliminate porosity, see Figure 1-16(a). However, parts made by the indirect squeeze casting process may be sound near the gate where pressure is applied but may exhibit higher levels of porosity away from the gate making certain areas of the casting weaker. The metal is forced from the injection chamber into the mould cavity which promotes turbulence during filling, trapping gas pockets and oxide films that weaken the casting. In the indirect squeeze-casting process an expected non-uniform pressure distribution during solidification is shown in Figure 1-16(b).

### 1.4.3 Metal compression forming (MCF)

In this process the pressure is applied on the entire mould face which produces a uniformly sound part with forging properties. The MCF process and the expected uniform pressure distribution during solidification are shown in Figure 1-17. Due to the uniform pressure over the entire casting, the MCF process is capable of producing parts with uniformly superior mechanical properties while retaining the near net shape, complexity in geometry, high productivity and relatively low cost of the die-casting process [5].

### 1.4.4 Different processes to produce a billets in a semisolid state

Metals have been processed either in the liquid state (casting) or in the solid state (forging). Processing aluminium alloys in the semisolid state is an intermediate route between forging and casting [21]. The basic semisolid process involves vigorous agitation of the molten metal during earlier stages of solidification so as to break up the solid dendrites into small spherulites, see Figure 1-18.

Two main processes, shown in Figure 1-19, are available to industry for the exploitation of the original concept. The first method is the “rheocasting” process that consists of the preparation of a gel, constant mechanical churn and of its moulding at the same temperature of the preparation. The second method is the thixoforming process where ingots are prepared in the first stage from structured gels which will be reheated to a plastic state in order to permit their moulding by pressure die-casting or by forging as shown in Figure 1-18 and Figure 1-19.

There are many different processes based on the behaviour of an alloy in a thixotropic semisolid state but all are based on solid globular dendrites dispersed in a liquid eutectic phase. In this state the material looks like a solid but shows a pseudoplastic (viscosity decreases with the increasing shear rate) and thixotropic behaviour (viscosity decreases

with the shear stress application time) [23]. Some billets in the reheating state have the consistency of butter-like and it is possible to cut the billet with a blade Figure 1-18 or to move it mechanically, placing it in a die like a solid and then injecting it by a piston (like a liquid). This is due to the reduced viscosity due to the shear forces applied during the forming operations. The different steps for the thixoforming process are shown in Figure 1-19. The material has to be subjected to a preliminary procedure for obtaining thixotropic feedstock billets, which has a structure suitable for injection in the semisolid state, see Figure 1-20. Many routes are available for aluminium alloys in order to reach the specific billet structure, which the more common methods are presented.

#### **1.4.4.1 Mechanical stirring casting**

A gel produced by agitation in a crucible between the liquidus and the solidus temperature is shown in Figure 1-19(a) and Figure 1-20. This thixotropic gel is then moulded directly to castings with the lost-wax process by centrifugal casting. The advantage of this technology consists of the elimination of plastic billet handling as in the case of thixoforming. The rheocaster eliminates the need for transfer of the gel because the bascule crucible is used also as a mould for producing billets Figure 1-19. The advantage of this technology is the precision of the permissible controls and the capability to obtain any type of gel with different solid fractions [21], see Figure 1-20(a).

#### **1.4.4.2 Electromagnetic or magneto-hydrodynamic (MHD) agitation**

In this process the solidifying material is agitated by electromagnetic forces induced in the metal shown in Figure 1-20(c) and Figure 1-20(d) and a certain shear rate to solidification rate ratio is maintained. A globular structure non-dendritic material can be obtained via this process and it is by far the most commonly used process presently in the aluminium industry to continuously cast semisolid metal (SSM) billets [13, 21].

#### **1.4.4.3 Stir casting by ultrasonic-waves**

The melt metal is held in a ceramic crucible and a waveguide that is linked to ultrasonic transducer which is dipped in the melt as shown in Figure 1-21. During the fabrication of metal matrix with embedded nano-sized particles, the close environment was covered by an inert gas and the temperature was above the melting point [24].

#### **1.4.4.4 Passive stir casting**

In this case the liquid metal is forced to flow through fixed obstacles or static mixers as shown in Figure 1-20 (b). Reference is made to the melted injection into dies as semisolid (MIDAS) process [21].

#### **1.4.4.5 Extrusion**

The process relies on a metal re-crystallizing at elevated temperature after it has been sufficiently cold worked. The cold-worked metal is brought to a temperature in the semisolid state where first re-crystallization and then partial melting occur [13, 21]. The newly re-crystallized grains tend to be spheroidal in shape and the state of thixotropy can be achieved Figure 1-20 (e)

#### **1.4.4.6 Grain refinement by continuous casting**

Continuous casting with additions of grain refining elements is an option to obtain thixotropic structures Figure 1-20(f).

#### **1.4.4.7 Pressure die-casting (PID)**

In this process a billet is moulded under pressure from the liquid state at the desired size. Flow and thermal condition are controlled in which a fine dendritic structure without porosity will be the outcome. At the same time a component (conventional with porosity) can be cast [21]. The role of this component is to act as an overflow in order to obtain a porosity-free billet and to reduce the production cost of feedstock as shown in Figure 1-22.

### **1.5 Mathematical modelling**

#### **1.5.1 Introduction**

A computational model is a mathematical model that requires extensive resources to study the behaviour of a complex system by simulation. The system under study is often a complex nonlinear system for which simple, intuitive analytical solutions are not readily available. Rather than deriving an analytical solution to the problem, experimentation with the mathematical model is done by changing the parameters of the system in the computer and studying the differences in the outcome of the experiments. Theories of operation of the model can be derived/deduced from these computational experiments [25].

Computer simulations vary from computer programs that run a few minutes to network-based groups of computers running for hours, to ongoing simulations that run for days. The

scale of events being simulated has exceeded anything using the traditional mathematical modelling [26, 27].

### 1.5.2 Simulation or modelling

Traditionally, forming large models of systems has been via a mathematical model which attempts to find analytical solutions to problems and thereby enable the prediction of the behaviour of the system from a set of parameters and initial conditions [28].

While computer simulations might use some algorithms from purely mathematical models, computers can combine simulations with reality or actual events such as generating input responses to simulate test subjects who are no longer present.

Note that the term computer simulation is broader than computer modelling which implies that all aspects are being modelled in the computer representation. However, computer simulation also includes generating inputs from simulated users to run actual computer software or equipment with only part of the system being modelled. An example would be flight simulators which can run machines as well as actual flight software.

### 1.5.3 Modelling types

Computer models can be classified according to several independent pairs of attributes [25, 28, 29], including:

- Stochastic or deterministic (and as a special case of deterministic, chaotic)
- Steady-state or dynamic
- Continuous or discrete (and as an important special case of discrete, discrete event or DE models)
- Local or distributed.

Equations define the relationships between elements of the modelled system and attempt to find a state in which the system is in equilibrium. Such models are often used in simulating physical systems as a simpler modelling case before dynamic simulation is attempted.

- Dynamic simulations model changes in a system in response to (usually changing) input signals.
- Stochastic models use random number generators to model chance or random events;
- A discrete event simulation (DES) manages events in time. Most computer, logic-test and fault-tree simulations are of this type. In this type of simulation the simulator maintains a queue of events sorted by the simulated time they should occur. The simulator reads the queue and triggers new events as each event is

processed. It is not important to execute the simulation in real time. It is often more important to be able to access the data produced by the simulation to discover logic defects in the design or the sequence of events.

- A continuous dynamic simulation performs numerical solution of differential-algebraic equations or differential equations (either partial or ordinary). Periodically, the simulation program solves all the equations and uses the numbers to change the state and output of the simulation. Applications include macro-micro solidification, astrophysics (galaxies movement), chemical process, climate predictions and electrical circuits.

#### **1.5.4 Brief history for solidification modelling**

The evolution in the solidification field has been achieved with the combined development of two main areas; numerical solutions and the increased power for computers to handle large calculations. Therefore, the actual sophistication provided for the possible solutions available.

Analytical solutions were first employed in the solidification field in the early 20th century for 1-D problems for relatively simple boundary conditions [30, 31], which have been setting the standards for a group of specific problems that numerical methods have been compared against. Mathematical modelling for 2-D using finite-difference has been developed and their results match with the solutions available [32, 33, 34]. The foundation for semi-solid metal research was developed in the early 1970's where the state of the matter is neither solid nor liquid entirely [13, 21]. Finite element methods are applied to different solidification problems involving Lagrangian or Eulerian system for transient heat and phase-change process [35, 36, 37, 38]

The enthalpy method approach using finite element techniques is used to obtain an approximation for phase-change problems for the complex and non-linear heat transfer analysis [39, 40]. However, finite elements methods have been divided fundamentally into two categories, front tracking (adaptive) methods and fixed domain methods. The former provides for an accurate account for the phase-change but involving complex meshing and re-meshing techniques which have to cater for stretching/collapsing of the phase-change [41, 42, 43]. Although fixed domain methods have been favoured due to their versatility and ease of implementation, their drawback has been the inaccuracy when a discontinuity is present [44, 45, 46, 47, 48, 49]

Stochastic models follow the nucleation and growth of each individual grain whereas deterministic models rely on averaged quantities and equations that are solved on a macroscopic scale.

Some stochastic models also incorporate dendrite tip growth models [50]. However other stochastic models which simulate solidification at a microscopic scale and allow the solution of solute diffusion equations during solidification and the application of solid/liquid interface front tracking methods to the surfaces of the individual dendritic grains, have no need to include dendrite tip growth models [50, 51, 52, 53]

Deterministic models incorporating equiaxed grains most often consider that the grains are static, although models are now attempting to take into account equiaxed grain movement during solidification [53].

Phase-field technique used the same concept as the adaptive method, tracking the phase-change. However, it is applied for a numerical simulation of microstructure evolution in solidification processes involving convection in the liquid phase [54, 55, 56, 57] and a similar approach is found in the cellular automata method [7]

Deterministic models permit modelling at the scale of actual castings, directionally solidified alloys, etc. However they do not permit the accurate modelling of those microstructural factors that are likely to contribute to the columnar to equiaxed transition (CET) such as solute diffusion, interdendritic convection, evolution of equiaxed grain morphology, etc. Stochastic models offer the opportunity to examine the effects of microstructural factors but are severely limited by the sizes of the domains that can be modelled. It is evident that the CET is governed by a complex set of interacting phenomena including the local thermal and solute fields and the number/size of the equiaxed grains.

Analytical and numerical approaches have been developed to increase and involve a close approximation to the solidification problem both macroscopic and microscopic. Chapter 2 presents a brief review for the most influential methods applied to the field. The introduction for the non-physical enthalpy method (NEM) is presented in chapter 3, highlighting the accurate identification of the source term and its complete annihilation. This is shown in the non-physical capacitance results; however the temperature results indicate an improvement in some cases but in the vast majority are very close with the results compared against to the control volume capacitance method. A further investigation on the capability of non-physical enthalpy method to handle more than one discontinuity with mushy zone in the solidification process is presented in chapter 4. Chapters 3 and 4 respectively, involve the non-physical enthalpy method with single

discontinuity and more than one discontinuity with mushy zone. In chapter 5 results are presented covering more than one point, tracking the discontinuity passing throughout the models and analysing the potentiality of the method to annihilate them.



Figure 1-1 The oldest existing copper casting [58]

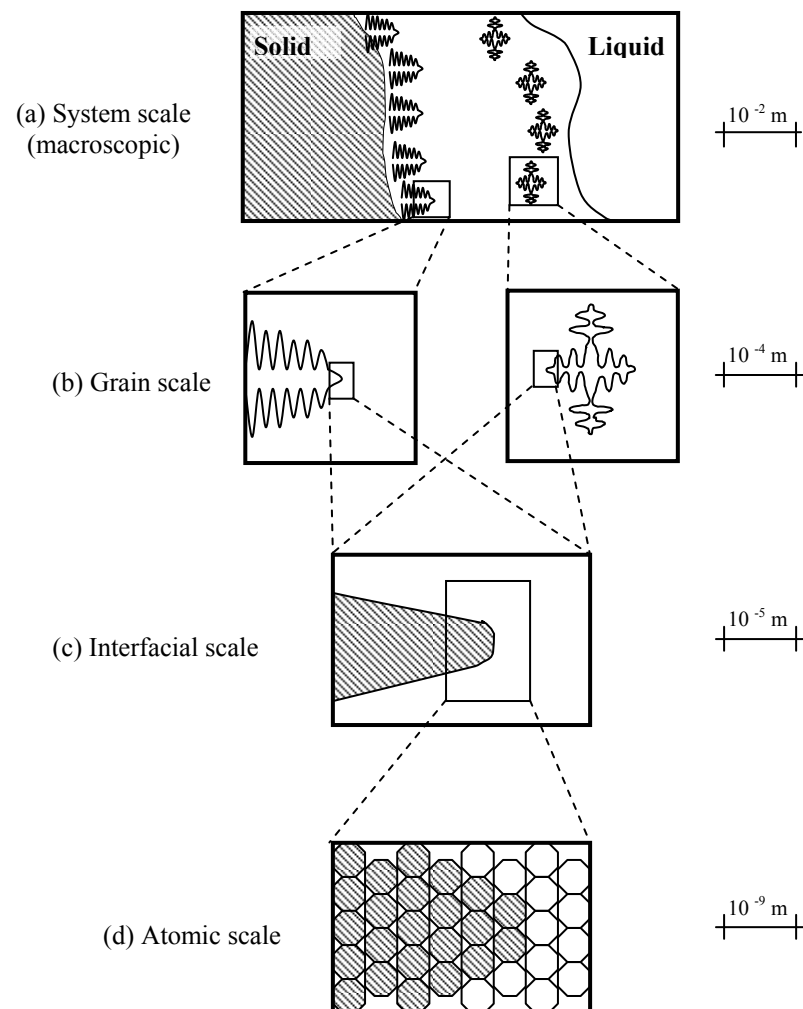
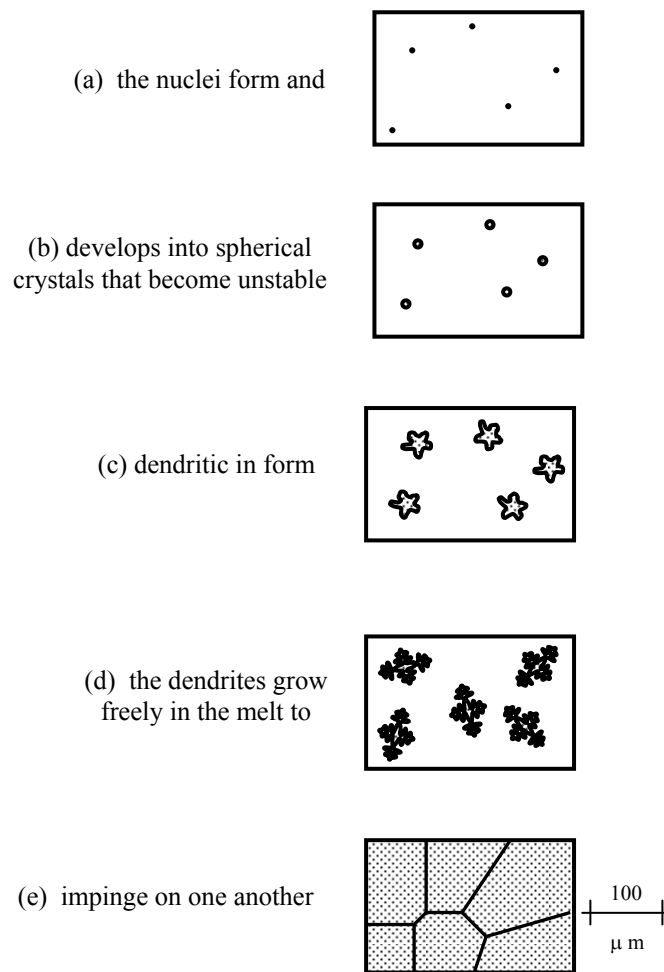
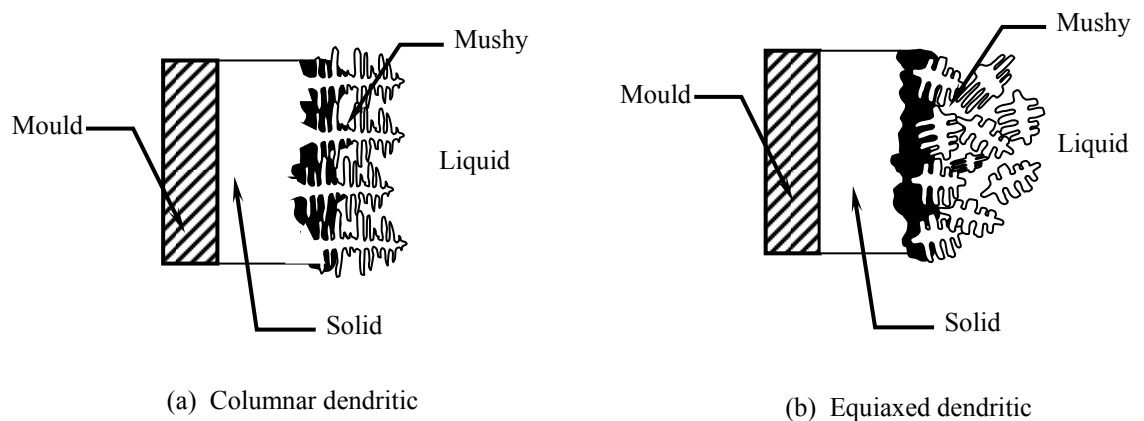


Figure 1-2 Dendritic solidification at different physical scales [59]





**Figure 1-3 Equiaxed solidification process**



**Figure 1-4 Columnar and equiaxed solidification**

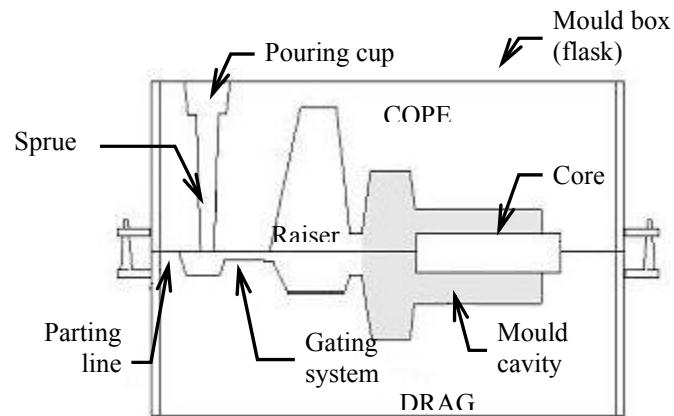


**Figure 1-5 Typical two part sand mould [9]**

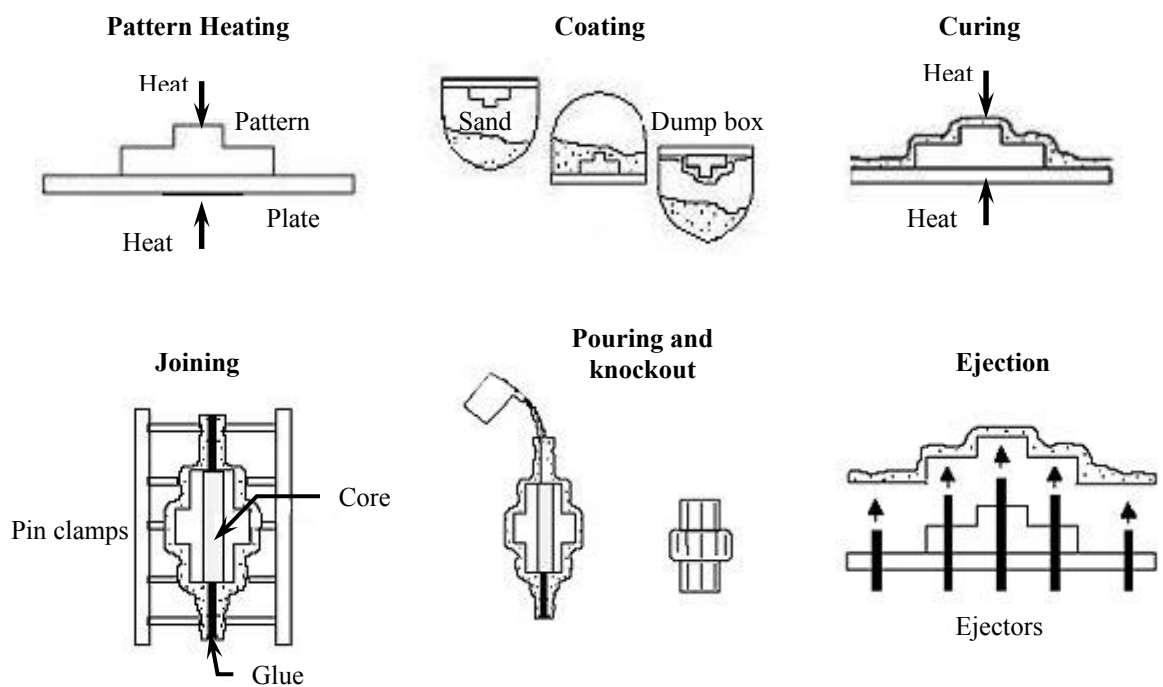


**Figure 1-6 Shell moulding process [10]**

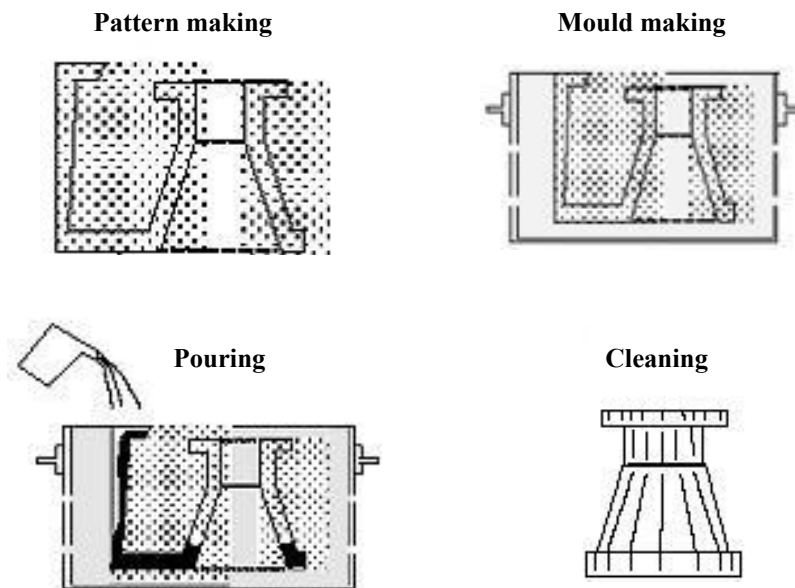


Figure 1-7 Lost foam casting process [10]

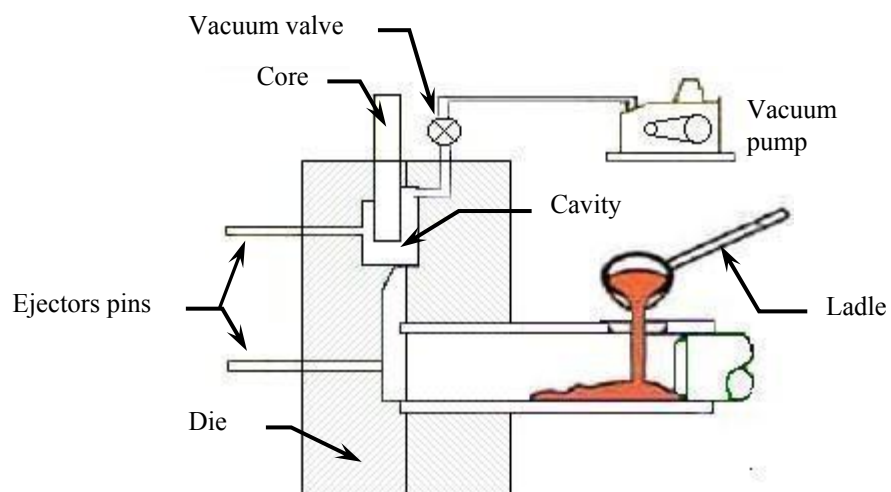
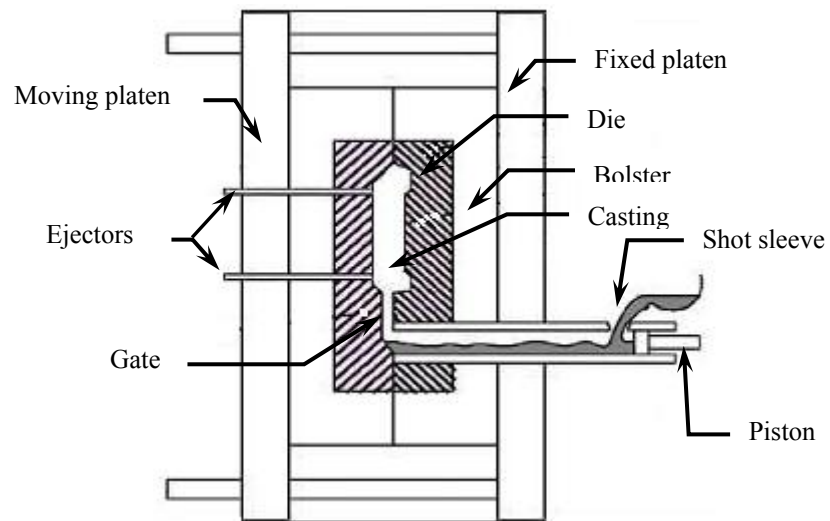
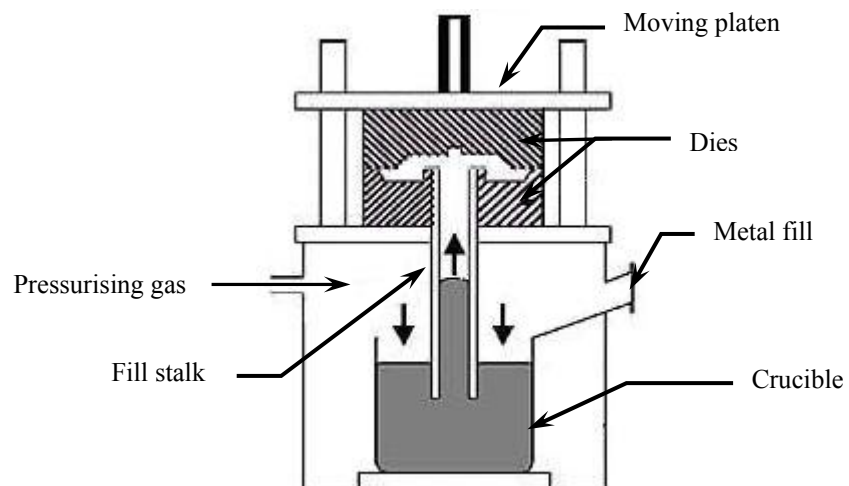


Figure 1-8 Vacuum process [5]



**Figure 1-9 High pressure die-casting process (cold chamber) [5]**



**Figure 1-10 Low pressure die-casting process (hot chamber) [5]**

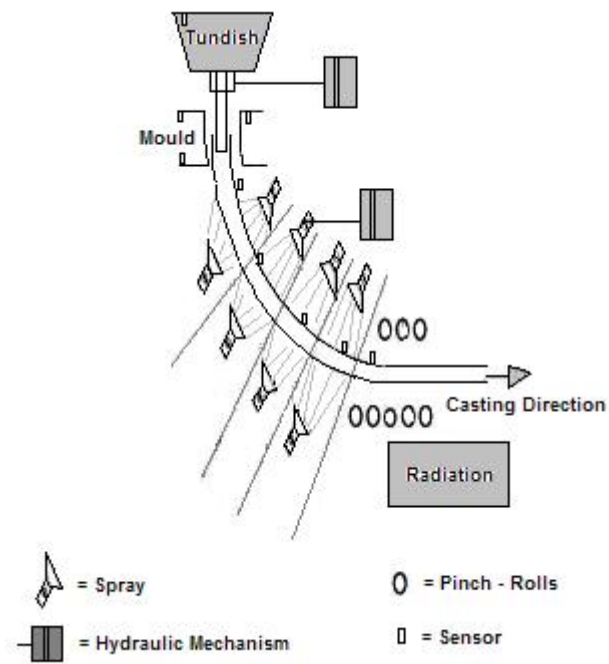


**Figure 1-11 Continuous casting process typical scheme [60]**

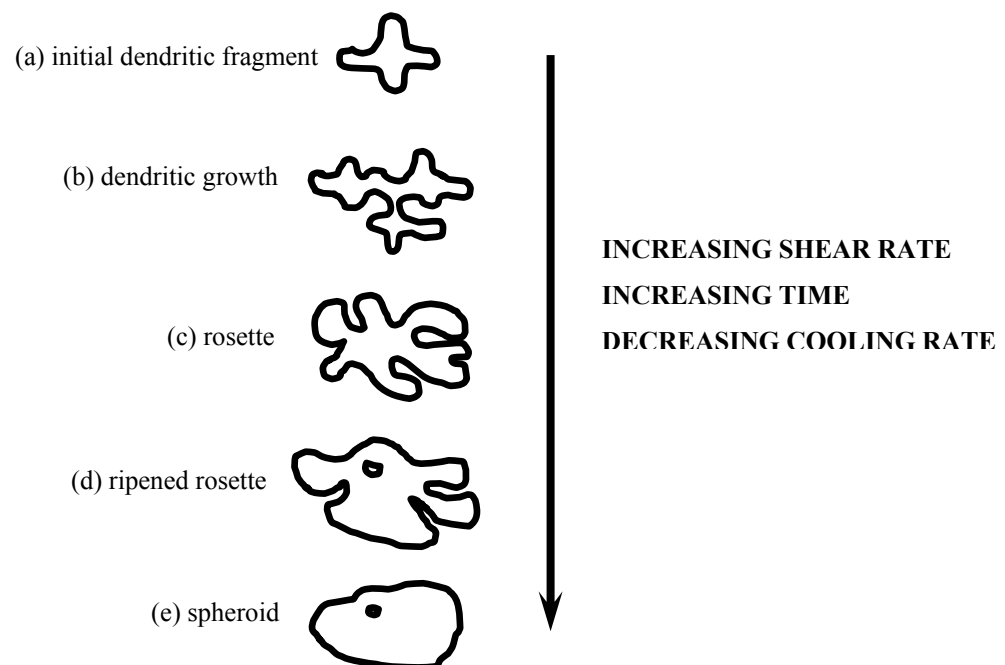


**Figure 1-12 Particle evolution during solidification in combination with agitation**

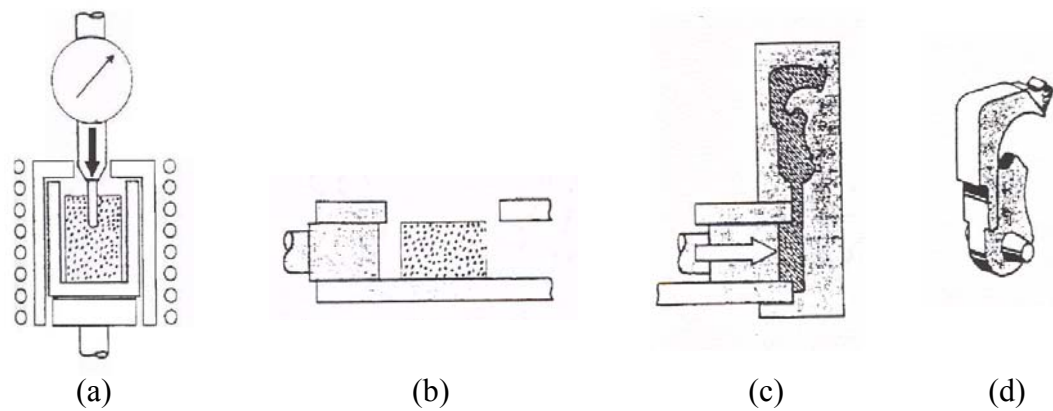


**Figure 1-13 Thixocasting process; (a) heating the billet into the semisolid state, (b) charge in the casting machine, (c) die-casting process and (d) finished model [21]**

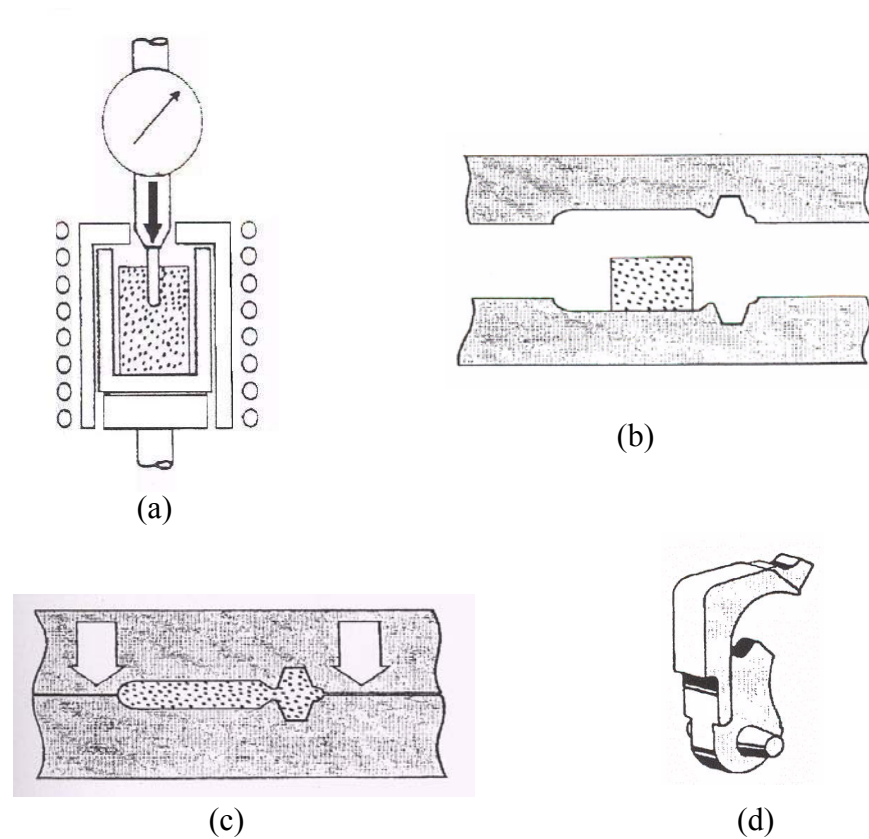


**Figure 1-14 Thixoforging process; (a) heating the billet into the semisolid state, (b) charge in the forging machine, (c) forging process and (d) finished model [21]**

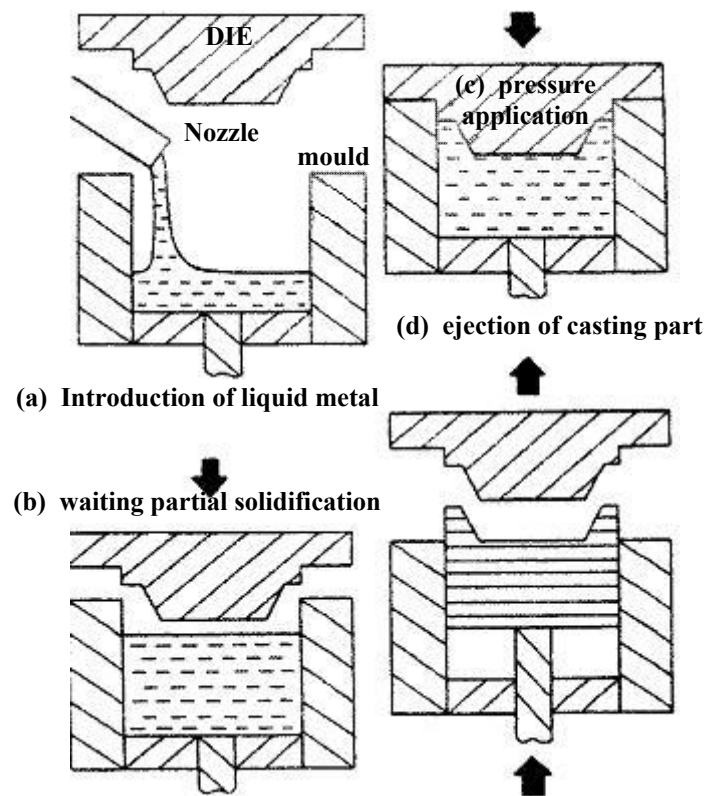


Figure 1-15 Squeeze casting [23]

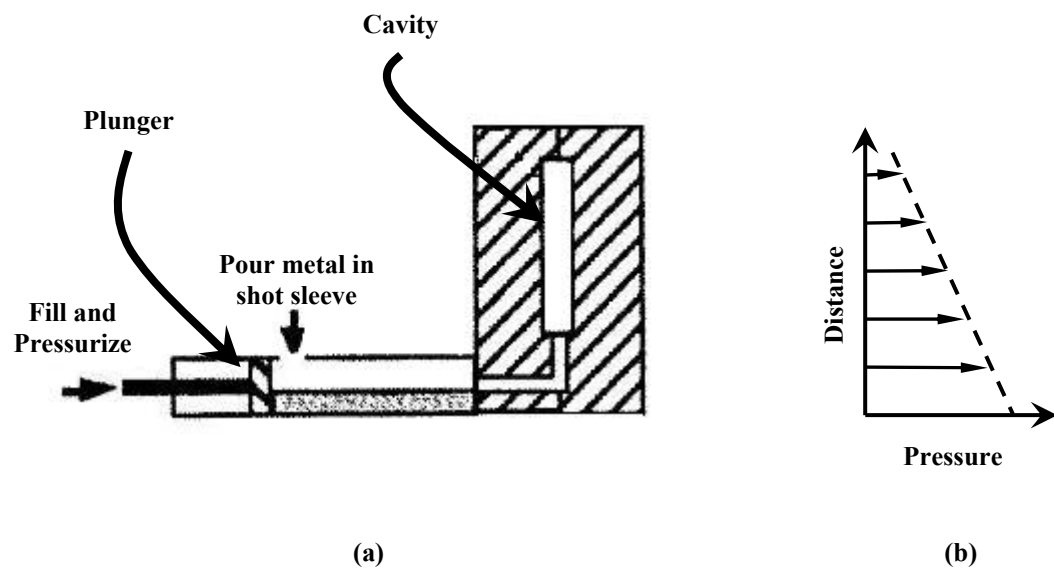


Figure 1-16 Indirect squeeze casting; (a) Metal poured into shot sleeve; (b) resulting non-uniform pressure profile in the die cavity [23]

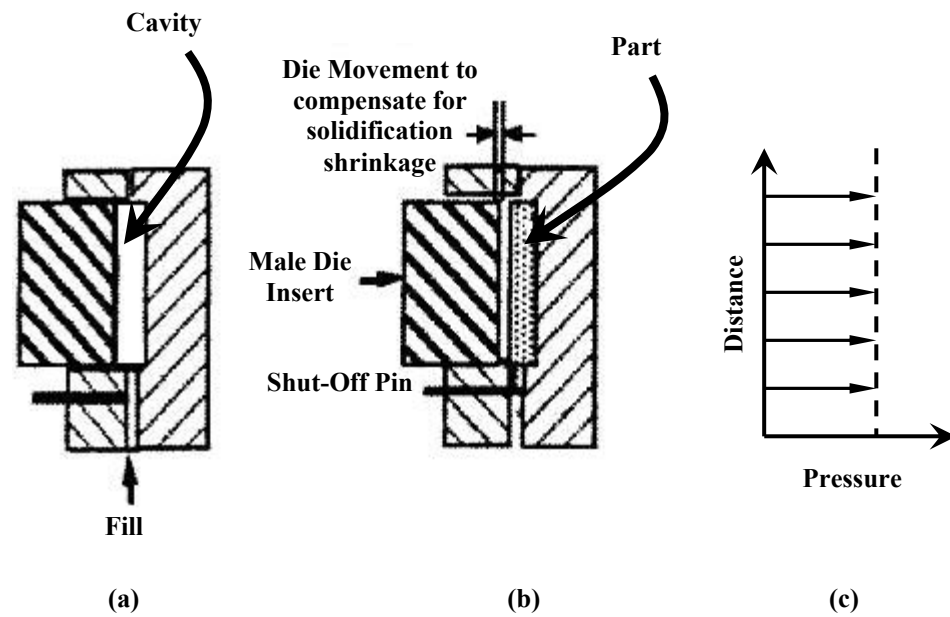


Figure 1-17 Metal compression forming; (a) Shut-off pin is withdrawn for filling; (b) shut-off pin is engaged and the male die pressurizes the cavity; (c) resulting uniform pressure profile in the cavity [23]

## The principle of Thixoforming

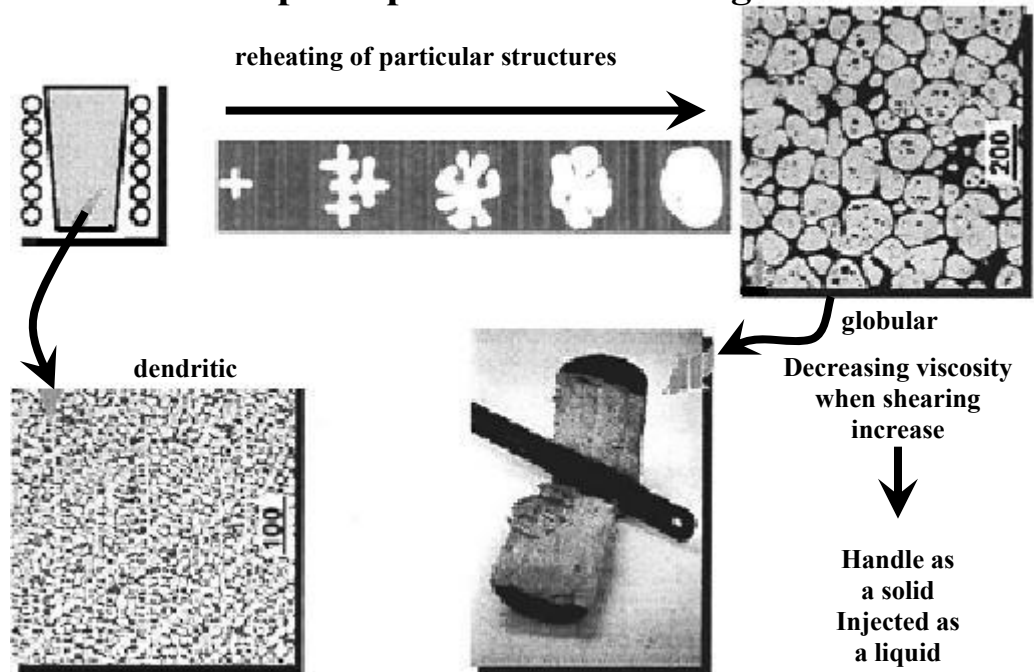


Figure 1-18 Thixoforming process [23]



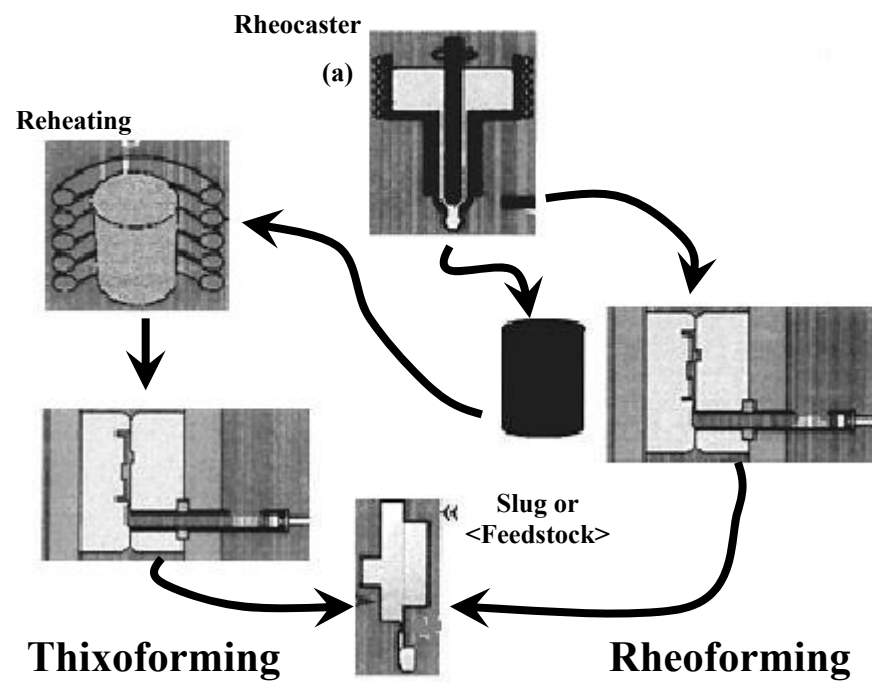


Figure 1-19 Thixoforming and rheocasting [23]

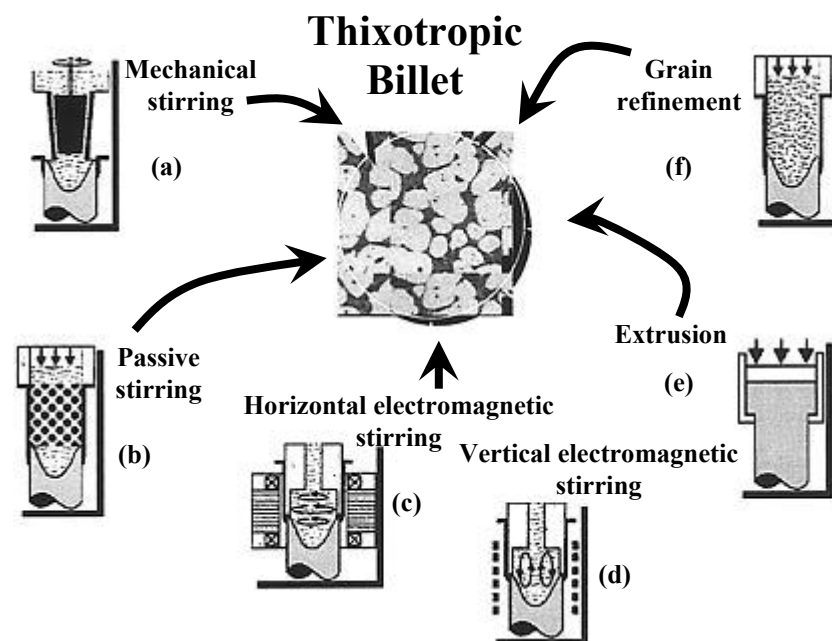


Figure 1-20 Different elaboration processes of billets for thixocasting [23]

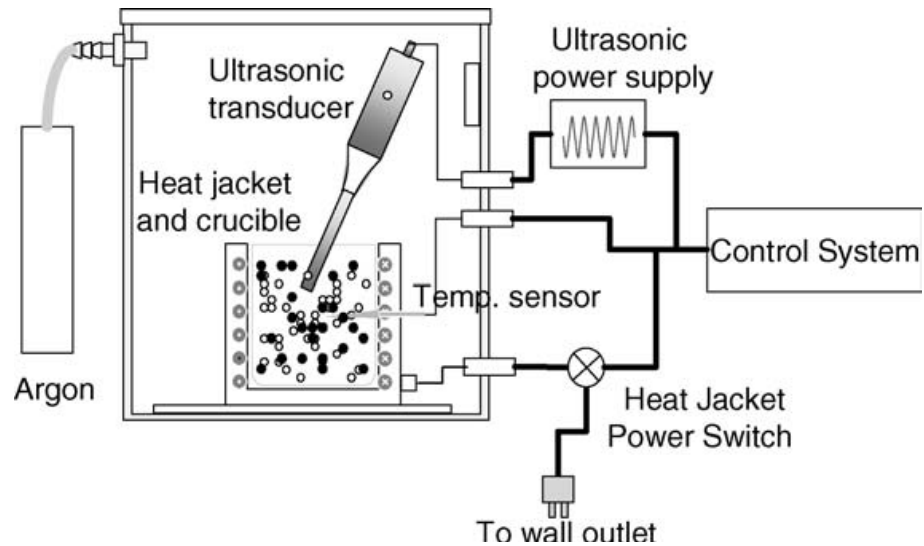
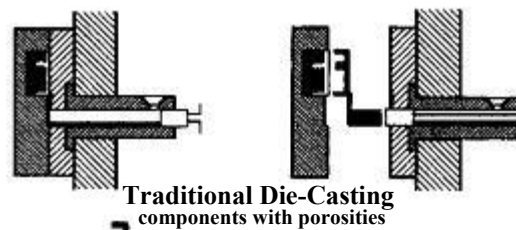


Figure 1-21 Casting stir ultra-sonic process [24]

### Step 1



### Step 2

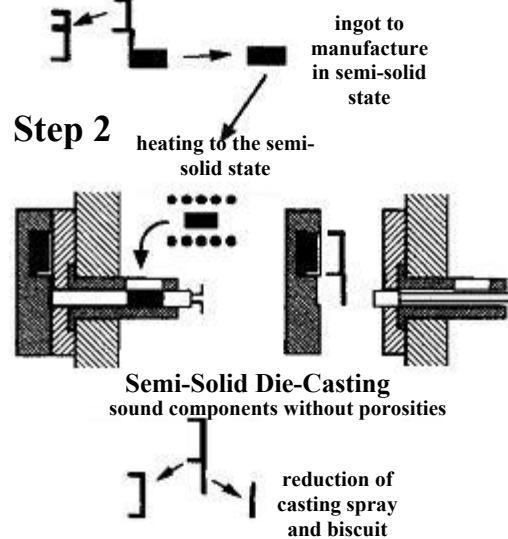


Figure 1-22 PID process [23]

# 2 SOLIDIFICATION METHODS                      MODELLING

---

## ***2.1 Introduction***

The solidification/melting of metals during various casting methods in the foundry provides a source of important practical problems which may be resolved economically with the aid of computational models of the heat transfer processes involved. Experimental design analysis is often prohibitively expensive and the geometries and the complex boundary conditions encountered preclude any analytical solution to the problems posed. Thus, the motivation for numerical simulation and the use of a computational design system is clear, where several mathematical/computational modelling techniques have been brought to bear in this area.

The growing use of computational modelling techniques in recent years reflects the potential economic benefits they offer to many industrial processes including casting methods in the foundry. Numerical simulation of the thermal and mechanical behaviour of

both castings and moulds permit designers to create robust effective products whilst simultaneously minimising process costs and waste. The desired mechanical properties of the finished casting can be controlled by predicting, via numerical experimentation, the effects of using different mould materials and the placement of various chill and/or cooling lines. Waste associated with raisers can be significantly reduced by optimising their magnitude and location.

The representation of latent effects is an important feature in the modelling of solidification problems, which is involved when the matter is subject to a phase-change. Consequently, a boundary separating two different phases develops and moves in the matter during the process. Transport properties vary considerably between phases which result in totally different rates of energy, mass and momentum transport from one phase to another. In these problems the position of the moving boundary cannot be identified in advance but has to be determined as an important constituent of the solution. Moving boundary problems are associated with time-dependent boundary problems, where the position of the moving boundary must be determined as a function of time and space. Although these were studied as early as 1831 by Lamé and Clapeyron [61], a sequence of articles [62, 63] written by Stefan has given his name to this family of problems which resulted from his study of the melting of the polar ice cap around 1890.

Solidification/melting is accompanied by the release/absorption of latent heat at the solid–liquid discontinuity. When a conventional alloy or an impure metal is cooled from a liquid state it begins to solidify at a liquidus temperature ( $T_{\text{liq}}$ ) and solidifies completely at the solidus temperature ( $T_{\text{sol}}$ ). There is no sharp demarcation between the solid and liquid phases. A two-phase mixture region, termed as the mushy zone, separates the two phases. Pure metals and eutectic alloys undergo phase-change isothermally, i.e. solidification occurs at a constant temperature

In the early days of modelling solidification/melting problems, analytical methods were the only means available to provide an understanding of physical processes involving the moving boundary. Although analytical methods offer an exact solution and are mathematically elegant, analytical solutions are predominantly applicable to one-dimensional cases of an infinite or semi-infinite region with simple initial and boundary conditions and constant thermal properties [30, 31]. Practical solidification/melting problems are rarely one dimensional, initial and boundary conditions are always complex, thermophysical properties can vary with phases, temperatures and concentration and various transport mechanisms (for example, convection, conduction, diffusion and radiation) can happen simultaneously. Mathematical modelling and computer simulation

often become the most economical and fast approaches to provide a broad understanding of the practical processes involving the moving boundary problems. Nowadays in most engineering applications, recourse for solving the moving boundary problems has been made to numerical analyses that utilize finite difference, finite element or boundary element methods. The success of finite element and boundary element methods lies in their ability to handle complex geometries but they are acknowledged to be more time consuming in terms of computing and programming.

One-dimensional diffusion-controlled problems were initially the focus for early researchers using very simple geometries due to constraints in the tools available at that time. The analytical solutions developed during this period have served as a foundation of this discipline and are still used today as standard references to validate the numerical models. The advent of computers has enabled the consideration of multidimensional problems with more complex geometries. New progress for the analysis in the solidification/melting problems commenced with the birth of numerical methods. Perhaps owing to the limited power of the earlier computers, the numerical models during this second period of progress were developed and based on one equation (e.g., energy or diffusion equation) and omitted convection. More sophisticated numerical models have been developed to handle multidimensional phenomena involving convection as well as the presence of the moving boundary in complex geometries.

The succeeding sections will summarize the major developments in mathematical analyses of the phase-change problems involved in melting and solidification phenomena. Due to the vast research field, only some of the well known and novel numerical methods available will be presented and compared for the phase-change problem.

## **2.2 Analytical methods**

### **2.2.1 Neumann's method**

The simplest phase-change problem is the one-phase problem first solved analytically [62]. One-phase designates only one of the phases (liquid) being active, the other phase staying at its solidification temperature. Stefan's solution with constant thermo-physical properties shows that the rate of solidification/melting in a semi-infinite region is governed by a dimensionless number. This is known as the Stefan number (St)

$$St = \frac{c_\ell (T_i - T_{liq})}{L} \quad (2.1)$$

where  $c_\ell$  is the heat capacity of the liquid,  $L$  is the latent heat release,  $T_i$  and  $T_{\text{liq}} = T_{\text{sol}}$  are the temperatures of the surrounding and phase changing point respectively for isothermal solidification.

On a more realistic scenario Neumann [31] extended Stefan's solution to the two-phase problem, the initial state of the phase-change material is assumed to be liquid, for a solidification process but its initial temperature is not equal to the phase-change temperature and its temperature during the solidification is not maintained at a constant value. When solidification on a semi-infinite slab ( $0 < x < \infty$ ) is considered initially liquid with a uniform temperature  $T_{\text{liq}} \leq T_\ell$  and a constant temperature is imposed on the surface  $x = 0$  whilst assuming constant thermo-physical properties, the governing equations for the heat conduction in the liquid and solid domain on 1-D problem are respectively

$$\frac{\partial T_\ell}{\partial t} = \kappa_\ell \frac{\partial^2 T_\ell}{\partial x^2} \quad \text{for } X(t) < x, \quad t > 0 \quad (2.2)$$

$$\frac{\partial T_s}{\partial t} = \kappa_s \frac{\partial^2 T_s}{\partial x^2} \quad \text{for } 0 < x < X(t), \quad t > 0 \quad (2.3)$$

where  $\kappa_\ell$  and  $\kappa_s$  are the thermal diffusivity in the liquid and solid domain respectively. However the interface temperature at the moving front is defined by equation (2.4) for the isothermal case

$$T(X(t), t) = T_{\text{liq}} = T_{\text{sol}} \quad t > 0 \quad (2.4)$$

where  $X(t)$  is the position of the solidification interface (moving boundary). Figure 2-1 illustrates this problem more clearly

The thermal energy equation at the moving front, which is known as the Stefan condition is defined by equation (2.5)

$$k_s \frac{\partial T_s}{\partial x} - k_\ell \frac{\partial T_\ell}{\partial x} = L\rho \frac{dX}{dt} \quad \text{for } x = X(t), \quad t > 0 \quad (2.5)$$

where  $k_s$  and  $k_\ell$  are the solid and liquid thermal conductivity respectively. An initial condition, Dirichlet's condition, is defined in equation (2.6) that states the initial temperature for the entire domain which is higher than the phase-change temperature. Boundary conditions provide the temperature at the beginning of the domain in equation (2.7) and in equation (2.8) which defines the temperature for the rest of the domain

$$T(x,0) = T_0 > T_{liq} \quad \text{for } x > 0, \quad X(0) = 0 \quad (2.6)$$

$$T(0,t) = T_w < T_{liq} \quad \text{for } t > 0 \quad (2.7)$$

$$T(x,t) = T_0 \quad \text{for } x \rightarrow \infty, \quad t > 0 \quad (2.8)$$

The moving front position at any particular time in equation (2.9) is defined by  $\kappa_s$  and  $\lambda$ , which are the thermal diffusivity and the solution of the transcendental equation (2.12)

$$X(t) = 2\lambda\sqrt{\kappa_s t} \quad (2.9)$$

Temperature in the liquid phase and solid phase are defined in equations (2.10) and (2.11) respectively, which each domain is treated as completely separate domain

$$T(x,t) = T_0 + (T_{liq} - T_0) \frac{(1 - \text{erf}(x/2\sqrt{\kappa_\ell t}))}{(1 - \text{erf}(\lambda\sqrt{\kappa_s/\kappa_\ell}))} \quad (2.10)$$

$$T(x,t) = T_w + (T_{liq} - T_w) \frac{\text{erf}(x/2\sqrt{\kappa_s t})}{\text{erf} \lambda} \quad (2.11)$$

Therefore the transcendental equation for the moving front is defined in equation (2.12) which is the result of substitution of equations (2.9) to (2.11) into equation (2.5)

$$\frac{k_\ell e^{-\lambda^2 \frac{\kappa_s}{\kappa_\ell}} (T_0 - T_{liq}) \sqrt{\kappa_s/\kappa_\ell}}{(\text{erf}(\lambda\sqrt{\kappa_s/\kappa_\ell}) - 1)} - \frac{k_s e^{-\lambda^2} (T_w - T_{liq})}{\text{erf}(\lambda)} = L\rho_s \lambda \sqrt{\pi \kappa_s} \quad (2.12)$$

Although, the Neumann's solution shown in equation (2.12) is only for moving boundary problems in the rectangular coordinate system, solutions in other coordinate systems are available, i.e. solution for the cylindrical coordinate system can be found in [64] .

### 2.2.2 Heat balance integral method

Exact analytical solutions exist only for semi-infinite problems with parameters constant in each phase and constant initial and imposed temperatures. They are not applicable to problems with constant imposed flux as previously shown, therefore for most realistic cases, approximations have been applied. An integral equation [65] has been developed that expresses the overall heat balance of the system by integrating the one-dimensional heat conduction equation with respect to the spatial variable and inserting boundary conditions which can be described as follow:

- (a) assume that the temperature distribution depends on the spatial variable in a particular form which is consistent with the boundary conditions, e.g. a polynomial relationship;
- (b) integrate the heat conduction equation with respect to the spatial variable over the appropriate interval and substitute the assumed form of the temperature distribution to attain the heat balance integral;
- (c) solve the integral equation to obtain the time dependence of the temperature distribution and of moving boundaries.

The heat balance integral method has been extensively applied to different problems and has often been modified with the intention of improving and easing the mathematical analysis. Selecting a satisfactory approximation to the temperature distribution is a major difficulty with this method. The mathematical manipulations required for the heat balance integral method, even for the relatively simple problems, can be very complicated and cumbersome. For instance, the use of a high-order polynomial makes this approach highly complicated whilst the accuracy of the solution is not necessarily improved.

## 2.3 Numerical methods

A number of techniques have been used to solve the problem of the heat transfer in melting/solidification. These include the finite difference methods (FDM) and finite element methods (FEM). Other related processes such as welding, crystal growth, latent heat storage and ground freezing in addition to metal casting have benefited from these methods.



Two types of numerical formulation have been used to solve the phase-change or Stefan problems which generally are known as strong and weak numerical methods. The fundamental difference between them is related to the moving front or discontinuity treatment in the problem.

### 2.3.1 Strong numerical methods for solving a phase-change problem

Locating moving boundaries and finding temperature profiles at each time step using a strong formulation, are the main focus for these methods with numerical solutions that are applicable to problems involving one or two phases in one space dimension. For two-dimensional cases rather complicated schemes must be used. Hence, with the strong solution much more computational time is required. It is very difficult to apply a strong solution to a problem with fluid flow involved on a three-dimensional case.

#### 2.3.1.1 Fixed grid methods

Various schemes have been proposed for approximating both the Stefan condition on the moving boundary and the partial differential equation at the adjacent grid points. From the 1-D solidification problem equations (2.2), (2.4) to (2.8), the heat flow equation is approximated by finite difference replacements for the derivatives in order to calculate values of temperature  $T_{i,n}$ , at  $x_i = i \Delta x$  and time  $t_n = n \Delta t$  on a fixed grid in the  $(x, t)$  plane. At any time  $t_n = n \Delta t$ , the moving boundary will be located between two adjacent grid points; for instance, between  $(i) \Delta x$  and  $(i + 1) \Delta x$ , as shown in Figure 2-2.

$$T_{i,n+1} = T_{i,n} + \left( \frac{\kappa \Delta t}{\Delta x^2} \right) [T_{i-1,n} - 2T_{i,n} + T_{i+1,n}] \quad i = 0, i-1 \quad (2.13)$$

$$p_{n+1} = p_n - \left( \frac{\kappa \Delta t}{\Delta x^2 T_{sol}} \right) \left\{ \frac{p_n}{p_n + 1} T_{i-1,n} - \frac{1}{p_n} T_{i,n} \right\} \quad (2.14)$$

The new temperature  $T_{i,n+1}$  is calculated using the previous temperature at the previous step; hence the variation of the location of the moving boundary is known by applying an interpolation, which involved the temperature in the adjacent grid points. Similarly, the new position  $p_{n+1}$  is calculated in equation (2.14)

If a moving boundary is found between two grid points at any time two fictitious temperatures are introduced both obtained by a quadratic extrapolation from the

temperatures in the solid and liquid regions. Then the solidification temperature and the current position of the moving boundary are incorporated in the fictitious temperatures formulation and the temperature near of the moving boundary is calculated by a standard approximation, this technique on a solidification problem with superheated liquid in a semi-infinite domain can be found in [66]. For the movement of the interface an approximation is used according to the Taylor extrapolation formula. A variant for this method has been developed using a spatial mesh refinement on both sides of the moving boundary [67]. Another application for this method involved explicit finite difference approximations to solve two-phase solidification problems in both two and three space dimensions [33]. Some numerical schemes have been developed based on an auxiliary set of differential equations which express the fact that the moving boundary is an isotherm. Close to the boundary, formulae for unequal intervals were incorporated into the auxiliary equations. Standard finite difference approximations to the heat flow equation were used at grid points far enough from the moving boundary. To avoid loss of accuracy associated with singularities, which can arise when the moving boundary is too near a grid point, localized quadratic temperature profiles were applied. The mathematical manipulations are very lengthy and complex indeed.

The major advantage of fixed grid methods is that these methods can handle multidimensional problems efficiently without much difficulty. Thus, the numerical treatment of the moving boundary can be achieved through simple modifications of existing heat transfer codes. As such they have come into common use for modelling a variety of complex moving boundary problems. Two excellent surveys of the fixed grid methods can be found in [68] and [46].

A setback for the fixed grid methods is when the moving front moves a distance larger than a space increment in a time step. This constraint that depends on the velocity of the moving boundary may largely increase the array size (i.e. memory) and the CPU-time if computations are to be performed for extended times. The problems associated with the fixed grid method can be avoided by using variable grid methods. In variable grid methods the exact location of the moving boundary is evaluated on a grid at each step. The grid can be either interface fitting or dynamic.

### **2.3.1.2 Variable grid methods**

Moving front is tracked continuously with variable grid methods. The solid and liquid domains are treated as two separated domains, hence are also known as two-domain methods. Moving meshes are involved therefore the mesh is updated, which conforms to

the moving front or discontinuity. The energy equation is solved separately in each phase with the temperature prescribed to be the melting temperature on the moving front. The latent heat release is treated as a special boundary condition relating the solid and liquid domains [69].

The simplest option for front tracking is iteratively to adjust the position of the nodes close to the solid-liquid discontinuity. For a planar solid-liquid discontinuity it is possible to adjust the time step forcing the moving front to be on a node at every time step.

For two-dimensional problems, front tracking requires some special approaches such as co-ordinate transformation, continuously deformed grid re-meshing and then use of space-time finite elements.

Variable time step methods where a uniform spatial grid but a non-uniform time steps are used, have been repeatedly employed to solve two-phase and one-dimensional problems. It has been attempted to determine a variable time step, as part of the solution, such that the moving boundary coincides with a grid line in space [69, 70]. Fully implicit finite difference equations are used as well as the Stephan condition for updating the time step which improves the stability that develops as the depth of the moving boundary increases. Other variable methods are based on variable space grids, also known as dynamic grids, where the number of spatial intervals is kept constant and the spatial intervals are adjusted in such a manner so that the moving boundary lies on a particular grid point. Thus, in these methods, the spatial intervals are a function of time. The substantial temperature derivative of each grid point is defined by equation (2.15).

$$\left. \frac{dT}{dt} \right|_i = \left. \frac{\partial T}{\partial x} \right|_t \left. \frac{dx}{dt} \right|_i + \left. \frac{\partial T}{\partial t} \right|_x \quad (2.15)$$

where the grid point, specific time and position for the evaluation of each derivative are  $i$ ,  $t$  and  $x$  respectively, the moving rate of each grid point is related to the moving front by

$$\left. \frac{dx}{dt} \right|_i = \frac{x}{X(t)} \frac{dX}{dt} \quad (2.16)$$

The governing equation for one-dimensional problems is obtained by substituting equations (2.16) and (2.2) into (2.15),

$$\left. \frac{dT}{dt} \right|_i = \frac{x}{X(t)} \frac{dX}{dt} \frac{\partial T}{\partial x} + \kappa \frac{\partial^2 T}{\partial x^2} \quad (2.17)$$

The position of the moving boundary  $X(t)$  is updated at each step by using a finite difference form of the Stefan condition on the moving front.

Although multidimensional problems are more complex with this method, solutions have been obtained for several two-dimensional problems [32, 71]. The complications due to the non-uniform grid size around the moving boundary can be avoided by methods where the entire uniform grid system moves with the velocity of the moving boundary. Two schemes presented in [34] obtain the interpolated values of temperatures at the new grid points to be used for the next step in terms of polynomials.

### 2.3.2 Weak numerical methods for solving a phase-change problem

Weak numerical methods are based on reformulating the Stefan condition implicitly and incorporate a new governing equation which applies over the entire region of a fixed domain. These methods are referred to as weak numerical solutions in which explicit attention to the nature of the moving boundary is avoided. They are the apparent capacity method, the effective capacity method, the heat integration method, the source based method, the enthalpy method and so on. These methods treat both the solid and liquid regions as one continuous region and the phase boundary is never explicitly determined. Hence, they are also identified as single – domain methods. Enthalpy methods account for the latent heat released/absorbed at the moving front, discontinuity, which avoids the explicit enforcement of the temperature at the discontinuity. Since the energy equation is the same for both phases, the position of the discontinuity need not be tracked explicitly. A large number of papers in this area have been published therefore only several prevalent methods will be discussed

#### 2.3.2.1 Apparent heat capacity methods

The heat capacity of the material in the phase-change temperature range is increased in order to account for the latent heat release/absorbed during this phase. Hence, the apparent heat capacity can be defined for the latent heat released/absorbed uniformly in the phase-change temperature range as

$$c_{app} = \begin{cases} c_s & T < T_{sol} \quad \text{solid phase} \\ c_{in} & T_{sol} < T < T_{liq} \quad \text{solid/liquid phase} \\ c_\ell & T > T_{liq} \quad \text{liquid phase} \end{cases} \quad (2.18)$$

where the capacity in the interface phase is defined by (2.19) and  $\Omega_{cv}$  is the domain control volume

$$c_{in} = \frac{\left\{ \int_{\Omega_{cv}} c(T) dT + L \right\}}{(T_{liq} - T_{sol})} \quad (2.19)$$

Therefore, the energy equation in terms of the apparent heat capacity becomes

$$\rho c_{app} \frac{\partial T}{\partial t} = \text{div}(k \nabla T) \quad (2.20)$$

A new governing equation is represented in equation (2.20), which can easily be discretised and solved numerically. The procedure for calculating the apparent heat capacity is as follows.

- 1) For the explicit finite difference formulation,  $c_{app}$  is determined using the temperatures at the grid points from the previous time step;
- 2) For the implicit formulation, two ways are available, the first is to evaluate  $c_{app}$  based on the previous time step temperatures and the second is according to the present time step temperatures by an iterative scheme.

This method has been applied using the finite element formulation in a generally applicable approach to one- and two-dimensional problems with both moving boundary and temperature-dependent physical properties [72].

Although the apparent heat capacity method is conceptually simple, it is apparent that the method does not perform well as compared with other methods [73]. The reason for such a drawback is that if, for a melting case, the temperature of a control volume rises from below the solidus to above the liquidus temperature in one time step, the absorption of the latent heat for that control volume is not accounted for. A similar flaw exists as the method is applied to solidification problems. As a result, very small time steps have to be used in this method in order to overcome its shortcoming. The consequence is poor

computational efficiency. Moreover, for pure materials, an artificial phase-change temperature range must be used to avoid making equation (2.19) undefined. Over this artificial phase-change temperature range, the latent heat is assumed to be released or absorbed. The introduction of an artificial phase-change temperature range can result in computational errors and simulation distortion of the real problem.

### 2.3.2.2 Effective capacity method

The effective capacity method performs an integration over the element domain rather than determining an apparent capacity in terms of the nodal temperature. This method introduced an effort to improve the apparent capacity method [73]. Therefore the effective capacitance is defined as

$$c_{\text{eff}} = \frac{\left( \int_{\Omega_{\text{cv}}} c_{\text{app}} dV \right)}{V_{\text{cv}}} \quad (2.21)$$

where  $c_{\text{eff}}$ ,  $c_{\text{app}}$  and  $V_{\text{cv}}$  are effective heat capacity, apparent heat capacity and volume of the control volume  $\Omega_{\text{cv}}$  respectively.

The effective capacity method performs significantly better than the apparent heat capacity method. It has been applied from 1-D to 3-D using implicit and explicit finite difference and implicit finite element formulations.

The effective capacity method ensures that correct account is made for the latent heat release/absorption by evaluating equation (2.21) at each step and its solution is independent of the artificial phase-change temperature range. An assumption of a large artificial phase-change temperature range is not required. The results produced are relatively insensitive to the time step and generally precise both on the entire domain and near the moving boundary [74].

Although the effective capacity method is accurate, it is also troublesome to implement. The numerical integration is substantially expensive, especially if thermal gradients are steep in the phase-change temperature range.

### 2.3.2.3 Heat integration method

For the solidification case, if the temperature of any control volume drops below the solidification temperature, the material in that control volume is assumed to undergo a phase-change. Even though the temperature of that control volume is set back to the

solidification temperature, an equivalent amount of heat due to setting the temperature back is added to the enthalpy that only accounts for that control volume. Once the enthalpy in the account is equal to the latent heat, the temperature is allowed to drop based on the energy equation. The procedure can be expressed mathematically

$$(T_{\text{liq}} - T_i) c_{\text{in}} = L \quad (2.22)$$

where the fictitious temperature drop  $(T_{\text{liq}} - T_i)$  is the algebraic sum of temperature differences between the temperature calculated by the energy equation at each time step and the solidification temperature. The capacitance at the interface phase is  $c_{\text{in}}$  where the latent heat is released/absorbed.

The heat integration method has been applied, using the finite element method, for transient thermal problems including a moving boundary in both a pure substance and an alloy [75]. The heat integration method can be easily applied for multidimensional problems with isothermal or non-isothermal phase-change involved. The method is computationally economical. However, the accuracy of the solution strongly depends on the time step and the prediction in the region of the moving boundary is often inaccurate [73].

#### **2.3.2.4 Source based method**

The source based method introduces an extra term into the governing heat equation and represents any additional heat from either a heat source (e.g. latent heat release during solidification) or heat sink (e.g. latent heat absorption during the melting) which is introduced into the general form of the energy equation [76]. The source method is derived from a standard enthalpy formulation which separates sensible heat and latent heat in the transient term of the energy equation

$$\rho \frac{\partial(cT + L)}{\partial t} = \text{div}(k \nabla T) \quad (2.23)$$

where is made use of the rather simplistic approach  $h = cT + L$ , which the term  $cT$  and  $L$  are related with sensible and latent heat respectively. Therefore from equation (2.23) the energy equation using the source formulation becomes

$$\rho c \frac{\partial T}{\partial t} = \text{div}(k \nabla T) + S \quad (2.24)$$

where the latent heat is now included in the source term  $S$  as

$$S = -\rho \frac{\partial L}{\partial t} \quad (2.25)$$

The source based method has become popular over the years [46, 73, 76] as one of the important factors for its success is that the algorithms can handle the heat source or heat sink easily and can be adapted to the existing numerical codes which have been widely used in the public domain. The overall accuracy of this method is fairly good, especially for non-isothermal phase-change problems since the latent heat content is directly related to the temperature of the grid point which is computationally efficient. Although the method may introduce unreasonable predictions around the moving boundary for isothermal phase-change problems without using excessive underrelaxation for convergence, the solution oscillation can be eliminated by the linearization of the discretised source term [76].

### 2.3.2.5 Enthalpy method

The evolution of the latent heat can be accounted by using the enthalpy definition and its relationship with the temperature, which represents the basic feature for the enthalpy method. The heat conduction-controlled phase equation can be expressed as

$$\rho \frac{\partial h}{\partial t} = \text{div}(k \nabla T) \quad (2.26)$$

where  $h$  is the enthalpy in the system and the relationship between the enthalpy and temperature can be defined in terms of the latent heat released during the phase-change. This relationship is usually assumed to be a step function for isothermal phase-change and a linear function for non-isothermal phase-change, mushy, cases. Enthalpy–temperature curves for both cases are shown in Figure 2-3. The enthalpy as a function of temperature for both cases is given by



$$h = \begin{cases} C_s T & T \leq T_{\text{sol}} & \text{solid phase} \\ C_\ell T + L & T > T_{\text{liq}} & \text{liquid phase} \end{cases} \Bigg\} T_{\text{sol}} = T_{\text{liq}} \quad (2.27)$$

$$h = \begin{cases} c_s T & T < T_{\text{sol}} & \text{solid phase} \\ c_{\text{in}} T + \frac{L(T - T_{\text{sol}})}{(T_{\text{liq}} - T_{\text{sol}})} & T_{\text{sol}} \leq T \leq T_{\text{liq}} & \text{solid / liquid phase} \\ c_\ell T + L + c_{\text{in}}(T_{\text{liq}} - T_{\text{sol}}) & T \geq T_{\text{liq}} & \text{liquid phase} \end{cases} \left. \vphantom{\begin{cases} c_s T \\ c_{\text{in}} T + \frac{L(T - T_{\text{sol}})}{(T_{\text{liq}} - T_{\text{sol}})} \\ c_\ell T + L + c_{\text{in}}(T_{\text{liq}} - T_{\text{sol}}) \end{cases}} \right\} \begin{array}{l} \text{for} \\ \text{non - isothermal} \\ \text{phase change} \end{array} \quad (2.28)$$

where  $c_s$ ,  $c_{\text{in}}$  and  $c_\ell$  are the heat capacity for solid, interface and liquid phase. For the isothermal case, equation (2.27), the temperature at the interface is  $T_{\text{sol}} = T_{\text{liq}}$ . However for the non-isothermal case, equation (2.28),  $T_{\text{sol}} < T_{\text{liq}}$  and  $L$  represents the latent heat released for solidification. The enthalpy method has been found more complex and expensive than other methods [73]. The computational cost increases with mesh refinement. An oscillation appears in the phase-change case with large ratio of latent heat to sensible heat. However, the enthalpy method gives accurate solutions especially for solidification of metal in which a phase-change temperature range exists. Furthermore, the solution is independent of the time step and phase-change temperature range

Discussion of the enthalpy method has also been comprehensively covered by Voller and co-workers [39, 46, 76, 77, 78, 79]. Although the basic enthalpy method does not perform well for modelling isothermal phase-change problems, Voller proposed and assumed that when the moving boundary is in the control volume, the enthalpy change rate is proportional to the state change rate of the control volume which improves the accuracy of the prediction. This is represented by the relationship

$$\frac{dh}{dt} = \pm L \frac{dV_\ell}{dt} \quad (2.29)$$

where  $V_\ell$  is the liquid fraction in the control volume; the negative sign in equation (2.29) is for melting and the positive sign is for solidification. While the material in the control volume undergoes phase-change, the enthalpy of the control volume must follow

$$c_\ell T_{\text{liq}} \leq h \leq c_\ell T_{\text{liq}} + L \quad (2.30)$$

Based on equation (2.29), the following equations can be obtained:

$$V_\ell = \frac{h - c_\ell T_{\text{liq}}}{L} \quad \text{for solidification} \quad (2.31)$$

$$V_\ell = \frac{L + c_\ell T_{\text{liq}} - h}{L} \quad \text{for melting} \quad (2.32)$$

The accuracy of the predictions is greatly improved by this efficient algorithm technique [76, 77, 78]. As a result, the enthalpy method has been generalized so that more general forms of the enthalpy–temperature function can be handled. For example, cases in which an explicit enthalpy–temperature relationship cannot be found. The method has been extended to three-dimensional cases and its effectiveness has also been demonstrated.

### 2.3.3 Numerical methods for solving convection/diffusion phase-change problems

Convection flow in the liquid phase has received less attention than conduction due to computer limitations in the past and considerable complexities entailed in the mathematical treatment. Although energy transport in phase-change processes is important since the evolution and efficiency of the processes are affected by the heat transfer. However convection is increased by the buoyancy forces as a consequence of the temperature field changes and/or concentration gradients in the liquid phase which are involved in the phase-change processes. The convection affects not only the rate of solidification/melting but also the resulting structure and distribution of the solutes in the liquid phase of a multi-component system, which has been reported by number of researchers [80, 81, 82]

The Navier–Stokes mass and momentum conservation equations on a Newtonian fluid to determine quantitatively the convection can be written as equations (2.33) and (2.34), respectively.

$$\frac{\partial \rho}{\partial t} + \nabla \cdot (\rho \underline{v}) = 0 \quad (2.33)$$

$$\rho \frac{D \underline{v}}{Dt} = -\nabla p + \mu \nabla^2 \underline{v} + \rho \underline{g} \quad (2.34)$$

where  $\underline{v}$  is the velocity field of the fluid with the density  $\rho$  under the action of the pressure, viscosity and body forces, which are  $\nabla p$ ,  $\mu \nabla^2 \underline{v}$  and  $\rho \underline{g}$  respectively.

Because of the nonlinearity of the Navier–Stokes equations, their analytical solutions relevant to phase-change problems are available only for a few simple cases, e.g. the analytical solution for the 1-D momentum equation [83]. Development of numerical methods linked closely with the availability of more powerful computers has made the Navier–Stokes equations solvable. Two widely used numerical approaches, the stream-function–vorticity and the primitive variable formulations, will be discussed in the next sections.

### 2.3.3.1 Stream function-vorticity formulation

The stream-function–vorticity formulation is quite often applied in computational fluid dynamics for solving two-dimensional problems. For two-dimensional incompressible flow where the density variations are neglected, the stream function ( $\Psi$ ) and vorticity ( $\omega$ ) are represented in the equations

$$u = \frac{\partial \Psi}{\partial y}, \quad v = -\frac{\partial \Psi}{\partial x} \quad (2.35)$$

$$\omega = \frac{\partial v}{\partial x} - \frac{\partial u}{\partial y} \quad (2.36)$$

Therefore, the continuity equation is automatically satisfied since

$$\frac{\partial u}{\partial x} + \frac{\partial v}{\partial y} = \frac{\partial^2 \Psi}{\partial x \partial y} - \frac{\partial^2 \Psi}{\partial y \partial x} = 0 \quad (2.37)$$

An important drawback in the primitive variable formulation is that the Navier-Stokes and the continuity equations have to be solved separately. However, the stream-function–vorticity formulation can be transformed into the Navier-Stokes equations form by using the vorticity transport equation which gives

$$\frac{D\omega}{Dt} = \nu \nabla^2 \omega \Rightarrow \nabla^2 \Psi = -\omega \quad (2.38)$$

Therefore, rather than use the primitive variable formulations from equations (2.33) and (2.34) it is convenient to use the stream-function-vorticity formulation which is defined in the equation system (2.38)

Thermal and fluid flow simulation of solidification in a rectangular enclosure with adiabatic boundaries have been obtained via the stream-function–vorticity formulation and the alternating directional implicit (ADI) method by [84]. The density variation causing the natural convection was handled by the Boussinesq approximation. The velocity distribution, stream lines and isotherm patterns, which were obtained along with the interface movement with time, indicated that natural convection has a significant effect on the shape of the interface. The coupled, nonlinear, simultaneous equations were solved using the ADI finite difference scheme. The agreement between predicted results and the existing experimental data appeared to be reasonably good.

Even though the stream-function-vorticity formulation has shown important positive features for the solution of the Navier-Stokes equations, it has also shown some disadvantages such as cumbersome implementation of boundary conditions, the effort of extracting the pressure from the vorticity which affects the computational efficiency and a required outcome to determine the thermo-physical properties. However, the major drawback is that it cannot be easily extended to 3-D.

### **2.3.3.2 Primitive variable formulation**

This section is concerned with the substitution of Navier–Stokes equations where account is taken of the velocities and pressure as dependant variables, which is the primitive variable form. Two techniques are discussed.

For the first technique the nonlinear governing equations are discretised by finite difference methods based on a term by term Taylor series approximation which is known as the marker and cell (MAC) method [85, 86, 87]. The pressure is located at the cell centre and the velocities at the walls on a staggered mesh. Massless marker particles are used to move in the local fluid velocity on every cell in the computational domain. A layer of fictitious cells adjacent to the computational domain is used to impose the boundary conditions. At each time step, new velocities in terms of an estimated pressure are obtained from the discretised momentum equations. Thus, each cell is iteratively adjusted and velocity changes are induced. The process is repeated until the continuity equation is satisfied, then the marker particles are moved to their new position ready for the next time step.

This method has been applied on cases which have showed reasonable agreement with experimental results, e.g. flow patterns during the filling of a cylindrical vessel from the top free surface and the fluid flow during the filling of a rectangular mould from the side.

Although the MAC method is easily implemented on existing codes due to its explicit nature, time-step limitations impose a major drawback to the method. Time step restrictions are implemented in order to eliminate the possibility that material movement and momentum transport passes through more than one cell at a time. It has been observed that refinement meshing worsens its performance [85].

The control volume method represents an alternative to solve Navier-Stokes equation in the category of the primitive variable formulation. The well known SIMPLE and SIMPLER algorithms, which are acronym for Semi-Implicit Method for Pressure Linked Equations and Revised respectively, are the basis for any commercial computational fluid dynamic software using this approach today [88]. In this technique, the equations of the mass, momentum, energy and species conservation are expressed in a general differential equation of the form

$$\frac{\partial}{\partial t}(\rho\phi) + \nabla \cdot (\rho\mathbf{u}\phi) = \nabla \cdot (\Gamma_\phi \nabla \phi) + S_\phi \quad (2.39)$$

where  $\phi$  is a general variable,  $\Gamma_\phi$  is the diffusion coefficient and  $S_\phi$  is a source term. The four terms in equation (2.39) represent the unsteady term, the convection term, the diffusion term and the source term. The dependent variable  $\phi$  can denote a variety of different quantities such as the mass fraction of a chemical species, the enthalpy or the temperature, or a velocity component. Accordingly, for each of these variables, an appropriate meaning must be given to the diffusion coefficient and the source term,  $\phi$ ,  $\Gamma_\phi$  and  $S_\phi$  for the different equations shown in (2.40) to (2.43).

$$\frac{\partial \rho}{\partial t} + \nabla \cdot (\rho \mathbf{u}) = 0 \quad (2.40)$$

$$\frac{\partial}{\partial t}(\rho \mathbf{v}) + \nabla \cdot (\rho \mathbf{u} \mathbf{v}) = \nabla \cdot (\mu \nabla \mathbf{v}) + S^v - \nabla p \quad (2.41)$$

$$\frac{\partial}{\partial t}(\rho h) + \nabla \cdot (\rho \mathbf{u} h) = \nabla \cdot (k \nabla h) + S_h \quad (2.42)$$

$$\frac{\partial}{\partial t}(\rho C_A) + \nabla \cdot (\rho u C_A) = \nabla \cdot (D \nabla C_A) + S_C \quad (2.43)$$

where conservation equations (2.40) to (2.43) represent mass, momentum, energy and species and the source term for the momentum, energy and species are represented by  $S^v$ ,  $S_h$  and  $S_C$  respectively. However, the species equation requires to define  $C_A$  and  $D$ , which are concentration and diffusion coefficients

This technique has been applied to a number of cases, e.g. the melting process where heat convection in the liquid phase is non-negligible, melting pure gallium and its numerical solution was validated by comparison with precise experimental results [77]. The simulation of a melting process where a heat source, heat sink and natural convection are coupled has been solved by integrating the enthalpy method in to the SIMPLER algorithm [89, 90, 91].

## **2.4 Methods for microstructure simulation**

Microstructure prediction from macro-transport models that solve the mass, momentum, energy and species macroscopic conservation differential equations is very limited. Solidification models that can integrate the transformation kinetics into the macro-transport models are being developed [59, 91]. Various techniques which include the continuum (deterministic) approach [92] and the stochastic (probabilistic) approach [50, 51, 93] have been applied in order to model and generate information on microstructure evolution. These techniques have been used to predict various features of solidifying materials such as dendritic structure, fraction of phases, structural transition, microsegregation and even mechanical properties.

Although this research is focused on the macro-modelling it is of interest to briefly examined the advances in microstructure solidification [7]. Discussed here are: modelling of microstructure formation using phase-field or front-tracking-type methods; modelling of solidification processes and microstructural features using averaging methods; modelling of grain structure formation using physically based Cellular Automata or "Granular Dynamics" methods. All three are important since the macroscopic scale of a solidification process (typically cm-m), the grain size (typically mm-cm) and the characteristic length of the microstructure ( $\mu\text{m}$ ) encompass six orders of magnitude and cannot be taken into account simultaneously. It should be emphasized that the smallest size of the microstructure ( $\mu\text{m}$ ) is still three to four orders of magnitude larger than the size of the atoms or molecules or the thickness of the solid-liquid interface.

### 2.4.1 Modelling of microstructure

Simulation at this level normally requires following the interface separating the solid and liquid phases (front tracking). This has been achieved successfully in simple two-dimensional geometry using either the boundary element method (BEM) or the finite element method (FEM). In the first technique only the interface is meshed and Greens functions are used to solve the diffusion problem. In the second method, dynamic re-meshing of the domain is necessary. These methods are accurate but difficult to implement even in two dimensions [94].

In pseudo-front-tracking techniques [56], the solid-liquid interface is spread over only one mesh of the finite difference (FDM) or finite volume (FVM) mesh and re-meshes. Here the concept of the volume fraction of solid (or liquid) is introduced, which is equal to unity in the solid, zero in the liquid and intermediate for the "interface meshes".

### 2.4.2 Modelling of processes and average microstructural features

Modelling of solidification processes and microstructural features has benefited from two main contributions. Firstly, the introduction of averaged conservation equations previously developed for two phase media [80, 95]. Secondly, the couplings of these equations with microscopic models of solidification describing grain structure formation and other microstructural features (e.g. secondary arm spacing, microsegregation model, etc.)

### 2.4.3 Modelling of grain structures using stochastic methods

The prediction of morphology transitions (from outer equiaxed to columnar and from columnar to equiaxed) [96, 97] is also quite difficult with averaging methods. In order to overcome these shortcomings, stochastic methods have been developed over the past two decades [51, 52]. It should be pointed out that the stochastic aspect is only related to nucleation (random location and orientation of nuclei) whereas growth is usually treated in a deterministic way. Two types of models can be distinguished:

Cellular Automata (CA) have been developed for dendritic grain structures and can treat arbitrary shapes and grain competition [51, 94, 98]. In this technique, the solidification domain is mapped with a regular arrangement of cells and each grain is described by a set of cells, those located at the boundary (i.e. in contact with liquid cells) being active for the calculation of the growth process.

In "Granular Dynamics" (GD) techniques, the surface of each grain is subdivided into an ensemble of small facets [55, 99]. The growth stage of each grain is then described by a set of parameters, e.g. the position of its centre, the radial positions of its facets and their

status (contact with the liquid or with another grain), etc. This latter technique is more appropriate for nearly spherical morphologies (e.g. equiaxed eutectics or globulitic grains) and can handle the transport of equiaxed grains fairly well.

## **2.5 Conclusion**

Experience has been accumulated in the numerical simulation of convection/diffusion processes coupled with phase-change. Numerical techniques for such complex phenomena are being developed by scientists and engineers in different disciplines. The popularity of some methods is based on experience gained. Numerical methods based on the weak solution in conjunction with the control volume scheme in the fixed domain can be highly recommended for multidimensional melting and solidification problems. However, with increasing interest in modelling of microstructure evolution occurring during solidification, new solidification models are constantly under development, improving accuracy and predicting the peculiar characteristics of microstructure.

With the advent of very powerful computers, advanced numerical methods and better understanding of the physical phenomena involved in solidification, it is not surprising that computer simulations are becoming increasingly used for the modelling of macro-microstructure formation and associated characteristics or defects which provides an important incentive for public-private institutions or individuals to continue this type of research.



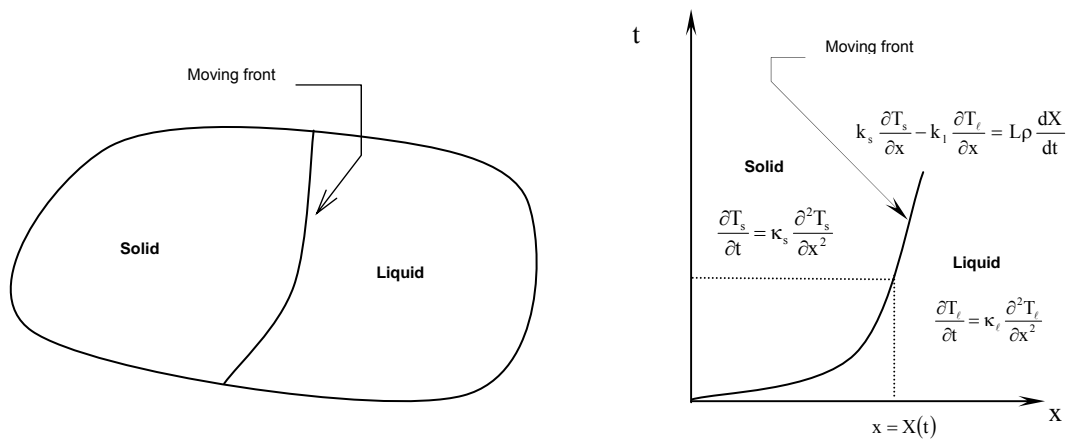


**Figure 2-1 Representation for two-phase Stefan problem**

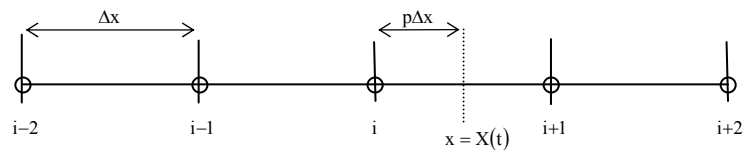


**Figure 2-2 1-D fixed grid with a moving front**

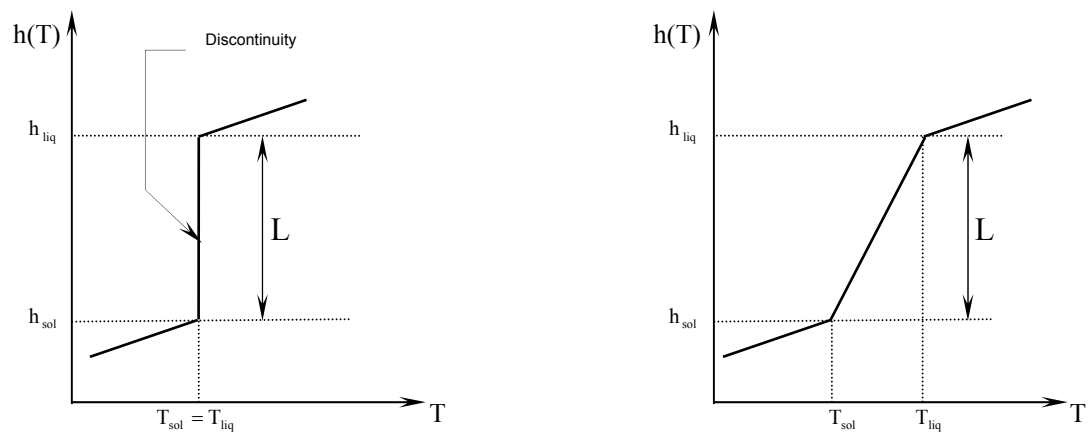


**Figure 2-3 Latent heat release for isothermal and mushy solidification**

# 3 A NON-PHYSICAL ENTHALPY METHOD FOR THE NUMERICAL SOLUTION OF ISOTHERMAL SOLIDIFICATION

---

## ***3.1 Introduction***

Sophisticated computational approaches exist for the accurate and efficient modelling of solidification processes. Models and methods have been developed to account for complex boundary conditions, moving boundaries, varying thermo-physical properties, macro and micro transport processes used in the prediction of defects such as segregation and porosity [31, 39, 40, 69, 73, 100, 101, 102, 103, 104]. Fundamental to the many approaches, in the absence of convection, is the efficient solution to the diffusion equation. Many of the numerical methods for the solution of the diffusion equation can be viewed as classical and are commonly employed in commercial software. The methods can be classified into two

groups; front tracking (adaptive) and fixed domain methods [100]. Front tracking (adaptive) methods provide for an accurate description of isothermal solidification but at the cost of complex meshing and re-meshing strategies, generally needed to cater for phase-front distortion, birth and collapse [45, 46, 70]. The solidification of a pure or eutectic substance is of particular interest here as it gives rise to a material discontinuity. Although adaptive methods provide for high accuracy in the presence of a material discontinuity their complexity has resulted in the favouring of fixed-domain approaches [36, 40, 105]. As an aside, it of interest to note that much research is ongoing into finite element methods for the incorporation of discontinuities; these include the extended and discontinuous Galerkin finite element methods [106, 107, 108]. For these methods however, the focus is on geometric (strong) discontinuities and are not readily applicable to isothermal solidification. Fixed domain methods tend to be more versatile and easier to implement but it is evident from the literature they can suffer inaccuracy particularly when material discontinuities are present. Four fixed domain methods are commonly employed to solve solidification problems; these are the so-called enthalpy [39, 105, 109, 110], capacitance [101, 111, 112], fictitious heat flow [40, 75] and temperature recovery (or heat integration) techniques [113]. Good reviews of the existing traditional techniques are given by Voller et al. [46] and Dalhuijsen et al. [68]. Each of the fixed domain methods attempts to incorporate the latent heat release on solidification either by artificially increasing the enthalpy, thermal capacitance or by inclusion of a source term. Capacitance methods for example involve the specification of artificial element or nodal capacitances in an attempt to cater for the release of latent energy. The apparent heat capacitance method is particularly prone to error in the presence of a material discontinuity [114]. It is demonstrated with the introduction of control volume capacitance methods (CVCM) in references [114] and [115] that large energy fluctuations are presented in the established capacitance methods. Source-based methods similar to the fictitious heat flow method are particularly attractive as existing heat transfer codes can be easily modified to include source terms. A particular feature of the method is the arbitrariness of the source term as the totality or part of the latent heat can be incorporated. In the method proposed here, the source term is determined to remove completely the discontinuity. High accuracy does not necessarily accompany source-term approaches although it is important to be clear what the term 'high accuracy' means. Temperature predictions are often used as the sole criterion for assessing the success of these techniques. This does not necessarily provide an adequate measure of the success, which is particularly the case for the capacitance techniques for example. Differing approaches for the determination of capacitance and

sources are presented in the literature [46] each typically and ultimately justified by comparison with analytical temperatures but suffering large energy fluctuations nonetheless [115].

In this chapter, the focus is on isothermal solidification where the source term is selected to remove the discontinuity from the governing transport equations. In so doing, mathematical credence is given to the use of continuous shape function across a discontinuity. Any other choice for the source term, whilst not invalid, has the effect of amortising the discontinuity over an element but manifesting at the element edges. The approach presented here allows for the simultaneous specification of both capacitance and source whilst at the same time ensuring total discontinuity annihilation unlike any existing method. Established in the chapter is a completely novel procedure for the removal of weak discontinuities from the governing FE equations; this is the principal and important contribution. The work extends the ideas developed in references [116, 117], which are restricted to capacitance formulations for phase-change problems described via transport equations. The approach adopted here is founded on transport equations for an arbitrary control volume (CV) moving relative to the transporting material. The movement of the CV is achieved by transport via an arbitrarily stipulated regular velocity field  $\underline{v}^*$ . A non-physical enthalpy  $\hat{h}$ , dependent on  $\underline{v}^*$ , is defined on the CV via transport equations. This gives rise to the peculiar concept that  $\hat{h}$  is dependent on the type of analysis selected, i.e. is not moving-frame invariant, in the sense that different results are obtained with different moving frame, for example, Eulerian (which is the focus of this chapter) and Lagrangian approaches produce different results. Likewise, tracking a discontinuity provides yet another answer. However, it is demonstrated in this chapter how  $\hat{h}$  obtained for a particular CV transported by  $\underline{v}^*$  (say) can be determined at a discontinuity moving within the CV. This involves developing transport equations that impart relative moving-frame invariance on  $\hat{h}$ , which is central to the analysis of the discontinuous physics with non-physical variables. Introduced in this chapter is the concept of weighted-transport equations. This is utilised to establish a finite element method that is applicable to discontinuous problems without approximation. Each element takes the form of a control volume so relatively sophisticated approaches are required to cater for discontinuities and/or traversing boundaries.

The concept of a moving CV is presented in Section 3.2 along with governing transport and partial differential equations. Non-physical variables are introduced in Section 3.3

along with equivalent governing partial differential equations. Discontinuous non-physical variables are discussed in Sections 3.4 and 3.5. In Section 3.6, finite element systems are developed for the solution of the transport equations developed. Of concern in Section 3.7 and 3.8 are the theories required to annihilate discontinuities from the transport finite element equations. Various forms of the discontinuity annihilated FE transport equations are presented in Section 3.9. In the sections that follow the details relating to the implementation and testing of the non-physical enthalpy method (NEM) in an Eulerian frame are described.

### 3.2 Conservation law for a moving CV

The formulation proposed here can be related in a restricted sense to the arbitrary Lagrangian Eulerian (ALE) formulation [35]. The ALE formulation permits independent control volume (CV) movement in a computational reference system (CRS). The Material reference system (MRS), spatial and CRS co-ordinates are denoted by  $\mathbf{X}$ ,  $\mathbf{x}$  and  $\chi^*$ , respectively [118]. The material derivative  $D/Dt = \partial/\partial t|_{\mathbf{x}}$  and CV derivative  $D^*/D^*t = \partial/\partial t|_{\chi^*}$  are related to the spatial derivative by the following expressions

$$\frac{D}{Dt} = \frac{\partial}{\partial t}\bigg|_{\mathbf{x}} + \underline{\mathbf{v}} \cdot \nabla \quad (3.1)$$

$$\frac{D^*}{D^*t} = \frac{\partial}{\partial t}\bigg|_{\mathbf{x}} + \underline{\mathbf{v}}^* \cdot \nabla \quad (3.2)$$

where  $\underline{\mathbf{v}} = D\mathbf{x}/Dt$  and  $\underline{\mathbf{v}}^* = D^*\mathbf{x}/D^*t$ .

Two other velocity fields are utilised in this chapter, i.e.  $\underline{\mathbf{v}}^+$  and  $\underline{\mathbf{v}}^\times$ , for the purpose of tracking discontinuities. The velocity field  $\underline{\mathbf{v}}^+$  is selected to match the velocity of a discontinuity  $\Gamma_i$  passing through domain  $\Omega$ . The velocity field  $\underline{\mathbf{v}}^\times$  selected in a similar fashion but restricted to an element domain  $\Omega_e$ . Similar identities to those found in equations (3.1) and (3.2) apply to these velocity fields also, i.e.  $D^+/D^+t = \partial/\partial t|_{\mathbf{x}} + \underline{\mathbf{v}}^+ \cdot \nabla$  and  $D^\times/D^\times t = \partial/\partial t|_{\mathbf{x}} + \underline{\mathbf{v}}^\times \cdot \nabla$ .

In the theory that follows the transport of  $\Omega$  is governed by one of the diffeomorphisms (differentiable one-to-one mappings)  $\mathbf{x}(\boldsymbol{\chi}^*, t)$ ,  $\mathbf{x}(\boldsymbol{\chi}^+, t)$  and  $\mathbf{x}(\boldsymbol{\chi}^\times, t)$  which are obtainable on solution of the differential equations  $\partial \mathbf{x} / \partial t (\boldsymbol{\chi}^*, t) = \underline{\mathbf{v}}^*$ ,  $\partial \mathbf{x} / \partial t (\boldsymbol{\chi}^+, t) = \underline{\mathbf{v}}^+$  and  $\partial \mathbf{x} / \partial t (\boldsymbol{\chi}^\times, t) = \underline{\mathbf{v}}^\times$ , respectively, where  $\underline{\mathbf{v}}^*$ ,  $\underline{\mathbf{v}}^+$  and  $\underline{\mathbf{v}}^\times$  are specified regular velocity fields. Moreover, not only is the velocity field  $\underline{\mathbf{v}}^*$  used in the transport of the computational frame (mesh movement) but also it is used generally to describe movement of the system domain under consideration.

Although in this chapter attention is generally restricted to mappings between points from the MRS and CRS to the spatial system (physical domain) it is evident that mapping between the MRS and CRS can also exist. This latter map is useful when seeking an analytical solution or for a numerical approach that updates the geometry subsequent to any analysis (e.g. updated Lagrangian).

### 3.2.1 Relationships between temporal derivatives

Consider the situation where  $\mathbf{x}^* \equiv \mathbf{x}(\boldsymbol{\chi}^*, t) = \mathbf{x}(\mathbf{X}, t) \equiv \mathbf{x}$ , thus providing a relationship between  $\boldsymbol{\chi}^*$  and  $\mathbf{X}$ . Equating the differential of each gives  $d\mathbf{x}_i^* = J_{ij}^* d\chi_j + v_i^* dt = J_{ij} dX_j + v_i dt = d\mathbf{x}_i$ , where the Jacobian matrices are  $J_{ij}^* = \partial \mathbf{x}_i^* / \partial \chi_j$  and  $J_{ij} = \partial \mathbf{x}_i / \partial X_j$ . If a material point  $\mathbf{X}$  is fixed, then  $J_{ij}^* V_j = v_i - v_i^*$ , where  $V_j = D\chi_j / Dt$  and similarly if  $\boldsymbol{\chi}^*$  is fixed, then  $J_{ij} V_j^* = -(v_i - v_i^*)$ , where  $V_j^* = D^* X_j / D^* t$ . The velocities in small case ( $\underline{\mathbf{v}}$  and  $\underline{\mathbf{v}}^*$ ) are measurable (because they reside in the physical domain) whilst the velocities in upper case ( $\underline{\mathbf{V}}$  and  $\underline{\mathbf{V}}^*$ ) relate to reference domains so are not directly measurable (see Figure 3-1). Note that temporal derivatives  $D/Dt$  and  $D^*/D^* t$  can be related in three ways, i.e.  $D^*/D^* t = D/Dt + (v_i^* - v_i) \partial / \partial x_i$  ( $\boldsymbol{\chi}^*$  and  $\mathbf{X}$  fixed) obtained on subtraction of (3.1) from (3.2),  $D^*/D^* t = D/Dt + V_i^* \partial / \partial X_i$  ( $\boldsymbol{\chi}^*$  fixed) and  $D/Dt = D^*/D^* t + V_i \partial / \partial \chi_i$  ( $\mathbf{X}$  fixed), where summation is performed over repeating suffices. Note also that  $D^*/D^* t = D/Dt + [(J^{-1})_{ij} (v_j^* - v_j)]^T \partial / \partial \chi_i$  and  $D/Dt = D^*/D^* t + [(J^{*-1})_{ij} (v_j - v_j^*)]^T \partial / \partial X_i$  in the case of  $\boldsymbol{\chi}^*$  and  $\mathbf{X}$  fixed. It is assumed here that the inverse Jacobian exists, which is assured for diffeomorphisms  $\mathbf{x}(\boldsymbol{\chi}^*, t)$  and  $\mathbf{x}(\mathbf{X}, t)$ .

Although most researchers [117] adopt the map  $\chi^*(X, t)$  in place of the map  $x(\chi^*, t)$ , it is evident from the analysis above that there is little discernable difference between the two approaches. Saying that, the latter approach focuses directly on the physical domain and the velocities  $\underline{v}$  and  $\underline{v}^*$  are directly measurable in that domain. Moreover, the transport equations tend to be simpler in form in the physical domain. It is a simple matter to show that the following proposition holds:

### 3.2.2 Proposition

An energy conservation law for a moving domain  $\Omega$  defined by the diffeomorphism  $x(\chi^*, t)$ , is

$$\frac{D^*}{D^*t} \int_{\Omega} \rho h dV + \int_{\Gamma} \rho h (\underline{v} - \underline{v}^*) \cdot \underline{n} d\Gamma = - \int_{\Gamma} \underline{q} \cdot \underline{n} d\Gamma + \int_{\Omega} \rho Q dV \quad (3.3)$$

where  $h$  is the specific enthalpy,  $\rho$  is the density,  $\underline{v}$  is the material velocity,  $\underline{q} \cdot \underline{n}$  is the heat flux and  $Q$  is the heat source term.

Note the use of  $D^*/D^*t$  rather than the ordinary derivative  $d/dt$  in equation (3.3) even though these are identical when applied to a function of  $t$ . Thus, even though  $\int_{\Omega} \rho h dV$  is a function of  $t$  the use of the derivative  $D^*/D^*t$  in (3.3) is intended to immediately relay the notion that  $\Omega$  is a control volume transported through  $\underline{v}^*$ . Although  $\underline{v}^*$  is present in equation (3.3) it cannot influence the value of  $h$  as this would be physically meaningless. It is demonstrated in [116] that with the transport of  $\Omega$  through  $\underline{v}^*$ , the appearance of the integral  $-\int_{\Gamma} \rho h \underline{v}^* \cdot \underline{n} d\Gamma$  ensures that  $h$  is independent of  $\underline{v}^*$ . This is also clear from a physical perspective since the term  $\int_{\Gamma} \rho h \underline{v}^* \cdot \underline{n} d\Gamma$  accounts for the gain in  $\rho h$  with the movement of the boundary  $\Gamma$ . Another transport equation of interest here is

$$\frac{D^*}{D^*t} \int_{\Omega} \rho dV + \int_{\Gamma} \rho (\underline{v} - \underline{v}^*) \cdot \underline{n} d\Gamma = 0 \quad (3.4)$$



for transport of mass.

The governing partial differential equation can be obtained from (3.3) by application of a Reynold-type transport Theorem and the Divergence Theorem, i.e. substitution of

$$\frac{D^*}{D^*t} \int_{\Omega} \rho h dV = \int_{\Omega} \left( \frac{D^* \rho h}{D^*t} + \rho h \operatorname{div} \underline{v}^* \right) dV \quad (3.5)$$

$$\int_{\Gamma} \rho h (\underline{v} - \underline{v}^*) \cdot \underline{n} d\Gamma = \int_{\Omega} \operatorname{div} (\rho h (\underline{v} - \underline{v}^*)) dV \quad (3.6)$$

$$\int_{\Gamma} \underline{q} \cdot \underline{n} d\Gamma = \int_{\Omega} \operatorname{div} (\underline{q}) dV \quad (3.7)$$

into (3.3) gives

$$\rho \frac{D^* h}{D^*t} + \rho (\underline{v} - \underline{v}^*) \cdot \nabla h = -\operatorname{div}(\underline{q}) + \rho Q \quad (3.8)$$

where use is made of the continuity equation  $D^* \rho / D^*t + \rho \operatorname{div} \underline{v}^* + \operatorname{div} [\rho (\underline{v} - \underline{v}^*)] = 0$  in the derivation of (3.8), which is obtainable from equation (3.4).

It is important to appreciate that equation (3.8), although unusual in appearance, is identical to  $\rho Dh/Dt = -\operatorname{div}(\underline{q}) + \rho Q$ , which is the governing partial differential heat equation expected for the transport problem under consideration. Use of the identity  $D^*/D^*t + (\underline{v} - \underline{v}^*) \cdot \nabla = D/Dt$  in (3.8) gives this result, which reinforces the maxim that physical laws are unaffected by the choice and transport of the control volume on which the analysis is to be performed.

The derivation of equation (3.8) from the transport equation (3.4) requires, amongst other things, that both  $\rho$  and  $h$  possess a degree of smoothness on  $\Omega$ . At points of discontinuity the continuity equation and equation (3.8) will not be applicable despite the validity of equations (3.3) and (3.4). Prior to examining the behaviour at a material discontinuity it convenient at this stage to introduce an alternative transport equation that can be more readily solved using numerical techniques but also to define a non-physical enthalpy  $\hat{h}$  that behaves like a source rather than a jump at a material discontinuity.

### 3.3 Equivalent governing equations

A transport equation is constructed so that its solution is precisely that which satisfies equations (3.3) and (3.8). Consider then the identity

$$\frac{D^*}{D^* t} \int_{\Omega} \hat{h} dV = \frac{D^*}{D^* t} \int_{\Omega} \rho h dV + \int_{\Gamma} \rho h (\underline{v} - \underline{v}^*) \cdot \underline{n} d\Gamma = - \int_{\Gamma} \underline{q} \cdot \underline{n} d\Gamma + \int_{\Omega} \rho Q dV \quad (3.9)$$

which defines the non-physical enthalpy  $\hat{h}$  and in the absence of discontinuities the corresponding governing partial differential equation is

$$\frac{D^* \hat{h}}{D^* t} + \hat{h} \operatorname{div} \underline{v}^* = \rho \frac{D^* h}{D^* t} + \rho (\underline{v} - \underline{v}^*) \cdot \nabla h = -\operatorname{div}(\underline{q}) + \rho Q \quad (3.10)$$

where it is evident equation (3.8) is contained within equation (3.10).

Both equations (3.9) and (3.10) provide definitions for  $\hat{h}$  although it is expected (after certain issues are resolved) that equation (3.9) will facilitate the analysis of  $\hat{h}$  in the presence of discontinuities. It is evident by the manner in which  $\hat{h}$  is defined (i.e. satisfying a differential equation) that it is not unique, which as will be shown in subsequent sections is a property that can be used to good advantage. Similarly, non-physical density  $\hat{\rho}$  is defined via

$$\frac{D^*}{D^* t} \int_{\Omega} \hat{\rho} dV = \frac{D^*}{D^* t} \int_{\Omega} \rho dV + \int_{\Gamma} \rho (\underline{v} - \underline{v}^*) \cdot \underline{n} d\Gamma = 0 \quad (3.11)$$

with an accompanying partial differential equation

$$\frac{D^* \hat{\rho}}{D^* t} + \hat{\rho} \operatorname{div} \underline{v}^* = \frac{D^* \rho}{D^* t} + \rho \operatorname{div} \underline{v}^* + \operatorname{div} [\rho (\underline{v} - \underline{v}^*)] = 0 \quad (3.12)$$

This equation is readily solved for  $\hat{\rho}$ , since  $D^* \hat{\rho} / D^* t + \hat{\rho} \operatorname{div} \underline{v}^* = 0$  gives

$$\frac{1}{\hat{\rho}} \frac{D^* \hat{\rho}}{D^* t} = -\text{div} \underline{v}^* \Rightarrow \frac{D^* \ln \hat{\rho}}{D^* t} = -\text{div} \underline{v}^* \Rightarrow \frac{\hat{\rho}}{\hat{\rho}_0} = \exp \left[ - \int_{t_0}^t [\text{div} \underline{v}^*](\mathbf{x}^*(\mathbf{x}_0, s), s) ds \right] \quad (3.13)$$

which for  $\underline{v}^* \neq \underline{0}$  can be succinctly written as

$$\hat{\rho} = \hat{\rho}_0 \exp \left[ - \int_C \text{div} \underline{v}^* \left( \frac{\underline{v}^*}{\|\underline{v}^*\|^2} \right) \cdot d\underline{x}^* \right] \quad (3.14)$$

where  $\hat{\rho}_0$  is  $\hat{\rho}$  at  $t_0$  and  $C$  refers to a contour obtained on the integration of  $d\underline{x}^* = \underline{v}^* ds$ , i.e.  $\mathbf{x}^*(\mathbf{x}_0, t) = \mathbf{x}_0 + \int_{t_0}^t \underline{v}^*(\mathbf{x}^*(\mathbf{x}_0, s), s) ds$ .

With knowledge of  $\hat{\rho}$  a solution for  $\hat{h}$  can be constructed in the form  $\hat{h} = \hat{\rho} \hat{h}^*$ , since the left hand side (LHS) of equation (3.10) gives

$$\hat{\rho} \frac{D^* \hat{h}^*}{D^* t} + \hat{h}^* \left( \frac{D^* \hat{\rho}}{D^* t} + \hat{\rho} \text{div} \underline{v}^* \right) = \hat{\rho} \frac{D^* \hat{h}^*}{D^* t} = \rho \frac{D^* h}{D^* t} + \rho (\underline{v} - \underline{v}^*) \cdot \nabla h = \rho \frac{Dh}{Dt} \quad (3.15)$$

which for  $\underline{v}^* \neq \underline{0}$  on integration gives

$$\hat{h} = \hat{\rho} \left( \frac{\hat{h}_0}{\hat{\rho}_0} + \int_C \left( \frac{\rho}{\hat{\rho}} \right) \frac{Dh}{Dt} \left( \frac{\underline{v}^*}{\|\underline{v}^*\|^2} \right) \cdot d\underline{x}^* \right) \quad (3.16)$$

It is apparent on inspection of equation (3.16) that  $\hat{h}$  is not independent of  $\underline{v}^*$  and in the absence of discontinuities is defined (although not uniquely). Understanding the behaviour of  $\hat{h}$  in the presence of a discontinuity is of particular importance.

### 3.4 Discontinuities for non-physical equations

Consider a discontinuity present in  $\Omega$  in the form of an interface  $\Gamma_i$  between  $\Omega_\ell$  and  $\Omega_s$  (see Figure 3-2). To ascertain the behaviour of the non-physical enthalpy  $\hat{h}$  at the

discontinuity requires careful treatment. One approach might be to consider an arbitrary small volume enclosing  $\Gamma_i$  moving at velocity  $\underline{v}_i$ . The transport of the control volume is assumed to be governed by the regular velocity field velocity  $\underline{v}^+$  where  $\underline{v}^+ \cdot \underline{n} = \underline{v}_i \cdot \underline{n}$  at  $\Gamma_i$  and  $\underline{n}$  is a unit normal on  $\Gamma_i$ . Integrating equation (3.3) with respect to time gives

$$\int_{\Omega_*} \widehat{h} dV - \int_{\Omega_0} \widehat{h} dV = \int_{\Omega_*} \rho h dV - \int_{\Omega_0} \rho h dV + \int_{t_0}^t \int_{\Gamma(t')} \rho h (\underline{v} - \underline{v}^+) \cdot \underline{n} d\Gamma dt' = - \int_{t_0}^t \int_{\Gamma(t')} \underline{q} \cdot \underline{n} d\Gamma dt' \quad (3.17)$$

where for convenience the source term  $Q$  is neglected.

In the limit  $\text{vol}(\Omega_0) \rightarrow 0$ , with the restriction that  $\Gamma_i \subset \Omega_*$ , equation (3.17) reduces to

$$\begin{aligned} \int_{\Gamma_i} \widehat{h}' d\Gamma - \int_{\Gamma_i^0} \widehat{h}'_0 d\Gamma &= - \int_{t_0}^t \int_{\Gamma_i^{\ell}} \rho h_{\ell} (\underline{v}_{\ell} - \underline{v}^+) \cdot \underline{n}_{\ell} d\Gamma dt' - \int_{t_0}^t \int_{\Gamma_i^s} \rho h_s (\underline{v}_s - \underline{v}^+) \cdot \underline{n}_s d\Gamma dt' = \\ &= \int_{t_0}^t \int_{\Gamma_i^{\ell}} \underline{q} \cdot \underline{n}_{\ell} d\Gamma dt' + \int_{t_0}^t \int_{\Gamma_i^s} \underline{q} \cdot \underline{n}_s d\Gamma dt' \end{aligned} \quad (3.18)$$

where  $\widehat{h}'$  and  $\widehat{h}'_0$  are source terms at  $\Gamma_i$  and  $\Gamma_i^0$ , respectively.

It follows, from equation (3.18), that  $\widehat{h}$  is a distribution, so is only quantifiable in an integral sense at  $\Gamma_i$ . It is important to appreciate however, that (3.18) is only valid for the particular  $\underline{v}^+$  chosen, i.e.  $\underline{v}^+$  is a regular velocity field, where  $\underline{v}^+ \cdot \underline{n} = \underline{v}_i \cdot \underline{n}$  on  $\Gamma_i$ . This highlights a particular difficulty in that the behaviour of  $\widehat{h}$  depends on the analysis type. It is clear that the equation on the right hand side (RHS) of (3.18) gives rise to the jump condition  $\int \rho h (\underline{v} - \underline{v}^+) \cdot \underline{n} = - \int \underline{q} \cdot \underline{n}$  at  $\Gamma_i$ , where  $- \int \underline{q} \cdot \underline{n} = \int \underline{q}_s \cdot \underline{n}_s + \int \underline{q}_{\ell} \cdot \underline{n}_{\ell}$  and similarly for  $\int \rho h (\underline{v} - \underline{v}^+) \cdot \underline{n} = \rho_s h_s (\underline{v}_s - \underline{v}^+) \cdot (-\underline{n}_s) + \rho_{\ell} h_{\ell} (\underline{v}_{\ell} - \underline{v}^+) \cdot (-\underline{n}_{\ell})$ . An alternative form of equation (3.18) is obtained on letting  $t \rightarrow t_0$ , i.e.

$$\frac{D^+}{D^+ t} \int_{\Gamma_i} \widehat{h}' d\Gamma = \int_{\Gamma_i} \rho h (\underline{v} - \underline{v}^+) \cdot \underline{n} d\Gamma = - \int_{\Gamma_i} \underline{q} \cdot \underline{n} d\Gamma \quad (3.19)$$

where interchange of differentiation and integration for the left hand side (LHS) term is achieved using

$$\frac{D^+}{D^+t} \int_{\Gamma_i} \hat{h}' d\Gamma = \int_{\Gamma_i} \frac{D^+ \hat{h}'}{D^+t} d\Gamma + \int_{\Gamma_i} \hat{h}' \operatorname{div}_{\Gamma_i} \underline{v}^+ d\Gamma \quad (3.20)$$

where  $\operatorname{div}_{\Gamma_i} \underline{v}^+ = \operatorname{div} \underline{v}^+ - \langle D \underline{v}^+ \underline{n}_s, \underline{n}_s \rangle$  [119] with  $\underline{v}^+$  defined local to  $\Gamma_i$  and where  $(D \underline{v}^+)_{\ell m} = \partial v_\ell^+ / \partial x_m$  and  $\langle \cdot, \cdot \rangle$  stands for inner product. The derivative on the LHS of (3.20) is defined in the sense of (3.18). Thus

$$\frac{D^+ \hat{h}'}{D^+t} + \hat{h}' \operatorname{div}_{\Gamma_i} \underline{v}^+ = \rho h (\underline{v} - \underline{v}^+) \cdot \underline{n} \Big|_{\Gamma_i} = - \underline{q} \cdot \underline{n} \quad (3.21)$$

A solution to this equation is obtained on setting  $\hat{h}' = \hat{\rho}' \hat{h}'^+$  with  $\hat{\rho}'$  satisfying  $D^+ \hat{\rho}' / D^+t + \hat{\rho}' \operatorname{div}_{\Gamma_i} \underline{v}^+ \Big|_{\Gamma_i} = 0$ . It is worth re-emphasising that  $\hat{h}'$  is the particular solution tied to the choice of  $\underline{v}^+$  and restricted by the requirement that  $\underline{v}^+ \cdot \underline{n} = \underline{v}_i \cdot \underline{n}$  on  $\Gamma_i$ . This can be contrasted against the solution  $\hat{h} = \hat{\rho} h^*$  provided in Section 3.3, which is applicable for arbitrary  $\underline{v}^*$  on a continuum. A solution for the case  $\underline{v}^* \neq \underline{v}^+$  is needed and this requires the concept of relative moving frame invariance to be considered.

### 3.5 Moving CV in a moving CV

Consider the situation where  $\underline{v}^*$  and the CV are specified. In this case, the function  $\hat{h}$  is defined via the transport equation (3.9) or at points in a continuum by the partial differential equation (3.10). It is evident that equations (3.9) and (3.10) cannot be readily used to ascertain how  $\hat{h}$  behaves at a discontinuity. If a distribution like behaviour is present at the discontinuity, then equation (3.10) cannot be applied and at best can only be used to ascertain if  $\hat{h}$  jumps by approaching a point on  $\Gamma_i$  from either side. Equation (3.9) is of little use as  $\Omega$  is prescribed and not generally following  $\Gamma_i$ , i.e.  $\underline{v}^* \cdot \underline{n} \neq \underline{v}_i \cdot \underline{n}$ . This particular difficulty can be overcome by defining an additional transport equation for a CV transported by a velocity  $\underline{v}^+$  in the usual way. In this case it is important that  $\hat{h}$  is not dependent on  $\underline{v}^+$ . This is achieved with the transport equation

$$\begin{aligned}
\frac{D^+}{D^+t} \int_{\Omega^+} \hat{h} dV + \int_{\Gamma^+} \hat{h} (\underline{v}^* - \underline{v}^+) \cdot \underline{n} d\Gamma &= \frac{D^+}{D^+t} \int_{\Omega^+} \rho h dV + \int_{\Gamma^+} \rho h (\underline{v} - \underline{v}^+) \cdot \underline{n} d\Gamma = \\
&= - \int_{\Gamma^+} \underline{q} \cdot \underline{n} d\Gamma + \int_{\Omega^+} \rho Q dV \quad (3.22)
\end{aligned}$$

where  $\underline{v}^+$  governs the transport of  $\Omega^+$  in this equation.

### 3.5.1 Proposition

At points in a continuum equations (3.22) and (3.9) are satisfied by the same function  $\hat{h}$ .

#### Proof

It is sufficient to demonstrate that the LHS of (3.22) generates the LHS of equation (3.10).

$$\frac{D^+}{D^+t} \int_{\Omega^+} \hat{h} dV + \int_{\Gamma^+} \hat{h} (\underline{v}^* - \underline{v}^+) \cdot \underline{n} d\Gamma = \int_{\Omega^+} \left[ \frac{D^+ \hat{h}}{D^+t} + \hat{h} \operatorname{div}(\underline{v}^+) + \operatorname{div}(\hat{h} (\underline{v}^* - \underline{v}^+)) \right] dV$$

This implies that  $D^+ \hat{h} / D^+t + \hat{h} \operatorname{div}(\underline{v}^+) + \operatorname{div}(\hat{h} (\underline{v}^* - \underline{v}^+)) = \text{RHS (Eq. (3.10))}$ , as  $\Omega^+$  is arbitrary. Substitution of the identity  $D^+ / D^+t = D^* / D^*t + (\underline{v}^+ - \underline{v}^*) \cdot \nabla$  yields the LHS of equation (3.10) and the proof is complete.

Application of equation (3.22) to a CV following a boundary  $\Gamma_i$  with  $\underline{v}^+ \cdot \underline{n} = \underline{v}_i \cdot \underline{n}$  on  $\Gamma_i$  gives

$$\begin{aligned}
\frac{D^+}{D^+t} \int_{\Gamma_i} \hat{h}' dV + \int_{\Sigma_i} \hat{h}' (\underline{v}^* - \underline{v}^+) \cdot \underline{t} d\Sigma + \int_{\Gamma_i} \hat{h} (\underline{v}^* - \underline{v}^+) \cdot \underline{n} d\Gamma &= \\
&= \int_{\Gamma_i} \rho h (\underline{v} - \underline{v}^+) \cdot \underline{n} d\Gamma = - \int_{\Gamma_i} \underline{q} \cdot \underline{n} d\Gamma \quad (3.23)
\end{aligned}$$

where, as in Section 3.4, the outward square bracket signifies a jump and  $\underline{t}_n$  is an outward pointing unit normal on  $\Sigma_i = \Gamma \cap \Gamma_i$  ( $\Sigma_i$  is the boundary for  $\Gamma_i$ ) that is in a tangent plane of  $\Gamma_i$ .

The term  $\int_{\Sigma_i} \hat{h}'(\underline{v}^* - \underline{v}^+) \cdot \underline{t}_n d\Sigma$  is a consequence of  $\int_{\Gamma^+} \hat{h}(\underline{v}^* - \underline{v}^+) \cdot \underline{n} d\Gamma$  in equation (3.22), which does not vanish as the CV shrinks to  $\Gamma_i$  because of source-like behaviour of  $\hat{h}'$ . Equation (3.23) gives rise to the equation

$$\begin{aligned} \frac{D^+ \hat{h}'}{D^+ t} + \hat{h}' \operatorname{div}_{\Gamma_i} \underline{v}^+ + \operatorname{div}_{\Gamma_i} \left( \hat{h}' (\underline{v}_T^* - \underline{v}_T^+) \right) + (\hat{h}_\ell - \hat{h}_s) (\underline{v}^* - \underline{v}^+) \cdot \underline{n}_s \Big|_{\Gamma_i} = \\ = \left[ \rho h (\underline{v} - \underline{v}^+) \cdot \underline{n} \right] = - \left[ \underline{q} \cdot \underline{n} \right] \end{aligned} \quad (3.24)$$

where subscript T denotes tangent and use is made of the fact that  $(\underline{v}^* - \underline{v}^+) \cdot \underline{n}_s$  is continuous at  $\Gamma_i$ .

It can be demonstrated that  $\hat{h}'$  obtained from equation (3.24) is independent of  $\underline{v}^+$  however it is convenient to leave the proof to a latter section. It is evident (arising from non-uniqueness) that the source term can be specified, so that

$$\frac{D^+ \hat{h}'}{D^+ t} + \hat{h}' \operatorname{div}_{\Gamma_i} \underline{v}^+ + \operatorname{div}_{\Gamma_i} \left( \hat{h}' (\underline{v}_T^* - \underline{v}_T^+) \right) = \left[ \rho h (\underline{v} - \underline{v}^+) \cdot \underline{n} \right] = - \left[ \underline{q} \cdot \underline{n} \right] \quad (3.25)$$

ensuring that limiting values of  $\hat{h}_\ell$  and  $\hat{h}_s$  are equal at  $\Gamma_i$ . This equation can be contrasted against equation (3.21) in Section 3.4, where it is apparent that the additional term is  $\operatorname{div}_{\Gamma_i} \left( \hat{h}' (\underline{v}_T^* - \underline{v}_T^+) \right)$  arising because  $\underline{v}^* \neq \underline{v}^+$ . The property that limiting values of  $\hat{h}_\ell$  and  $\hat{h}_s$  are equal at  $\Gamma_i$  is particularly appealing as it gives rise to the possibility that  $\hat{h}$  can be reasonably approximated by continuous functions. This is despite the fact that  $\hat{h}$  is not defined at  $\Gamma_i$ . A continuous approximation for  $\hat{h}$  is applied over an element in the finite element method and the details are considered in the section that follows.

### 3.6 Finite elements equations

Finite element equations are typically derived using a variational principle (e.g. Hamilton, Virtual work, etc.) or, more generally by applying the method of weighted residuals to the governing partial differential equations. The latter approach is preferred here but the presence of discontinuities prevents its direct application in the usual way. Introduced here is the idea of a weighted transport equation facilitating immediately the incorporation of discontinuities. Consider then the following weighted-transport equation,

$$\begin{aligned} \frac{D^*}{D^*t} \int_{\Omega} W \hat{h} dV &= \frac{D^*}{D^*t} \int_{\Omega} W \rho h dV - \int_{\Omega} \rho h (\underline{v} - \underline{v}^*) \cdot \nabla W dV + \int_{\Gamma} W \rho h (\underline{v} - \underline{v}^*) \cdot \underline{n} d\Gamma = \\ &= \int_{\Omega} \nabla W \cdot \underline{q} dV - \int_{\Gamma} W \underline{q} \cdot \underline{n} d\Gamma + \int_{\Omega} \rho W Q dV \end{aligned} \quad (3.26)$$

where  $W$  is transported invariantly with  $\Omega$ , i.e.  $D^*W/D^*t = 0$ .

Note that spatial and temporal derivatives of  $\hat{h}$  and  $h$  are avoided, making (3.26) applicable when a discontinuity is in  $\Omega$ . Note also that on setting  $W = 1$ , equation (3.3) is returned. Applying (3.26) to an element domain  $\Omega_e$  and adopting a standard Galerkin weighting gives

$$\begin{aligned} \frac{D^*}{D^*t} \int_{\Omega_e} N_i \hat{h} dV &= \frac{D^*}{D^*t} \int_{\Omega_e} N_i \rho h dV - \int_{\Omega_e} \rho h (\underline{v} - \underline{v}^*) \cdot \nabla N_i dV + \int_{\Gamma_e} N_i \rho h (\underline{v} - \underline{v}^*) \cdot \underline{n} d\Gamma = \\ &= \int_{\Omega_e} \nabla N_i \cdot \underline{q} dV - \int_{\Gamma_e} N_i \underline{q} \cdot \underline{n} d\Gamma + \int_{\Omega_e} \rho N_i b dV \end{aligned} \quad (3.27)$$

where  $N_i$  is a shape function and  $\Omega_e$  is an element domain and  $\Gamma_e$  is its boundary.

Note that continuity of  $W$  and  $h$  (in the absence of discontinuities) is required to ensure  $\int_{\Gamma_e} W \rho h (\underline{v} - \underline{v}^*) \cdot \underline{n} d\Gamma$  is uniquely defined at element boundaries. No such restriction is imposed on the function  $\hat{h}$ , which can be discontinuous at element boundaries. It should be appreciated that like  $\Omega$  the movement of  $\Omega_e$  is dictated by the specified velocity  $\underline{v}^*$ . Integration of the LHS and RHS of (3.27) over a time interval  $[t_n, t_{n+1}]$  gives



$$\int_{\Omega_e^{n+1}} N_i \hat{h}^{n+1} dV - \int_{\Omega_e^n} N_i \hat{h}^n dV = \int_{t_n}^{t_{n+1}} \int_{\Omega_e(t)} \nabla N_i \cdot \underline{q} dV dt - \int_{t_n}^{t_{n+1}} \int_{\Gamma_e(t)} N_i \underline{q} \cdot \underline{n} d\Gamma dt + \int_{t_n}^{t_{n+1}} \int_{\Omega_e(t)} \rho N_i Q dV dt \quad (3.28)$$

The significance of this equation is that no advection terms are present, raising the expectation that any difference equations formed can be stabilised. Similarly, equating the left and middle of equation (3.27) gives

$$\begin{aligned} \int_{\Omega_e^{n+1}} N_i \hat{h}^{n+1} dV - \int_{\Omega_e^n} N_i \hat{h}^n dV &= \int_{\Omega_e^{n+1}} N_i \rho^{n+1} h^{n+1} dV - \int_{\Omega_e^n} N_i \rho^n h^n dV - \\ &\quad - \int_{t_n}^{t_{n+1}} \int_{\Omega_e} \rho h (\underline{v} - \underline{v}^*) \cdot \nabla N_i dV dt + \int_{t_n}^{t_{n+1}} \int_{\Gamma_e} N_i \rho h (\underline{v} - \underline{v}^*) \cdot \underline{n} d\Gamma dt \end{aligned} \quad (3.29)$$

This equation establishes the link between  $\hat{h}$  and  $h$ ; a simplified form can be obtained by summing over  $i$  to give

$$\int_{\Omega_e^{n+1}} \hat{h}^{n+1} dV - \int_{\Omega_e^n} \hat{h}^n dV = \int_{\Omega_e^{n+1}} \rho^{n+1} h^{n+1} dV - \int_{\Omega_e^n} \rho^n h^n dV + \int_{t_n}^{t_{n+1}} \int_{\Gamma_e} \rho h (\underline{v} - \underline{v}^*) \cdot \underline{n} d\Gamma dt \quad (3.30)$$

Consider further a linear approximation of  $\hat{h}$  over  $\Omega_e$ , i.e.  $\hat{h} = \sum_{j=1}^{m_e} N_j \hat{h}_j$ . This approximation may appear inappropriate at first sight bearing in mind the distribution like behaviour of  $\hat{h}$  on  $\Gamma_i$ . If continuity is desirable at element interfaces then the analysis of Section 3.5 showed that a source term  $\hat{h}'$  satisfying a form of equation (3.23) or equivalently the differential equation (3.25) must be incorporated in some manner for any element containing a discontinuity. It is desirable to isolate the source terms embedded in equations (3.28) and (3.29) to firstly legitimize the element continuous approximations for  $W$  and  $\hat{h}$  but secondly to benefit any numerical solution algorithm.

An alternative strategy is to neglect the source term but allow for step discontinuities to appear at element interfaces. In this case the effect of the distribution is felt through increases and decreases in  $\hat{h}$ . One advantage arising from discontinuities at the element boundaries is that  $\hat{h}$  can be determined without recourse to information about  $\hat{h}$  in adjoining elements. It is apparent from solution (3.16) that  $\hat{h}$  is not uniquely determined

by  $\hat{h}$  since  $\hat{h}_0$  is completely arbitrary. Thus it is permissible to have discontinuities in  $\hat{h}$  at element interface whilst at the same time ensure continuity for  $h$  on an element domain. The various approaches are depicted in Figure 3-3 but focus in this chapter on the source approach depicted in Figure 3-3(c), where the source term  $\hat{h}'$  is provided by an analytical treatment on an element. To remove the discontinuities from equation (3.28) and (3.29) require establishing relationships between different transport derivatives and matching these on an element domain.

### 3.7 Matching transport derivatives

The velocity  $\underline{v}^+$  field is typically selected to track a discontinuity and facilitates the establishment of analytical results. Similarly, the velocity field  $\underline{v}^*$  is specified to be used in a computational frame and is used to describe the motion of elements in the FE formulation outlined in Section 3.6. It is advantageous to perform analytical type analysis in a computational frame on the governing transport equations without recourse to the governing partial differential equations. To do this it is necessary to establish the relationship between the derivative  $D^+\left(\int_{\Omega^+} \hat{h} dV\right)/D^+t + \int_{\Gamma^+} \hat{h}(\underline{v}^* - \underline{v}^+) \cdot \underline{n} d\Gamma$  and  $D^*\left(\int_{\Omega^*} \hat{h} dV\right)/D^*t$  found in equations (3.22) and (3.9), respectively.

#### 3.7.1 Proposition

The smooth orientable boundaries  $\Gamma^+$  and  $\Gamma^*$  of  $\Omega^+$  and  $\Omega^*$  respectively, are equal (i.e.  $\Gamma^+ = \Gamma^*$ ) if and only if  $\underline{v}^* \cdot \underline{n} = \underline{v}^+ \cdot \underline{n}$  and  $\Gamma^+ = \Gamma^*$  at time  $t = t_0$ .

##### Proof

Consider a point  $\underline{x} \in \Gamma^+$  and note that  $\underline{dx}^+ = \underline{v}^+ dt = \underline{v}_T^+ dt + \underline{v}_N^+ dt = \underline{dx}_T^+ + \underline{dx}_N^+$  and similarly for  $\underline{dx}^*$ , where subscripts T and N denote tangent and normal. Thus, if  $\underline{v}^* \cdot \underline{n} = \underline{v}^+ \cdot \underline{n}$  then  $\underline{dx}_N^+ = \underline{dx}_N^*$  and it follows (with  $\Gamma^+ = \Gamma^*$  at time  $t = t_0$ ) that  $\Gamma^+ = \Gamma^*$ ,  $\forall t$ . Conversely, if  $\Gamma^+ = \Gamma^*$ ,  $\forall t$ , then  $\underline{dx}_N^+ = \underline{dx}_N^*$  and thus  $\underline{v}^* \cdot \underline{n} = \underline{v}^+ \cdot \underline{n}$ .

Although Proposition 7.1 was restricted to a set with a smooth boundary it can be applied to a Lipschitz continuous boundary, where at a point of discontinuity in normal curvature, a necessary and sufficient requirement for limiting values of  $\underline{v}^* \cdot \underline{n}$  and  $\underline{v}^+ \cdot \underline{n}$  to match is that  $\underline{v}^* = \underline{v}^+$ . This essentially infers that points of discontinuity are mapped to points of discontinuity in the transport process. It follows immediately from Proposition 7.1 that the derivatives  $D^+ \left( \int_{\Omega^+} \hat{h} dV \right) / D^+ t + \int_{\Gamma^+} \hat{h} (\underline{v}^* - \underline{v}^+) \cdot \underline{n} d\Gamma$  and  $D^* \left( \int_{\Omega^*} \hat{h} dV \right) / D^* t$  are equal when  $\Gamma^+ = \Gamma^*$  although it is not necessary for  $\underline{v}^* = \underline{v}^+$  but only that  $\underline{v}^* \cdot \underline{n} = \underline{v}^+ \cdot \underline{n}$  at the boundary. Consider then a discontinuity moving through the domain  $\Omega$ , where  $\underline{v}^* \cdot \underline{n} = \underline{v}^+ \cdot \underline{n}$  on  $\Gamma$  but  $\underline{v}^* \neq \underline{v}^+$  and  $\underline{v}^+ \cdot \underline{n}$  equals  $\underline{v}_i \cdot \underline{n}$ , the normal velocity of the discontinuity  $\Gamma_i$ . In this case

$$\begin{aligned} \frac{D^*}{D^* t} \int_{\Omega} \hat{h} dV &= \frac{D^+}{D^+ t} \int_{\Omega} \hat{h} dV + \int_{\Gamma} \hat{h} (\underline{v}^* - \underline{v}^+) \cdot \underline{n} d\Gamma = \\ &= \frac{D^+}{D^+ t} \int_{\Omega/\Gamma_i} \hat{h} dV + \frac{D^+}{D^+ t} \int_{\Gamma_i} \hat{h}' d\Gamma + \int_{\Sigma_i} \hat{h}' (\underline{v}^* - \underline{v}^+) \cdot \underline{n} d\Sigma \end{aligned} \quad (3.31)$$

where  $\Omega/\Gamma_i = \{\underline{x} : \underline{x} \in \Omega \text{ and } \underline{x} \notin \Gamma_i\}$  and  $\Sigma_i = \Gamma \cap \Gamma_i$ .

Rearranging equation (3.31) gives

$$\frac{D^+}{D^+ t} \int_{\Omega/\Gamma_i} \hat{h} dV = \frac{D^*}{D^* t} \int_{\Omega} \hat{h} dV - \frac{D^+}{D^+ t} \int_{\Gamma_i} \hat{h}' d\Gamma - \int_{\Sigma_i} \hat{h}' (\underline{v}^* - \underline{v}^+) \cdot \underline{n} d\Sigma \quad (3.32)$$

which illustrates how source terms can be removed from  $D^* \left( \int_{\Omega^*} \hat{h} dV \right) / D^* t$ , since both sides of this equation are absent of source terms.

### 3.8 Matching on an element domain

It has been shown in the previous section that in order to relate two transport derivatives involving two velocities  $\underline{v}^*$  and  $\underline{v}^+$  on a domain  $\Omega$  the condition  $\underline{v}^* \cdot \underline{n} = \underline{v}^+ \cdot \underline{n}$  must be invoked. This condition ensures that the transport of the boundary  $\Gamma$  of  $\Omega$  is identical for

both velocities. Here  $\underline{v}^+$  matches the normal velocity of the discontinuity  $\Gamma_i$  and  $\underline{v}^*$  is the velocity dictating the movement of the mesh. However, there is little expectation that the condition  $\underline{v}^* \cdot \underline{n} = \underline{v}^+ \cdot \underline{n}$  applies on an element boundary  $\Gamma_e$ . In a situation where a front passes through an element it is convenient to follow this with a control volume that matches the proportion of the front in the element. This can be achieved with an appropriate velocity  $\underline{v}^\times$  that has the property  $\underline{v}_i \cdot \underline{n}_i = \underline{v}^\times \cdot \underline{n}_i$  on  $\Gamma_i$  and  $\underline{v}^* \cdot \underline{n}_e = \underline{v}^\times \cdot \underline{n}_e$  on  $\Gamma_e$ , where  $\underline{n}_i$  and  $\underline{n}_e$  are unit normals on  $\Gamma_i$  and  $\Gamma_e$ , respectively. In a 2-D space, for point  $\underline{x} \in \Gamma_e \cap \Gamma_i$ , where  $\underline{n}_i \neq \underline{n}_e$ , the two conditions  $\underline{v}_i \cdot \underline{n}_i = \underline{v}^\times \cdot \underline{n}_i$  and  $\underline{v}^* \cdot \underline{n}_e = \underline{v}^\times \cdot \underline{n}_e$  define  $\underline{v}^\times$  at  $\underline{x}$ . A problem can occur if  $\underline{n}_i = \underline{n}_e$ , which can happen when a front leaves or enters a domain with normals aligned. It is evident, although not problematic, that for a 3-D space that  $\underline{v}^\times$  is not defined uniquely at  $\underline{x} \in \Gamma_e \cap \Gamma_i$  by the two conditions  $\underline{v}_i \cdot \underline{n}_i = \underline{v}^\times \cdot \underline{n}_i$  and  $\underline{v}^* \cdot \underline{n}_e = \underline{v}^\times \cdot \underline{n}_e$ . With  $\underline{v}^+$  defined appropriately it is now possible to match derivatives and in particular consider the term appearing on the LHS in the FE transport equation (3.27), i.e.

$$\begin{aligned} \frac{D^*}{D^*t} \int_{\Omega_e} N_i \hat{h} dV &= \frac{D^\times}{D^\times t} \int_{\Omega_e} N_i \hat{h} dV + \int_{\Gamma_e} \hat{h} (\underline{v}^* - \underline{v}^\times) \cdot \underline{n} d\Gamma = \frac{D^\times}{D^\times t} \int_{\Omega_e / \Gamma_i^e} N_i \hat{h} dV + \frac{D^\times}{D^\times t} \int_{\Gamma_i^e} N_i \hat{h}' dV + \\ &\quad + \int_{\Sigma_i^e} N_i \hat{h}' (\underline{v}^* - \underline{v}^\times) \cdot \underline{t} n d\Sigma + \int_{\Gamma_i^e} \hat{h}' (\underline{v}_N^* - \underline{v}_N^\times) \cdot \nabla N_i d\Gamma \end{aligned} \quad (3.33)$$

where  $\Gamma_i^e$  is that portion of  $\Gamma_i$  contained in  $\Omega_e$ .

### 3.8.1 Proposition

The transport equation for the portion of  $\Gamma_i$  passing through an element is described

$$\frac{D^\times}{D^\times t} \int_{\Gamma_i^e} \hat{h}' d\Gamma + \int_{\Sigma_i^e} \hat{h}' (\underline{v}^* - \underline{v}^\times) \cdot \underline{t} n d\Sigma = \int_{\Gamma_i^e} \left[ \rho \hat{h} (\underline{v} - \underline{v}^\times) \cdot \underline{n} \right] d\Gamma - \int_{\Gamma_i^e} \underline{q} \cdot \underline{n} d\Gamma \quad (3.34)$$

where  $\underline{n}$  is an outward pointing unit normal on  $\Sigma_i^e$  (the boundary for  $\Gamma_i^e$ ) that is in a tangent plane of  $\Gamma_i^e$ .

### Proof

Application of Reynold's and Stoke's Theorems to the first two terms in equation (3.34) generates

$$\frac{D^\times \widehat{h}'}{D^\times t} + \widehat{h}' \operatorname{div}_{\Gamma_i} \underline{v}^\times + \operatorname{div}_{\Gamma_i} \left( \widehat{h}' (\underline{v}_T^* - \underline{v}_T^\times) \right) = \left[ \rho h (\underline{v} - \underline{v}^\times) \cdot \underline{n} \right] = - \left[ \underline{q} \cdot \underline{n} \right] \quad (3.35)$$

which can be contrasted against that provided by equation (3.25).

Consider the regular velocity field  $\underline{v}_N$  such that for  $\mathbf{x} \in \Gamma_i^t$ ,  $\underline{v}^+ = \underline{v}_N + \underline{v}_T^+$  and  $\underline{v}^\times = \underline{v}_N + \underline{v}_T^\times$ . Define the mapping  $\mathbf{x}^N$  such that  $D^N \mathbf{x}^N / D^N t = \underline{v}_N$  and note that the points  $\mathbf{x}^N(\mathbf{x}, t + \Delta t)$ ,  $\mathbf{x}^+(\mathbf{x}, t + \Delta t)$  and  $\mathbf{x}^\times(\mathbf{x}, t + \Delta t)$  all belong to  $\Gamma_i^{t+\Delta t}$ . Consider further

$$\begin{aligned} \frac{D^\times \widehat{h}'}{D^\times t} - \frac{D^N \widehat{h}'}{D^N t} &= \lim_{\Delta t \rightarrow 0} \frac{\widehat{h}'(\mathbf{x}_{t+\Delta t}^\times, t + \Delta t) - \widehat{h}'(\mathbf{x}, t)}{\Delta t} - \lim_{\Delta t \rightarrow 0} \frac{\widehat{h}'(\mathbf{x}_{t+\Delta t}^N, t + \Delta t) - \widehat{h}'(\mathbf{x}, t)}{\Delta t} \\ &= \lim_{\Delta t \rightarrow 0} \frac{\widehat{h}'(\mathbf{x}_{t+\Delta t}^\times, t + \Delta t) - \widehat{h}'(\mathbf{x}_{t+\Delta t}^N, t + \Delta t)}{\Delta t} = (\underline{v}^\times - \underline{v}_N) \cdot \nabla_{\Gamma_i} \widehat{h}' = \underline{v}_T^\times \cdot \nabla_{\Gamma_i} \widehat{h}' \end{aligned} \quad (3.36)$$

where  $\mathbf{x}_{t+\Delta t}^\times = \mathbf{x}^\times(\mathbf{x}, t + \Delta t)$  and similarly for  $\mathbf{x}_{t+\Delta t}^N$ .

Substitution of identity (3.36) in to equation (3.35) gives:

$$\frac{D^N \widehat{h}'}{D^N t} + \widehat{h}' \operatorname{div}_{\Gamma_i} \underline{v}_N + \operatorname{div}_{\Gamma_i} \left( \widehat{h}' \underline{v}_T^* \right) = \left[ \rho h (\underline{v} - \underline{v}^\times) \cdot \underline{n} \right] = - \left[ \underline{q} \cdot \underline{n} \right] \quad (3.37)$$

which confirms that the tangential component of the  $\underline{v}^\times$  is not involved in the governing equation for  $\widehat{h}'$ . Substitution of identity

$$\frac{D^+ \widehat{h}'}{D^+ t} = \frac{D^N \widehat{h}'}{D^N t} + \underline{v}_T^+ \cdot \nabla_{\Gamma_i} \widehat{h}' \quad (3.38)$$

into equation (3.25) gives identically equation (3.37), confirming the validity of transport equation (3.34).

### Corollary 3.8.1

An immediate corollary to this proposition is that  $\hat{h}'$  is independent of the choice of velocity field tracking the discontinuity.

Established thus far is the necessary theory required to remove sources from an element domain and consequently it is possible to remove discontinuities from the governing FE transport equations.

## 3.9 Details of FEM for transport

The full system of FE transport equations that require solution are:

$$\begin{aligned} \frac{D^*}{D^*t} \int_{\Omega_e/\Gamma_i} N_i \hat{h} dV &= \int_{\Omega_e} \nabla N_i \cdot \underline{q} dV - \int_{\Gamma_e} N_i \underline{q} \cdot \underline{n} d\Gamma + \int_{\Omega_e} \rho N_i Q dV \\ &\quad + \int_{\Gamma_i^e} \hat{h}' (\underline{v}_N^* - \underline{v}_N^\times) \cdot \nabla N_i d\Gamma + \int_{\Gamma_i^e} N_i \underline{q} \cdot \underline{n} d\Gamma \end{aligned} \quad (3.39)$$

$$\begin{aligned} \frac{D^*}{D^*t} \int_{\Omega_e/\Gamma_i} N_i \hat{h} dV &= \frac{D^*}{D^*t} \int_{\Omega_e} N_i \rho h dV - \int_{\Omega_e} \rho h (\underline{v} - \underline{v}^*) \cdot \nabla N_i dV + \int_{\Gamma_e} N_i \rho h (\underline{v} - \underline{v}^*) \cdot \underline{n} d\Gamma \\ &\quad + \int_{\Gamma_i^e} \hat{h}' (\underline{v}_N^* - \underline{v}_N^\times) \cdot \nabla N_i d\Gamma - \int_{\Gamma_i^e} N_i \rho h (\underline{v} - \underline{v}^\times) \cdot \underline{n} d\Gamma \end{aligned} \quad (3.40)$$

$$\begin{aligned} \frac{D^\times}{D^\times t} \int_{\Gamma_i^e} N_i \hat{h}' d\Gamma + \int_{\Sigma_i^e} N_i \hat{h}' (\underline{v}^* - \underline{v}^\times) \cdot \underline{t} n d\Sigma + \int_{\Gamma_i^e} \hat{h}' (\underline{v}_N^* - \underline{v}_N^\times) \cdot \nabla N_i d\Gamma &= \\ = \int_{\Gamma_i^e} N_i \rho h (\underline{v} - \underline{v}^\times) \cdot \underline{n} d\Gamma = - \int_{\Gamma_i^e} N_i \underline{q} \cdot \underline{n} d\Gamma \end{aligned} \quad (3.41)$$

where equations (3.39) and (3.40) are obtained on application of equation (3.33) to equation (3.27) and the validity of equation (3.41) is proven on application of Stoke's and Reynolds transport theorems to LHS equation of (3.41) to give

$$\int_{\Gamma_i^e} \left( \frac{D^\times N_i \hat{h}'}{D^\times t} + N_i \hat{h}' \operatorname{div}_{\Gamma_i} \underline{v}^\times \right) d\Gamma + \int_{\Gamma_i^e} \operatorname{div}_{\Gamma_i} (N_i \hat{h}' (\underline{v}_T^* - \underline{v}_T^\times)) d\Gamma + \int_{\Gamma_i^e} \hat{h}' (\underline{v}_N^* - \underline{v}_N^\times) \cdot \nabla N_i d\Gamma =$$

$$= - \int_{\Gamma_i^e} N_i \underline{q} \cdot \underline{n} d\Gamma \quad (3.42)$$

After cancellation of terms using equation (3.35) and dividing by  $\hat{h}'$ , equation (3.42) in differential form reduces to (see Appendix for details).

$$\frac{D^\times N_i}{D^\times t} + (\underline{v}^* - \underline{v}^\times) \cdot \nabla N_i = \frac{D^* N_i}{D^* t} = 0 \quad (3.43)$$

since by definition  $N_i$  is invariant with respect to the derivative  $D^*/D^* t$ .

It is important to appreciate that no discontinuity is present on the LHS of equations (3.39) and (3.40). In addition the integrals on the LHS of equations (3.39) and (3.40) are evaluated in the sense of Lebesgue. Thus, the source term makes no contribution, the set  $\Omega_e / \Gamma_i$  is not partitioned into two separate domains and  $\Gamma_i$  is null in  $\Omega_e$ , having zero Lebesgue measure. Consequently the RHS of these equations is also absent of discontinuities, achieved primarily as a consequence of isolating the source term. The real power of the non-physical approach is revealed here by its ability to isolate and annihilate discontinuities in transport equations. The annihilation theory provides for the exact annihilation of discontinuities as no approximations are involved. The concepts are therefore widely applicable to problems involving discontinuities although the efficient application of the theory might be restricted by the solution methodology, which may involve approximations.

Many options are available for the simplification and solution of these equations and one approach involves the direct substitution of (3.41) in (3.39) and (3.40) and the replacement of (3.40) and (3.41) with an element and discontinuity transport equations, i.e.

$$\begin{aligned} \frac{D^*}{D^* t} \int_{\Omega_e / \Gamma_i} N_i \hat{h} dV &= \int_{\Omega_e} \nabla N_i \cdot \underline{q} dV - \int_{\Gamma_e} N_i \underline{q} \cdot \underline{n} d\Gamma + \int_{\Omega_e} \rho N_i QV - \\ &\quad - \int_{\Gamma_i^e} N_i ] \rho h (\underline{v} - \underline{v}_i) \cdot \underline{n} d\Gamma + \int_{\Gamma_i^e} \hat{h}' (\underline{v}_N^* - \underline{v}_N^\times) \cdot \nabla N_i d\Gamma \end{aligned} \quad (3.44)$$

$$\frac{D^*}{D^* t} \int_{\Omega_e / \Gamma_i} \hat{h} dV = \frac{D^*}{D^* t} \int_{\Omega_e} \rho h dV + \int_{\Gamma_e} \rho h (\underline{v} - \underline{v}^*) \cdot \underline{n} d\Gamma - \int_{\Gamma_i^e} ] \rho h (\underline{v} - \underline{v}^\times) \cdot \underline{n} d\Gamma \quad (3.45)$$

A further simplification is achieved with the removal of the term  $\int_{\Gamma_i^e} \hat{h}'(\underline{v}_N^* - \underline{v}_N^\times) \cdot \nabla N_i d\Gamma$  in equation (3.44). This can be postulated by the realisation that the principal purpose of this term is to annihilate the discontinuity in the integral  $\int_{\Omega_e} \nabla N_i \cdot \underline{q} dV$ . Thus, with  $\underline{q} = -k\nabla T$  and temperature approximated by  $T = \sum_{j=1}^{m_e} N_j T_j$  (i.e. the discontinuity is ignored), then  $\int_{\Gamma_i^e} \hat{h}'(\underline{v}_N^* - \underline{v}_N^\times) \cdot \nabla N_i d\Gamma$  should also be ignored. The validity of this postulation is demonstrated explicitly in the next section. The solution of (3.44) and (3.45) using a hybrid source-capacitance approach forms the focus of the results section. Each non-physical variable  $\hat{h}$  is to be approximated by  $\hat{h} = \sum_{j=1}^{m_e} N_j \hat{h}_j$  on an element. The integrals involving jump terms in (3.44) and (3.45) are considered as source terms in this formulation. Integration of the two equations gives

$$\begin{aligned} \int_{\Omega_e^{n+1}/\Gamma_i^{n+1}} N_i \hat{h}^{n+1} dV - \int_{\Omega_e^n/\Gamma_i^n} N_i \hat{h}^n dV = & - \int_{t_n}^{t_{n+1}} \int_{\Omega_e(t)} k \nabla N_i \cdot \nabla T dV dt - \int_{t_n}^{t_{n+1}} \int_{\Gamma_e(t)} N_i \underline{q} \cdot \underline{n} d\Gamma dt + \\ & + \int_{t_n}^{t_{n+1}} \int_{\Omega_e(t)} \rho N_i Q dV dt - \int_{t_n}^{t_{n+1}} \int_{\Gamma_i^e(t)} N_i \hat{h} (\underline{v} - \underline{v}^\times) \cdot \underline{n} d\Gamma dt \end{aligned} \quad (3.46)$$

$$\begin{aligned} \int_{\Omega_e^{n+1}/\Gamma_i} \hat{h}^{n+1} dV - \int_{\Omega_e^n/\Gamma_i} \hat{h}^n dV = & \int_{\Omega_e^{n+1}} \rho^{n+1} \hat{h}^{n+1} dV - \int_{\Omega_e^n} \rho^{n+1} \hat{h}^n dV + \int_{t_n}^{t_{n+1}} \int_{\Gamma_e(t)} \rho \hat{h} (\underline{v} - \underline{v}^*) \cdot \underline{n} d\Gamma dt - \\ & - \int_{t_n}^{t_{n+1}} \int_{\Gamma_i^e(t)} \hat{h} (\underline{v} - \underline{v}^\times) \cdot \underline{n} d\Gamma dt \end{aligned} \quad (3.47)$$

The nodal values of  $\hat{h}_j$  are to be determined by an assembled form of equation (3.46). Special treatment is required for discontinuous elements with element types depicted in Figure 3-3(c) considered. Equation (3.47) provides the linkage between physical and non-physical variables and is not assembled but considered here as a constraint on system (3.46).



### 3.10 Isothermal solidification in an Eulerian frame

The general theory simplifies substantially on a stationary mesh ( $\underline{v}^* = \underline{0}$ ) in situations where material movement is sufficiently small to be negligible ( $\underline{v} = \underline{0}$ ) as depicted on Figure 3-4. In this case equations (3.46) and (3.47) reduce to

$$\frac{\partial}{\partial t} \int_{\Omega_e/\Gamma_i} N_i \hat{h} dV = - \int_{\Omega_e} \mathbf{k} \nabla N_i \cdot \nabla T dV - \int_{\Gamma_e} N_i \underline{q} \cdot \underline{n} d\Gamma + \int_{\Omega_e} \rho N_i Q dV + \int_{\Gamma_i^e} N_i \left[ \rho \mathbf{h} \underline{v}^\times \cdot \underline{n} \right] d\Gamma \quad (3.48)$$

$$\frac{\partial}{\partial t} \int_{\Omega_e/\Gamma_i} \hat{h} dV = \frac{\partial}{\partial t} \int_{\Omega_e} \rho h dV + \int_{\Gamma_i^e} \left[ \rho \mathbf{h} \underline{v}^\times \cdot \underline{n} \right] d\Gamma \quad (3.49)$$

It is of interest to examine the form of the non-physical enthalpy  $\hat{h}$ , which is obtainable from equation (3.10), which for this case reduces to  $\partial \hat{h} / \partial t = \rho \partial h / \partial t = \rho c \partial T / \partial t$ . It is important to appreciate that  $\hat{h}$  is only needed at points of continuity. In the case of temperature independent material parameters, integration gives  $\hat{h} - \hat{h}^n = \int_{t_n}^t \rho c (\partial T / \partial s) ds = \rho c (T - T^n)$ . In principal, direct substitution for  $\hat{h}$  in equation (3.48) is possible, so avoiding the use of (3.49). In practice however, accurate evaluation of the integrals involved is a source of difficulty. Moreover, the relationship does suggest the existence of an identity of the form  $\hat{h} = \hat{c} T$ , where  $\hat{c}$  is a non-physical variable. It is important to appreciate that because  $\hat{h}$  is not unique, so there is little requirement to include constants suggested by the relationship  $\hat{h} - \hat{h}^n = \rho c (T - T^n)$ . In addition,  $\hat{c}$  is also non-unique and non-physical and should not be confused with material volumetric specific capacitance  $\rho c$ .

It is of interest also to examine the nature of the source term  $\hat{h}'$ , where  $\hat{h}'$  and  $\underline{v}^\times$  are assumed spatially invariant on  $\Gamma_i^e$  the portion of  $\Gamma_i$  in the element. Then equation (3.35) reduces to

$$\frac{D^\times \hat{h}'}{D^\times t} = \left[ \rho \mathbf{h} (\underline{v} - \underline{v}^\times) \cdot \underline{n} \right] = -\rho_s \underline{v}_i \cdot \underline{n}_s [h_\ell - h_s]_{\Gamma_i} = -\rho_s L (\underline{v}_i \cdot \underline{n}_s) \quad (3.50)$$

which on integration gives  $\widehat{h}'(t) - \widehat{h}'_n = -\rho_s L \int_{t_n}^t \underline{v}_i \cdot \underline{n}_s ds = -\rho_s L (X(t) - X^n)$ , where  $\int_{t_n}^t \underline{v}_i \cdot \underline{n}_s ds = X(t) - X^n$ , with  $X$  denoting the position of the discontinuity measured in the direction of  $\underline{v}_N^\times$ . This suggests a relationship of the form  $\widehat{h}' = -\rho_s L X$ , where again non-uniqueness facilitates the neglect of constant terms. This relationship is approximate, so not recommended for use in the full system of FE equations. Consider further the postulation in Section 3.9 that  $-\int_{t_n}^{t_{n+1}} \int_{\Gamma_i^e} \widehat{h}' \underline{v}^\times \cdot \nabla_{\Gamma_i} N_i d\Gamma dt$  annihilates the discontinuity in  $\int_{t_n}^{t_{n+1}} \int_{\Omega_e} \nabla N_i \cdot \underline{q} dV dt$ . On a small volume  $\Delta V$  swept by the discontinuity over time  $\Delta t$  the relationship  $\Delta X = \Delta V / A = \underline{v}_i^\times \cdot \underline{n}_s \Delta t$  applies. At time interval  $\alpha \Delta t$ , where  $\alpha \in [0, 1]$  the following measure relationship holds

$$\begin{aligned} \int_{\Delta t \Delta V} \nabla N_i \cdot \underline{q} dV dt &= \nabla N_i \cdot \underline{q}_\ell \Delta V \Delta t + \alpha \nabla N_i \cdot (\underline{q}_s - \underline{q}_\ell) \Delta V \Delta t = \\ &= \nabla N_i \cdot \underline{q}_\ell \Delta V \Delta t - \alpha \rho_s L \nabla N_i \cdot \underline{n}_s (\underline{v}_i^\times \cdot \underline{n}_s) \Delta V \Delta t \end{aligned} \quad (3.51)$$

where use is made of jump condition  $[\text{ph}(\underline{v} - \underline{v}^\times) \cdot \underline{n}] = -\rho_s L \underline{v}_i \cdot \underline{n}_s = -[\underline{q}] \cdot \underline{n} = (\underline{q}_s - \underline{q}_\ell) \cdot \underline{n}_s$  and recognition that  $\underline{q}_s - \underline{q}_\ell = -(\underline{q}_s - \underline{q}_\ell) \underline{n}_s$ . Similarly, with  $\widehat{h}'_\alpha - \widehat{h}'_0 = -\rho_s L \alpha \Delta X$  the measure relationship

$$\begin{aligned} -\int_{\Delta t} \widehat{h}'_\alpha \underline{v}^\times \cdot \nabla_{\Gamma_i} N_i A dt &= -\widehat{h}'_0 \underline{v}_i \cdot \nabla_{\Gamma_i} N_i A \Delta t + \alpha \rho_s L \nabla_{\Gamma_i} N_i \cdot \underline{n}_s (\underline{v}_i \cdot \underline{n}_s) A \Delta X \Delta t = \\ &= -\widehat{h}'_0 \underline{v}_i \cdot \nabla_{\Gamma_i} N_i A \Delta t + \alpha \rho_s L \nabla_{\Gamma_i} N_i \cdot \underline{n}_s (\underline{v}_i \cdot \underline{n}_s) \Delta V \Delta t \end{aligned} \quad (3.52)$$

It is evident on comparison that the terms on the far RHS of equations (3.51) and (3.52) are identical and of opposite sign and will be eliminated on addition. Thus the postulation in Section 3.9 is valid and illustrated here is an example how the source term  $\widehat{h}'$  removes a discontinuity. It is worth emphasising here the importance of this result which provides the first analytical justification for the neglect of the discontinuity that appears the integral

$$\int_{t_n}^{t_{n+1}} \int_{\Omega_e} \nabla N_i \cdot \underline{q} dV dt.$$

### 3.11 System assembly and solution

Defined in Section 3.10 via the relationship  $\hat{h} = \hat{c}T$  is the concept of non-physical capacitance. Substitution of this identity into equations (3.48) and (3.49) gives on integration

$$\begin{aligned} \hat{c}^e \left[ \int_{\Omega_e/\Gamma_i^{n+1}} N_i T^{n+1} dV - \int_{\Omega_e/\Gamma_i^n} N_i T^n dV \right] = & - \int_{t_n}^{t_{n+1}} \int_{\Omega_e} k \nabla N_i \cdot \nabla T dV dt - \int_{t_n}^{t_{n+1}} \int_{\Gamma_e} N_i \underline{q} \cdot \underline{n} d\Gamma dt + \\ & + \int_{t_n}^{t_{n+1}} \int_{\Omega_e} \rho N_i Q dV dt + \int_{t_n}^{t_{n+1}} \int_{\Gamma_i^e(t)} N_i \left[ \rho h \underline{v}^\times \cdot \underline{n} \right] d\Gamma dt \end{aligned} \quad (3.53)$$

$$\hat{c}^e = \frac{\int_{\Omega_e} \rho^{n+1} h^{n+1} dV - \int_{\Omega_e} \rho^n h^n dV + \int_{t_n}^{t_{n+1}} \int_{\Gamma_i^e(t)} \left[ \rho h \underline{v}^\times \cdot \underline{n} \right] d\Gamma dt}{\int_{\Omega_e/\Gamma_i} T^{n+1} dV - \int_{\Omega_e/\Gamma_i} T^n dV} \quad (3.54)$$

where for simplicity  $\hat{c}^e$  it is assumed both spatially and temporally invariant on element  $\Omega_e$  and over time interval  $[t_n, t_{n+1}]$ .

The non-physical capacitance obtained from equation (3.54) can be reasonably approximated (although not applied here) by the expression  $f_s \rho_s c_s + f_\ell \rho_\ell c_\ell$ , where element volume fractions  $f_s = V_s/V_e$  and  $f_\ell = V_\ell/V_e$  and where  $V_e$  is the volume of the element. Although at first sight a somewhat surprising approximation it arises because equation (3.54) is absent of any discontinuity, i.e. latent heat affects are annihilated.

It is convenient to represent the term  $S_e = \int_{t_n}^{t_{n+1}} \int_{\Gamma_i^e(t)} N_i \left[ \rho h \underline{v}^\times \cdot \underline{n} \right] d\Gamma dt$  on the far RHS of equation (3.53) in two parts, i.e.  $S_e = S_e^{n+1} + S_e^n$ , where  $S_e^{n+1} = \hat{c}_s^e \int_{\Omega_e} N_i T^{n+1} dV$  and  $S_e^n = -\hat{c}_s^e \int_{\Omega_e} N_i T^n dV$ , where the source capacitance  $c_s^e$  is evaluated from

$$\hat{c}_s^e = \frac{\int_{t_n}^{t_{n+1}} \int_{\Gamma_i^e(t)} \left[ \rho h \underline{v}^\times \cdot \underline{n} \right] d\Gamma dt}{\int_{\Omega_e/\Gamma_i^{n+1}} T^{n+1} dV - \int_{\Omega_e/\Gamma_i^n} T^n dV} \quad (3.55)$$

Approximation of the temperature field in the usual way  $T = \sum_{j=1}^m N_j T_j$  gives an assembled system of the form

$$(\bar{C} - \bar{C}_s)(T^{n+1} - T^n) + \Delta t^n \mathbf{K}(\theta T^{n+1} + (1 - \theta)T^n) = \Delta t^n (\theta \mathbf{Q}^{n+1} + (1 - \theta)\mathbf{Q}^n) \quad (3.56)$$

where an implicit method ( $\theta = 1$ ) is utilised for the predictions and the capacitance matrices  $\bar{C}$  and  $\bar{C}_s$  are diagonal, i.e. a lumped approximation is adopted. The solution of (3.56) is coupled to the solution of (3.54) and (3.55) which provides a non-linear system of equations. A simple bisection technique is applied to converge on  $\bar{c}_s$  and the linear systems of equations for each iterate are solved using a SOR [120] method. The bisection technique is a simple method and is utilised to provide a just comparison in numerical experiments between the proposed method and the method outlined in reference [115], which uses the same approach.

### 3.12 Integral evaluation

The evaluation of the integrals in (3.54) and (3.55) is achieved using the relationships

$$h_s(T) = h_{sol} + \int_{T_{sol}}^T c_s(T') dT' \quad T < T_{liq} \quad (3.57)$$

$$h_\ell(T) = h_{liq} + \int_{T_{liq}}^T c_\ell(T') dT' \quad T > T_{sol} \quad (3.58)$$

where  $h_{liq} = h_{sol} + L$  and  $T_{sol} = T_{liq}$ , where  $L$  is the latent heat released per unit mass.

A single expression for specific enthalpy, valid in the liquid and solid phases is

$$h_m = g_s h_s + g_\ell h_\ell = h_{sol} + g_\ell L + g_s \int_{T_{sol}}^T c_s(T') dT' + g_\ell \int_{T_{liq}}^T c_\ell(T') dT' \quad (3.59)$$

where is made of expressions (3.57) and (3.58), where  $g_s$  and  $g_\ell$  are the solid and liquid mass fractions, respectively.

The enthalpy for an element is obtained on multiplication of equation (3.59) with density and integration over the element domain. It is reasonable to restrict attention to linear elements as these are usually satisfactory for temperature predictions. Moreover, identification of isotherms within the element is relatively straightforward and integration can generally be performed analytically. Typical linear elements are presented in Figure 3-5. The enthalpy of an element at time  $t_n$  is simply,

$$\begin{aligned} \int_{\Omega_e} \rho^n h^n dV = \int_{\Omega_e} \rho^n \left( h_{\text{sol}} + g_\ell L + g_s \int_{T_{\text{sol}}}^T c_s(T') dT' + g_\ell \int_{T_{\text{liq}}}^T c_\ell(T') dT' \right) dV = M_e h_{\text{sol}} + \\ + LM_\ell^n + \int_{\Omega_s} \rho_s \int_{T_{\text{sol}}}^{T^n} c_s(T') dT' dV + \int_{\Omega_\ell} \rho_\ell \int_{T_{\text{liq}}}^{T^n} c_\ell(T') dT' dV \end{aligned} \quad (3.60)$$

where  $\Omega_s$  and  $\Omega_\ell$  are the spatial domains occupied by the solid and liquid, respectively. Moreover,  $M_e^n$  represent the mass of the element and  $M_\ell^n$  is the mass of the liquid phase within the element. For isothermal solidification (3.60) reduces to,

$$\int_{\Omega_e} \rho^n h^n dV = M_e^n h_{\text{sol}} + M_\ell^n L + \rho_s c_s \int_{\Omega_s^n} (T^n - T_{\text{sol}}) dV + \rho_\ell c_\ell \int_{\Omega_\ell^n} (T^n - T_{\text{liq}}) dV \quad (3.61)$$

for constant densities and capacitances

A similar expression can be obtained for time  $t_{n+1}$  and on subtracting one from the other the change in enthalpy for the element can easily be obtained. Additionally, the accurate evaluation of the integral  $\int_{t_n}^{t_{n+1}} \int_{\Gamma_i^e(t)} \rho h \underline{v}^\times \cdot \underline{n} d\Gamma dt$  is required. Recall that the term  $\rho h \underline{v}^\times \cdot \underline{n}$  is obtained on setting  $\underline{v} = \underline{0}$  in the expression  $-\rho h (\underline{v} - \underline{v}^\times) \cdot \underline{n}$ . Note however, that continuity  $-\rho (\underline{v} - \underline{v}^\times) \cdot \underline{n} = 0$  gives  $\rho_s (\underline{v}_s - \underline{v}_i) \cdot \underline{n}_s + \rho_\ell (\underline{v}_\ell - \underline{v}_i) \cdot \underline{n}_\ell = 0$ , which reduces to  $-\rho_s \underline{v}_i \cdot \underline{n}_s = \rho_\ell (\underline{v}_\ell - \underline{v}_i) \cdot \underline{n}_s$ , where it is assumed that  $\underline{v}_s = \underline{0}$  but for  $\rho_s \neq \rho_\ell$  this infers that  $\underline{v}_\ell \neq \underline{0}$ . It follows that  $-\rho h (\underline{v} - \underline{v}^\times) \cdot \underline{n} = \rho_s h_s (\underline{0} - \underline{v}_i) \cdot \underline{n}_s - \rho_\ell h_\ell (\underline{v}_\ell - \underline{v}_i) \cdot \underline{n}_s = \rho_s L \underline{v}_i \cdot \underline{n}_s$ . If on the other hand  $\underline{v}_\ell = \underline{0}$ , then for  $\rho_s \neq \rho_\ell$ ,  $\underline{v}_s \neq \underline{0}$  and the jump condition  $-\rho h (\underline{v} - \underline{v}^\times) \cdot \underline{n}$  gives  $\rho_\ell L \underline{v}_i \cdot \underline{n}_s$ . The assumption  $\underline{v}_s = \underline{0}$  provides a variable mass element, whilst  $\underline{v}_\ell = \underline{0}$  gives

a constant mass element and the corresponding choices for  $\int \rho \mathbf{h} \mathbf{v}^\times \cdot \mathbf{n} d\Gamma$  are  $\rho_s L \mathbf{v}_i \cdot \mathbf{n}_s$  and  $\rho_\ell L \mathbf{v}_i \cdot \mathbf{n}_s$ , respectively. Note, in addition that  $dV_i = \mathbf{v}_i \cdot \mathbf{n}_s d\Gamma dt$ , where  $dV_i$  is a measure of the volume of the element swept by the movement of the phase boundary. Thus for a constant mass element the integral is determined using

$$\int_{t_n}^{t_{n+1}} \int_{\Gamma_i^e(t)} \rho \mathbf{h} \mathbf{v}^\times \cdot \mathbf{n} d\Gamma dt = \rho_\ell L \int_{t_n}^{t_{n+1}} \int_{\Gamma_i^e(t)} \mathbf{v}_i \cdot \mathbf{n}_s d\Gamma dt = \rho_\ell L V_i = \rho_\ell L (V_\ell^n - V_\ell^{n+1}) = (M_\ell^n - M_\ell^{n+1}) L \quad (3.62)$$

where  $V_\ell^n$  is the volume of liquid in the element at time  $t_n$ .

It is of interest to note that the numerator in equation (3.54) gives

$$\begin{aligned} \int_{\Omega_c} \rho^{n+1} \mathbf{h}^{n+1} dV - \int_{\Omega_c} \rho^n \mathbf{h}^n dV + \int_{t_n}^{t_{n+1}} \int_{\Gamma_i^e(t)} \rho \mathbf{h} \mathbf{v}^\times \cdot \mathbf{n} d\Gamma dt = \\ = (M_e^{n+1} - M_e^n) h_{sol} + (M_\ell^{n+1} - M_\ell^n) L - (M_\ell^{n+1} - M_\ell^n) L + \dots \end{aligned} \quad (3.63)$$

where the 3-dot ellipsis refers to sensible heats that follow; it is apparent that all latent heat terms are removed as predicted by the theory. Similarly, if the variable mass assumption is invoked then the RHS of equation (3.62) is  $(M_s^{n+1} - M_s^n) L$  and equation (3.63) becomes

$$\begin{aligned} \int_{\Omega_c} \rho^{n+1} \mathbf{h}^{n+1} dV - \int_{\Omega_c} \rho^n \mathbf{h}^n dV + \int_{t_n}^{t_{n+1}} \int_{\Gamma_i^e(t)} \rho \mathbf{h} \mathbf{v}^\times \cdot \mathbf{n} d\Gamma dt = (M_e^{n+1} - M_e^n) h_{sol} + (M_\ell^{n+1} - M_\ell^n) L + (M_s^{n+1} - M_s^n) L + \dots \\ = (M_e^{n+1} - M_e^n) (h_{sol} + L) + \dots = (M_e^{n+1} - M_e^n) h_{liq} + \dots \end{aligned} \quad (3.64)$$

where it is apparent that latent heat effects are not completely annihilated.

The problem here is that energy transported into the element is neglected but remedied by adding the flux integral  $-\int_{t_n}^{t_{n+1}} \int_{\Gamma^e} \rho \mathbf{h} \mathbf{v} \cdot \mathbf{n} d\Gamma dt$  to equation (3.64). It is demonstrated in reference [115] that a lower-bound approximation for this integral is  $-(M_e^{n+1} - M_e^n) h_{liq}$ . Adding this to equation (3.64) ensures the complete annihilation of the discontinuity as predicted by the theory. A constant mass element is assumed for the results presented in the following section.

### 3.13 Numerical experiments

In this section the Non-physical Enthalpy Method (NEM) is compared against Analytical and/or Control Volume Capacitance Method (CVCVM) solutions for some typical problems. Both the NEM and CVCVM ensure that the energy loss/gain from an element is consistent with temperature change unlike effective and temporal capacitance approaches. It should be recognised that the representation  $S_e = S_e^{n+1} + S_e^n = \int_{t_n}^{t_{n+1}} \int_{\Gamma_i^e(t)} N_i \left[ \rho h \underline{v}^x \cdot \underline{n} \right] d\Gamma dt$  with  $S_e^{n+1} = \hat{c}_s^e \int_{\Omega_e} N_i T^{n+1} dV$  and  $S_e^n = -\hat{c}_s^e \int_{\Omega_e} N_i T^n dV$  yields a CVCVM with  $\hat{c}_{cvcvm}^e = \hat{c}^e - \hat{c}_s^e$ . The performance of the NEM matches that of the CVCVM with differing results arising from the convergence on the source capacitance  $\hat{c}_s^e$  rather than the CVCVM capacitance  $\hat{c}_{cvcvm}^e$ .

Four problems are considered, which are:

1. Prescribed temperature verification on an element to highlight the differences between  $\hat{c}^e$  and  $\hat{c}_{cvcvm}^e$ .
2. Isothermal solidification of a 1-D semi-infinite slab for an initial liquid state to a solid state.
3. Isothermal solidification at a 2-D semi-infinite corner, which is assessed by predictions along a diagonal ray.
4. Isothermal solidification of a 3-D cube solidification.

The analysis of more complicated/practical problems is not deemed necessary here as the approach is shown to give near identical performance to the CVCVM, which has been thoroughly tested in pressure die casting for a range of complex component geometries [115, 116].

#### 3.13.1 Isothermal solidification for 1-D element

Consider the 1-D linear element depicted in Figure 3-5 subjected to a decreasing temperature field  $T_2^{n+1} = T_1^{n+1} + T_{diff}$ , where  $T_{diff}$  is the temperature difference between the nodes of the element. The temperature difference between the nodes is set to: 5, 10 and 20°C and  $T_1^n = T_{liq} + 1$  with  $T_{liq} - 21 \leq T_1^{n+1} < T_{liq} + 1$ . The temperature range is selected

to ensure the material is initially liquid and ends up completely solid. The material properties are given in the first column of Table 3.1, under the heading of material 1 and are approximately those for Zinc.

Depicted in Figure 3-6 and Figure 3-7 are the non-physical capacitances  $\hat{c}_{\text{cvcm}}^e$  and  $\hat{c}^e$  for the CVCm and the NEM respectively. It is evident on comparison of Figure 3-6 and Figure 3-7 that the variation of  $\hat{c}_{\text{cvcm}}^e$  is an order of magnitude greater than that of  $\hat{c}^e$  obtained from equation (3.54). This illustrates that the discontinuous latent heat effect has been effectively removed with the inclusion of the term  $\int_{t_n}^{t_{n+1}} \int_{\Gamma_i^e(t)} \left[ \rho h \underline{v}^\times \cdot \underline{n} \right] d\Gamma dt$  in equation (3.54). This is demonstrated analytically in equations (3.62) and (3.63) but also demonstrated numerically in Figure 3-6. As mentioned in Section 3.12,  $f_s \rho_s c_s + f_\ell \rho_\ell c_\ell$  provides a reasonable approximation for  $\hat{c}^e$ , where in this case  $\rho_s c_s = 2.76 \text{ MJ/m}^3 \text{ } ^\circ\text{C}$  and  $\rho_\ell c_\ell = 3.30 \text{ MJ/m}^3 \text{ } ^\circ\text{C}$ , which can be compared against the numerical values provided in Figure 3-7.

### 3.13.2 1-D semi-infinite domain with phase-change.

Isothermal solidification of a semi-infinite slab with a fixed temperature boundary condition has a known analytical solution [31]. The mesh used for the test is depicted in Figure 3-8 along with boundary and initial conditions. The material properties are given in the first column of the Table 3.1, which are those for zinc. Temperature histories and profiles and information on the non-physical capacitances are provided in Figure 3-9 to Figure 3-11, for different locations along the slab. Excellent accuracy for temperature histories and profiles for both the NEM and CVCm is obtained as illustrated in Figure 3-9 and Figure 3-10. The behaviour of the non-physical capacitances  $\hat{c}_{\text{cvcm}}^e$  and  $\hat{c}^e$  is shown in Figure 3-11 and mirrors that shown in Figure 3-6 and Figure 3-7. The spikes in value of  $\hat{c}_{\text{cvcm}}^e$  correspond with the phase front passing through the elements at the stipulated spatial locations. The behaviour of  $\hat{c}^e$  appears near invariant on the scale adopted in the plots and illustrates the effectiveness of procedure for discontinuity annihilation.



### 3.13.3 2-D semi-infinite domain with phase-change.

The isothermal solidification semi-infinite corner problem is considered where mesh boundary and initial conditions are depicted in Figure 3-12. The authors are unaware of an analytical solution for this case although a solution with solidification absent does exist [31]. A modified form of the solution given in reference [31] with solid and liquid phases identified is

$$T_s(x, y, t) = T_{\text{wall}} + \left( \frac{T_{\text{liq}} - T_{\text{wall}}}{\text{erf}(\lambda)^2} \right) \text{erf}\left(\frac{x}{2\sqrt{\kappa_s t}}\right) \text{erf}\left(\frac{y}{2\sqrt{\kappa_s t}}\right) \quad (3.65)$$

$$T_\ell(x, y, t) = T_\infty + \left( \frac{T_{\text{liq}} - T_\infty}{1 - \text{erf}\left(\lambda \sqrt{\frac{\kappa_s}{\kappa_\ell}}\right)^2} \right) \left[ 1 - \text{erf}\left(\frac{x}{2\sqrt{\kappa_\ell t}}\right) \text{erf}\left(\frac{y}{2\sqrt{\kappa_\ell t}}\right) \right] \quad (3.66)$$

where  $\kappa_s = k_s / \rho_s c_s$  and  $\kappa_\ell = k_\ell / \rho_\ell c_\ell$  are the thermal diffusivities for the solid and liquid phases respectively and attention is restricted here to a problem where  $\kappa_s = \kappa_\ell$ .

The condition  $\kappa_s = \kappa_\ell$  ensures that if  $T_s = T_\ell = T_{\text{liq}}$  a unique representation for the phase front is obtained from both equations (3.65) and (3.66). The parameter  $\lambda$  is selected to ensure that the jump condition  $-\rho_\ell L \underline{v}_i \cdot \underline{n}_s = (\underline{q}_s - \underline{q}_\ell) \cdot \underline{n}_s$  is matched precisely along the diagonal where  $\sqrt{2} \underline{n}_s = \underline{i} + \underline{j}$ . If  $L \neq 0$  the jump condition is not matched at all points on the phase front but is matched at all points for  $L = 0$ . Accuracy of the analytical result improves as  $L \rightarrow 0$ , which is compared against the results obtained from the CVCM and the NEM. The material properties are those from the second column in the Table 3.1, where it is apparent that a relatively small value of latent heat is chosen. The temperature history for selected points along the diagonal is displayed in Figure 3-13, where good agreement is obtained. Temperature profiles along the diagonal at different time are displayed in Figure 3-14, where again reasonable accuracy is evident. The position of the phase front with time measured along the diagonal is shown in Figure 3-15. Excellent accuracy is apparent from both the CVCM and the NEM.

### 3.13.4 3-D cube domain with phase-change.

The isothermal solidification of a cube is considered where mesh boundary and initial conditions are depicted in Figure 3-16. Although an analytical solution is unavailable, different time steps and mesh densities are tested to ascertain the relative sensitivities of the CVCM and the NEM. Given in Table 3.2 and Table 3.3 are the approximate program execution times for each of the methods along with results pertaining to the three error norms

$$\max_{i,n} |T_i^n - T_i^{nb}|, \quad \max_{i,n} \left| \frac{X_s^n - X_s^{nb}}{X_L} \right| \times 100, \quad \max_{i,n} \left| \frac{E^n - E^{nb}}{E_{total}^{nb}} \right| \times 100$$

where  $i$  and  $n$  represents the nodal position along the cube diagonal and time step, respectively. Moreover,  $X_s$  and  $E$  are the position of the solidus front and the energy loss from the cube surface, respectively. The subscript  $b$  indicates benchmark values, which since no analytical solution is available, are taken as the results obtained using NEM with  $\Delta x = 0.50$  mm (6000 elements) and  $\Delta t = 0.005$  s. The tests were performed using an implicit Euler time-stepping algorithm and the non-linear equations were solved using a bisection method. The material properties are taken from column 1 in Table 3.1, which corresponds to Zinc. However, in order to provide a sterner test for the methods the latent heat is increased from 130 kJ/kg (test case 1) to 260 kJ/kg (test case 2).

It is evident on comparison of Table 3.2 and Table 3.3 that comparable results are obtained for both methods with a slightly improved performance delivered by the NEM. The temperature histories for various time-steps are presented in Figure 3-17 for the two test cases. Comparable performance is delivered by the two methods with the NEM outperforming the CVCM for test case 2 for time steps  $\Delta t = 0.5$  s and  $\Delta t = 0.1$  s in particular. The behaviour of the non-physical capacitances  $\hat{c}_{cvcm}^e$  and  $\hat{c}^e$  is shown in Figure 3-18 for an element for various time steps for the two test cases. The behaviour of  $\hat{c}^e$  is reasonably invariant as consequence of the ability of the NEM to annihilate the discontinuity in the heat flux at the phase front. Also highlighted is the non-physical nature of  $\hat{c}_{cvcm}^e$ , whose behaviour varies in a non-physical manner changing demonstrably with time-step. A particular feature of both methods is their extraordinary accuracy for relatively large time-steps. This results because both methods maintain consistency between temperature and energy change, i.e. the energy lost from an element corresponds

exactly with the temperature change unlike traditional capacitance and source-based methods.

The results shown in Table 3.3 and Figure 3-19 demonstrate the relative insensitivity of both methods to mesh density. Moreover, the energy loss norm errors presented in Table 3.3 shows only a small discrepancy between fine and coarse meshes, which is further evidence of the benefits of a control volume transport equation methodology. The behaviour of the non-physical capacitances  $\hat{c}_{\text{cvcm}}^e$  and  $\hat{c}^e$  is shown in Figure 3-20 and Figure 3-22 for an element at a specified location varying with mesh density for the two test cases. The behaviour of  $\hat{c}^e$  is reasonably invariant as anticipated but again the non-physical nature of  $\hat{c}_{\text{cvcm}}^e$  is highlighted. Temperature histories at specified points along the diagonal of the cube on a fine mesh ( $\Delta x = 0.50$  mm) and relatively small time-step ( $\Delta t = 0.005$  s) are presented in Figure 3-21. Near identical results are obtained from both methods.

### 3.14 Conclusions

Presented in the chapter 3 is the concept of non-physical enthalpy for the precise removal discontinuities arising in phase-change problems. The following conclusions can be drawn for the work presented:

1. Non-physical enthalpy  $\hat{h}$  is well defined and possesses the property of limiting continuity at a discontinuity in physical enthalpy  $h$ .
2. Non-physical enthalpy  $\hat{h}$  behaves as a source (denoted  $\hat{h}'$ ) on a discontinuity, where  $\hat{h}'$  is well defined.
3. Non-physical enthalpy  $\hat{h}$  is non-physical in the sense that its numerical values are not moving-frame invariant; depending on  $\underline{V}^*$  the velocity of the computational frame.
4. Transport FE element equations are established in the chapter.
5. The source-like behaviour of  $\hat{h}$  facilitates the precise removal of discontinuities from the governing system of transport FE equations.
6. Numerical solution of the governing system of transport FE equations provides excellent accuracy and is computationally competitive.

Table 3.1 Material properties for numerical test

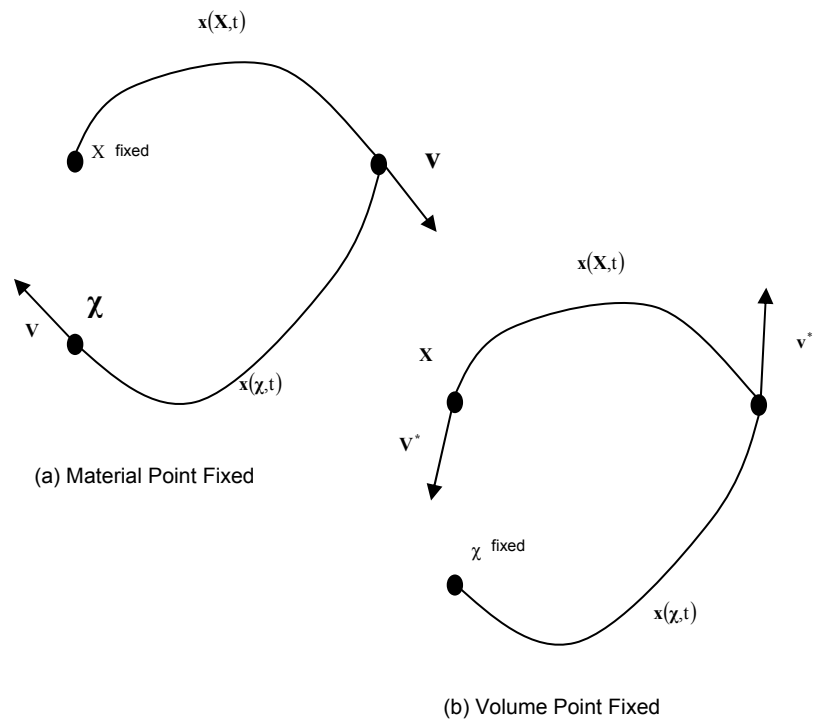
Material Properties	units	Material 1 (pure zinc)	Material 2 (water-like)
Thermal conductivity — solid	$\frac{\text{W}}{\text{m}^\circ\text{C}}$	100	1
Thermal conductivity — liquid		50	1
Heat capacitance — solid	$\frac{\text{J}}{\text{kg}^\circ\text{C}}$	400	1
Heat capacitance — liquid		500	1
Density — solid	$\frac{\text{kg}}{\text{m}^3}$	6900	1
Density — liquid		6600	1
Latent heat	$\frac{\text{kJ}}{\text{kg}}$	130	0.1923
Solidus temperature	$^\circ\text{C}$	400	0
Liquidus temperature			

Table 3.2 Performance data for various time-steps using a constant mesh density of  
 $\Delta x = \Delta y = \Delta z = 1.00$  mm equivalent to 750 elements

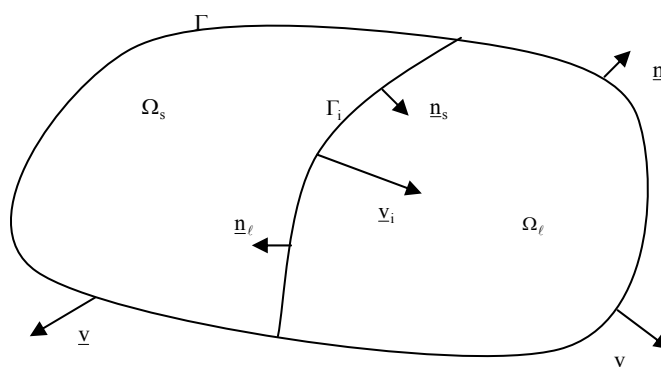
Method	$\Delta t = 0.005$ s		$\Delta t = 0.025$ s		$\Delta t = 0.1$ s		$\Delta t = 0.5$ s	
	Test 1	Test 2	Test 1	Test 2	Test 1	Test 2	Test 1	Test 2
Program execution time (s)								
CVCM	16.60	30.60	3.91	6.36	0.86	2.05	0.375	0.656
NEM	16.70	31.50	3.94	6.28	0.80	3.5	0.406	0.734
Temperature error norm ( $^{\circ}\text{C}$ )								
CVCM	4.02	3.84	2.49	4.43	11.07	14.18	7.64	4.74
NEM	3.90	3.79	2.41	4.42	11.07	5.89	7.64	4.72
Solidus front error norm (per cent)								
CVCM	0.0825	0.62	1.32	1.66	9.5	9.18	14.80	5.48
NEM	0.0536	0.62	0.49	1.66	9.5	5.32	14.80	5.48
Energy loss error norm (per cent)								
CVCM	1.208	0.511	1.7568	0.511	2.77	2.046	6.9462	2.353
NEM	1.188	0.511	1.7568	0.460	2.77	1.023	6.9462	2.353

Table 3.3 Performance data for various mesh densities using time-step  $\Delta t = 0.005$  s

Method	$\Delta x = 0.5$ mm		$\Delta x = 1.0$ mm		$\Delta x = 1.67$ mm	
	Test 1	Test 2	Test 1	Test 2	Test 1	Test 2
Program execution time (s)						
CVCM	131.09	248.59	16.60	30.60	3.625	7.187
NEM	135.07	251.28	16.70	31.50	3.797	6.828
Temperature error norm ( $^{\circ}\text{C}$ )						
CVCM	0.08	0.34	3.96	3.84	5.29	5.92
NEM	0.0	0.0	3.90	3.79	5.29	5.81
Solidus front error norm (per cent)						
CVCM	0.064	0.1107	0.0825	0.62	8.42	8.74
NEM	0.0	0.0	0.0536	0.62	8.42	8.00
Energy loss error norm (per cent)						
CVCM	0.0	0.0	1.2084	0.511	2.26	1.64
NEM	0.0	0.0	1.1882	0.511	2.26	1.64



**Figure 3-1 Velocities in reference domain**



**Figure 3-2 Liquid and solid domains in a solidifying body**

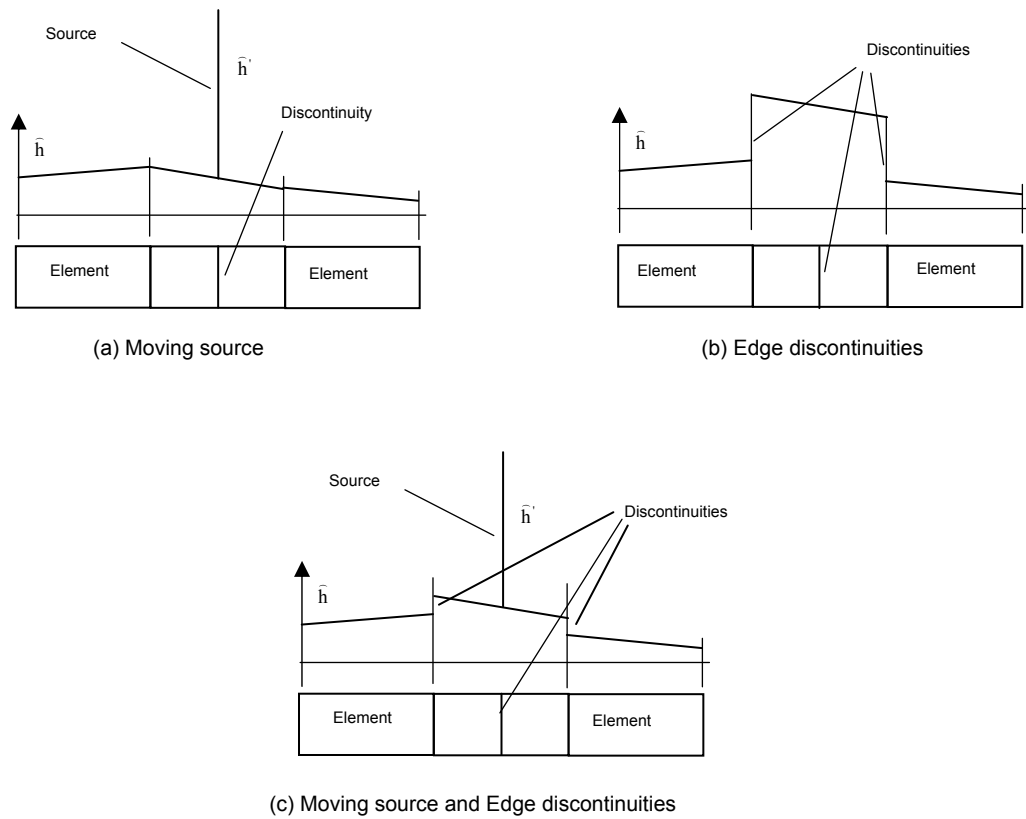


**Figure 3-3 Non-physical behaviour on 1-D elements**

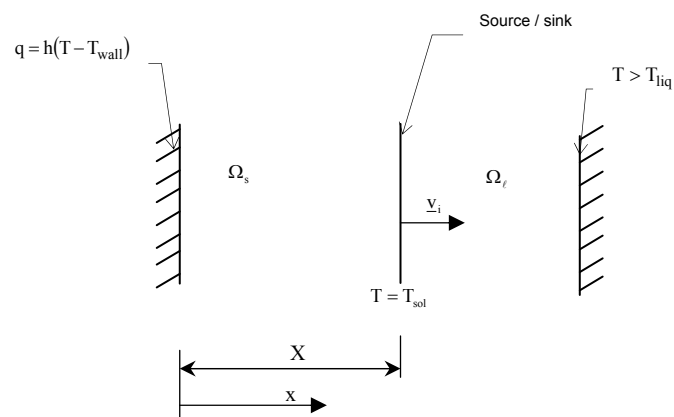


**Figure 3-4 1-D solidification problem on an Eulerian frame**



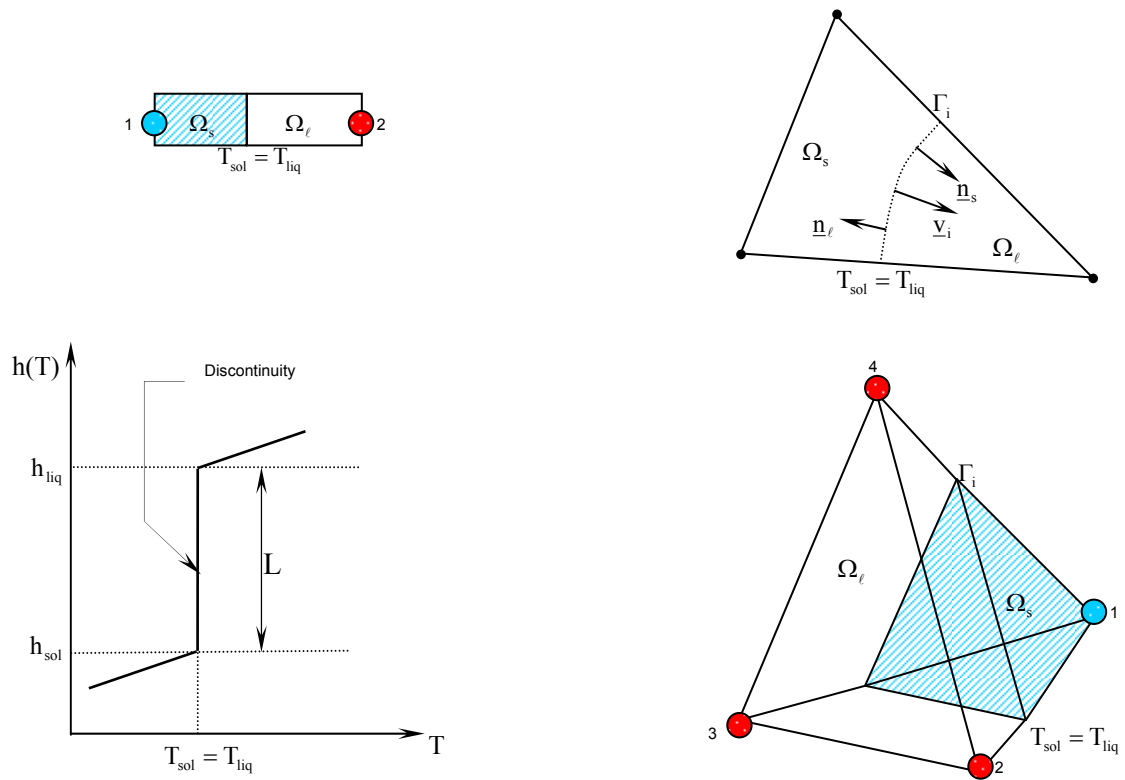


Figure 3-5 Isothermal solidification and linear elements

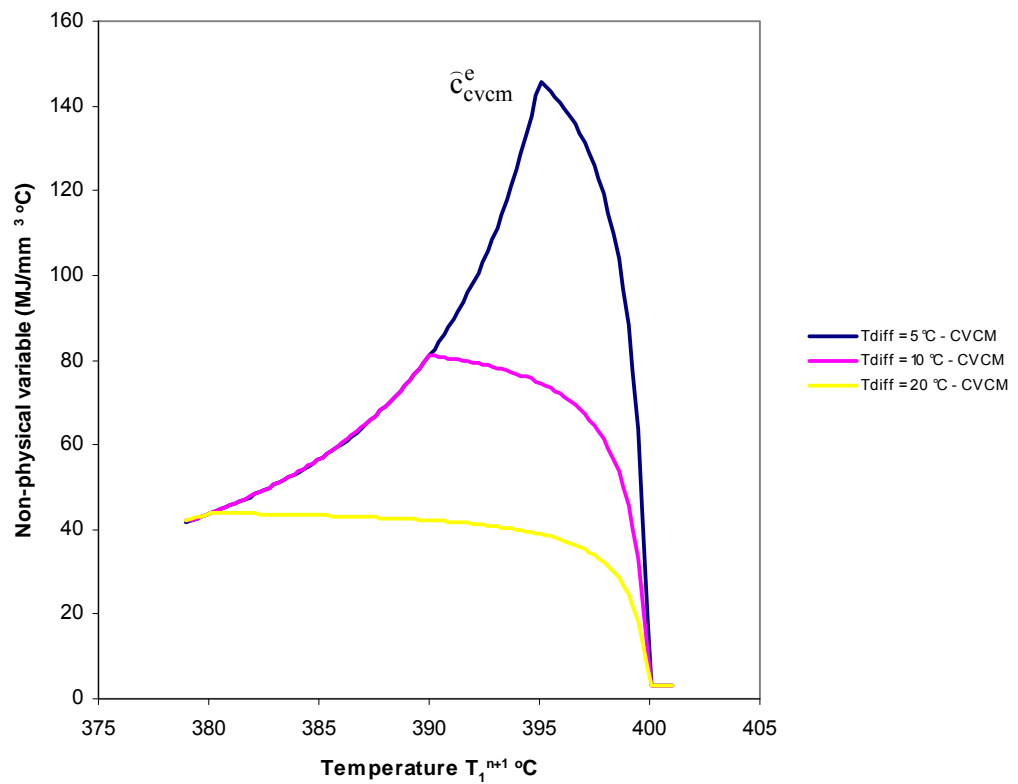


Figure 3-6 Non-physical variable profile for phase-change 1-D element - CVCM

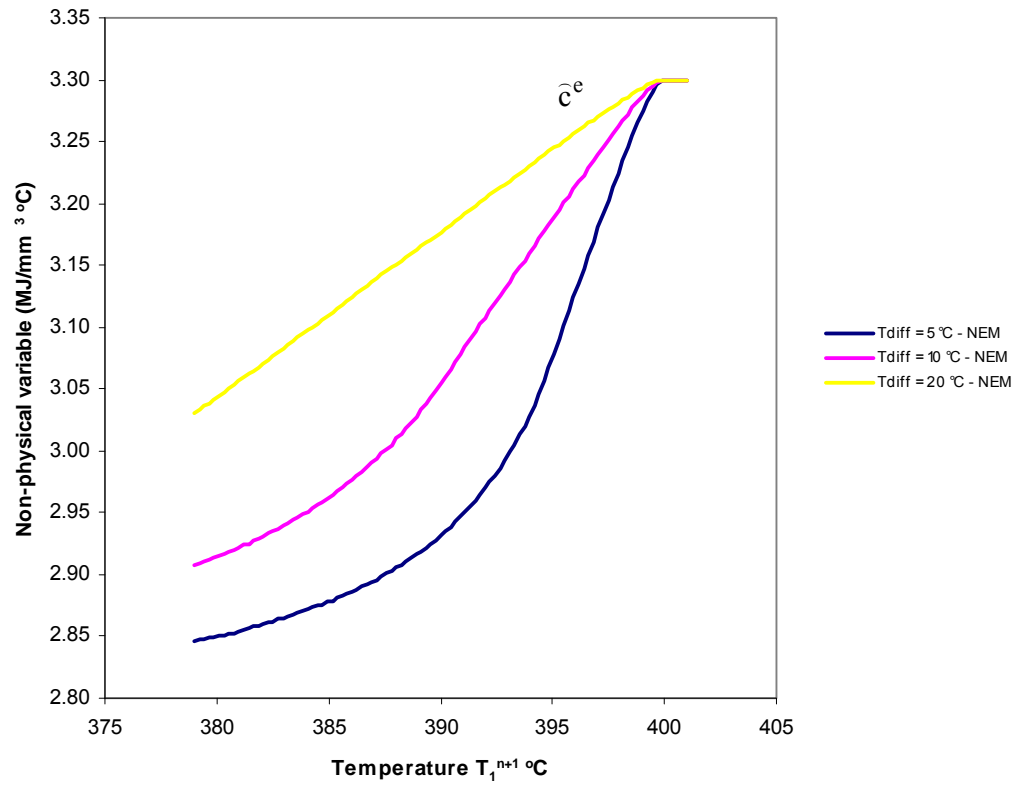


Figure 3-7 Non-physical variable profile for phase-change 1-D element - NEM

#### 1-D SEMI-INFINITE SLAB PROBLEM

$$k \frac{\partial T}{\partial x}(0) = h(T_{\text{amb}} - T)$$

$$T_{\text{amb}} = 0^\circ\text{C}, \quad T_{\text{init}} = 450^\circ\text{C}$$

$$h = 10^4 \text{ W/m}^2\text{C}$$

$$\frac{\partial T}{\partial x}(60) = 0$$

$$\Delta x \text{ (mm)}$$

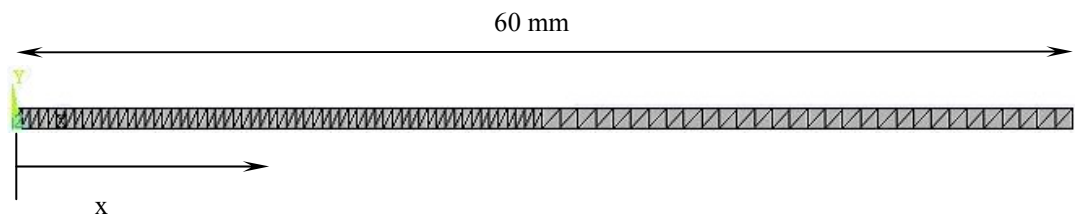


Figure 3-8 Mesh for 1-D semi-infinite slab problem

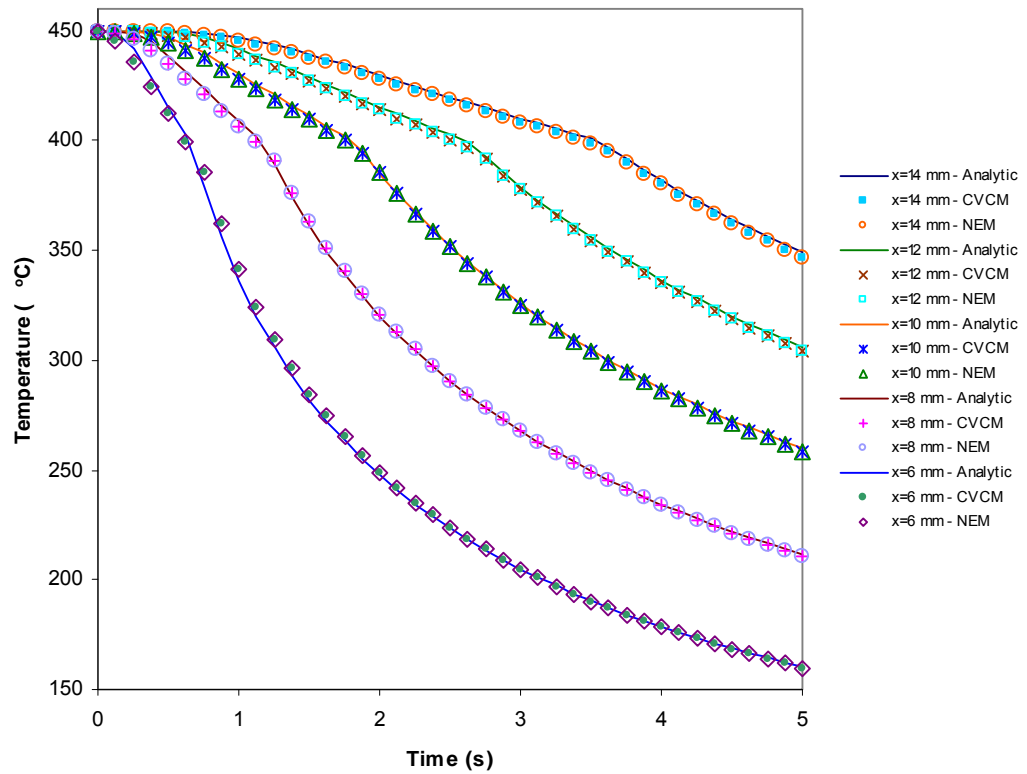


Figure 3-9 Temperature history for phase-change 1-D semi-infinite slab

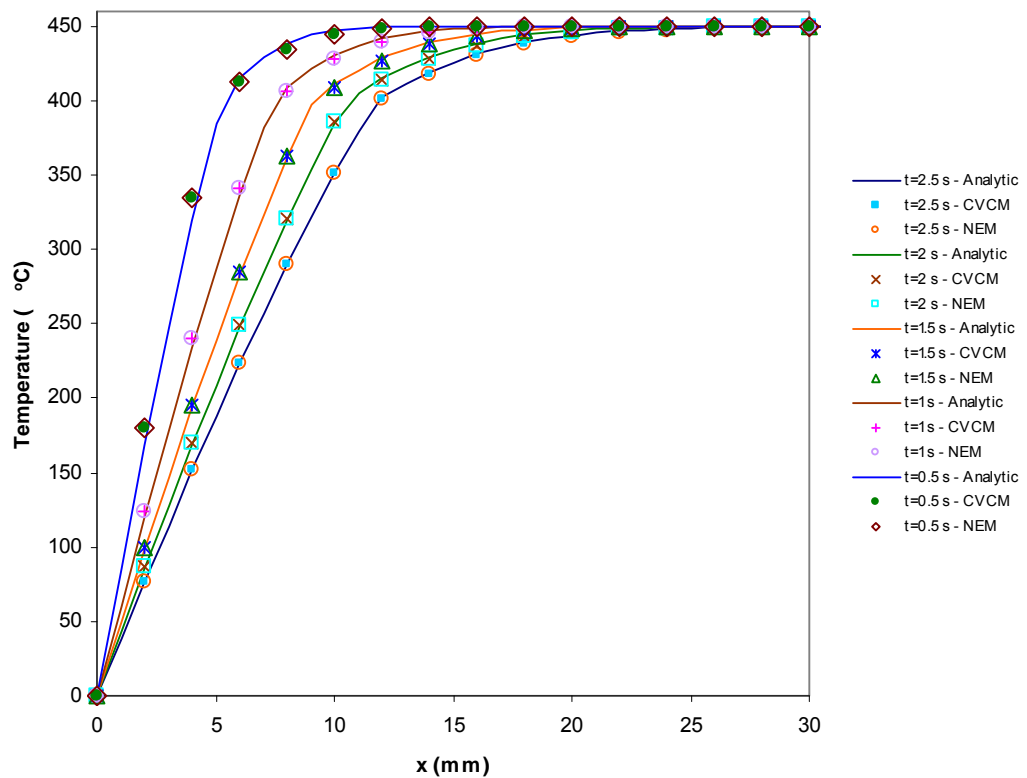


Figure 3-10 Temperature profile comparison for phase-change 1-D semi-infinite slab

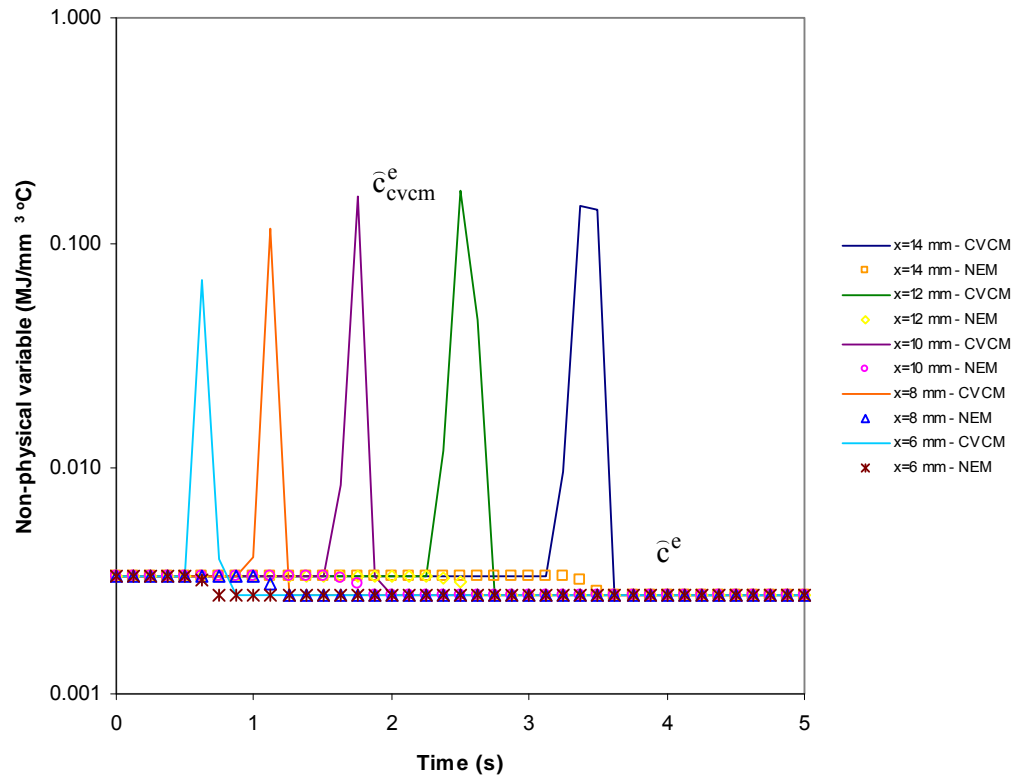


Figure 3-11 Non-physical variable history for phase-change 1-D semi-infinite slab

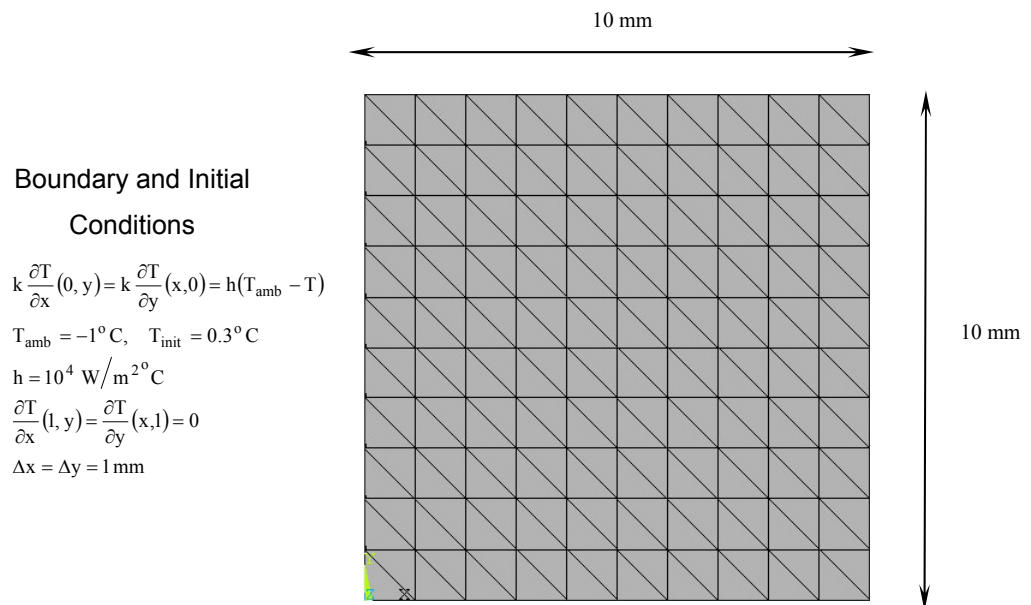


Figure 3-12 Mesh for 2-D semi-infinite corner

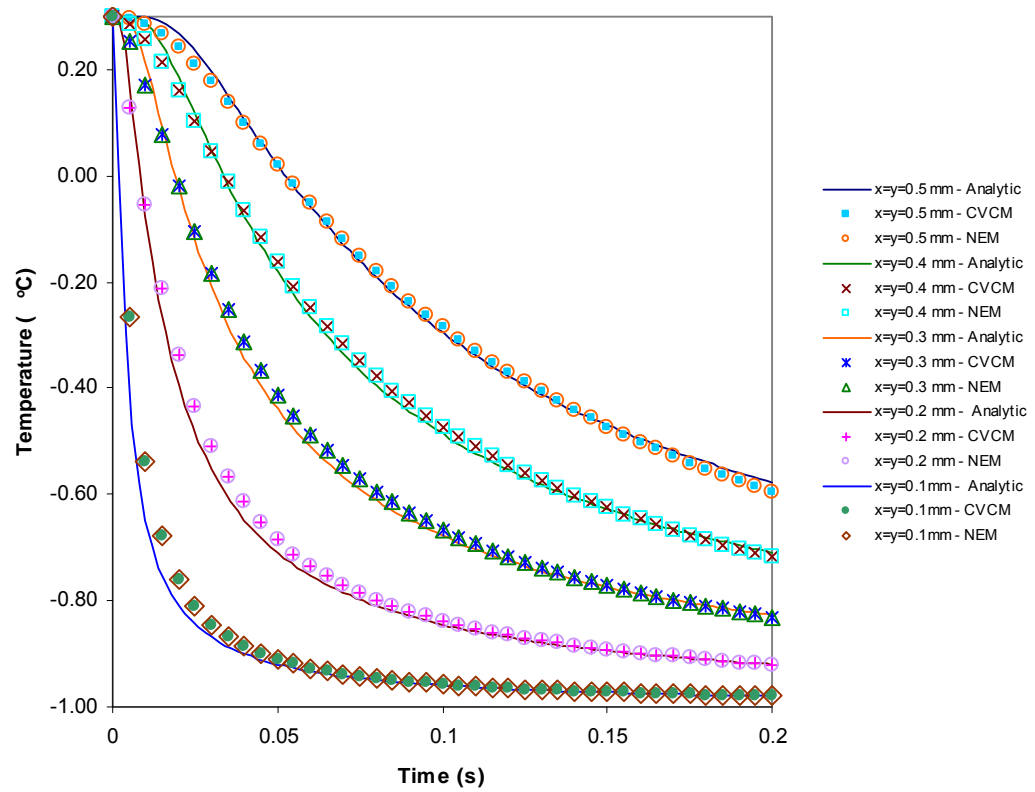


Figure 3-13 Temperature history for phase-change 2-D semi-infinite corner

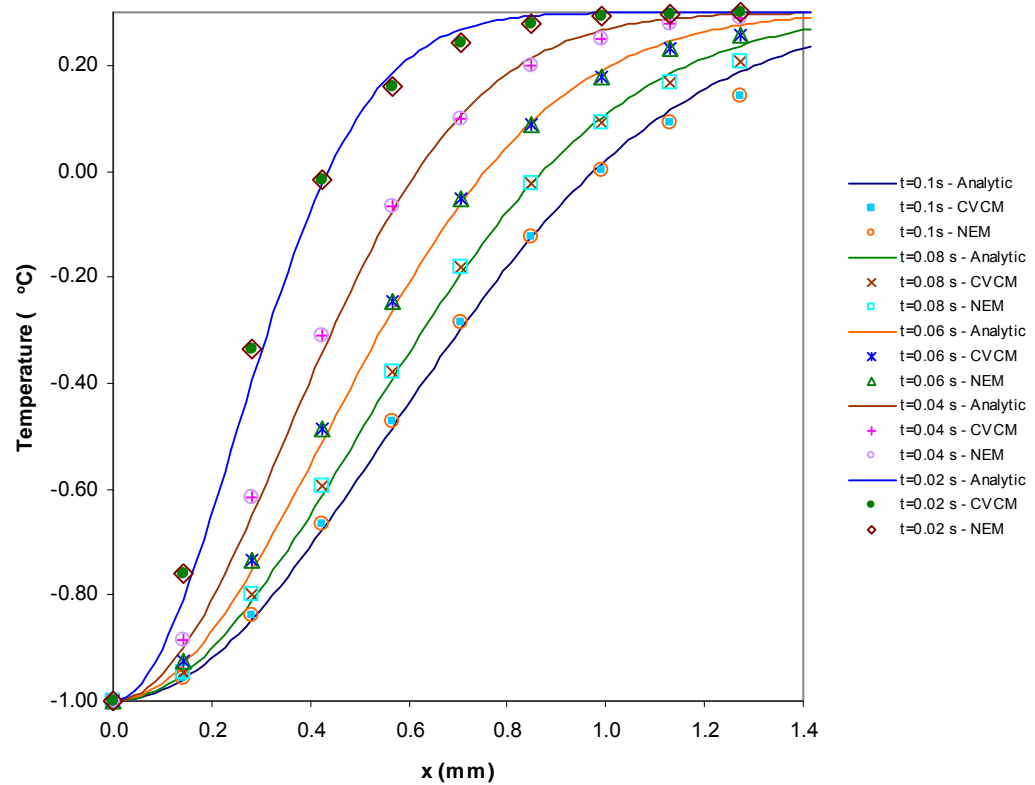


Figure 3-14 Temperature profile comparison for 2-D semi-infinite corner

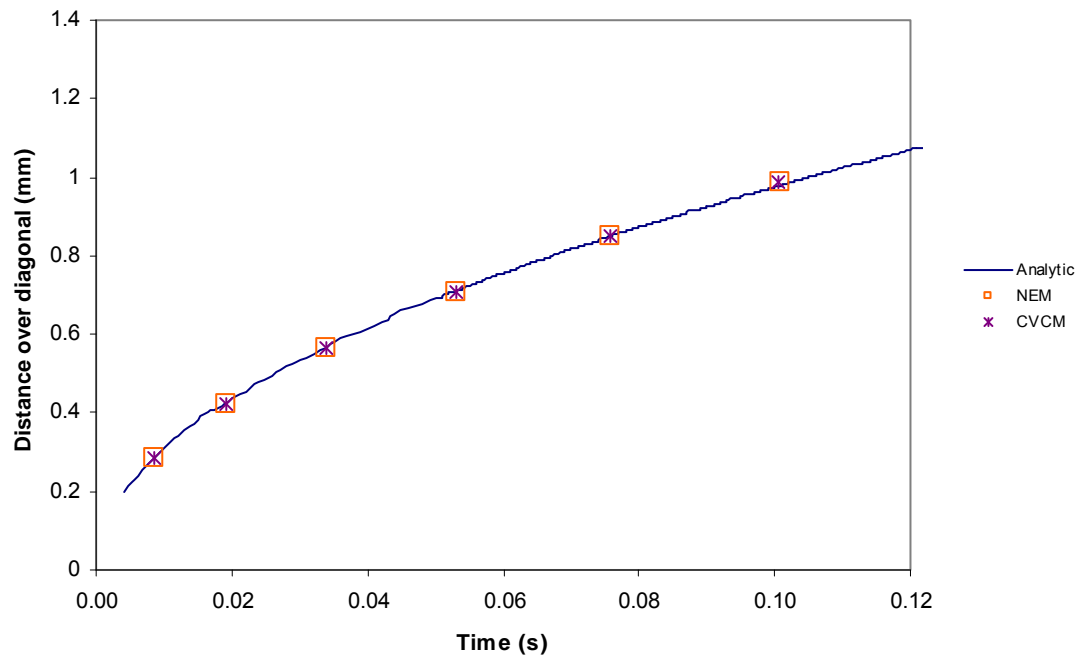


Figure 3-15 Solidification Front moving over 2-D semi-infinite corner diagonal

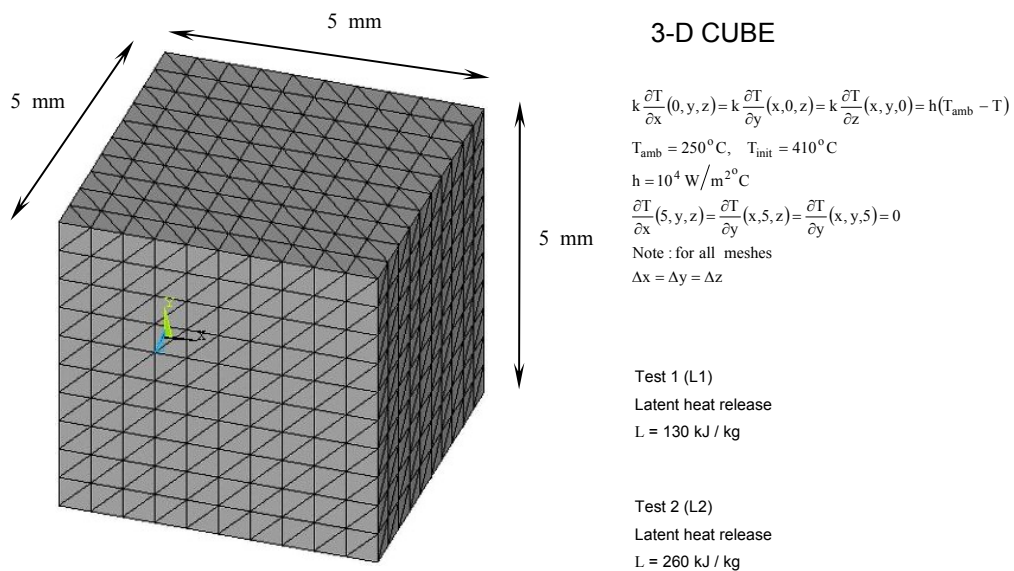


Figure 3-16 Mesh for 3-D cube problem

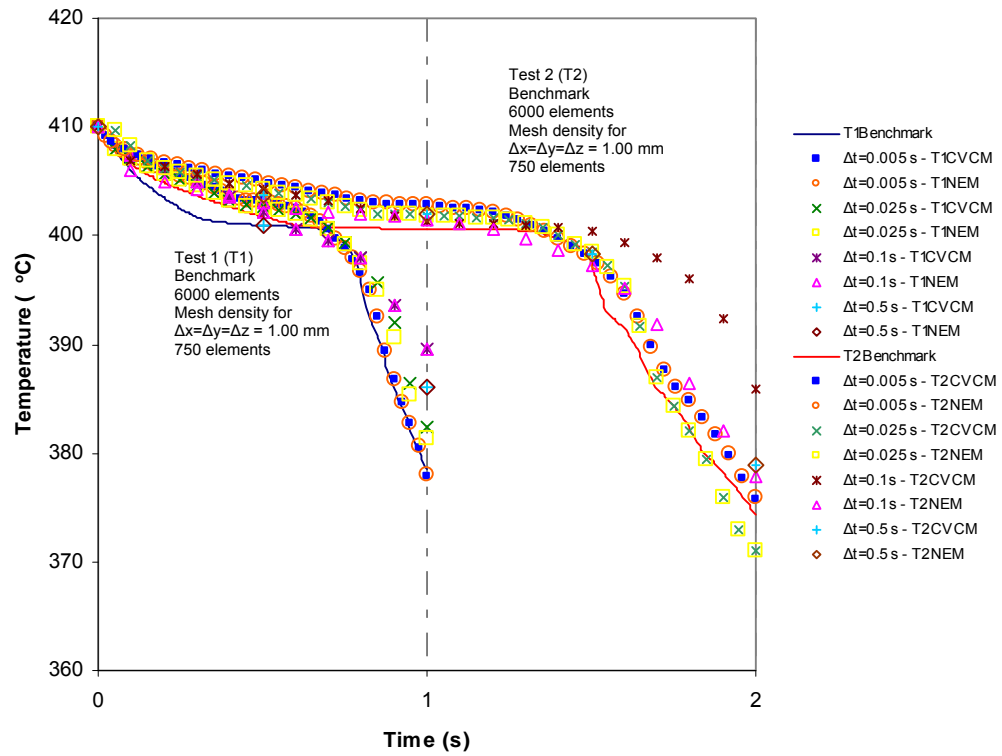


Figure 3-17 Temperature history CVCM - NEM comparison on a 3-D Cube using same mesh density at specific point over diagonal  $x=y=z=2$  mm

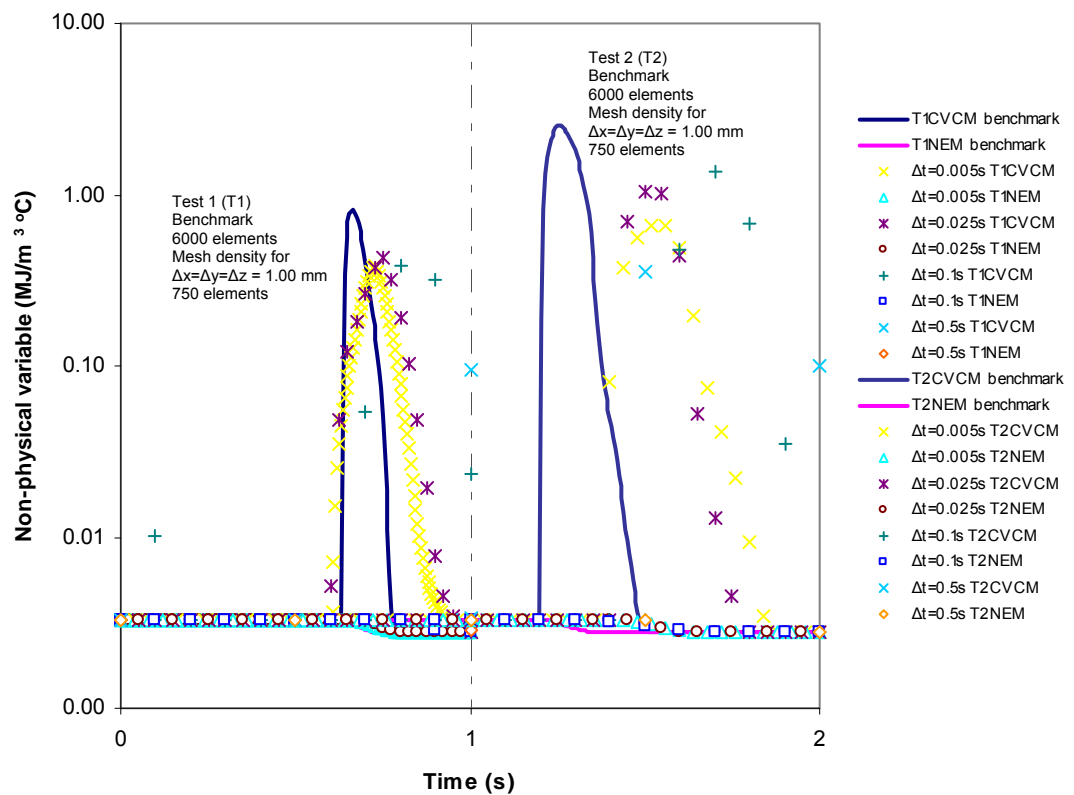
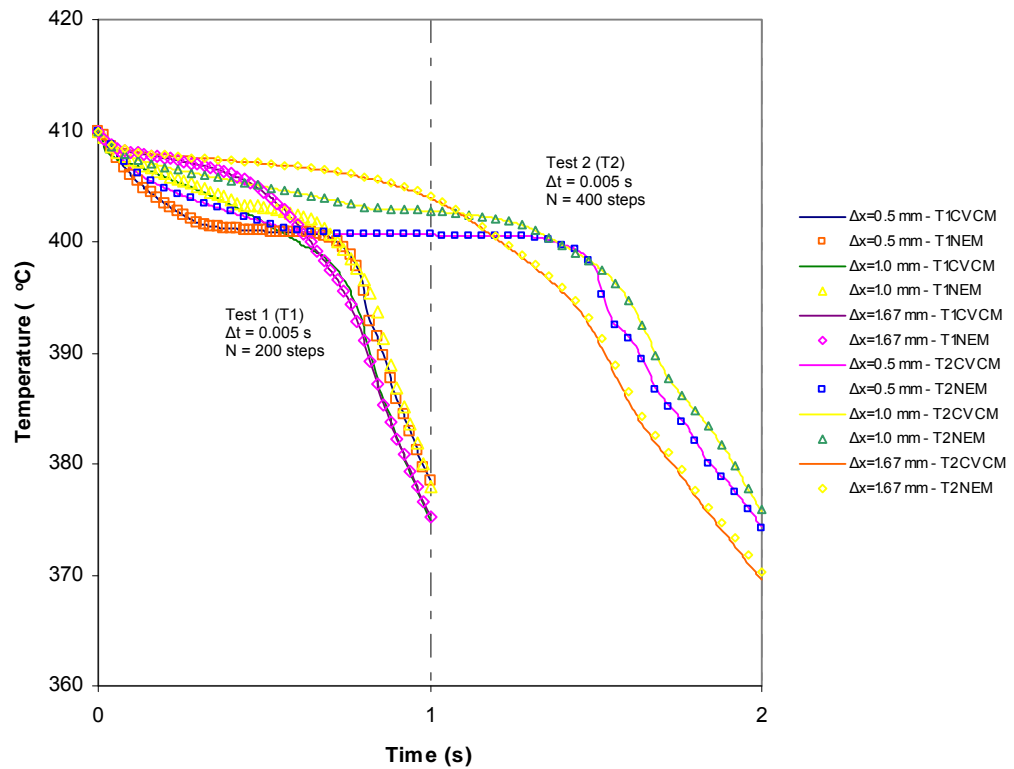
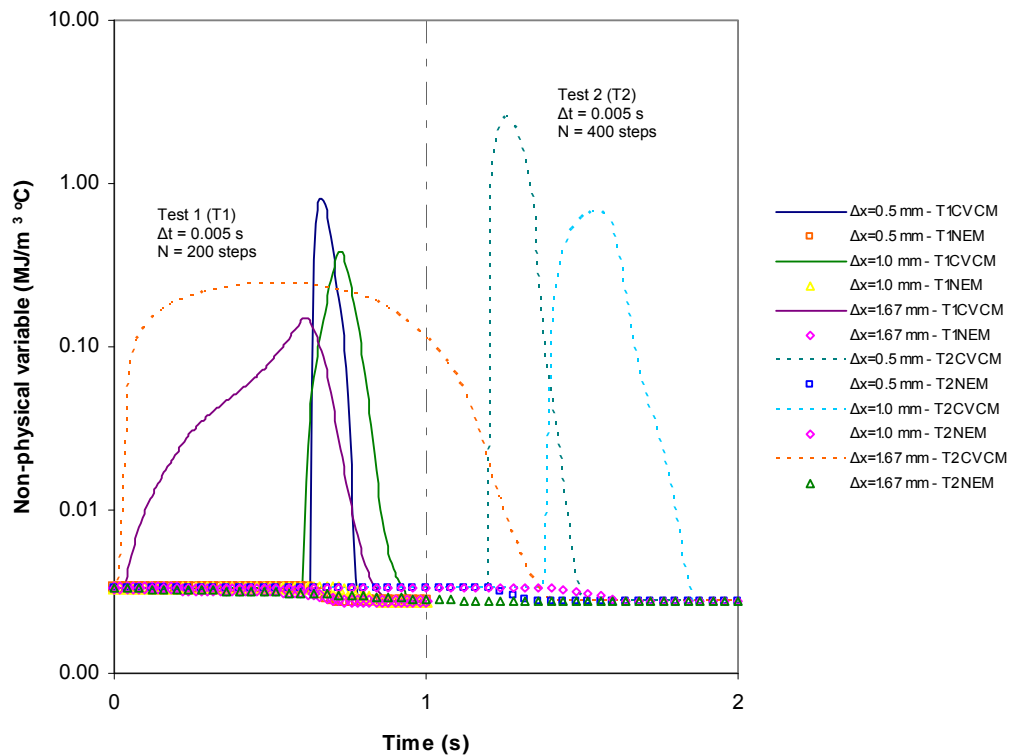


Figure 3-18 CVCM - NEM non-physical variable comparison on a 3-D Cube using same mesh density at specific point over diagonal  $x=y=z=2$  mm



**Figure 3-19 Temperature history CVCM - NEM comparison on a 3-D Cube using different mesh density at a specific point over the diagonal  $x=y=z=2$  mm**



**Figure 3-20 CVCM - NEM non-physical variable comparison on a 3-D Cube using different mesh density at a specific point over the diagonal  $x=y=z=2$  mm**



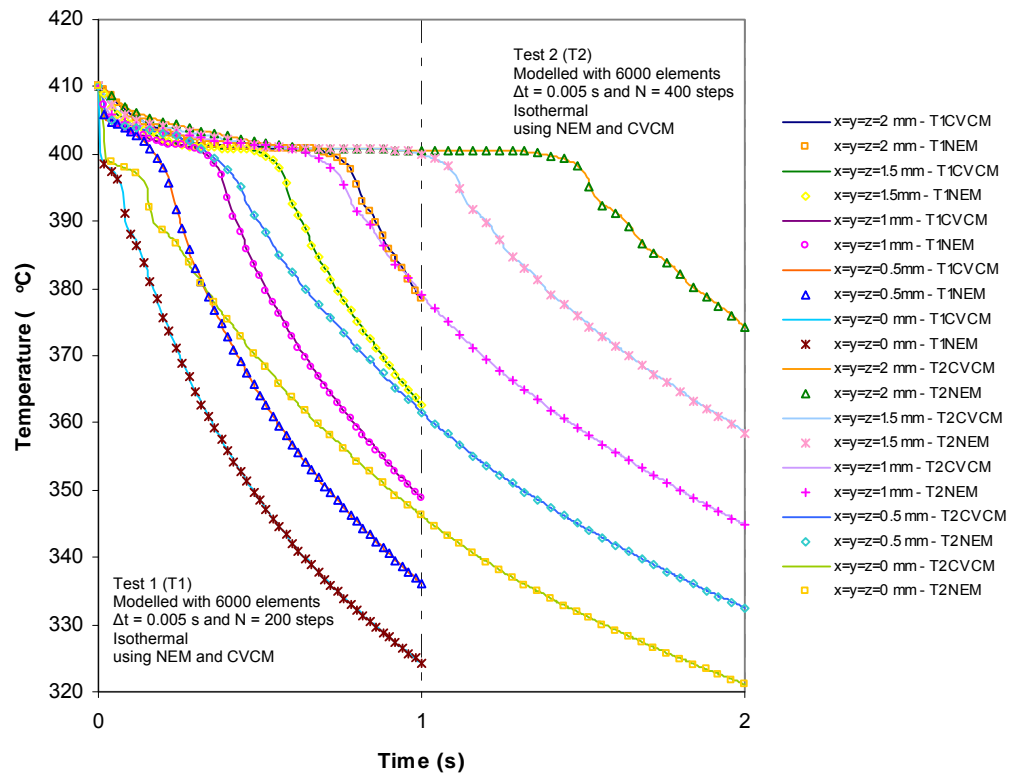


**Figure 3-21 Temperature history for Isothermal solidification at different points over the cube diagonal using same mesh density**

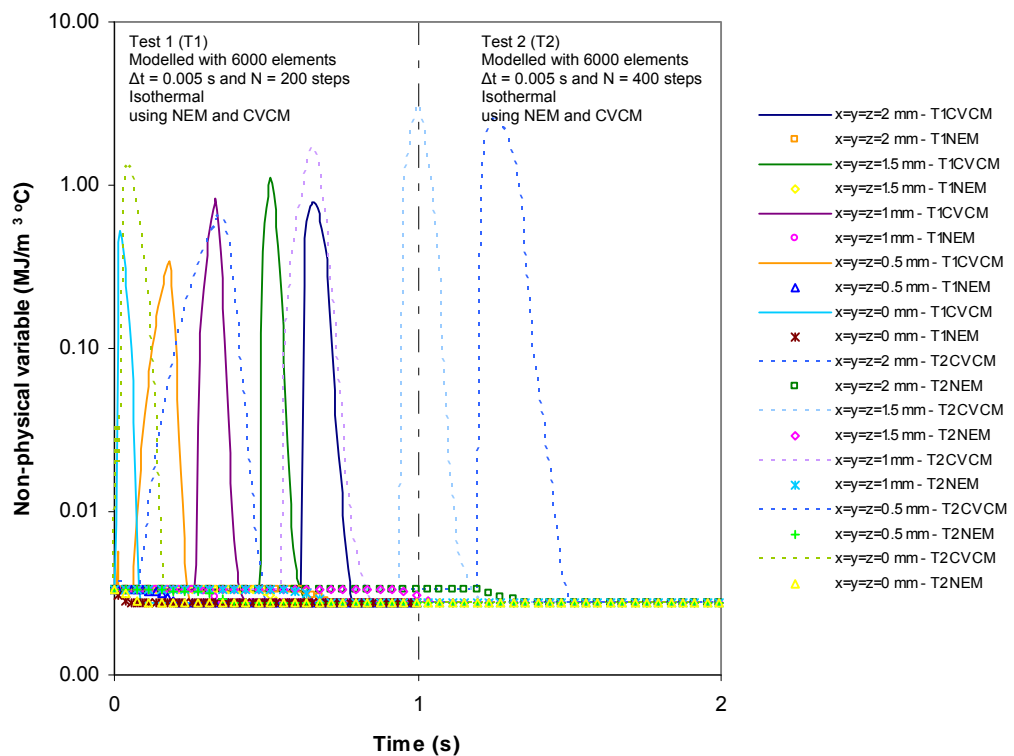


**Figure 3-22 Non-physical variable comparison for Isothermal solidification at different points over the cube diagonal using same mesh density**

# 4 WEAK DISCONTINUITY ANNIHILATION IN SOLIDIFICATION MODELLING

---

## ***4.1 Introduction***

The development of efficient mesh-based methods for modelling moving boundary problems continues to be of interest to the research community [31, 39, 40] . Moving boundary problems offer substantial challenges and many numerical approaches have been proposed. In the area of solidification modelling some of the numerical approaches can now be viewed as classical and are commonly employed in commercial codes. The methods can be classified into two groups; front tracking (adaptive) and fixed domain methods [100]. Front tracking (adaptive) methods provide for an accurate description of isothermal solidification but at the cost of complex meshing and re-meshing strategies, generally needed to cater for phase-front distortion, element birth and collapse [45, 70].

Although adaptive methods provide for high accuracy in the presence of a material discontinuity their complexity has resulted in the favouring of fixed-domain approaches [36, 40, 46, 105, 106]. Fixed domain methods tend to be more versatile and easier to implement but it is evident from the literature they can suffer inaccuracy particularly when material discontinuities are present. Four fixed domain methods are commonly employed to solve solidification problems; these are the so-called enthalpy [39, 46, 105, 110], capacitance [101, 111, 112], fictitious heat flow [40, 75] and temperature recovery (or heat integration) techniques [113]. Good reviews of the existing traditional techniques are given by Voller et al. [46] and Dalhuijsen et al. [68].

In order to account for the poor performance displayed by fixed-domain methods in the presence of discontinuities an alternative approach has recently been proposed involving the use of non-physical variables for the precise removal of discontinuities [121]. The method itself can be categorised as a fixed-domain method as no mesh modification is required although a material discontinuity must be tracked. The method is founded on the solution of weighted transport equations, introduced for the first time in reference [121] and unlike differential equations, directly incorporate material discontinuities.

In this chapter the method presented in reference [121] is further investigated and extended to cater for the presence of multiple discontinuities which are present in the solidification of complex metallic alloys. This can result in elements having more than one discontinuity present which can be problematic and cannot be accounted for using existing element enrichment approaches. In references [122, 123] the extended finite element (XFEM) and level-set methods are applied to a single-discontinuity isothermal solidification. Features of the methods are: a level-set description of the front; Galerkin least-squares stabilization and shock capture for the level set equation; local temperature enrichment and; penalty method enforcement of the temperature interface condition. The method presented in this chapter does not require temperature enrichment, penalty enforcement nor a level-set description of a front since intrinsic to solidification is an implicit description of the interface. The ability to annihilate multiple discontinuities without element enrichment is a particular highlight of the proposed procedure.

The basic concepts underpinning the use of transport equations on a moving control volume are presented in Section 4.2, where transport derivatives associated with the moving control volume are established. In Section 4.3 non-physical enthalpy and density are defined and are shown to be non-Galilean in nature and hence require careful treatment especially when discontinuities are present. The difficulty is that analysis of a discontinuity requires a particular choice of moving control volume, i.e. one that tracks the

discontinuity. Because non-physical variables are non-Galilean in nature a change in control volume results in a change in the value of the non-physical variable. This problem is overcome with the concept of relative invariance, which is achieved with the appropriate transport equation introduced in Section 4.3 and applied to a single discontinuity in Section 4.4. It is shown in Section 4.4 that non-physical enthalpy has a source-like behaviour on a discontinuity but also possesses limiting continuity, i.e. if the discontinuity is approached in the limit the non-physical variable appears continuous. Multiple discontinuities are introduced in Section 4.5, where the source-like behaviour of the non-physical variable is used to great effect to eliminate the discontinuities from the governing transport equations. Introduced in Section 4.6 is the concept of weighted transport equations which is an alternative route for the derivation of the governing finite element equations. Although absent from the literature it is an appropriate approach when discontinuities are present in the solution domain. It is demonstrated how the method presented in Section 4.5 can be used to extract all the discontinuities rendering the governing equation continuous. A particular drawback with the formulation is that the governing system of equations is more complicated and new variables are introduced. In order to make the approach practicable simplifications are considered in Section 4.7 and continued into Section 4.8 with a focus on solidification in an Eulerian frame. Discretised equations along with the integral evaluation methods are presented in Section 4.9 and Section 4.10. Finally results are presented for some relatively simple geometries in Section 4.11 to demonstrate the numerical efficacy of the approach.

## 4.2 Basic concepts

The transport equations for non-physical variables are non-Galilean in nature, which is a feature that requires some explanation. Consider first transport equations for enthalpy and density, which are

$$\frac{D^*}{D^*t} \int_{\Omega} \rho h dV + \int_{\Gamma} \rho h (\underline{v} - \underline{v}^*) \cdot \underline{n} d\Gamma = - \int_{\Gamma} \underline{q} \cdot \underline{n} d\Gamma + \int_{\Omega} \rho Q dV \quad (4.1)$$

and

$$\frac{D^*}{D^*t} \int_{\Omega} \rho dV + \int_{\Gamma} \rho (\underline{v} - \underline{v}^*) \cdot \underline{n} d\Gamma = 0 \quad (4.2)$$

where  $h$  is specific enthalpy,  $\rho$  is density,  $\underline{v}$  is material velocity,  $\underline{q} \cdot \underline{n}$  is heat flux and  $Q$  is a heat source term and where  $\Omega$  is a control volume which is transported at velocity  $\underline{v}^* = D^* \underline{x} / D^* t$ , i.e.  $\Omega$  is time dependent and is a portion of the physical space and moves relative to the physical material.

It is possible to consider a reference control volume  $\Omega^*$  and define a mapping between points  $\chi^* \in \Omega^*$  and points  $\underline{x} \in \Omega$ , i.e. for  $\chi^* \mapsto \underline{x}(\chi^*, t)$ , so that  $\underline{v}^* = D^* \underline{x} / D^* t = \partial \underline{x}(\chi^*, t) / \partial t$ , where the time partial derivative is partial in the sense that  $\chi^*$  is held constant when performing the derivative, see Figure 4-1. This concept is essentially identical to that used when defining the material derivative  $D/Dt$  and material velocity  $\underline{v} = D\underline{x}/Dt = \partial \underline{x}(\underline{X}, t) / \partial t$  but material points are not necessarily tracked in the case of the mapping  $\chi^* \mapsto \underline{x}(\chi^*, t)$ . Note the use of  $D^*/D^*t$  rather than the ordinary derivative  $d/dt$  in equations (4.1) and (4.2) even though these are identical when applied to a function of  $t$ . Although the integrals  $\int_{\Omega} \rho h dV$  and  $\int_{\Omega} \rho dV$  are functions of  $t$  the derivative  $D^*/D^*t$  is used to immediately to relay the notion that  $\Omega$  is a control volume transported through  $\underline{v}^*$ . Although  $\underline{v}^*$  is present in equations (4.1) and (4.2) it cannot influence the value of  $h$  and  $\rho$  as this would be physically meaningless.

One of the principal advantages of using equation (4.1) rather than the governing partial differential equation is that it naturally accounts for discontinuities in  $h$  and  $\rho$ . This property is as a consequence of integration being performed prior to temporal differentiation. Standard Theorems can be applied to equations (4.1) and (4.2) in the absence of any discontinuity to arrive at the governing partial differential equations. Application of a Reynold-type transport Theorem and the Divergence Theorem to equation (4.2) gives

$$\frac{D^*}{D^*t} \int_{\Omega} \rho dV = \int_{\Omega} \left( \frac{D^* \rho}{D^*t} + \rho \operatorname{div} \underline{v}^* \right) dV \quad (4.3)$$

$$\int_{\Gamma} \rho (\underline{v} - \underline{v}^*) \cdot \underline{n} d\Gamma = \int_{\Omega} \operatorname{div} (\rho (\underline{v} - \underline{v}^*)) dV \quad (4.4)$$

which provides the equation

$$\frac{D^* \rho}{D^* t} + \rho \operatorname{div} \underline{v}^* + \operatorname{div}(\rho(\underline{v} - \underline{v}^*)) = 0 \quad (4.5)$$

which is a generalised form of the continuity equation.

Note that the standard Lagrangian and Eulerian forms of the continuity equation are obtained on setting  $\underline{v}^* = \underline{v}$  (since  $D^*/D^*t \equiv D/Dt$ ) and  $\underline{v}^* = \underline{0}$  (since  $D^*/D^*t \equiv \partial/\partial t$ ), i.e.  $D\rho/Dt + \rho \operatorname{div} \underline{v} = 0$  and  $\partial\rho/\partial t + \operatorname{div}(\rho \underline{v}) = 0$  are obtained. Note also the direct substitution of the identity  $D^*/D^*t \equiv D/Dt + (\underline{v}^* - \underline{v}) \cdot \nabla$  into equation (4.5) gives  $D\rho/Dt + \rho \operatorname{div} \underline{v} = 0$  and similarly substitution of  $D^*/D^*t \equiv \partial/\partial t + \underline{v}^* \cdot \nabla$  gives  $\partial\rho/\partial t + \operatorname{div}(\rho \underline{v}) = 0$ . This analysis confirms that density transport is governed by a single unique partial differential equation and is not dependent on the control volume velocity  $\underline{v}^*$ . A similar analysis can also be applied to equation (4.1) to give

$$\rho \frac{D^* h}{D^* t} + \rho(\underline{v} - \underline{v}^*) \cdot \nabla h = -\operatorname{div}(\underline{q}) + \rho Q \quad (4.6)$$

where it is appreciated that although  $\underline{v}^*$  appears in equation (4.6) the value of  $h$  is independent of  $\underline{v}^*$ .

The governing partial differential equations for density and enthalpy are essentially unique although their appearance can alter as a consequence of the temporal derivatives employed. Thus under the restrictive assumption that velocity  $\underline{v}^*$  is a constant and on consideration of a non-rotating frame moving relative to the reference frame with velocity  $\underline{v}^*$ , then it is evident that equations (4.5) and (4.6) are invariant under a Galilean transformation.

### 4.3 Definition of non-physical enthalpy and density

Transport equations are utilised to define non-physical enthalpy  $\hat{h}$  and density  $\hat{\rho}$ . The prime motivation for the definition of these variables is source-like behaviour that can result at a discontinuity in the associated physical variable [121]. The transport equation definitions are:

$$\frac{D^*}{D^* t} \int_{\Omega} \hat{\rho} dV = \frac{D^*}{D^* t} \int_{\Omega} \rho dV + \int_{\Gamma} \rho(\underline{v} - \underline{v}^*) \cdot \underline{n} d\Gamma = 0 \quad (4.7)$$

and

$$\frac{D^*}{D^*t} \int_{\Omega} \hat{h} dV = \frac{D^*}{D^*t} \int_{\Omega} \rho h dV + \int_{\Gamma} \rho h (\underline{v} - \underline{v}^*) \cdot \underline{n} d\Gamma = - \int_{\Gamma} \underline{q} \cdot \underline{n} d\Gamma + \int_{\Omega} \rho Q dV \quad (4.8)$$

where in the absence of discontinuities the corresponding governing partial differential equations are

$$\frac{D^* \hat{\rho}}{D^*t} + \hat{\rho} \operatorname{div} \underline{v}^* = \frac{D^* \rho}{D^*t} + \rho \operatorname{div} \underline{v}^* + \operatorname{div} [\rho (\underline{v} - \underline{v}^*)] = 0 \quad (4.9)$$

and

$$\frac{D^* \hat{h}}{D^*t} + \hat{h} \operatorname{div} \underline{v}^* = \rho \frac{D^* h}{D^*t} + \rho (\underline{v} - \underline{v}^*) \cdot \nabla h = -\operatorname{div}(\underline{q}) + \rho Q \quad (4.10)$$

where it is evident equations (4.5) and (4.6) are contained within equations (4.9) and (4.10), respectively.

The non-physical density  $\hat{\rho}$  and enthalpy  $\hat{h}$  are shown to be well defined although non-unique in reference [121]. Equation (4.9) is readily solved for  $\hat{\rho}$ , since  $D^* \hat{\rho} / D^*t + \hat{\rho} \operatorname{div} \underline{v}^* = 0$  gives  $D^* \ln \hat{\rho} / D^*t = -\operatorname{div} \underline{v}^*$  with the requirement that  $\hat{\rho} > 0$  and if  $\underline{v}^* \neq \underline{0}$  this equation can be integrated to give  $\hat{\rho} = \hat{\rho}_0 \exp \left[ \int_C \operatorname{div} \underline{v}^* \left\| \underline{v}^* \right\|^{-2} \underline{v}^* \cdot d\underline{x}^* \right]$ , where  $\hat{\rho}_0$  is  $\hat{\rho}$  at  $t_0$  and  $C$  refers to a contour obtained on the integration of  $d\underline{x}^* = \underline{v}^* dt$ . With knowledge of  $\hat{\rho}$  a solution for  $\hat{h}$  can be constructed in the form  $\hat{h} = \hat{\rho} \hat{h}^*$ , since equation (4.10) reduces to  $\hat{\rho} D^* \hat{h}^* / D^*t = \rho Dh / Dt$  and integration gives  $\hat{h} = \hat{\rho} \left( \hat{\rho}_0^{-1} \hat{h}_0 + \int_C \hat{\rho}^{-1} \rho Dh / Dt \left\| \underline{v}^* \right\|^{-2} \underline{v}^* \cdot d\underline{x}^* \right)$ . It is apparent of this relationship that  $\hat{h}$  is not independent of  $\underline{v}^*$ . It is evident on inspection that equations (4.9) and (4.10) are not invariant under a Galilean transformation as confirmed by the dependence of  $\hat{\rho}$  and  $\hat{h}$  on  $\underline{v}^*$ .

Because of the dependence of non-physical variables on the velocity of the control volume careful consideration must be given to their determination. Standard control volume methods for the description of a discontinuity travelling through  $\Omega$  do not apply as the solutions obtained can depend of the front velocity. The problem is that the control volume tracking a discontinuity will in general not be moving with velocity  $\underline{v}^*$  and consequently the nature of the non-physical variable is changed. Techniques for the analysis and determination of physical variables on a different moving control volume are required. Consider then a control volume transported by a velocity  $\underline{v}^+$  in the usual way, where  $D^+/D^+t = \partial/\partial t|_x + \underline{v}^+ \cdot \nabla$  and  $\partial \mathbf{x}/\partial t(\chi^+, t) = \underline{v}^+$ . In this case it is important that  $\hat{h}$  is not dependent on  $\underline{v}^+$  which is achieved with the transport equations

$$\frac{D^+}{D^+t} \int_{\Omega^+} \hat{\rho} dV + \int_{\Gamma^+} \hat{\rho}(\underline{v}^* - \underline{v}^+) \cdot \underline{n} d\Gamma = \frac{D^+}{D^+t} \int_{\Omega^+} \rho dV + \int_{\Gamma^+} \rho(\underline{v} - \underline{v}^+) \cdot \underline{n} d\Gamma = 0 \quad (4.11)$$

and

$$\frac{D^+}{D^+t} \int_{\Omega^+} \hat{h} dV + \int_{\Gamma^+} \hat{h}(\underline{v}^* - \underline{v}^+) \cdot \underline{n} d\Gamma = \frac{D^+}{D^+t} \int_{\Omega^+} \rho h dV + \int_{\Gamma^+} \rho h(\underline{v} - \underline{v}^+) \cdot \underline{n} d\Gamma = - \int_{\Gamma^+} \underline{q} \cdot \underline{n} d\Gamma + \int_{\Omega^+} \rho Q dV \quad (4.12)$$

where  $\underline{v}^+$  governs the transport of  $\Omega^+$  in these equations and where in the absence of discontinuities the corresponding governing partial differential equations are

$$\frac{D^+ \hat{\rho}}{D^+t} + \hat{\rho} \text{div} \underline{v}^+ + \text{div}[\hat{\rho}(\underline{v}^* - \underline{v}^+)] = \frac{D^+ \rho}{D^+t} + \rho \text{div} \underline{v}^+ + \text{div}[\rho(\underline{v} - \underline{v}^+)] = 0 \quad (4.13)$$

and

$$\frac{D^+ \hat{h}}{D^+t} + \hat{h} \text{div} \underline{v}^+ + \text{div}[\hat{h}(\underline{v}^* - \underline{v}^+)] = \rho \frac{D^+ h}{D^+t} + \rho(\underline{v} - \underline{v}^+) \cdot \nabla h = -\text{div}(\underline{q}) + \rho Q \quad (4.14)$$



Substitution of  $D^+/D^+t \equiv D^*/D^*t + (\underline{v}^* - \underline{v}^+) \cdot \nabla$  into equations (4.13) and (4.14) yields equations (4.9) and (4.10) respectively and thus confirming that  $\hat{\rho}$  and  $\hat{h}$  as defined by transport equations (4.11) and (4.12) are independent of  $\underline{v}^+$ .

Prior to analysing the behaviour of non-physical variables at discontinuities it is necessary to be able to apply transport equations without recourse to the underlying partial differential equations. It is evident that the derivative  $D^*\left(\int_{\Omega^*} \hat{h} dV\right)/D^*t$  on the left hand side (LHS) of equation (4.8) equals  $D^+\left(\int_{\Omega^+} \hat{h} dV\right)/D^+t + \int_{\Gamma^+} \hat{h}(\underline{v}^* - \underline{v}^+) \cdot \underline{n} d\Gamma$  on the LHS of equation (4.12) if and only if  $\underline{v}^* \cdot \underline{n} = \underline{v}^+ \cdot \underline{n}$  and  $\Gamma^+ = \Gamma^*$  at time  $t = t_0$ . The condition ensures that the boundaries match (i.e.  $\Gamma^+ = \Gamma^*$ ) and that  $\int_{\Gamma^+} \hat{h}(\underline{v}^* - \underline{v}^+) \cdot \underline{n} d\Gamma = 0$ .

#### 4.4 A single discontinuity in the domain

Consider a discontinuity present in  $\Omega$  in the form of an interface  $\Gamma_i$  between  $\Omega_\ell$  and  $\Omega_s$  as depicted in Figure 4-2(a). Consider an arbitrary small volume  $\Omega_i$  enclosing  $\Gamma_i$  whose transport is assumed to be governed by the regular velocity field velocity  $\underline{v}^+$  which matches the normal velocity of  $\Gamma_i$  and  $\underline{n}$  is a unit normal on  $\Gamma_i$ . It is assumed also that at the boundary of  $\Omega$  that  $\underline{v}^* \cdot \underline{n} = \underline{v}^+ \cdot \underline{n}$ . Consider then the application of equation (4.11) to  $\Omega$ ,  $\Omega_\ell$ ,  $\Omega_s$  and  $\Omega_i$ , i.e.

$$\frac{D^+}{D^+t} \int_{\Omega} \hat{\rho} dV + \int_{\Gamma} \hat{\rho}(\underline{v}^* - \underline{v}^+) \cdot \underline{n} d\Gamma = \frac{D^*}{D^*t} \int_{\Omega} \hat{\rho} dV = \frac{D^+}{D^+t} \int_{\Omega} \rho dV + \int_{\Gamma} \rho(\underline{v} - \underline{v}^+) \cdot \underline{n} d\Gamma = 0 \quad (4.15)$$

$$\frac{D^+}{D^+t} \int_{\Omega_\ell} \hat{\rho} dV + \int_{\Gamma_i^\ell} \hat{\rho}(\underline{v}^* - \underline{v}^+) \cdot \underline{n}_\ell d\Gamma = \frac{D^+}{D^+t} \int_{\Omega_\ell} \rho dV + \int_{\Gamma_\ell} \rho(\underline{v} - \underline{v}^+) \cdot \underline{n} d\Gamma + \int_{\Gamma_i^\ell} \rho(\underline{v} - \underline{v}^+) \cdot \underline{n}_\ell d\Gamma = 0 \quad (4.15b)$$

$$\frac{D^+}{D^+t} \int_{\Omega_s} \hat{\rho} dV + \int_{\Gamma_i^s} \hat{\rho}(\underline{v}^* - \underline{v}^+) \cdot \underline{n}_s d\Gamma = \frac{D^+}{D^+t} \int_{\Omega_s} \rho dV + \int_{\Gamma_s} \rho(\underline{v} - \underline{v}^+) \cdot \underline{n} d\Gamma + \int_{\Gamma_i^s} \rho(\underline{v} - \underline{v}^+) \cdot \underline{n}_s d\Gamma = 0 \quad (4.15c)$$

$$\begin{aligned} & \frac{D^+}{D^+t} \int_{\Omega_i} \hat{\rho} dV + \int_{\Gamma_i^+ - \Gamma_i^\ell - \Gamma_i^s} \hat{\rho}(\underline{v}^* - \underline{v}^+) \cdot \underline{n} d\Gamma + \int_{\Gamma_i^\ell} \hat{\rho}(\underline{v}^* - \underline{v}^+) \cdot (-\underline{n}_\ell) d\Gamma + \int_{\Gamma_i^s} \hat{\rho}(\underline{v}^* - \underline{v}^+) \cdot (-\underline{n}_s) d\Gamma = \\ & = \frac{D^+}{D^+t} \int_{\Omega_i} \rho dV + \int_{\Gamma_i^+ - \Gamma_i^\ell - \Gamma_i^s} \rho(\underline{v} - \underline{v}^+) \cdot \underline{n} d\Gamma + \int_{\Gamma_i^\ell} \rho(\underline{v} - \underline{v}^+) \cdot (-\underline{n}_\ell) d\Gamma + \int_{\Gamma_i^s} \rho(\underline{v} - \underline{v}^+) \cdot (-\underline{n}_s) d\Gamma = 0 \end{aligned} \quad (4.15d)$$

where  $\Gamma_i^t$  is the boundary for  $\Omega_i$ .

Observe that the addition of equations (4.15b) and (4.15c) results in (4.15) confirming that equation (4.15) embodies the physics of a discontinuity. In addition, in the limit  $\text{vol}(\Omega_i) \rightarrow 0$  with  $\Gamma_i^\ell, \Gamma_i^s \rightarrow \Gamma_i$ , so that  $\underline{n}_s = -\underline{n}_\ell$ , equation (4.15d) reduces to

$$\frac{D^+}{D^+t} \int_{\Gamma_i} \hat{\rho}' d\Gamma + \int_{\Sigma_i} \hat{\rho}' (\underline{v}^* - \underline{v}^+) \cdot \underline{t} n d\Sigma + \int_{\Gamma_i} \hat{\rho} (\underline{v}^* - \underline{v}^+) \cdot \underline{n} [d\Gamma = \int_{\Gamma_i} \hat{\rho} (\underline{v} - \underline{v}^+) \cdot \underline{n} [d\Gamma = 0 \quad (4.16)$$

where  $\underline{t}n$  is a outward pointing unit normal on  $\Sigma_i = \Gamma \cap \Gamma_i$  ( $\Sigma_i$  is the boundary for  $\Gamma_i$ ) that is in a tangent plane of  $\Gamma_i$  and where the outward pointing brackets signify a jump, i.e.

$$\hat{\rho} (\underline{v} - \underline{v}^+) \cdot \underline{n} [ = \rho_s (\underline{v}_s - \underline{v}_{\Gamma_i}^+) \cdot (-\underline{n}_s) + \rho_\ell (\underline{v}_\ell - \underline{v}_{\Gamma_i}^+) \cdot (-\underline{n}_\ell) = 0 \quad (4.17)$$

and

$$\hat{\rho} (\underline{v}^* - \underline{v}^+) \cdot \underline{n} [ = \hat{\rho}_s (\underline{v}^* - \underline{v}^+) \cdot (-\underline{n}_s) + \hat{\rho}_\ell (\underline{v}^* - \underline{v}^+) \cdot (-\underline{n}_\ell) = (\underline{v}^* - \underline{v}^+) \cdot (-\underline{n}_\ell) (\hat{\rho}_\ell - \hat{\rho}_s) = 0 \quad (4.18)$$

and where it is assumed that  $\hat{\rho}$  is continuous at  $\Gamma_i$ , i.e.  $\hat{\rho}_\ell = \hat{\rho}_s$ .

Note that with the assumed continuity of  $\hat{\rho}$  at  $\Gamma_i$  equation (4.16) reduces to

$$\frac{D^+ \hat{\rho}}{D^+t} \int_{\Gamma_i} d\Gamma + \int_{\Sigma_i} \hat{\rho}' (\underline{v}^* - \underline{v}^+) \cdot \underline{t} n d\Sigma = \int_{\Gamma_i} \hat{\rho} (\underline{v} - \underline{v}^+) \cdot \underline{n} [d\Gamma = 0 \quad (4.19)$$

which is the governing transport equation for the source  $\hat{\rho}'$ .

It should be recognised that continuity of  $\hat{\rho}$  at  $\Gamma_i$  is assured if  $\hat{\rho}'$  satisfies equation (4.19) or the corresponding partial differential equation

$$\frac{D^+ \hat{\rho}}{D^+t} + \hat{\rho}' \text{div}_{\Gamma_i} \underline{v}^+ + \text{div}_{\Gamma_i} (\hat{\rho}' (\underline{v}_T^* - \underline{v}_T^+)) = \hat{\rho} (\underline{v} - \underline{v}^+) \cdot \underline{n} [ = 0 \quad (4.20)$$

where  $\text{div}_{\Gamma_i} \underline{v}^+ = \text{div} \underline{v}^+ - \langle Dv^+ \underline{n}_s, \underline{n}_s \rangle$  [119] and where  $(Dv^+)_{\ell m} = \partial v_\ell^+ / \partial x_m$  and  $\langle \cdot, \cdot \rangle$  stands for inner product.

It is evident that  $\hat{\rho}' = 0$  is a solution to equations (4.19) and (4.20) which arises because no jump is present in the mass flux at  $\Gamma_i$ . Thus, non-physical density  $\hat{\rho}$  has no source term associated with it unlike non-physical enthalpy  $\hat{h}$  whose source term is described by the transport equation

$$\frac{D^+}{D^+t} \int_{\Gamma_i} \hat{h}' dV + \int_{\Sigma_i} \hat{h}' (\underline{v}^* - \underline{v}^+) \cdot \underline{n} d\Sigma = \int_{\Gamma_i} \rho h (\underline{v} - \underline{v}^+) \cdot \underline{n} d\Gamma = - \int_{\Gamma_i} \underline{q} \cdot \underline{n} d\Gamma \quad (4.21)$$

and corresponding partial differential equation

$$\frac{D^+ \hat{h}'}{D^+t} + \hat{h}' \operatorname{div}_{\Gamma_i} \underline{v}^+ + \operatorname{div}_{\Gamma_i} (\hat{h}' (\underline{v}_T^* - \underline{v}_T^+)) = \rho h (\underline{v} - \underline{v}^+) \cdot \underline{n} = - \underline{q} \cdot \underline{n} \quad (4.22)$$

where as with density it is assumed that at  $\Gamma_i$ ,  $\hat{h}_\ell = \hat{h}_s$ , i.e. continuity of  $\hat{h}$  is invoked by  $\hat{h}'$  satisfying equations (4.21) and (4.22).

The jump terms are  $\underline{q} \cdot \underline{n} = \underline{q}_s \cdot (-\underline{n}_s) + \underline{q}_\ell \cdot (-\underline{n}_\ell)$  and similarly for enthalpy  $\rho h (\underline{v} - \underline{v}^+) \cdot \underline{n} = \rho_s h_s (\underline{v}_s - \underline{v}^+) \cdot (-\underline{n}_s) + \rho_\ell h_\ell (\underline{v}_\ell - \underline{v}^+) \cdot (-\underline{n}_\ell)$ .

## 4.5 Multiple discontinuities

Consider the partition of domain  $\Omega$  into  $K+1$  non-overlapping open domains  $\Omega_k$  such that  $\overline{\Omega} = \bigcup_{k=1}^{K+1} \overline{\Omega}_k$  as depicted in Figure 4-2(b). The interface boundaries  $\Gamma_k$  are obtained on intersection of the closed domains  $\overline{\Omega}_k$  and  $\overline{\Omega}_{k+1}$ , i.e.  $\Gamma_k = \overline{\Omega}_k \cap \overline{\Omega}_{k+1}$  and it is recognised that  $K$  can change with time. Consider further the assumed existence of velocity fields  $\underline{v}_k^+$ ,  $k=1, 2, \dots, K$ , where on the boundary of  $\Omega$ ,  $\underline{v}_k^+ \cdot \underline{n} = \underline{v}^* \cdot \underline{n}$  and where  $\underline{v}_k^+$  matches the normal velocity of the boundary  $\Gamma_k$  although there is no requirement for  $\underline{v}_k^+$  to match the normal velocity of  $\Gamma_i$  for  $i \neq k$ .

Consider then the extraction of a discontinuity from equation (4.8) which is achieved by

$$\frac{D^*}{D^*t} \int_{\Omega} \hat{h} dV = \frac{D_k^+}{D_k^+t} \int_{\Omega} \hat{h} dV + \int_{\Gamma} \hat{h} (\underline{v}_k^+ - \underline{v}^*) \cdot \underline{n} d\Gamma = \frac{D_k^+}{D_k^+t} \int_{\Omega/\Gamma_k} \hat{h} dV + \frac{D^+}{D^+t} \int_{\Gamma_k} \hat{h}' dV + \int_{\Sigma_k} \hat{h}' (\underline{v}_k^+ - \underline{v}^*) \cdot \underline{n} d\Sigma \quad (4.23)$$

which reveals the power of a non-physical approach with the isolation of a discontinuity using the source-like property, where  $D_k^+/D_k^+t$  is the temporal derivative associated with  $\underline{v}_k^+$  in the usual way and  $\Omega/\Gamma_k$  signifies that integration is performed on  $\Omega$  but does not include source behaviour on  $\Gamma_k$ , i.e. essentially Lebesgue integration.

Rearrangement of equation (4.23) provides

$$\frac{D^*}{D^*t} \int_{\Omega/\Gamma_k} \widehat{h} dV = \frac{D^*}{D^*t} \int_{\Omega} \widehat{h} dV - \frac{D_k^+}{D_k^+t} \int_{\Gamma_k} \widehat{h}' dV - \int_{\Sigma_k} \widehat{h}' (\underline{v}_k^+ - \underline{v}^*) \cdot \underline{n} d\Sigma \quad (4.24)$$

where the LHS of equation (4.24) is absent one source term.

It is possible to deduce that more generally the removal of multiple sources is achieved through

$$\frac{D^*}{D^*t} \int_{\Omega/\{\Gamma_k:k=1:K\}} \widehat{h} dV = \frac{D^*}{D^*t} \int_{\Omega} \widehat{h} dV - \sum_{k=1}^K \frac{D_k^+}{D_k^+t} \int_{\Gamma_k} \widehat{h}' dV - \sum_{k=1}^K \int_{\Sigma_k} \widehat{h}' (\underline{v}_k^+ - \underline{v}^*) \cdot \underline{n} d\Sigma \quad (4.25)$$

where  $\Omega/\{\Gamma_k:k=1:K\}$  signifies that source terms are excluded from the integration domain.

Application of equation (4.25) to transport equation (4.8) and on utilisation of equation (4.21) yields

$$\begin{aligned} \frac{D^*}{D^*t} \int_{\Omega/\{\Gamma_k:k=1:K\}} \widehat{h} dV &= \frac{D^*}{D^*t} \int_{\Omega} \widehat{h} dV - \sum_{k=1}^K \frac{D_k^+}{D_k^+t} \int_{\Gamma_k} \widehat{h}' dV - \sum_{k=1}^K \int_{\Sigma_k} \widehat{h}' (\underline{v}_k^+ - \underline{v}^*) \cdot \underline{n} d\Sigma = \frac{D^*}{D^*t} \int_{\Omega} \rho h dV + \\ &+ \int_{\Gamma} \rho h (\underline{v} - \underline{v}^*) \cdot \underline{n} d\Gamma - \sum_{k=1}^K \int_{\Gamma_k} \rho h (\underline{v} - \underline{v}_k^+) \cdot \underline{n} d\Gamma = - \int_{\Gamma} \underline{q} \cdot \underline{n} d\Gamma + \int_{\Omega} \rho Q dV + \sum_{k=1}^K \int_{\Gamma_k} \underline{q} \cdot \underline{n} d\Gamma \end{aligned} \quad (4.26)$$

which is an equation absent of jump terms and consequently discontinuities.

In some respects the use of the jump terms to remove discontinuities is expected although it is not transparently obvious that the result is continuous however this is confirmed by the LHS of equation (4.26). Things are a little more involved on application of the finite element method which is applied here in transport form.

## 4.6 Finite Element Equations

A finite element system can be derived by adopting a weighted transport equation of the form

$$\begin{aligned} \frac{D^*}{D^*t} \int_{\Omega} W \hat{h} dV &= \frac{D^*}{D^*t} \int_{\Omega} W \rho h dV - \int_{\Omega} \rho h (\underline{v} - \underline{v}^*) \cdot \nabla W dV + \int_{\Gamma} W \rho h (\underline{v} - \underline{v}^*) \cdot \underline{n} d\Gamma = \\ &= \int_{\Omega} \nabla W \cdot \underline{q} dV - \int_{\Gamma} W \underline{q} \cdot \underline{n} d\Gamma + \int_{\Omega} \rho W Q dV \end{aligned} \quad (4.27)$$

where  $W$  is transported invariantly with  $\Omega$ , i.e.  $D^*W/D^*t = 0$ .

Note that with an equation of this form both spatial and temporal derivatives of  $\hat{h}$  and  $h$  are avoided, making (4.27) applicable when a discontinuity is in  $\Omega$ . This approach is unseen in the literature although is identical to the weighted residual method if discontinuities are not involved. Note also that on setting  $W = 1$ , the governing transport equation (4.8) is returned. Applying (4.27) to an element domain  $\Omega_e$  and adopting a standard Galerkin weighting gives

$$\begin{aligned} \frac{D^*}{D^*t} \int_{\Omega_e} N_i \hat{h} dV &= \frac{D^*}{D^*t} \int_{\Omega_e} N_i \rho h dV - \int_{\Omega_e} \rho h (\underline{v} - \underline{v}^*) \cdot \nabla N_i dV + \int_{\Gamma_e} N_i \rho h (\underline{v} - \underline{v}^*) \cdot \underline{n} d\Gamma = \\ &= \int_{\Omega_e} \nabla N_i \cdot \underline{q} dV - \int_{\Gamma_e} N_i \underline{q} \cdot \underline{n} d\Gamma + \int_{\Omega_e} \rho N_i b dV \end{aligned} \quad (4.28)$$

where  $N_i$  is a shape function and  $\Omega_e$  is an element domain and  $\Gamma_e$  is its boundary.

It is recognised that discontinuities and source terms are present in equation (4.28) and the removal of these is required. It has been shown in the previous section that in order to relate two transport derivatives involving two velocities  $\underline{v}^*$  and  $\underline{v}_k^+$  on a domain  $\Omega$  the condition  $\underline{v}^* \cdot \underline{n} = \underline{v}_k^+ \cdot \underline{n}$  must be invoked on the boundary. This condition ensures that the transport of the boundary  $\Gamma$  of  $\Omega$  is identical for both velocities. Here  $\underline{v}_k^+$  matches the normal velocity of the discontinuity  $\Gamma_k$  and  $\underline{v}^*$  is the velocity dictating the movement of the mesh. However, there is little expectation that the condition  $\underline{v}^* \cdot \underline{n} = \underline{v}_k^+ \cdot \underline{n}$  applies on an element boundary  $\Gamma_e$ . In a situation where a front passes through an element it is convenient to follow this with a control volume that matches the proportion of the front in

the element. This can be achieved with an appropriate velocity  $\underline{v}_k^\times$  matches the normal velocity of  $\Gamma_k$  and  $\underline{v}^* \cdot \underline{n}_e = \underline{v}_k^\times \cdot \underline{n}_e$  on  $\Gamma_e$ , where  $\underline{n}_e$  is the unit normal on  $\Gamma_e$ . With  $\underline{v}^+$  defined appropriately it is now possible to match derivatives and in particular consider the term appearing on the LHS in the FE transport equation (4.28), i.e.

$$\begin{aligned} \frac{D^*}{D^*t} \int_{\Omega_e} N_i \widehat{h} dV &= \frac{D_k^\times}{D_k^\times t} \int_{\Omega_e} N_i \widehat{h} dV + \int_{\Gamma_e} \widehat{h} (\underline{v}^* - \underline{v}_k^\times) \cdot \underline{n} d\Gamma = \\ &= \frac{D_k^\times}{D_k^\times t} \int_{\Omega_e / \Gamma_k^e} N_i \widehat{h} dV + \frac{D_k^\times}{D_k^\times t} \int_{\Gamma_k^e} N_i \widehat{h}' dV + \int_{\Sigma_k^e} N_i \widehat{h}' (\underline{v}^* - \underline{v}_k^\times) \cdot \underline{n} d\Gamma \end{aligned} \quad (4.29)$$

where  $\Gamma_k^e$  is that portion of  $\Gamma_k$  contained in  $\Omega_e$ .

Rearrangement of this equation gives

$$\frac{D_k^\times}{D_k^\times t} \int_{\Omega_e / \Gamma_k^e} N_i \widehat{h} dV = \frac{D^*}{D^*t} \int_{\Omega_e} N_i \widehat{h} dV - \frac{D_k^\times}{D_k^\times t} \int_{\Gamma_k^e} N_i \widehat{h}' dV - \int_{\Sigma_k^e} N_i \widehat{h}' (\underline{v}^* - \underline{v}_k^\times) \cdot \underline{n} d\Gamma \quad (4.30)$$

and as with equation (4.24) a source term is removed from the first integral on the right hand side (RHS) of equation (4.30).

The full system of FE transport equations with multiple discontinuities removed are:

$$\begin{aligned} \frac{D^*}{D^*t} \int_{\Omega_e / \{\Gamma_k : k \in K_e\}} N_i \widehat{h} dV &= \int_{\Omega_e} \nabla N_i \cdot \underline{q} dV - \int_{\Gamma_e} N_i \underline{q} \cdot \underline{n} d\Gamma + \int_{\Omega_e} \rho N_i Q dV \\ &+ \sum_{k \in K_e} \int_{\Gamma_k^e} \widehat{h}' (\underline{v}_N^* - \underline{v}_{kN}^\times) \cdot \nabla N_i d\Gamma + \sum_{k \in K_e} \int_{\Gamma_k^e} N_i \underline{q} \cdot \underline{n} d\Gamma \end{aligned} \quad (4.31)$$

$$\begin{aligned} \frac{D^*}{D^*t} \int_{\Omega_e / \{\Gamma_k : k \in K_e\}} N_i \widehat{h} dV &= \frac{D^*}{D^*t} \int_{\Omega_e} N_i \rho h dV - \int_{\Omega_e} \rho h (\underline{v} - \underline{v}^*) \cdot \nabla N_i dV + \int_{\Gamma_e} N_i \rho h (\underline{v} - \underline{v}^*) \cdot \underline{n} d\Gamma \\ &+ \sum_{k \in K_e} \int_{\Gamma_k^e} \widehat{h}' (\underline{v}_N^* - \underline{v}_{kN}^\times) \cdot \nabla N_i d\Gamma - \sum_{k \in K_e} \int_{\Gamma_k^e} \rho h (\underline{v} - \underline{v}_k^\times) \cdot \underline{n} d\Gamma \end{aligned} \quad (4.32)$$

$$\frac{D_k^\times}{D_k^\times t} \int_{\Gamma_k^e} N_i \widehat{h}' d\Gamma + \int_{\Sigma_k^e} N_i \widehat{h}' (\underline{v}^* - \underline{v}_k^\times) \cdot \underline{n} d\Sigma + \int_{\Gamma_k^e} \widehat{h}' (\underline{v}_N^* - \underline{v}_{kN}^\times) \cdot \nabla N_i d\Gamma =$$

$$= \int_{\Gamma_k^e} N_i \mathbf{j} \mathbf{p} \mathbf{h} (\underline{\mathbf{v}} - \underline{\mathbf{v}}_k^\times) \cdot \underline{\mathbf{n}} d\Gamma = - \int_{\Gamma_k^e} N_i \mathbf{j} \mathbf{q} \cdot \underline{\mathbf{n}} d\Gamma \quad (4.33)$$

where  $\underline{\mathbf{v}}_N^* = \underline{\mathbf{v}}^* - \underline{\mathbf{v}}_T^*$ ,  $\underline{\mathbf{v}}_{kN}^\times = \underline{\mathbf{v}}_k^\times - \underline{\mathbf{v}}_{kT}^\times$  and  $\Omega_e / \{\Gamma_k : k \in K_e\}$  signifies that integration is in the sense of Lebesgue and where  $K_e = \{k : \Omega_e \cap \Gamma_k \neq \emptyset\}$  which is a subset of  $\{k : k = 1 : K\}$ .

Note that the LHS of equations (4.31) and (4.32) are continuous and consequently so is the RHS, so discontinuities have been annihilated.

Transport equation (4.33) is of a form that requires some justification. Application of Reynolds Transport equation and Stokes Theorem to equation (4.33) gives

$$\begin{aligned} \int_{\Gamma_k^e} \frac{D_k^\times N_i \widehat{\mathbf{h}}'}{D_k^\times t} + N_i \widehat{\mathbf{h}}' \operatorname{div}_{\Gamma_k} \underline{\mathbf{v}}_k^\times d\Gamma + \int_{\Gamma_k^e} \operatorname{div}_{\Gamma_k} N_i \widehat{\mathbf{h}}' (\underline{\mathbf{v}}_T^* - \underline{\mathbf{v}}_{kT}^\times) d\Gamma + \int_{\Gamma_k^e} \widehat{\mathbf{h}}' (\underline{\mathbf{v}}_N^* - \underline{\mathbf{v}}_{kN}^\times) \cdot \nabla N_i d\Gamma = \\ = \int_{\Gamma_k^e} N_i \mathbf{j} \mathbf{p} \mathbf{h} (\underline{\mathbf{v}} - \underline{\mathbf{v}}_k^\times) \cdot \underline{\mathbf{n}} d\Gamma = - \int_{\Gamma_k^e} N_i \mathbf{j} \mathbf{q} \cdot \underline{\mathbf{n}} d\Gamma \end{aligned} \quad (4.34)$$

where subscripts T and N refer to tangential and normal components, respectively.

Since equation (4.34) applies equally to any portion of  $\Gamma_i^e$  the equivalent partial differential equation can be deduced and is of the form

$$\begin{aligned} \frac{D_k^\times N_i \widehat{\mathbf{h}}'}{D_k^\times t} + N_i \widehat{\mathbf{h}}' \operatorname{div}_{\Gamma_k} \underline{\mathbf{v}}_k^\times + \operatorname{div}_{\Gamma_k} N_i \widehat{\mathbf{h}}' (\underline{\mathbf{v}}_T^* - \underline{\mathbf{v}}_{kT}^\times) + \widehat{\mathbf{h}}' (\underline{\mathbf{v}}_N^* - \underline{\mathbf{v}}_{kN}^\times) \cdot \nabla N_i = \\ = N_i \mathbf{j} \mathbf{p} \mathbf{h} (\underline{\mathbf{v}} - \underline{\mathbf{v}}_k^\times) \cdot \underline{\mathbf{n}} = - N_i \mathbf{j} \mathbf{q} \cdot \underline{\mathbf{n}} \end{aligned} \quad (4.35)$$

Application of Leibniz law to the derivatives and on rearrangement, equation (4.35) reduces to

$$\begin{aligned} \widehat{\mathbf{h}}' \left[ \frac{D_k^\times N_i}{D_k^\times t} + (\underline{\mathbf{v}}_T^* - \underline{\mathbf{v}}_{kT}^\times) \cdot \nabla_{\Gamma_k} N_i + (\underline{\mathbf{v}}_N^* - \underline{\mathbf{v}}_{kN}^\times) \cdot \nabla N_i \right] + N_i \left[ \frac{D_k^\times \widehat{\mathbf{h}}'}{D_k^\times t} + \widehat{\mathbf{h}}' \operatorname{div}_{\Gamma_k} \underline{\mathbf{v}}_k^\times + \operatorname{div}_{\Gamma_k} \widehat{\mathbf{h}}' (\underline{\mathbf{v}}_T^* - \underline{\mathbf{v}}_{kT}^\times) \right] = \\ = N_i \mathbf{j} \mathbf{p} \mathbf{h} (\underline{\mathbf{v}} - \underline{\mathbf{v}}_k^\times) \cdot \underline{\mathbf{n}} = - N_i \mathbf{j} \mathbf{q} \cdot \underline{\mathbf{n}} \end{aligned} \quad (4.36)$$

which in turn implies

$$\frac{D_k^{\times} \hat{h}'}{D_k^{\times} t} + \hat{h}' \operatorname{div}_{\Gamma_k} \underline{v}_k^{\times} + \operatorname{div}_{\Gamma_k} \hat{h}' (\underline{v}_T^* - \underline{v}_{kT}^{\times}) = \left[ \rho h (\underline{v} - \underline{v}_k^{\times}) \cdot \underline{n} \right] = - \left[ \underline{q} \cdot \underline{n} \right] \quad (4.37)$$

and

$$\frac{D_k^{\times} N_i}{D_k^{\times} t} + (\underline{v}_T^* - \underline{v}_{kT}^{\times}) \cdot \nabla_{\Gamma_k} N_i + (\underline{v}_N^* - \underline{v}_{kN}^{\times}) \cdot \nabla N_i = \frac{D_k^{\times} N_i}{D_k^{\times} t} + (\underline{v}^* - \underline{v}_k^{\times}) \cdot \nabla N_i = \frac{D^* N_i}{D^* t} = 0 \quad (4.38)$$

where equations (4.37) and (4.38) confirm the validity of equation (4.33)

It is important to appreciate that no discontinuity is present on the LHS of equations (4.31) and (4.32). In addition the integrals on the LHS of equations (4.31) and (4.32) are evaluated in the sense of Lebesgue. Thus, the source term makes no contribution, the set  $\Omega_e / \{\Gamma_k : k \in K_e\}$ , where  $K_e = \{k : \Omega_e \cap \Gamma_k \neq \emptyset\}$  and  $\emptyset$  is the null set, is not partitioned into separate domains and  $\Gamma_k$  is null in  $\Omega_e$ , having zero Lebesgue measure. Consequently the right-hand side of these equations is also absent of discontinuities, achieved primarily as a consequence of isolating the source term. The real power of the non-physical approach is revealed here by its ability to isolate and annihilate discontinuities in transport equations.

#### 4.7 Simplified finite element equations

Although equations (4.31) and (4.32) are absent of discontinuities they are evidently more complicated than the original system as new variables have been introduced. It is anticipated that solving equation (4.31) to (4.33) is unlikely to be computationally competitive without some form of simplification and efficient resolution of the discontinuity property. Equation (4.31) can be viewed as the continuous system that replaces the original discontinuous system of finite element equations whilst equations (4.32) and (4.33) can be viewed as constraints on this system and are required to be reduced in some manner. Many options are available for the simplification and solution of equations (4.32) and (4.33) and one possible approach is the direct use of the expressions:

$$\bar{\rho} = \bar{\rho}_0 \exp \left[ \int_C \operatorname{div} \underline{v}^* \left\| \underline{v}^* \right\|^{-2} \underline{v}^* \cdot d\underline{x}^* \right], \quad \hat{h}^* = \bar{\rho}_0^{-1} \hat{h}_0 + \int_C \bar{\rho}^{-1} \rho D h / D t \left\| \underline{v}^* \right\|^{-2} \underline{v}^* \cdot d\underline{x}^* \quad \text{and} \quad \hat{h} = \bar{\rho} h^*,$$

to link physical and non-physical variables and remove equation (4.32). The disadvantage of this approach is that contour integrals are required to be evaluated and of course these expressions are limited to areas away from any discontinuity. A similar strategy is



applicable to  $\widehat{h}'_k$  for the removal of equation (4.33), i.e. consider setting  $\widehat{h}'_k = \widehat{\rho}'_k \widehat{h}'_{k,*}$  and substituting in equation (4.37) to give

$$\widehat{h}'_{k,*} \left( \frac{D_k^\times \widehat{\rho}'_k}{D_k^\times t} + \widehat{\rho}'_k \operatorname{div}_{\Gamma_k} (\underline{v}_{kN}^\times + \underline{v}_T^*) \right) + \widehat{\rho}'_k \frac{D_k^\times \widehat{h}'_{k,*}}{D_k^\times t} = \left[ \rho h (\underline{v} - \underline{v}_k^\times) \cdot \underline{n} \right] = - \left[ \underline{q} \cdot \underline{n} \right] \quad (4.39)$$

where it is assumed that  $\widehat{h}'_k$  is spatially invariant on  $\Gamma_k$  a property arising from the invariance of jump condition  $\left[ \rho h (\underline{v} - \underline{v}_k^\times) \cdot \underline{n} \right] = - \left[ \underline{q} \cdot \underline{n} \right]$  along an isotherm.

The solution to equation (4.39) for  $\underline{v}_k^\times \neq 0$  is

$$\widehat{\rho}'_k = \widehat{\rho}'_{k0} \exp \left[ \int_C \operatorname{div}_{\Gamma_k} (\underline{v}_{kN}^\times + \underline{v}_{kT}^*) \frac{\underline{v}_k^\times}{\|\underline{v}_k^\times\|^2} \cdot d\underline{x}_k^\times \right] \quad (4.40)$$

and

$$\widehat{h}'_k = \widehat{\rho}'_k \left( \frac{\widehat{h}'_{k0}}{\widehat{\rho}'_{k0}} + \int_C \widehat{\rho}'_k{}^{-1} \left[ \rho (\underline{v} - \underline{v}_k^\times) \cdot \underline{n} \right] \frac{\underline{v}_k^\times}{\|\underline{v}_k^\times\|^2} \cdot d\underline{x}_k^\times \right) \quad (4.41)$$

where  $\widehat{\rho}'_{k0}$  and  $\widehat{h}'_{k0}$  are  $\widehat{\rho}'_k$  and  $\widehat{h}'_k$  at  $t = t_0$  and  $d\underline{x}_k^\times = \underline{v}_k^\times dt$ .

Unfortunately whilst this approach provides insight into the behaviour of the source term  $\widehat{h}'_k$ , a contour integral is required to be evaluated. Although in principal analytical expressions for  $\widehat{h}'_k$  and  $\widehat{h}$  can be used, in practice direct numerical approaches are preferred. Consider first the substitution of equation (4.33) into equation (4.31) and summation of equations (4.32) and (4.33) with respect to  $i$  to give

$$\begin{aligned} \frac{D^*}{D^* t} \int_{\Omega_e / \{\Gamma_k : k \in K_e\}} N_i \widehat{h} dV &= \int_{\Omega_e} \nabla N_i \cdot \underline{q} dV - \int_{\Gamma_e} N_i \underline{q} \cdot \underline{n} d\Gamma + \int_{\Omega_e} \rho N_i Q dV \\ &+ \sum_{k \in K_e} \int_{\Gamma_k^e} \widehat{h}' (\underline{v}_N^* - \underline{v}_{kN}^\times) \cdot \nabla N_i d\Gamma + \sum_{k \in K_e} \int_{\Gamma_k^e} N_i \left[ \underline{q} \cdot \underline{n} \right] d\Gamma \end{aligned} \quad (4.42)$$

$$\frac{D^*}{D^*t} \int_{\Omega_e / \{\Gamma_k : k \in K_e\}} \hat{h} dV = \frac{D^*}{D^*t} \int_{\Omega_e} \rho h dV + \int_{\Gamma_e} \rho h (\underline{v} - \underline{v}^*) \cdot \underline{n} d\Gamma - \sum_{k \in K_e} \int_{\Gamma_k^e} \rho h (\underline{v} - \underline{v}_k^*) \cdot \underline{n} d\Gamma \quad (4.43)$$

$$\frac{D_k^\times}{D_k^\times t} \int_{\Gamma_k^e} \hat{h}' d\Gamma + \int_{\Sigma_k^e} \hat{h}' (\underline{v}^* - \underline{v}_k^\times) \cdot \underline{t} n d\Sigma = \int_{\Gamma_k^e} \rho h (\underline{v} - \underline{v}_k^\times) \cdot \underline{n} d\Gamma = - \int_{\Gamma_k^e} \underline{q} \cdot \underline{n} d\Gamma \quad (4.44)$$

which is a simplified form of equations (4.31) to (4.32).

A further simplification is achieved with the removal of equation (4.44) and the removal of the term  $\sum_{k \in K_e} \int_{\Gamma_k^e} \hat{h}' (\underline{v}_N^* - \underline{v}_{kN}^\times) \cdot \nabla N_i$  in equation (4.42). This can be postulated by the realisation that the principal purpose of this term is to annihilate the discontinuities in the integral  $\int_{\Omega_e} \nabla N_i \cdot \underline{q} dV$ . Thus, with  $\underline{q} = -k \nabla T$  and temperature approximated by

$T = \sum_{j=1}^{m_e} N_j T_j$  (i.e. the discontinuities are ignored in  $\underline{q}$ ), then  $\sum_{k \in K_e} \int_{\Gamma_k^e} \hat{h}' (\underline{v}_N^* - \underline{v}_{kN}^\times) \cdot \nabla N_i$  should also be ignored. The governing equation (4.42) then reduces to

$$\frac{D^*}{D^*t} \int_{\Omega_e / \{\Gamma_k : k \in K_e\}} N_i \hat{h} dV = - \int_{\Omega_e} k \nabla N_i \cdot \nabla T dV - \int_{\Gamma_e} N_i \underline{q} \cdot \underline{n} d\Gamma + \int_{\Omega_e} \rho N_i Q dV + \sum_{k \in K_e} \int_{\Gamma_k^e} N_i \underline{q} \cdot \underline{n} d\Gamma \quad (4.45)$$

and is constrained by equation (4.43).

A particular difficulty associated with the solution of equations (4.45) and (4.43) is the lack of uniqueness of  $\hat{h}$ . This property although advantageous in some respects means that  $\hat{h}$  cannot be used directly to predict  $h$ . Moreover, since  $h$  is discontinuous and  $\hat{h}$  is not a simple direct relationship is not immediately apparent. However, both  $\hat{h}$  and  $h$  are related to temperature and a convenient approach is to set  $\hat{h} = \hat{c} T$ , where  $\hat{c}$  is a non-physical capacitance term. It should be appreciated that  $\hat{c}$  is not a physical parameter. Since the focus of the paper is on multiple discontinuity annihilation it is revealing to explore solidification involving negligible mass movement and zero mesh movement to provide further simplification.

### 4.8 Solidification in an Eulerian frame

The general theory simplifies substantially on a stationary mesh ( $\underline{v}^* = \underline{0}$ ) in situations where material movement is sufficiently small to be negligible ( $\underline{v} \approx \underline{0}$ ). Note however that setting  $\underline{v} = \underline{0}$  has certain implications associated with density change without mass movement. Recall that the term  $\int \rho h \underline{v}_k^\times \cdot \underline{n}$  is obtained on setting  $\underline{v} = \underline{0}$  in the expression  $-\int \rho h (\underline{v} - \underline{v}_k^\times) \cdot \underline{n}$ . Note however, that continuity  $-\int \rho (\underline{v} - \underline{v}_k^\times) \cdot \underline{n} = 0$  gives  $\rho_k (\underline{v}_k - \underline{v}_k^\times) \cdot \underline{n}_k + \rho_{k+1} (\underline{v}_{k+1} - \underline{v}_k^\times) \cdot \underline{n}_{k+1} = 0$ , where it is understood that the expression applies at interface  $\Gamma_k$ . This expression reduces to  $-\rho_k \underline{v}_k^\times \cdot \underline{n}_k = \rho_{k+1} (\underline{v}_{k+1} - \underline{v}_k^\times) \cdot \underline{n}_k$  with  $\underline{v}_k = \underline{0}$ . Observe that for  $\rho_k \neq \rho_{k+1}$  the expression infers that  $\underline{v}_{k+1} \neq \underline{0}$ . Moreover, it follows that  $-\int \rho h (\underline{v} - \underline{v}_k^\times) \cdot \underline{n} = \rho_k h_k (\underline{0} - \underline{v}_k^\times) \cdot \underline{n}_k - \rho_{k+1} h_{k+1} (\underline{v}_{k+1} - \underline{v}_k^\times) \cdot \underline{n}_k = \rho_k L_k \underline{v}_k^\times \cdot \underline{n}_k$ , where  $L_k$  is the latent energy release associated with  $\Gamma_k$ . If on the other hand it is assumed that  $\underline{v}_{k+1} = \underline{0}$ , then for  $\rho_k \neq \rho_{k+1}$ ,  $\underline{v}_k \neq \underline{0}$  and the jump condition  $-\int \rho h (\underline{v} - \underline{v}_k^\times) \cdot \underline{n}$  gives  $\rho_{k+1} L_k \underline{v}_k \cdot \underline{n}_k$ . The assumption  $\underline{v}_1$  equals the velocity of the solid which is stationary, i.e.  $\underline{v}_1 = \underline{v}_s = \underline{0}$  provides a variable mass element, whilst  $\underline{v}_{K+1} = \underline{v}_\ell = \underline{0}$  gives a constant mass element and the corresponding choices for  $\int \rho h \underline{v}^\times \cdot \underline{n}$  are  $\rho_k L_k \underline{v}_k \cdot \underline{n}_k$  and  $\rho_{k+1} L_k \underline{v}_k \cdot \underline{n}_k$ , respectively. The constant mass element is assumed here (i.e.  $\underline{v}_{K+1} = \underline{v}_\ell = \underline{0}$ ) to avoid the need to account for mass movement into the element.

In this case equations (4.45) and (4.43) reduce to

$$\frac{\partial}{\partial t} \int_{\Omega_e / \{\Gamma_k : k \in K_e\}} N_i \hat{h} dV = - \int_{\Omega_e} k \nabla N_i \cdot \nabla T dV - \int_{\Gamma_e} N_i \underline{q} \cdot \underline{n} d\Gamma + \int_{\Omega_e} \rho N_i Q dV + \sum_{k \in K_e \Gamma_k^e} \int N_i \underline{q} \cdot \underline{n} d\Gamma \quad (4.46)$$

$$\frac{\partial}{\partial t} \int_{\Omega_e / \{\Gamma_k : k \in K_e\}} \hat{h} dV = \frac{\partial}{\partial t} \int_{\Omega_e} \rho h dV + \sum_{k \in K_e \Gamma_k^e} \int \rho h \underline{v}_k^\times \cdot \underline{n} d\Gamma \quad (4.47)$$

It is of interest to give further justification for some of the simplifications suggested in Section 4.7. Note that  $\hat{\rho} = \hat{\rho}^n \exp \left[ \int_C \text{div} \underline{v}^* \left\| \underline{v}^* \right\|^{-2} \underline{v}^* \cdot d\underline{x}^* \right] = \hat{\rho}^n$  for  $\underline{v}^* = \underline{0}$  and it follows also that  $\hat{h} - \hat{h}^n = \int_{t_n}^t \rho \partial h / \partial s ds$ , which reduces to  $\hat{h} - \hat{h}^n = \rho c (T - T^n)$  for invariant material properties. This relationship provides justification for the identity  $\hat{h} = \hat{c}T$ , since

$\hat{h}^n$  is totally arbitrary and can simply be set to  $\rho c T^n$ . Although the relationship suggests that  $\hat{c} = \rho c$ , this will only occur under restricted circumstances.

It is interest also to examine the nature of the source term  $\hat{h}'$ , where  $\hat{h}'$  and  $\underline{v}^\times$  are assumed spatially invariant on  $\Gamma_k^e$  the portion of  $\Gamma_k$  in the element, for 1-D element on an Eulerian frame with two discontinuities is shown in Figure 4-6. Then equation (4.43) reduces to

$$\frac{D_k^\times \hat{h}'}{D_k^\times t} = \rho h (\underline{v} - \underline{v}_k^\times) \cdot \underline{n} = -\rho_{k+1} \underline{v}_k^\times \cdot \underline{n}_k [h_{k+1} - h_k]_{\Gamma_k} = -\rho_{k+1} L_k (\underline{v}_k^\times \cdot \underline{n}_k)_{\Gamma_k} \quad (4.48)$$

where  $L_k$  is latent heat released at boundary  $\Gamma_k$ .

Integration of equation (4.48) gives

$$\hat{h}'(t) - \hat{h}'_n = -\rho_{k+1} L_k \int_{t_n}^t \underline{v}_k^\times \cdot \underline{n}_k ds = -\rho_{k+1} L_k (X_k(t) - X_k^n), \text{ where } \int_{t_n}^t \underline{v}_k^\times \cdot \underline{n}_k ds = X_k(t) - X_k^n,$$

with  $X_k$  denoting the position of the  $k^{\text{th}}$  discontinuity measured in the direction of  $\underline{v}_{kN}^\times$ .

This suggests a relationship of the form  $\hat{h}' = -\rho_{k+1} L_k X_k$ , where again non-uniqueness facilitates the neglect of constant terms. This relationship is approximate, so not recommended for use in the full system of FE equations although does provide insight into the behaviour of  $\hat{h}'$ , for linear elements and temperature-enthalpy relationship is shown in Figure 4-3.

Consider further the postulation in the previous section that  $-\sum_{k \in K_c} \int_{\Gamma_k^e} \hat{h}' \underline{v}_{kN}^\times \cdot \nabla N_i$  annihilates the discontinuities in  $\int_{t_n}^{t_{n+1}} \int_{\Omega_e} \nabla N_i \cdot \underline{q} dV dt$ . On a small volume  $\Delta V$  swept by the boundary  $\Gamma_k$  over time  $\Delta t$  the relationship  $\Delta X_k = \Delta V_k / A = \underline{v}_k^\times \cdot \underline{n}_k \Delta t$  applies. At time interval  $\alpha \Delta t$ , where  $\alpha \in [0, 1]$  the following measure relationship holds

$$\begin{aligned} \int_{\Delta t \Delta V} \nabla N_i \cdot \underline{q} dV dt &= \nabla N_i \cdot \underline{q}_{k+1} \Delta V_k \Delta t + \alpha \nabla N_i \cdot (\underline{q}_k - \underline{q}_{k+1}) \Delta V_k \Delta t = \\ &= \nabla N_i \cdot \underline{q}_{k+1} \Delta V_k \Delta t - \alpha \rho_{k+1} L_k \nabla N_i \cdot \underline{n}_k (\underline{v}_k^\times \cdot \underline{n}_k) \Delta V \Delta t \end{aligned} \quad (4.49)$$

where use is made of jump condition

$$\rho h (\underline{v} - \underline{v}_k^\times) \cdot \underline{n} = -\rho_{k+1} L_k \underline{v}_k^\times \cdot \underline{n}_k = -\underline{q} \cdot \underline{n} = (\underline{q}_k - \underline{q}_{k+1}) \cdot \underline{n}_k \quad \text{and recognition that}$$

$\underline{q}_k - \underline{q}_{k+1} = -(\underline{q}_k - \underline{q}_{k+1})\underline{n}_k$ . Similarly, with  $\widehat{h}'_\alpha - \widehat{h}'_0 = -\rho_{k+1}L_k\alpha\Delta X_k$  the measure relationship is

$$\begin{aligned} -\int_{\Delta t} \widehat{h}'_\alpha \underline{v}_{kN}^\times \cdot \nabla N_i A dt &= -\widehat{h}'_0 \underline{v}_{kN}^\times \cdot \nabla N_i A \Delta t + \alpha \rho_{k+1} L_k \nabla N_i \cdot \underline{n}_k (\underline{v}_k^\times \cdot \underline{n}_k) A \Delta X_k \Delta t = \\ &= -\widehat{h}'_0 \underline{v}_k \cdot \nabla N_i A \Delta t + \alpha \rho_{k+1} L_k \nabla N_i \cdot \underline{n}_k (\underline{v}_k^\times \cdot \underline{n}_s) \Delta V_k \Delta t \end{aligned} \quad (4.50)$$

It is evident on comparison that the terms on the far RHS of equations (4.49) and (4.50) are identical and of opposite sign and will be eliminated on addition. Thus the postulation in the previous section is valid and illustrated here is an example how the source term  $\widehat{h}'$  removes a discontinuity. It is worth emphasising here the importance of this result which provides the first analytical justification for the neglect of the discontinuities that appears the integral  $\int_{t_n}^{t_{n+1}} \int_{\Omega_e} \nabla N_i \cdot \underline{q} dV dt$ .

#### 4.9 System assembly and solution

Defined in Section 4.8 via the relationship  $\widehat{h} = \widehat{c}T$  is the concept of non-physical capacitance. Substitution of this identity into equations (4.46) and (4.47) gives on integration

$$\begin{aligned} \widehat{c}^e \left[ \int_{\Omega_e} N_i T^{n+1} dV - \int_{\Omega_e} N_i T^n dV \right] &= - \int_{t_n}^{t_{n+1}} \int_{\Omega_e} k \nabla N_i \cdot \nabla T dV dt - \int_{t_n}^{t_{n+1}} \int_{\Gamma_e} N_i \underline{q} \cdot \underline{n} d\Gamma dt + \int_{t_n}^{t_{n+1}} \int_{\Omega_e} \rho N_i Q dV dt + \\ &+ \int_{t_n}^{t_{n+1}} \sum_{k \in K_e \Gamma_k^e(t)} \int N_i \rho h \underline{v}_k^\times \cdot \underline{n} d\Gamma dt \end{aligned} \quad (4.51)$$

$$\widehat{c}^e = \frac{\int_{\Omega_e} \rho^{n+1} h^{n+1} dV - \int_{\Omega_e} \rho^n h^n dV + \int_{t_n}^{t_{n+1}} \sum_{k \in K_e \Gamma_k^e(t)} \int \rho h \underline{v}_k^\times \cdot \underline{n} d\Gamma dt}{\int_{\Omega_e} T^{n+1} dV - \int_{\Omega_e} T^n dV} \quad (4.52)$$

where for simplicity  $\hat{c}^e$  it is assumed both spatially and temporally invariant on element  $\Omega_e$  and over time interval  $[t_n, t_{n+1}]$  and where it is recognised that the set  $K_e = \{k : \Omega_e \cap \Gamma_k \neq \emptyset\}$  can change over the time interval.

It is convenient to represent the term  $S_e = \int_{t_n}^{t_{n+1}} \sum_{k \in K_e} \int_{\Gamma_k^e(t)} N_i \left[ \rho h \mathbf{v}_k^\times \cdot \mathbf{n} \right] d\Gamma dt$  on the far RHS of equation (4.52) in two parts, i.e.  $S_e = S_e^{n+1} + S_e^n$ , where  $S_e^{n+1} = \hat{c}_s^e \int_{\Omega_e} N_i T^{n+1} dV$  and  $S_e^n = -\hat{c}_s^e \int_{\Omega_e} N_i T^n dV$ , where the source capacitance  $c_s^e$  is evaluated from

$$\hat{c}_s^e = \frac{\int_{t_n}^{t_{n+1}} \sum_{k \in K_e} \int_{\Gamma_k^e(t)} N_i \left[ \rho h \mathbf{v}_k^\times \cdot \mathbf{n} \right] d\Gamma dt}{\int_{\Omega_e} T^{n+1} dV - \int_{\Omega_e} T^n dV} \quad (4.53)$$

Approximation of the temperature field in the usual way  $T = \sum_{j=1}^m N_j T_j$  gives a familiar looking assembled system of equations of the form

$$(\hat{C} - \hat{C}_s)(T^{n+1} - T^n) + \Delta t^n K(\theta T^{n+1} + (1 - \theta)T^n) = \Delta t^n (\theta Q^{n+1} + (1 - \theta)Q^n) \quad (4.54)$$

where an implicit method ( $\theta = 1$ ) is utilised for the predictions and the capacitance matrices  $\hat{C}$  and  $\hat{C}_s$  are diagonal, i.e. a lumped approximation is adopted. The solution of (4.54) is coupled to the solution of (4.52) and (4.53) which provides a non-linear system of equations. A simple bisection technique is applied to converge on  $\hat{c}_s$  and the linear systems of equations for each iterate are solved using a SOR [120] method.

#### 4.10 Integral evaluation

The evaluation of the integrals in equations (4.51) and (4.52) requires the establishment of relationship between specific enthalpy and temperature. One approach is to assume the existence of specific enthalpy relationships for each material phase that occurs during the solidification process. For the formulation presented above it is convenient to assume that as a new material phase is formed latent energy is released. This approach also captures the possibility that no latent energy is released with the specification of zero latent heat for that particular transition, i.e.  $L_k = 0$  for the particular  $k$ . This approach provides for  $K + 1$

phases and  $K$  transition boundaries releasing latent heat  $L_k$  for  $k = 1, \dots, K$ . The specific enthalpy expression that applies to the material irrespective of the material phase combinations is

$$h = \sum_{k=1}^{K+1} g_k h_k^p \quad (4.55)$$

where  $g_k$  and  $h_k^p$  are the mass fractions and specific enthalpies associated with materials phases, respectively.

An alternative and slightly simpler approach for computational purposes is to assume the existence of specific enthalpies for the material combinations in  $\Omega_k$  existing during solidification. These can in fact be obtained from equation (4.55) and are denoted here as  $h_k^c$  for  $k = 1, \dots, K+1$ . Assume further the existence of specific heat capacitances for each material phase combination such that  $c_k^c = dh_k^c/dT$  then it follows for each region that

$$h_k^c(T) = h_{\Gamma_{k-1}^+}^c + \int_{T_{\Gamma_{k-1}}}^T c_k^c(T') dT' \quad (4.56)$$

for  $k = 2, \dots, K+1$  with  $T_{\Gamma_{k-1}} \leq T \leq T_{\Gamma_k}$  and  $\Gamma_{k-1}^+$  signifies that the boundary  $\Gamma_{k-1}$  is approached from within  $\Omega_k$ , which is necessary as  $h_{\Gamma_{k-1}^+}^c - h_{\Gamma_{k-1}^-}^c = L_{k-1}$ .

In the case  $k = 1$  the terms  $h_{\Gamma_{k-1}^+}^c$  and  $T_{\Gamma_{k-1}}$  are replaced by  $h_{\text{ref}}^c$  and  $T_{\text{ref}}$ , respectively to indicate reference enthalpy and temperature with  $h_{\text{ref}}^c = h_1^c(T_{\text{ref}})$ . A further simplification applied here is the assumption that  $c_k^c$  in  $\Omega_k^e$  are spatially and temporally invariant, which gives rise to linear specific enthalpy  $h_k^c$  and for  $k = 2, \dots, K$  the following relationship applies

$$h_k^c(T) = h_{\Gamma_{k-1}^+}^c + \int_{T_{\Gamma_{k-1}}}^T c_k^c dT' = h_{\Gamma_{k-1}^+}^c + c_k^c (T - T_{\Gamma_{k-1}}) = h_{\Gamma_{k-1}^+}^c + \frac{h_{\Gamma_k^-}^c - h_{\Gamma_{k-1}^+}^c}{T_{\Gamma_k} - T_{\Gamma_{k-1}}} (T - T_{\Gamma_{k-1}}) \quad (4.57)$$

with  $T_{\Gamma_{k-1}} \leq T \leq T_{\Gamma_k}$  with similar expressions for  $k = 1$  and  $k = K+1$ .

Consider the integral

$$\int_{\Omega_e} \rho^n h^n dV = \sum_{k=k_s^n}^{k_f^n} \int_{\Omega_k^n} \rho_k h_k^n dV = \sum_{k=k_s^n}^{k_f^n} M_k^n h_{\Gamma_{k-1}^+}^c + \sum_{k=k_s^n}^{k_f^n} \rho_k c_k^c \int_{\Omega_k^n} (T - T_{\Gamma_{k-1}}) dV \quad (4.58)$$

where  $k_s^n \leq k_f^n$  and  $k_s^n, k_f^n \in \{1, 2, \dots, K+1\}$  and it is assumed here that density  $\rho_k$  is spatially invariant in  $\Omega_k^n$ .

Recall also that  $h_{\Gamma_{k-1}^+}^c = L_{k-1} + h_{\Gamma_{k-1}^-}^c$ , which on substitution in equation (4.58) gives

$$\int_{\Omega_e} \rho^n h^n dV = \sum_{k=k_s^n}^{k_f^n} M_k^n L_{k-1} + \sum_{k=k_s^n}^{k_f^n} M_k^n h_{\Gamma_{k-1}^-}^c + \sum_{k=k_s^n}^{k_f^n} \rho_k c_k^c \int_{\Omega_k^n} (T - T_{\Gamma_{k-1}}) dV \quad (4.59)$$

where if  $k = k_s^n = 1$ , then  $L_{k-1}$ , which is undefined for this case is set to zero making equation (4.59) applicable for any  $k_s^n, k_f^n \in \{1, 2, \dots, K+1\}$  with  $k_s^n \leq k_f^n$ .

A similar expression to equation (4.59) can be obtained for time  $t_{n+1}$ , i.e.

$$\int_{\Omega_e} \rho^{n+1} h^{n+1} dV = \sum_{k=k_s^{n+1}}^{k_f^{n+1}} M_k^{n+1} L_{k-1} + \sum_{k=k_s^{n+1}}^{k_f^{n+1}} M_k^{n+1} h_{\Gamma_{k-1}^-}^c + \sum_{k=k_s^{n+1}}^{k_f^{n+1}} \rho_k c_k^c \int_{\Omega_k^{n+1}} (T - T_{\Gamma_{k-1}}) dV \quad (4.60)$$

where  $k_s^{n+1}, k_f^{n+1} \in \{1, 2, \dots, K+1\}$  reflect the number of discontinuities in  $\Omega_e$  at time  $t_{n+1}$ .

#### 4.10.1 Jump term evaluation

Consider the accurate evaluation of the integral  $\int_{t_n}^{t_{n+1}} \sum_{k \in K_e} \int_{\Gamma_k^e(t)} [\text{ph} \underline{v}_k^\times \cdot \underline{n}] d\Gamma dt$  and to facilitate this define  $k_s = \min\{k_s^n, k_s^{n+1}\}$  and  $k_f = \max\{k_f^n, k_f^{n+1}\}$  and observe that  $K_e \subset \{k : k_s \leq k \leq k_f\}$ . It is convenient to replace the expression  $\int_{t_n}^{t_{n+1}} \sum_{k \in K_e} \int_{\Gamma_k^e(t)} [\text{ph} \underline{v}_k^\times \cdot \underline{n}] d\Gamma dt$  with  $\sum_{k=k_s}^{k_f-1} \int_{t_n}^{t_{n+1}} \int_{\Gamma_k^e(t)} N_i [\text{ph} \underline{v}_k^\times \cdot \underline{n}] d\Gamma dt$ , where account is taken of discontinuities entering and leaving an element. As discussed in Section 4.8 a constant mass element is considered here for where  $[\text{ph} \underline{v}_k^\times \cdot \underline{n}]$  is replaced by  $-\rho_{k+1} L_k \underline{v}_k^\times \cdot \underline{n}_k$ . Consider then the integral



$$\begin{aligned}
\sum_{k=k_s+1}^{k_f} \int_{t_n}^{t_{n+1}} \int_{\Gamma_{k-1}^e(t)} \rho h \underline{v}_{k-1}^\times \cdot \underline{n} [d\Gamma dt] &= - \sum_{k=k_s+1}^{k_f} \rho_k L_{k-1} \int_{t_n}^{t_{n+1}} \int_{\Gamma_{k-1}^e(t)} \underline{v}_{k-1}^\times \cdot \underline{n} d\Gamma dt = \\
&= - \sum_{k=k_s+1}^{k_f} \rho_k L_{k-1} V_k^{\text{swept}} = - \sum_{k=k_s+1}^{k_f} L_{k-1} (M_k^{n+1} - M_k^n) \quad (4.61)
\end{aligned}$$

where  $V_k^{\text{swept}}$  is the swept volume resulting when  $\Gamma_k$  sweeps through the element  $\Omega_e$  and where  $\rho_{k+1} V_k^{\text{swept}} = M_{k+1}^{n+1} - M_{k+1}^n$  is recognised to readily account for a discontinuity leaving or entering an element and requires no special provision.

Combining equations (4.59), (4.60) and (4.61) gives

$$\begin{aligned}
\int_{\Omega_e} \rho^{n+1} h^{n+1} dV - \int_{\Omega_e} \rho^n h^n dV + \sum_{k=k_s+1}^{k_f} \int_{t_n}^{t_{n+1}} \int_{\Gamma_{k-1}^e(t)} \rho h \underline{v}_{k-1}^\times \cdot \underline{n} [d\Gamma dt] &= \\
&= \left[ \sum_{k=k_s^{n+1}}^{k_f^{n+1}} M_k^{n+1} L_{k-1} + \sum_{k=k_s^{n+1}}^{k_f^{n+1}} M_k^{n+1} h_{\Gamma_{k-1}^-}^c + \sum_{k=k_s^{n+1}}^{k_f^{n+1}} \rho_k c_k^c \int_{\Omega_k^{n+1}} (T - T_{\Gamma_{k-1}}) dV \right] - \\
&- \left[ \sum_{k=k_s^n}^{k_f^n} M_k^n L_{k-1} + \sum_{k=k_s^n}^{k_f^n} M_k^n h_{\Gamma_{k-1}^-}^c + \sum_{k=k_s^n}^{k_f^n} \rho_k c_k^c \int_{\Omega_k^n} (T - T_{\Gamma_{k-1}}) dV \right] - \sum_{k=k_s+1}^{k_f} L_{k-1} (M_k^{n+1} - M_k^n) \quad (4.62)
\end{aligned}$$

which reduces to

$$\begin{aligned}
\int_{\Omega_e} \rho^{n+1} h^{n+1} dV - \int_{\Omega_e} \rho^n h^n dV + \sum_{k=k_s}^{k_f} \int_{t_n}^{t_{n+1}} \int_{\Gamma_k^e(t)} \rho h \underline{v}_k^\times \cdot \underline{n} [d\Gamma dt] &= \sum_{k=k_s^{n+1}}^{k_f^{n+1}} \rho_k c_k^c \int_{\Omega_k^{n+1}} (T - T_{\Gamma_{k-1}}) dV - \\
&- \sum_{k=k_s^n}^{k_f^n} \rho_k c_k^c \int_{\Omega_k^n} (T - T_{\Gamma_{k-1}}) dV + \sum_{k=k_s^{n+1}}^{k_f^{n+1}} M_k^{n+1} h_{\Gamma_{k-1}^-}^c - \sum_{k=k_s^n}^{k_f^n} M_k^n h_{\Gamma_{k-1}^-}^c \quad (4.63)
\end{aligned}$$

where it is apparent that latent energy terms are annihilated in equation (4.62) to give equation (4.63) as predicted by the annihilation theory.

### 4.11 Numerical experiments

In this section the Non-physical Enthalpy Method (NEM) is compared against Analytical and/or Control Volume Capacitance Method (CVCM) solutions for some typical problems. Both the NEM and CVCM ensure that the energy loss/gain from an element is consistent with temperature change unlike effective and temporal capacitance approaches. It should

be recognised that the representation  $S_e = \int_{t_n}^{t_{n+1}} \sum_{k \in K_e} \int_{\Gamma_k^e(t)} N_i \left[ \rho h \underline{v}_k^\times \cdot \underline{n} \right] d\Gamma dt$  with  $S_e^{n+1} = \hat{c}_s^e \int_{\Omega_e} N_i T^{n+1} dV$  and  $S_e^n = -\hat{c}_s^e \int_{\Omega_e} N_i T^n dV$  yields a CVCM with  $\hat{c}_{cvcm}^e = \hat{c}^e - \hat{c}_s^e$ . The performance of the NEM matches that of the CVCM with differing results arising from the convergence on the source capacitance  $\hat{c}_s^e$  rather than the CVCM capacitance  $\hat{c}_{cvcm}^e$ .

Three problems are consider, which are:

1. Prescribed temperature verification on an element to highlight the differences between  $\hat{c}^e$  and  $\hat{c}_{cvcm}^e$  dealing with multi-discontinuities.
2. Solidification of a 1-D semi-infinite slab for an initial liquid state to a range of different states involving discontinuous transitions.
3. Solidification of a 3-D cube with multiple discontinuities, mushy and isothermal solidification processes.

The analysis presented is applied to relatively simple problems as it is not deemed necessary to analyse more complex/practical problems here as the approach is shown to give near identical performance to the CVCM, which has been thoroughly tested in pressure die casting for a range of complex component geometries [115, 116].

As part of the investigation into the performance of the NEM the concept of using a single discontinuity in place of a multiple discontinuities or processes involving no discontinuities is examined. The use of discontinuities in this way is common with analytical approaches but seldom adopted for numerical treatments because of the associated numerical convergence and instability problems posed. The NEM however is formulated to cater if not embrace discontinuities, so it is of interest to ascertain some results on the merits of this approach.

#### 4.11.1 Isothermal solidification for 1-D element

Consider the 1-D linear element depicted in Figure 4-3 subjected to a decreasing temperature field where  $T_2^{n+1} = T_1^{n+1} + T_{diff}$  and where  $T_{diff}$  is the temperature difference between the nodes of the element. The temperature difference between the nodes is set to: 10, 15 and 20°C and  $T_1^n = T_{liq} + 5$  with  $T_{liq} - 120 \leq T_1^{n+1} < T_{liq} + 5$ . The temperature range is selected to ensure the material is initially liquid and ends up completely solid. The material properties are given in the first column of Table 4.1, under the heading of material

1 and are approximately those for Al-4.5%Cu. However, in order to highlight the annihilation of source terms latent heat release is assumed to occur at the two transition boundaries. The magnitudes of the latent heat release in terms of the total latent heat release are set to  $L_1 = 0.15L$  and  $L_2 = 0.35L$  for demonstration purposes.

Depicted in Figure 4-4 and Figure 4-5 are the non-physical capacitances  $\hat{c}_{cvcm}^e$  and  $\hat{c}^e$  for the CVCM and the NEM respectively. It is evident on comparison of Figure 4-4 and Figure 4-5 that the variation of  $\hat{c}_{cvcm}^e$  is significantly greater than that of  $\hat{c}^e$  obtained from equation (4.52). This illustrates that the two discontinuities have been effectively removed with the presence of the term  $\int_{t_n}^{t_{n+1}} \sum_{k \in K_e} \int_{\Gamma_k^e(t)} N_i \left[ \rho h \underline{v}_k^x \cdot \underline{n} \right] d\Gamma dt$  in equation (4.52). This is demonstrated analytically in equations (4.62) and (4.63) but also demonstrated numerically in Figure 4-5. Note that the values  $\rho_s c_s = 2.52 \text{ MJ/m}^3 \text{ } ^\circ\text{C}$  and  $\rho_\ell c_\ell = 2.75 \text{ MJ/m}^3 \text{ } ^\circ\text{C}$  can be contrasted against the numerical values provided in Figure 4-5 to illustrate the effectiveness of the discontinuity annihilation.

#### 4.11.2 1-D semi-infinite domain with phase-change.

Solidification of a semi-infinite slab with a fixed temperature boundary condition and two discontinuities (see Figure 4-6) with the latent heat release distribution as in the previous example has no known analytical solution, hence the NEM is contrasted against the CVCM which has been extensively tested [115, 116]. A comparison with the analytical solution for a single discontinuity is performed in section 3.13.2 so not repeated here. The mesh used for the test is depicted in Figure 4-7 along with boundary and initial conditions. The material properties are given in the first column of the Table 4.1, which are those for Al-4.5%Cu. Temperature histories, profiles and information on the non-physical capacitances are provided in Figure 4-8 to Figure 4-10, for different locations along the slab. Excellent accuracy for temperature histories and profiles for both the NEM and CVCM is obtained as illustrated in Figure 4-8 and Figure 4-9. The behaviour of the non-physical capacitances  $\hat{c}_{cvcm}^e$  and  $\hat{c}^e$  is shown in Figure 4-10 and mirrors that shown in Figure 4-4 and Figure 4-5. The two spikes (one spike per discontinuity) in the value of  $\hat{c}_{cvcm}^e$  for each point chosen correspond with the discontinuities passing through the elements at the stipulated spatial locations. The behaviour of  $\hat{c}^e$  appears to match only in the section of the plots where the enthalpy distribution is continuous and illustrates the effectiveness of procedure for discontinuity annihilation.

### 4.11.3 3-D cube domain with various type of solidification.

The solidification of a cube is considered where mesh boundary, initial conditions and latent heat release are depicted in Figure 4-11 and Figure 4-12, respectively. Although an analytical solution is unavailable, different time steps and mesh densities are tested to ascertain the relative sensitivities of the CVCm and the NEM. Although, annihilation of multiple-discontinuities is the main concern of this paper, a series of tests were chosen in order to realise the feasibility of representing a complicated solidification process involving mushy or multiple discontinuities with a single discontinuity. It is expected that this approach is adequate for rapid solidification where the transition zone appears narrow on the spatial scale considered.

Given in Table 4.2 and Table 4.3 are the approximate program execution times for each of the methods along with results pertaining to the two error norms

$$\max_{i,n} |T_i^n - T_i^{nb}|, \quad \max_{i,n} \left| \frac{E^n - E^{nb}}{E_{total}^{nb}} \right| \times 100$$

where  $i$  and  $n$  represents the nodal position along the cube diagonal and time step, respectively. Moreover,  $T_i$  and  $E$  are the nodal temperature and the energy loss from the cube surface, respectively. The subscript  $b$  indicates benchmark values, which since no analytical solution are available, are taken as the results obtained using NEM with  $\Delta x = 0.50$  mm (6000 elements) and  $\Delta t = 0.005$  s. The tests were performed using an implicit Euler time-stepping algorithm and the non-linear equations were solved using a bisection method. The material properties are taken from column 2 in Table 4.1, which corresponds to Zamak-5.

It is evident on comparison of Table 4.2 that comparable results are obtained for both methods with a slightly improved performance delivered by the NEM. The results shown in Table 4.2, Figure 4-13 and Figure 4-15 demonstrate the relative insensitivity of both methods to mesh density. Moreover, the energy loss and temperature errors norms presented in Table 4.2 shows only a small discrepancy between fine and coarse meshes, which is further evidence of the benefits of a control volume transport equation methodology. It is of interest to note that in terms of program execution time, consistently the solidification processes modelled with NEM are faster than their counterpart modelled with CVCm. The behaviour of the non-physical capacitances  $\hat{c}^e$  and  $\hat{c}_{cvc}^e$  is shown in Figure 4-14 and Figure 4-16 for an element at a specified location varying with mesh

density for the three different solidification cases. The behaviour of  $\hat{c}^e$  is showing the anticipated smoothness continuity for mushy and multi-discontinuities process and reasonable invariant for the isothermal but again the non-physical nature of  $\hat{c}_{cvcm}^e$  is highlighted. Since two discontinuities are involved, each of the three points tested generates to rapid changes in  $\hat{c}_{cvcm}^e$  to capture the latent energy release. This is not the case for NEM because discontinuity annihilation means latent heat effects are not present to any significance degree in  $\hat{c}^e$ .

The temperature histories for various time-steps are presented in Figure 4-17 and Figure 4-19 for the three different test cases, which includes the single discontinuity approximation (i.e. isothermal solidification). Comparable performance is delivered by the two methods with the NEM outperforming the CVCM in terms of the program execution time; however in particular, both methods achieved relatively high accuracy for a relatively large time set  $\Delta t = 0.1s$ . The behaviour of the non-physical capacitances  $\hat{c}_{cvcm}^e$  and  $\hat{c}^e$  is shown in Figure 4-18 and Figure 4-20 for an element for various time steps for the three test cases. The behaviour of  $\hat{c}^e$  is reasonably invariant as consequence of the ability of the NEM to annihilate the discontinuity in the heat flux at the phase front for the isothermal solidification. Also highlighted is the non-physical nature of  $\hat{c}_{cvcm}^e$ , whose behaviour varies in a non-physical manner changing demonstrably with time-step. A particular feature of both methods is their extraordinary accuracy for relatively large time-steps. This results because both methods maintain consistency between temperature and energy change, i.e. the energy lost from an element corresponds exactly with the temperature change unlike traditional capacitance and source-based methods. Furthermore, in terms of energy loss and temperature error norms NEM achieved better results as shown in Table 4.3.

## 4.12 Conclusions

Presented in chapter 4 is the concept of non-physical enthalpy for the precise removal multiple discontinuities arising in phase-change problems. The following conclusions can be drawn for the work presented:

1. Non-physical enthalpy  $\hat{h}$  is well defined and possesses the property of limiting continuity at a discontinuity in physical enthalpy  $h$  but also behaves as a source (denoted  $\hat{h}'$ ) on a discontinuity, where  $\hat{h}'$  is well defined.
2. Non-physical enthalpy  $\hat{h}$  is non-physical in the sense that it is non-Galilean being dependent on the velocity  $\underline{v}^*$  of the computational frame.
3. A procedure for the removal of multiple discontinuities present in finite element equations in transport form has been established in the chapter.
4. Numerical solution of the governing system of transport FE equations provides excellent accuracy and is computationally competitive.

Table 4.1 Material properties for numerical test

Material Properties	units	Material 1 (Al-4.5%Cu)	Material 2 (Zamak-5)
Thermal conductivity – solid	$\frac{\text{W}}{\text{m}^\circ\text{C}}$	200	108
Thermal conductivity – liquid		90	50
Heat capacitance – solid	$\frac{\text{J}}{\text{kg}^\circ\text{C}}$	900	419
Heat capacitance – liquid		1100	505
Density – solid	$\frac{\text{kg}}{\text{m}^3}$	2800	6600
Density – liquid		2500	6800
Latent heat	$\frac{\text{kJ}}{\text{kg}}$	390	126
Solidus	$^\circ\text{C}$	548	380
Liquidus		646	386

Table 4.2 Performance data for various mesh densities

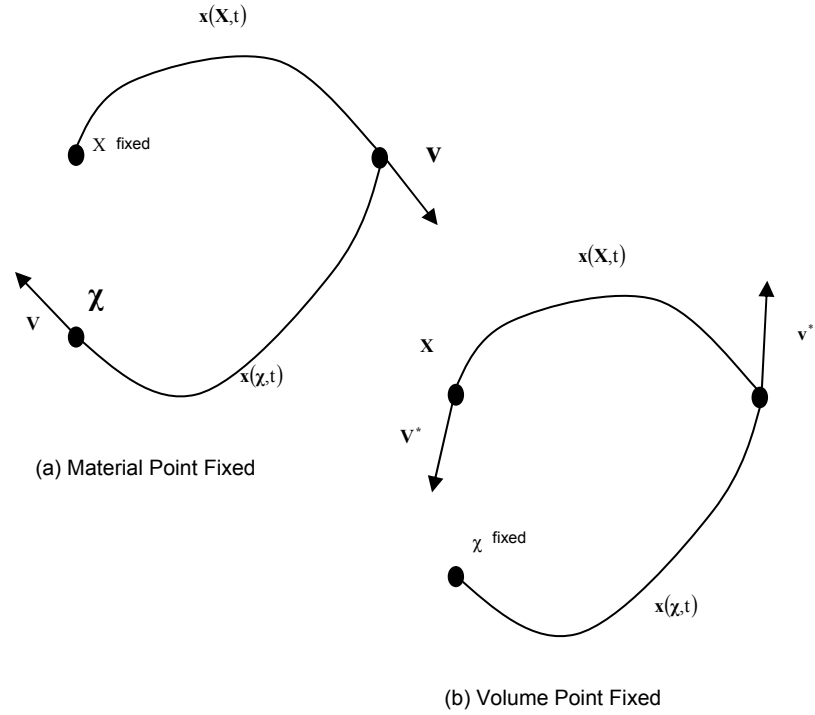
<b>MATERIAL PROPERTIES ZAMAK-5</b>					
Time step $\Delta t = 0.005s$ and $N = 300$ steps					
	Cube modelled with tetrahedron $\Delta x = \Delta y = \Delta z = 0.50mm$ with 6000 elements				
	<b>CVCM</b>			<b>NEM</b>	
	Mushy	Multi-discontinuities	Isothermal	Multi-discontinuities	Isothermal
Nodes in solid phase	1231	1225	1233	1215	1239
Program execution time (s)	36.86	36.67	39.16	34.33	37.86
Temperature error norm ( $^{\circ}C$ )	7.64	6.50	0.59	5.94	Test Case
Energy loss error norm (%)	3.01	1.11	0.15	2.67	Test Case
	Cube modelled with tetrahedron $\Delta x = \Delta y = \Delta z = 1.00mm$ with 750 elements				
	<b>CVCM</b>			<b>NEM</b>	
	Mushy	Multi-discontinuities	Isothermal	Multi-discontinuities	Isothermal
Nodes in solid phase	197	196	204	196	204
Program execution time (s)	6.719	5.031	5.266	4.875	4.672
Temperature error norm ( $^{\circ}C$ )	3.41	3.42	0.45	3.38	Test Case
Energy loss error norm (%)	2.02	1.69	0.07	1.69	Test Case
	Cube modelled with tetrahedron $\Delta x = \Delta y = \Delta z = 1.67mm$ with 162 elements				
	<b>CVCM</b>			<b>NEM</b>	
	Mushy	Multi-discontinuities	Isothermal	Multi-discontinuities	Isothermal
Nodes in solid phase	58	58	60	58	60
Program execution time (s)	2.328	2.219	2.469	2.031	2.188
Temperature error norm ( $^{\circ}C$ )	2.81	2.74	0.1	2.70	Test Case
Energy loss error norm (%)	1.92	1.76	0	1.68	Test Case

Test Case-specific approach other methods contrasted against

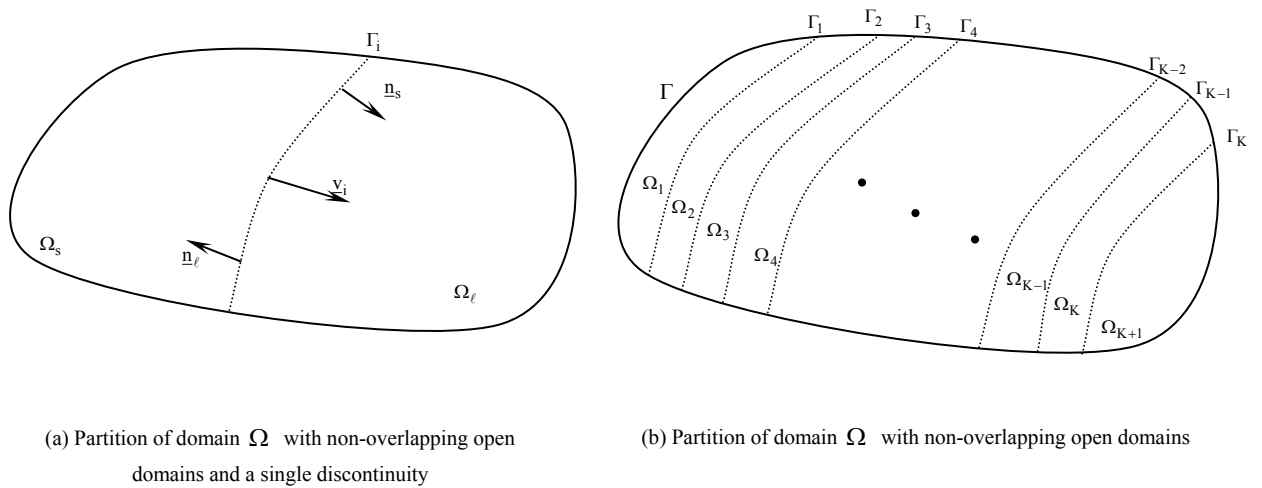


Table 4.3 Performance data for various time-steps

MATERIAL PROPERTIES ZAMAK-5				
Cube modelled with tetrahedron $\Delta x = \Delta y = \Delta z = 0.50\text{mm}$ with 6000 elements time step $\Delta t = 0.005\text{s}$ and $N = 300$ steps				
		Nodes in solid phase	Program execution time (s)	
CVCM-Mushy-benchmark		1231	36.86	
CVCM-Multi-discontinuities-benchmark		1225	36.67	
NEM-Multi-discontinuities-benchmark		1215	34.33	
Cube modelled with tetrahedron $\Delta x = \Delta y = \Delta z = 1.00\text{mm}$ with 750 elements				
Isothermal – CVCM				
	Nodes in solid phase	Program execution time (s)	Temperature error norm ( $^{\circ}\text{C}$ )	Energy loss error norm (%)
$\Delta t = 0.005\text{s}$ $N = 300$ steps	204	5.266	Mush-6.06 Mdis-5.88	Mush-2.76 Mdis-0.88
$\Delta t = 0.25\text{s}$ $N = 60$ steps	196	0.7031	Mush-10.57 Mdis-10.37	Mush-3.91 Mdis-1.99
$\Delta t = 0.1\text{s}$ $N = 15$ steps	196	0.4219	Mush-7.27 Mdis-7.02	Mush-1.14 Mdis-0.72
$\Delta t = 0.5\text{s}$ $N = 3$ steps	162	0.5156	Mush-14.11 Mdis-13.02	Mush-0.49 Mdis-2.32
Isothermal – NEM				
$\Delta t = 0.005\text{s}$ $N = 300$ steps	204	4.672	Mush-6.06 Mdis-5.75	Mush-2.68 Mdis-2.35
$\Delta t = 0.25\text{s}$ $N = 60$ steps	196	0.6562	Mush-10.57 Mdis-10.37	Mush-3.91 Mdis-3.57
$\Delta t = 0.1\text{s}$ $N = 15$ steps	196	0.4062	Mush-7.28 Mdis-7.03	Mush-1.14 Mdis-0.81
$\Delta t = 0.5\text{s}$ $N = 3$ steps	162	0.5312	Mush-14.11 Mdis-13.02	Mush-0.49 Mdis-0.81



**Figure 4-1 Velocities in reference domain**



**Figure 4-2 Control volume domain containing discontinuities**

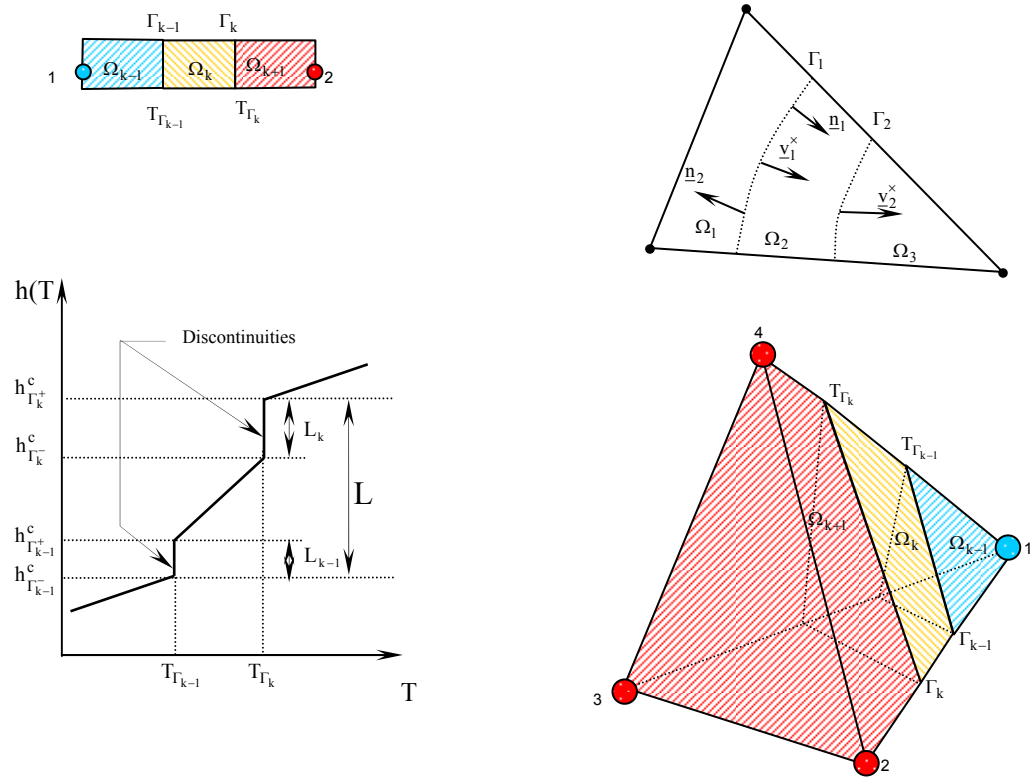


**Figure 4-3 Solidification with phase discontinuities and associated regions in a linear element**

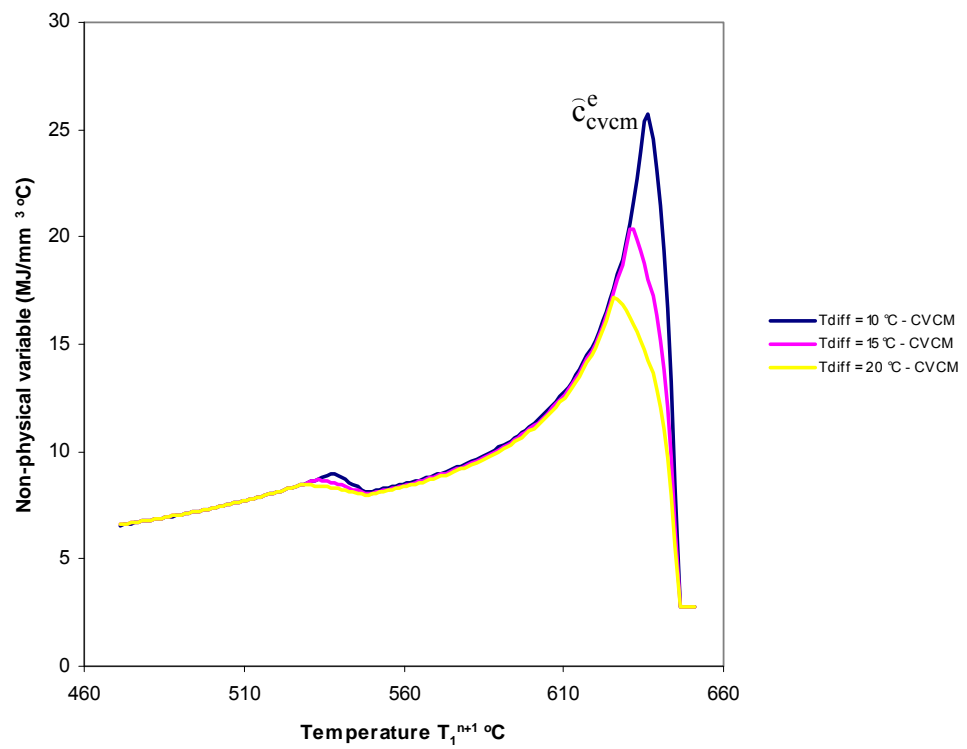


**Figure 4-4 Non-physical (CVCm) variable profile for phase-change in a 1-D element**

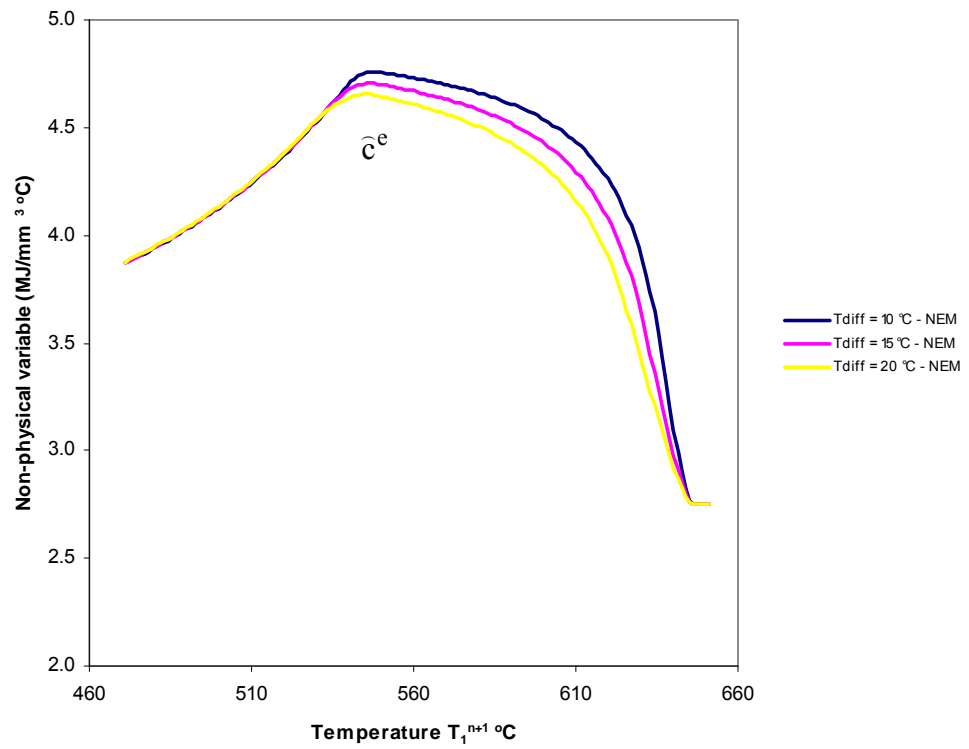


Figure 4-5 Non-physical variable (NEM) profile for phase-change 1-D element

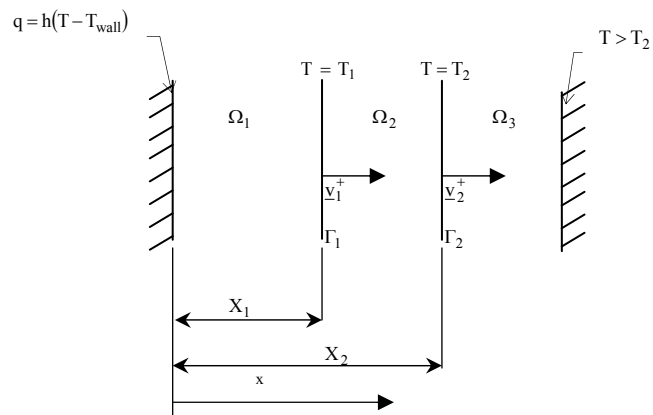


Figure 4-6 1-D solidification problem with two fronts on an Eulerian frame

## 1-D SEMI-INFINITE SLAB PROBLEM

$$k \frac{\partial T}{\partial x}(0) = h(T_{\text{amb}} - T)$$

$$T_{\text{amb}} = 0^\circ\text{C}, T_{\text{init}} = 660^\circ\text{C}$$

$$h = 10^4 \text{ W/m}^2\text{C}$$

$$\frac{\partial T}{\partial x}(60) = 0$$

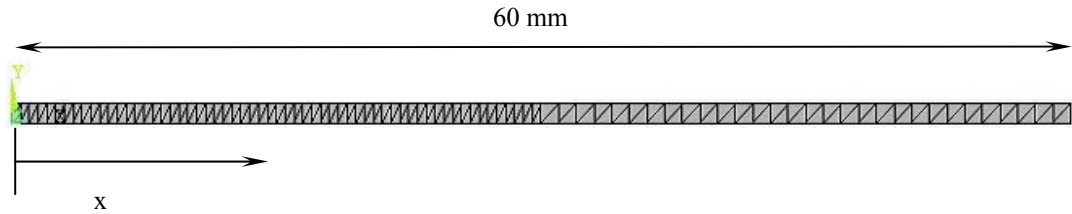


Figure 4-7 Mesh for 1-D semi-infinite slab problem

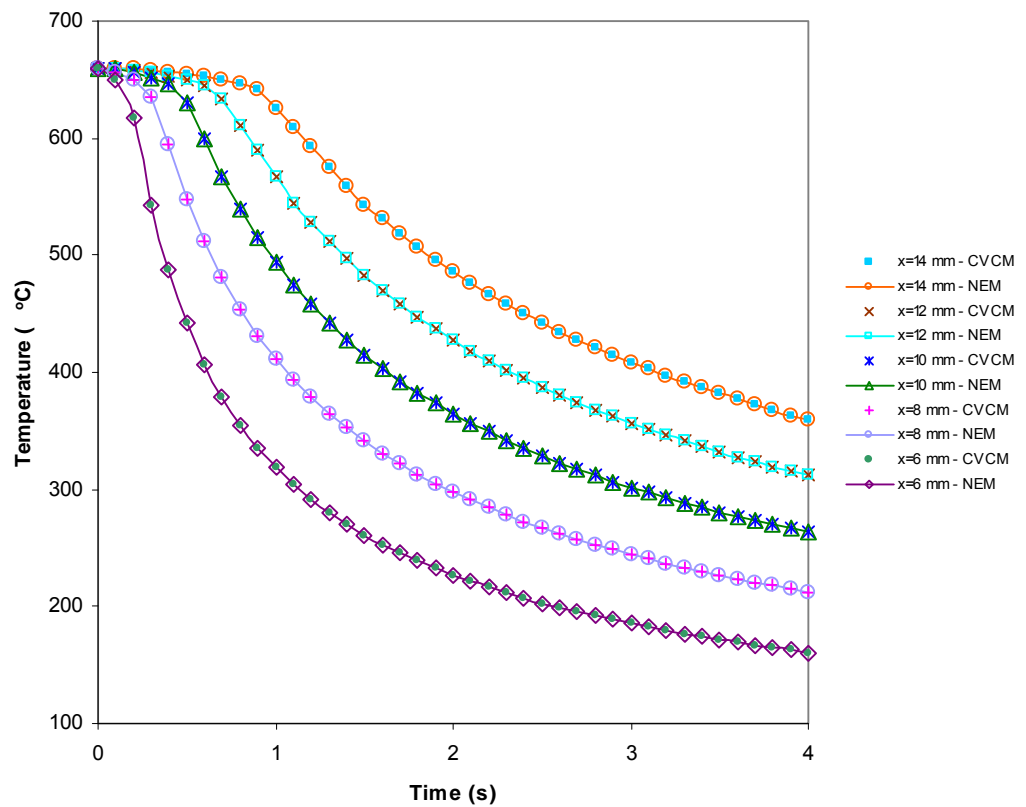


Figure 4-8 Temperature history for phase-change 1-D semi-infinite slab

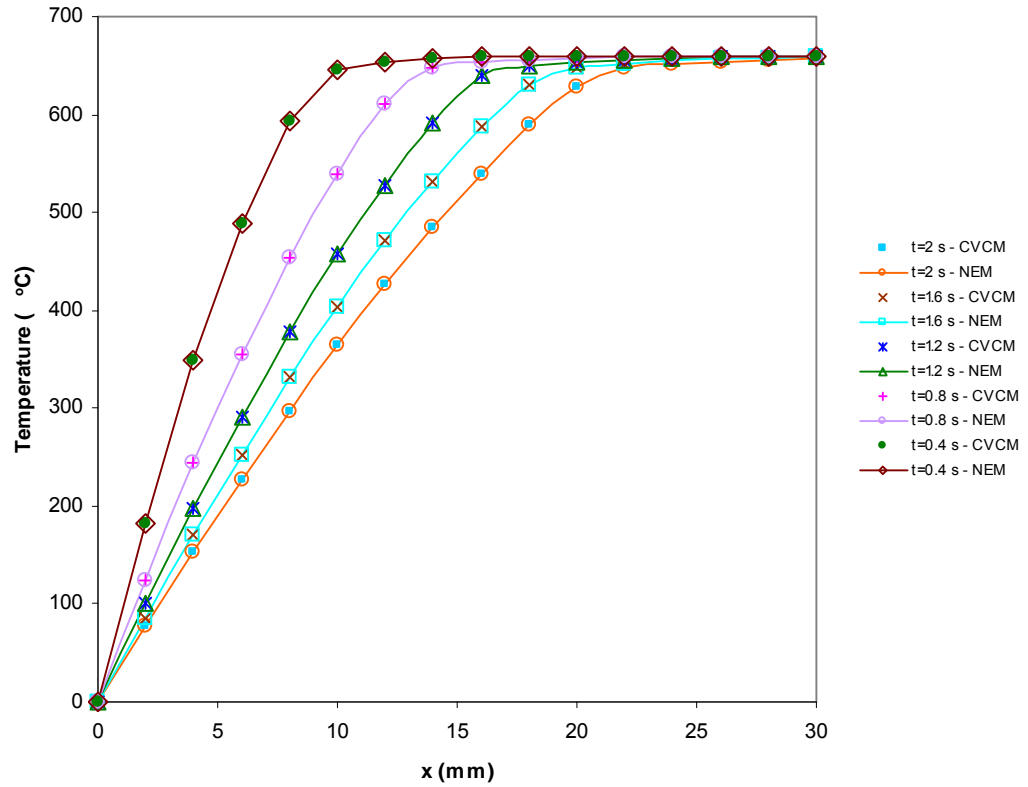


Figure 4-9 Temperature profile comparison for phase-change 1-D semi-infinite slab

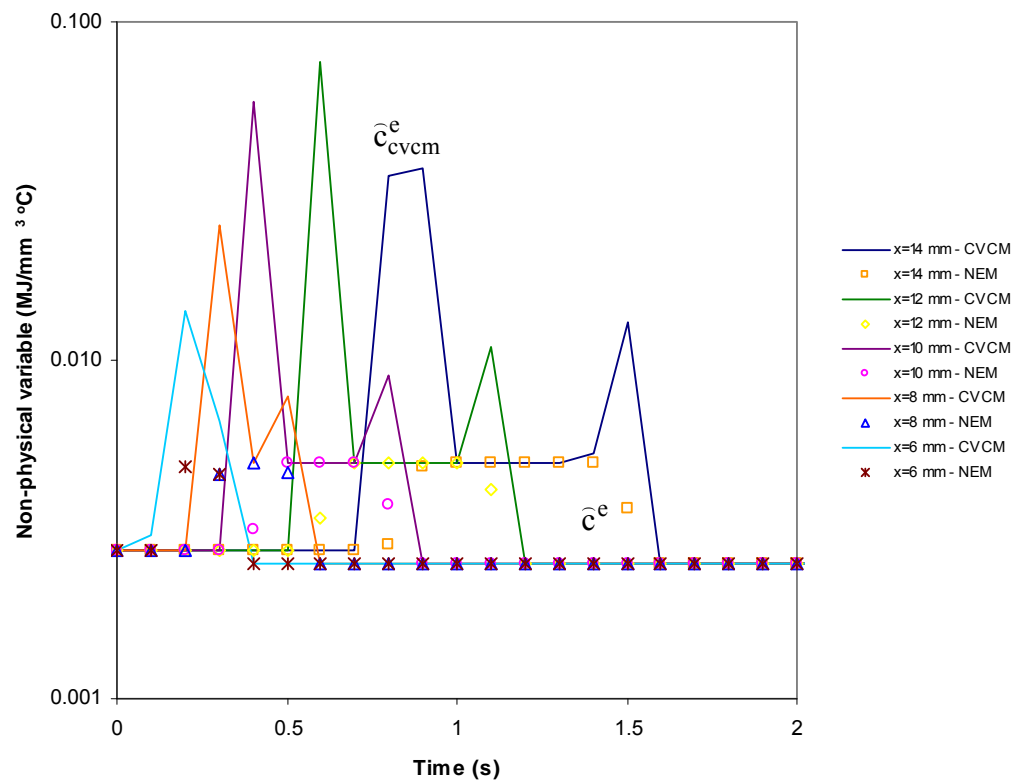


Figure 4-10 Non-physical variable history for phase-change 1-D semi-infinite slab

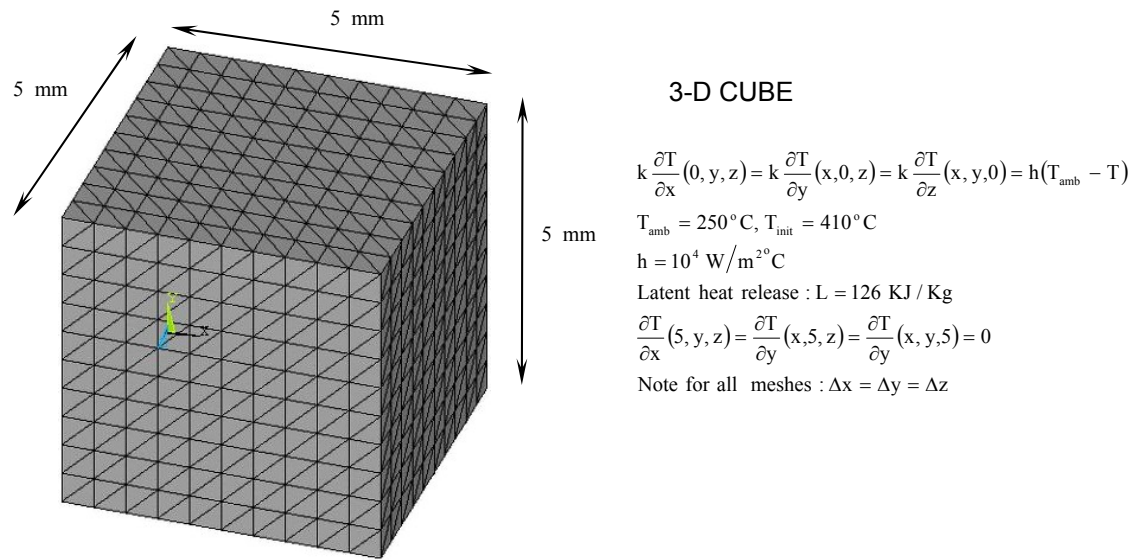


Figure 4-11 Mesh for 3-D cube problem

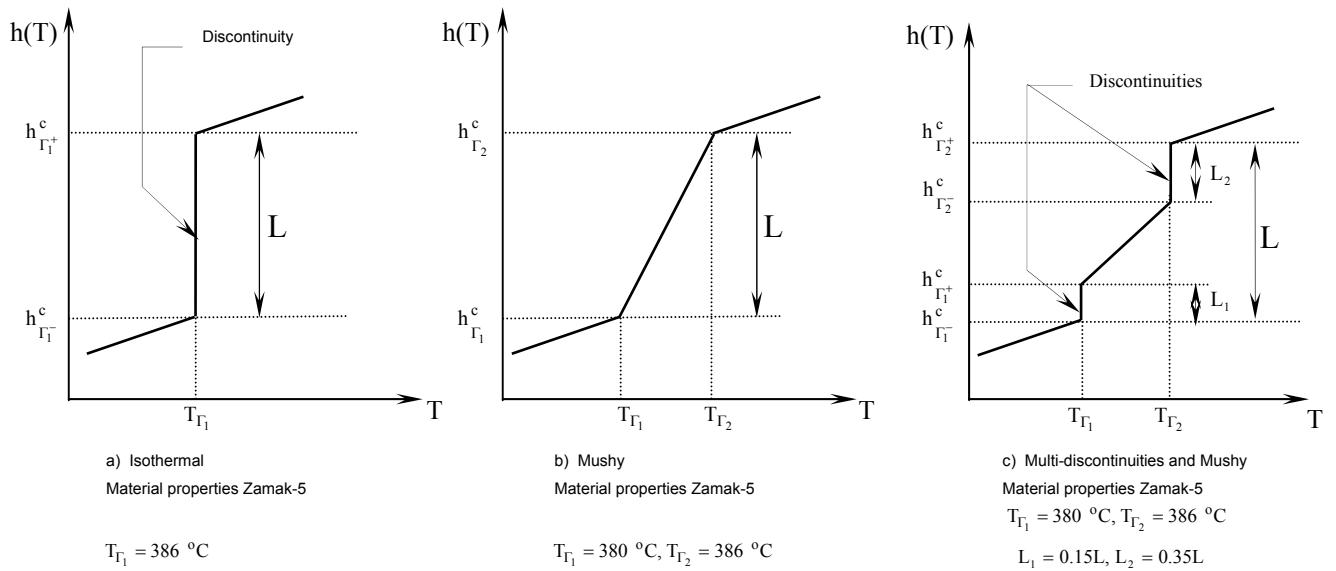
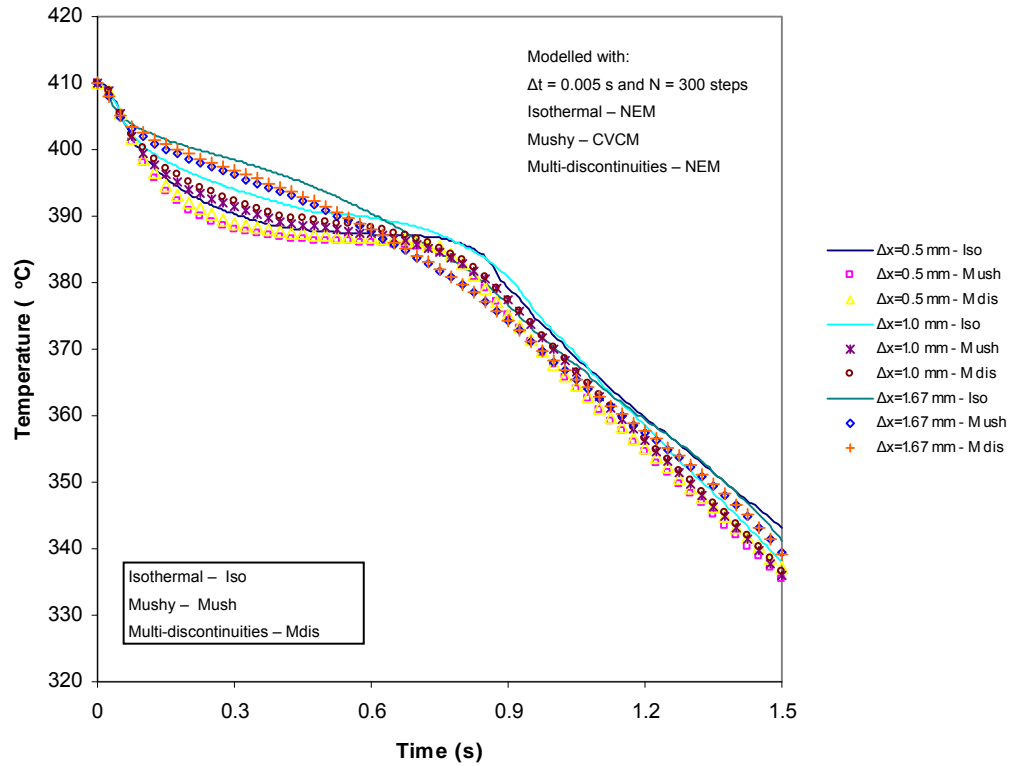
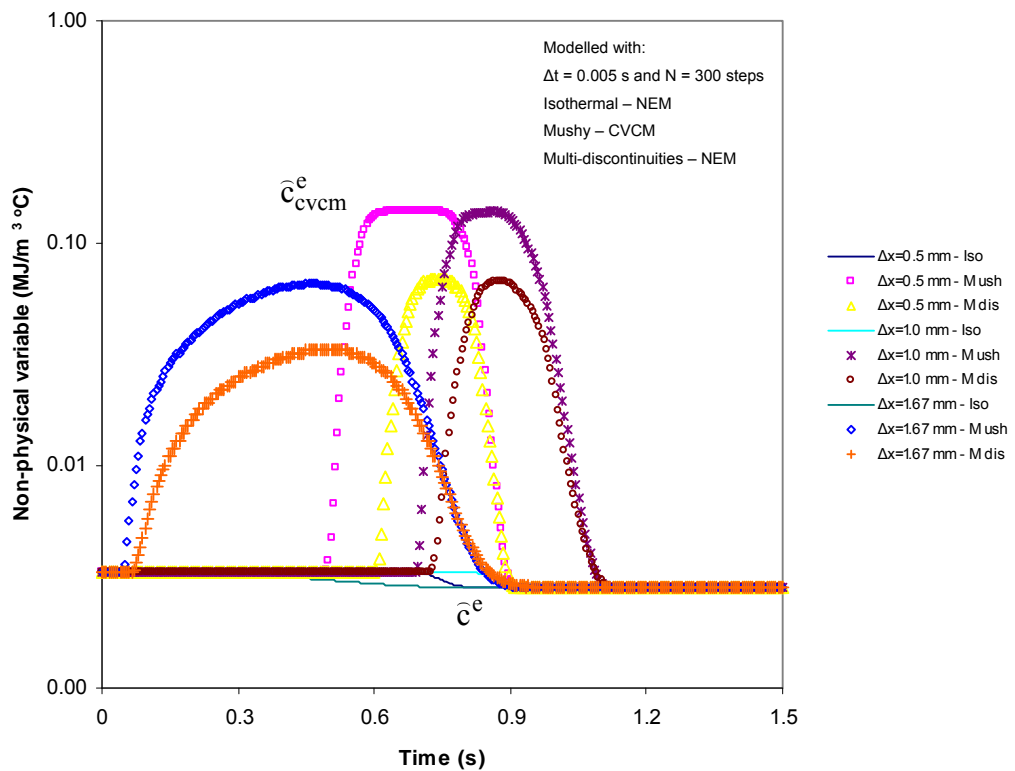


Figure 4-12 Latent heat release for different cases of solidification



**Figure 4-13 Isothermal Mushy and Multi-discontinuous solidification at  $x=y=z=2$  mm for different meshes**



**Figure 4-14 Non-physical variable behaviour for Isothermal, Mushy and Multi-discontinuous solidification on a point  $x=y=z=2$  mm**



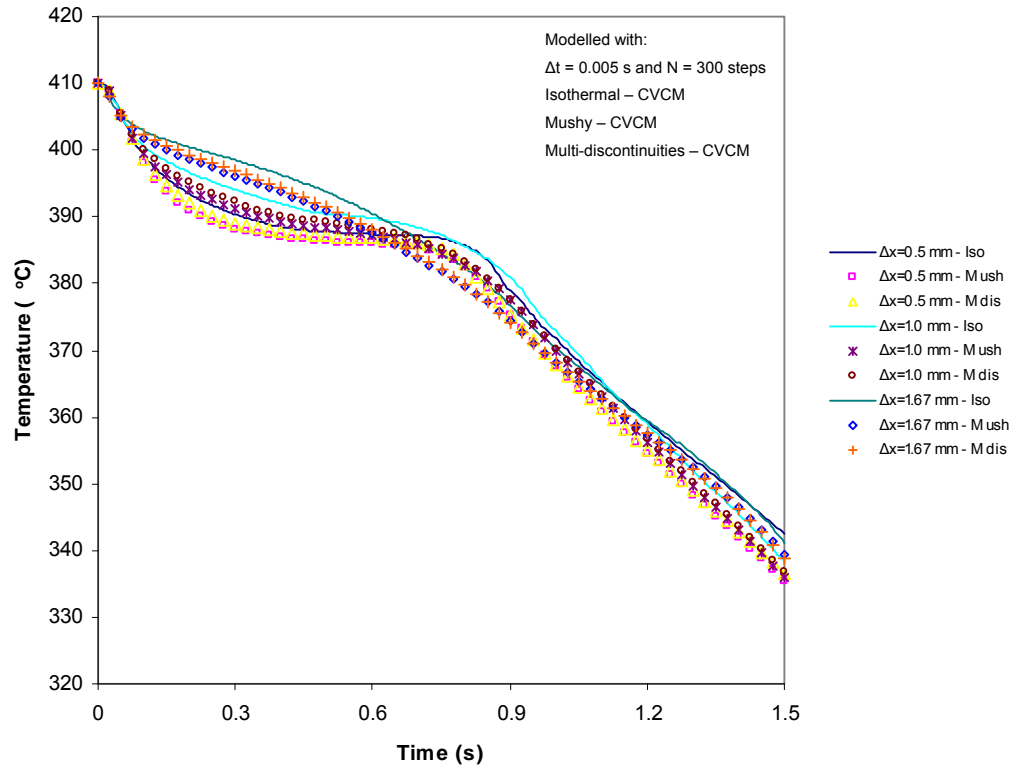


**Figure 4-15 Temperature history for Isothermal, Mushy and Multi-discontinuous solidification on a point  $x=y=z=2$  mm for different meshes**

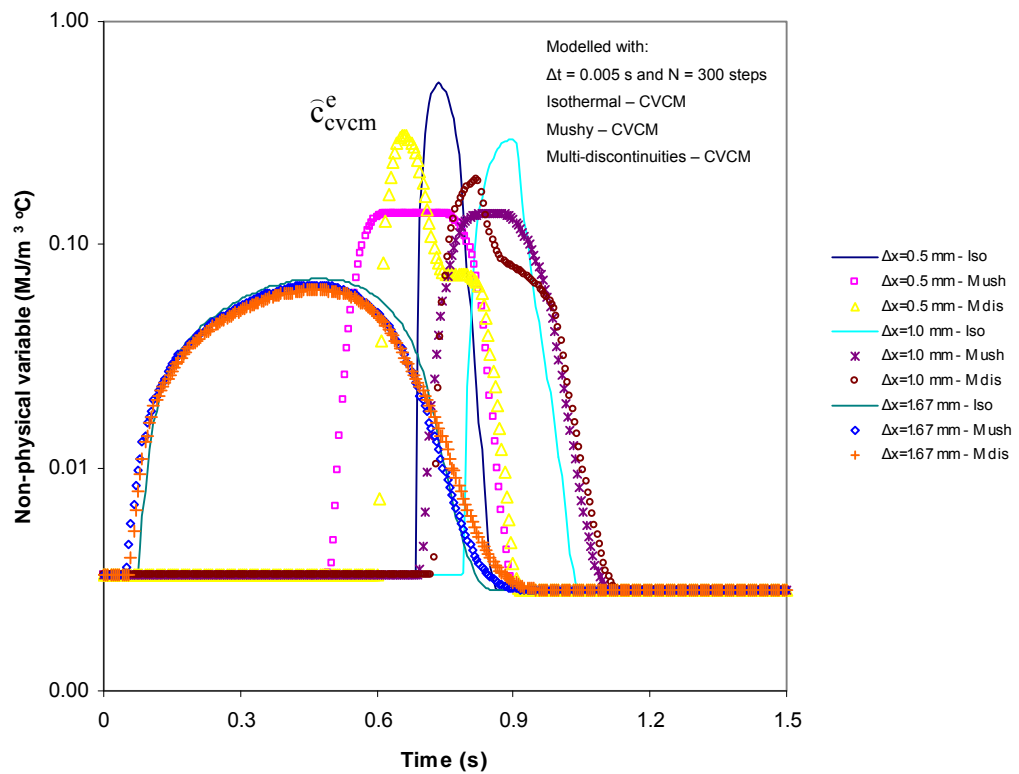


**Figure 4-16 Non-physical variable comparison for Isothermal, Mushy and Multi-discontinuous solidification on a point  $x=y=z=2$  mm for different meshes**

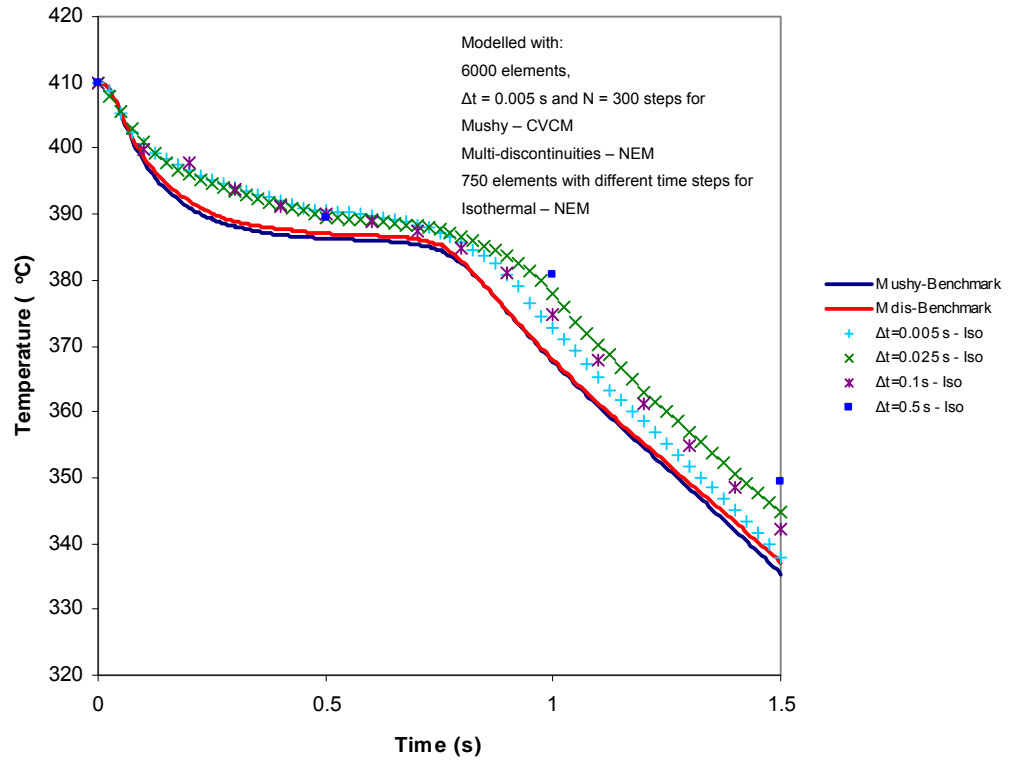


**Figure 4-17 Mushy and Multi-discontinuities solidification contrasted with single discontinuity NEM at  $x=y=z=2$  mm for different time steps**

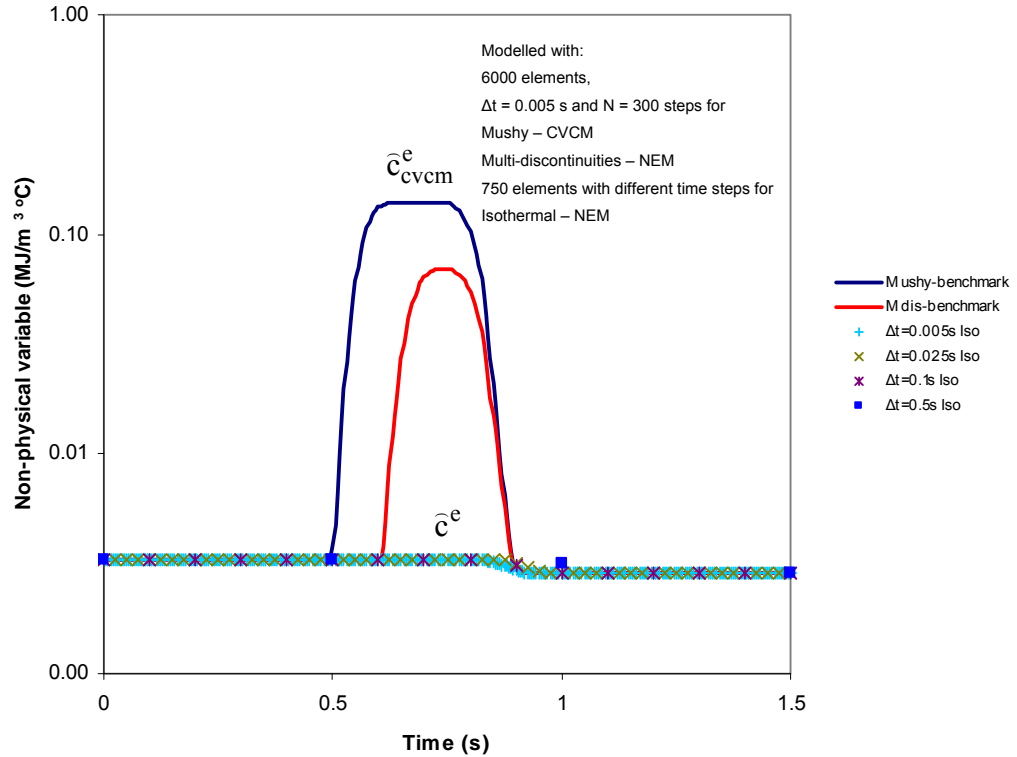


**Figure 4-18 Non-physical variable comparison at  $x=y=z=2$  mm for various time steps**

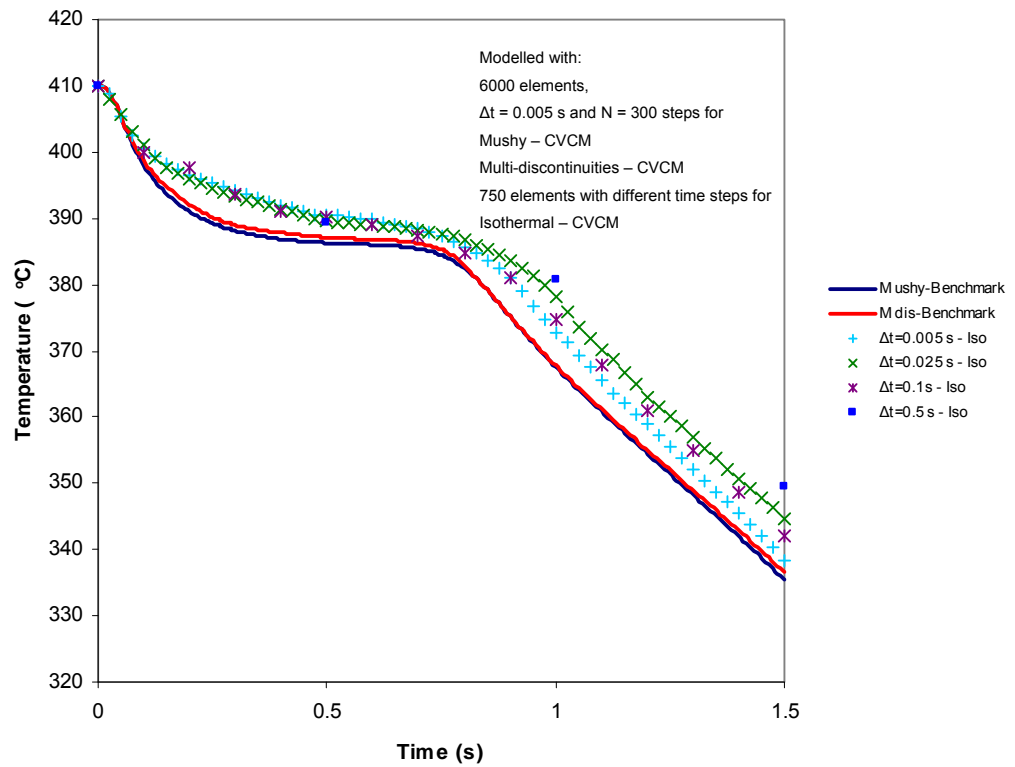


**Figure 4-19 Mushy and Multi-discontinuities solidification contrasted with single discontinuity CVCm at  $x=y=z=2$  mm for different time steps**

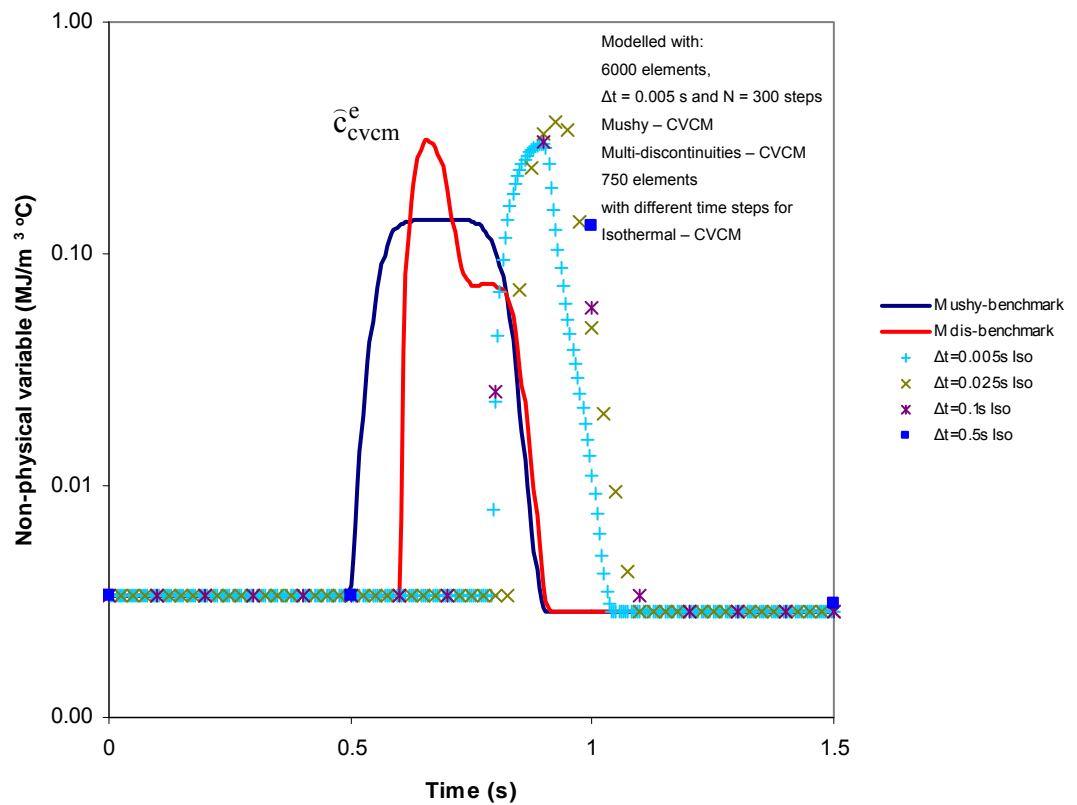


**Figure 4-20 Non-physical variable comparison at  $x=y=z=2$  mm for different time steps**

# 5 RESULTS

---

## ***5.1 Introduction***

Presented in chapter 3 and 4 is the theory underpinning the non-physical enthalpy method (NEM). Chapter 3 focuses on isothermal solidification and demonstrated is the method's ability to annihilate a single discontinuity. Further developments are discussed in chapter 4 where the annihilation of multiple discontinuities is demonstrated. Although a range examples were presented in chapters 3 and 4 ranging from a 1-D element to a 3-D cube, it is of interest to perform additional tests. Presented in this chapter is a comprehensive analysis of the mushy zone size effect on multi-discontinuous solidification in the form of results pertaining to the 3-D cube problem presented in chapter 3 and 4

## 5.2 Solidification with single discontinuity

Results for a single moving front (discontinuity) moving along the principal diagonal on a 3-D cube are being tracked for different size meshes with a fixed time step. Primarily, confirming the consistency of the method to identify and annihilate a discontinuity at points along the principal diagonal regardless of mesh size used and secondly, assessing the NEM performance in terms of stability and convergence. Material properties, initial and boundary conditions are shown in Table 3.1 and Figure 3-16, respectively.

### 5.2.1 Results using a fine mesh density

The mesh density used is  $\Delta x = \Delta y = \Delta z = 0.5 \text{ mm}$ , which in term of number of elements gives 6000 elements for a structure meshed domain. Enthalpy distribution and boundary and initial condition during isothermal solidification are shown in Figure 3-5 and Figure 3-16, respectively. For test 1 (L1) with the latent heat  $L = 130 \text{ kJ/kg}$ , temperature field comparison between CVCM and NEM along the principal diagonal in the 3-D cube is shown in Figure 5-1; results show that they are very close to each other with the maximum temperature error being  $0.12^\circ \text{C}$  at the point  $x = y = z = 1.5 \text{ mm}$ . In terms of time-step size and the number of time steps used are  $\Delta t = 0.005 \text{ s}$  and  $N = 200$ , respectively. However, the non-physical capacitance comparison between both methods, CVCM and NEM shown in Figure 5-2, has being consistence throughout all the points selected along the principal diagonal with the theory, which predicts the identification and annihilation of any discontinuity passing through an element. In order to provide a sterner test the latent heat release is increased to test 2 (L2)  $L = 260 \text{ kJ/kg}$ , similar results to the previous test are obtained for both temperature fields and non-physical capacitance comparisons between CVCM and NEM shown in Figure 5-3 and Figure 5-4, respectively. However, differences are apparent, i.e., the maximum temperature error is  $0.24^\circ \text{C}$  at the point  $x = y = z = 2.0 \text{ mm}$  and the maximum energy error norm is 0.143 located at the point  $x = y = z = 0.5 \text{ mm}$ . Although, the same mesh density has been kept for both test cases, the number of time steps was increased to  $N = 400$  as consequence of the increase in latent energy, which provokes a longer solidification time. Other results pertaining to the principal diagonal are shown in Table 5.1.

### 5.2.2 Results using a medium mesh density

The mesh density used is  $\Delta x = \Delta y = \Delta z = 1.0 \text{ mm}$ , which in term of number of elements gives 750 elements for a structure meshed domain. Initial and boundary conditions are kept constant for both test cases although, the time step size remain the same  $\Delta t = 0.005 \text{ s}$ , the number of time steps are  $N = 200$  and  $N = 400$  for the test 1 (L1) and test 2 (L2), respectively. For the test case (L1), the temperature field comparison along the principal diagonal points is shown in Figure 5-5, where the maximum temperature error is  $0.13^\circ \text{C}$  at the point  $x = y = z = 2.0 \text{ mm}$ . The non-physical variable comparison is shown in Figure 5-6, where the discontinuity has been tracked and annihilated along the principal diagonal and the maximum energy norm error is 0.44 located on the point  $x = y = z = 2.0 \text{ mm}$ . Similar response is found for the case test 2 (L2), where the temperature field is shown in Figure 5-7 and the maximum temperature error is  $0.51^\circ \text{C}$  at point  $x = y = z = 1.0 \text{ mm}$  however, for the non-physical capacitance shown in Figure 5-8 the maximum energy norm error is 1.32 located at the point  $x = y = z = 1.0 \text{ mm}$ , for other results along the principal diagonal see Table 5.1

### 5.2.3 Results using a coarse mesh density

In this case the mesh density used is  $\Delta x = \Delta y = \Delta z = 1.66 \text{ mm}$ , which in term of number of elements gives 162 elements for a structure meshed domain. Initial and boundary conditions are kept constant for both test cases although, the time step size remain the same  $\Delta t = 0.005 \text{ s}$ , the number of time steps are  $N = 200$  and  $N = 400$  for the test 1 (L1) and test 2 (L2), respectively. For the test case (L1), the temperature field comparison along the principal diagonal points is shown in Figure 5-9, where the maximum temperature error is  $0.13^\circ \text{C}$  at the point  $x = y = z = 2.0 \text{ mm}$ . The non-physical variable comparison is shown in Figure 5-10, where the discontinuity has been tracked and annihilated along the principal diagonal and the maximum energy norm error is 0.090 located on the point  $x = y = z = 2.0 \text{ mm}$ . Similar response is found for the case test 2 (L2), where the temperature field is shown in Figure 5-11 and the maximum temperature error is  $0.87^\circ \text{C}$  at point  $x = y = z = 0.0 \text{ mm}$  however, for the non-physical capacitance shown in Figure 5-12 the maximum energy norm error is 1.57 located at the point  $x = y = z = 2.0 \text{ mm}$ , for other results along the principal diagonal see Table 5.1

### 5.3 Solidification with multiple-discontinuities

Single and multiple discontinuous solidifications have been approximated using a narrow mushy solidification, which in chapter 4 has been analysed involving 1-D element, 1-D semi-infinite slab, 2-D semi-infinite corner and 3-D cube modelling. In this chapter the 3-D cube results are extended in order to provide a deeper understanding on the progression of the discontinuities along the principal diagonal in the single and multiple discontinuities cases. The process is modelled using the NEM that has been developed to deal with discontinuity annihilation but in this case (i.e. narrow mushy solidification) no discontinuities are involved. The results are contrasted against results obtained from the CVCM as no analytical solutions exist in this case.

Initial, boundary and latent heat release conditions are shown in Figure 4-11 and Figure 4-12, respectively. Although, different time steps and mesh densities were analysed in chapter 4 in the following sections the results are focused on the internal points along the principal diagonal for the 3-D cube for fine, medium and coarse mesh densities using a time step  $\Delta t = 0.005$  s over  $N = 300$  time steps. Material properties are shown in Table 4.1 column 2 correspond to Zamak-5. Although Zamak-5 is an alloy without discontinuities present, in order to compare both techniques, for the single discontinuity the temperature of transition is taken as  $T_{r_1} = 386^\circ\text{C}$  and for the multi-discontinuous case the temperatures of transition are  $T_{r_1} = 380^\circ\text{C}$  and  $T_{r_2} = 386^\circ\text{C}$ , where the latent heat release distribution are shown in Figure 4-12. Identical values of latent heat release are used despite the slightly different transition temperatures.

#### 5.3.1 Results using a fine mesh

The number of elements used is 6000 using a structured mesh with a mesh density of  $\Delta x = \Delta y = \Delta z = 0.5$  mm. The temperature field comparison between the single discontinuity solidification modelled with NEM and the mushy solidification modelled with CVCM clearly indicates an increase in the temperature error norm, see Table 5.2, where performance data for Isothermal, Multi-discontinuous and Mushy solidification is provided. This corresponds with the evaluation point along the principal diagonal in the 3-D cube however, if the comparison is made between the multi-discontinuous solidification modelled with NEM and the mushy solidification the magnitude of the error decreases but follows the same tendency like on the previous comparison, these are shown in Figure 5-13 and Table 5.2. The non-physical capacitance comparison shows the consistency from the

NEM to identify and annihilate the discontinuity for both cases, single and multi-discontinuous solidification, along the principal diagonal for the 3-D cube, see Figure 5-14.

### 5.3.2 Results using a medium mesh

The number of elements used is 750 using a structured mesh with a mesh density of  $\Delta x = \Delta y = \Delta z = 1.0 \text{ mm}$ . The temperature field comparison between the single discontinuity solidification modelled with NEM and the mushy solidification modelled with CVCM indicates an increase in the temperature error norm (see Table 5.2). This corresponds to the evaluation point along the principal diagonal in this case the magnitude of the error is not as high as in the previous case. If the comparison is made between the multi-discontinuous solidification modelled with NEM and the mushy solidification the magnitude of the error decreases even more but still follows the same tendency, these are shown in Figure 5-15 and Table 5.2. The non-physical capacitance comparison shows the consistency from the NEM to identify the discontinuity and annihilated for both cases, single and multi-discontinuous solidification, along the principal diagonal for the 3-D cube; see Figure 5-16.

### 5.3.3 Results using a coarse mesh

The number of elements used is 162 using a structured mesh with a mesh density of  $\Delta x = \Delta y = \Delta z = 1.66 \text{ mm}$ . The temperature field comparison among the single discontinuity solidification modelled with NEM, the mushy solidification modelled with CVCM and the multi-discontinuous solidification modelled with NEM shows a definite close agreement although, the maximum temperature error is found between the single discontinuity and the mushy solidifications, which is  $3.79^\circ \text{C}$  at point  $x = y = z = 0.0 \text{ mm}$  these are shown in Figure 5-17 and Table 5.2. The non-physical capacitance comparison shows the consistency from the NEM to identify the discontinuity and annihilate it, which is expected from the theory; see Figure 5-18.

## 5.4 Solidification involving two discontinuities with narrow and wide mushy zone

Single discontinuity and multi-discontinuities have been analysed in chapter 3 and chapter 4 with extended results on the previous two sections in this chapter. However, it is of interest to explore the influence of the mushy zone size in combination with discontinuous solidification. Three different cases are presented in order to provide further evidence to ascertain NEM capabilities to identify correctly any discontinuity present in the



solidification process regardless the transition zone size. In Appendix B is presented further details for the specific application of the NEM to this section

#### 5.4.1 Two discontinuities with narrow and wide mushy solidification for 1-D element

Consider the 1-D linear element depicted in Figure B-3 Solidification with phase discontinuities and associated regions in a linear element subjected to a prescribed temperature field to highlight the differences between  $\hat{c}^e$  and  $\hat{c}_{cvcm}^e$  when dealing with two defined discontinuities with narrow and wide mushy zones and when subjected to a decreasing temperature field. In this test  $T_2^{n+1} = T_1^{n+1} + T_{diff}$ , where  $T_1$  and  $T_2$  are nodal temperatures and  $T_{diff}$  is the temperature difference between the nodes of the element. The temperature difference between the nodes is set to: 10, 15 and 20°C and  $T_1^n = T_{liq} + 5$  with  $T_{liq} - 120 \leq T_1^{n+1} < T_{liq} + 5$ . The temperature range is selected to ensure the material is initially liquid and ends up completely solid. The material properties are given in the first column of Table 5.3, under the heading of material 1 and are approximately those for Al-4.5%Cu. However, in order to highlight the annihilation of source terms latent heat release is assumed to occur at the two transition boundaries, which define the mushy zone between the temperatures where latent heat is released and material phase is changed. In the narrow case the transition temperatures are  $T_{r_1} = 621^\circ\text{C}$  and  $T_{r_2} = 646^\circ\text{C}$  and for the wide case  $T_{r_1} = 548^\circ\text{C}$  and  $T_{r_2} = 646^\circ\text{C}$ . The magnitudes of the latent heat release in terms of the total latent heat release are set to  $L_1 = 0.15L$  and  $L_2 = 0.35L$  for demonstration purposes for both cases.

Depicted in Figure 5-19 and Figure 5-20 are the non-physical capacitances  $\hat{c}_{cvcm}^e$  and  $\hat{c}^e$  for the CVCm and the NEM respectively. It is evident on comparison of Figure 5-19 and Figure 5-20 that the variation of  $\hat{c}_{cvcm}^e$  is significantly greater than that of  $\hat{c}^e$  obtained from equation (4.52). This illustrates that the two discontinuities have been effectively removed with the presence of the term  $\int_{t_n}^{t_{n+1}} \sum_{k \in K_e} \int_{\Gamma_k^e(t)} N_i \left[ \rho h \underline{v}_k^\times \cdot \underline{n} \right] d\Gamma dt$  in equation (4.52). This is demonstrated analytically in equations (B-3) and (B-4), see Appendix B but also demonstrated numerically in Figure 5-20.

The mushy zone size effect is evident on  $\hat{c}_{cvcm}^e$  and  $\hat{c}^e$  is greater for the narrow case as the latent heat release or transition of the material phases happens on a narrow temperature

interval as opposed to the wider case, see Figure 5-19 and Figure 5-20. Note that the values  $\rho_s c_s = 2.52 \text{ MJ/m}^3 \text{ } ^\circ\text{C}$  and  $\rho_\ell c_\ell = 2.75 \text{ MJ/m}^3 \text{ } ^\circ\text{C}$  can be contrasted against the numerical values provided in Figure 5-20 to illustrate the effectiveness of the discontinuity annihilation.

#### 5.4.2 1-D semi-infinite slab domain with two discontinuities and linear mushy solidification, narrow and wide

Solidification of a semi-infinite slab with a fixed temperature boundary condition and two defined discontinuities with narrow and wide mushy zone, the latent heat release distribution as in the previous example has no known analytical solution, hence the NEM is contrasted against the CVCM which has been extensively tested [115, 116]. The mesh used for the test is depicted in Figure 5-21 along with boundary and initial conditions. The material properties are given in the first column of the Table 5.3, which are those for Al-4.5%Cu. For the narrow case, temperature histories, profiles and information on the non-physical capacitances are provided in Figure 5-22 to Figure 5-24 and for the wide case on Figure 5-25 to Figure 5-27, for different locations along the slab. Excellent accuracy for temperature histories and profiles for both the NEM and CVCM is obtained, for the narrow case can be seen in Figure 5-22 and Figure 5-23 and for the wide case in Figure 5-25 and Figure 5-26. The behaviour of the non-physical capacitances  $\hat{c}_{\text{cvcm}}^e$  and  $\hat{c}^e$  are shown in Figure 5-24 and Figure 5-27, which mirrors that shown in Figure 5-19 and Figure 5-20. The two spikes for each point chosen in value of  $\hat{c}_{\text{cvcm}}^e$  correspond with the discontinuities passing through the elements at the stipulated spatial locations, which in the narrow and wide cases are influenced and connected with the continuous mushy zone. The behaviour of  $\hat{c}^e$  appears to match only in the section of the plots where the enthalpy distribution is continuous and illustrates the effectiveness of procedure for discontinuity annihilation.

#### 5.4.3 3-D cube domain with linear mushy solidification, narrow and wide, and two discontinuities present

The solidification of a cube is considered where mesh boundary, initial conditions and latent heat release for the narrow and wide mushy zone are depicted in Figure 5-28 and Figure 5-29, respectively. Although an analytical solution is unavailable, different time steps and mesh densities are tested to ascertain the relative sensitivities of the CVCM and the NEM. Although, annihilation of multiple-discontinuities is the main concern of this

research, a series of tests were chosen in order to realise the feasibility of representing a complicated solidification process involving narrow or wide mushy with multiple discontinuities. It is expected that this approach is adequate for: a) rapid solidification where the transition zone appears narrow and b) slow solidification where the transition zone appears wide on the spatial scale.

Given in Table 5.4 and Table 5.5 are the approximate program execution times for each of the methods along with results pertaining to the two error norms

$$\max_{i,n} |T_i^n - T_i^{nb}|, \quad \max_{i,n} \left| \frac{E^n - E^{nb}}{E_{total}^{nb}} \right| \times 100$$

where  $i$  and  $n$  represents the nodal position along the cube diagonal and time step, respectively. Moreover,  $T_i$  and  $E$  are the nodal temperature and the energy loss from the cube surface, respectively. The subscript  $b$  indicates benchmark values, which since no analytical solution are available, are taken as the results obtained using NEM with  $\Delta x = 0.50$  mm (6000 elements) and  $\Delta t = 0.005$  s for both narrow and wide mushy solidification with the discontinuities involved. The tests were performed using an implicit Euler time-stepping algorithm and the non-linear equations were solved using a bisection method. The material properties are taken from column 2 in Table 5.3, which corresponds to Zamak-5.

It is evident on comparison of Table 5.4 that comparable results are obtained for both methods with a slightly improved performance delivered by the NEM. The results shown in Table 5.4, Figure 5-30 and Figure 5-32 demonstrate the relative insensitivity of both methods to mesh density; however it is clear that coarse mesh results for the narrow mushy zone have a greater temperature error norm using either NEM or CVCM technique. Moreover, the energy loss and temperature errors norms presented in Table 5.4 shows a small discrepancy between fine and coarse meshes, which is further evidence of the benefits of a control volume transport equation methodology. It is of interest to note that in terms of program execution time; consistently the solidification processes modelled with NEM are faster than their counterpart modelled with CVCM. The behaviour of the non-physical capacitances  $\hat{c}^e$  and  $\hat{c}_{cvcm}^e$  is shown in Figure 5-31 and Figure 5-33 for an element at a specified location varying with mesh density for the three different solidification cases. The behaviour of  $\hat{c}^e$  is showing the anticipated smoothness continuity for the two discontinuities with narrow and wide mushy solidification, Figure 5-31 and Figure 5-33 respectively but again the non-physical nature of  $\hat{c}_{cvcm}^e$  is highlighted.

Temperature history comparison between the two discontinuities with narrow and wide mushy solidification processes is depicted in Figure 5-34, where it is possible to identify that the narrow mushy solidification modelling provides the greatest temperature error. However, the non-physical variable comparison, Figure 5-35, shows clearly the appealing non-uniqueness feature for the non-physical variable technique.

The temperature histories for the two discontinuities with narrow and wide mushy solidification using various time-steps are presented in Figure 5-36 and Figure 5-38 respectively. Comparable performance is delivered by the NEM and the CVCM methods in terms of similar results for temperature and energy error norms; however for the execution time, mixed results were obtained particularly when NEM outperforming CVCM for the smallest two time steps,  $\Delta t = 0.005\text{ s}$  and  $\Delta t = 0.25\text{ s}$ . However, this is not the case for the largest time steps,  $\Delta t = 0.1\text{ s}$  and  $\Delta t = 0.5\text{ s}$ , for both cases of two discontinuities with narrow and wide mushy solidification (see Table 5.5). The behaviour of the non-physical capacitances  $\hat{c}_{\text{cvcm}}^e$  and  $\hat{c}^e$  is shown in Figure 5-37 and Figure 5-39 for an element for various time steps for the two discontinuities with narrow and wide solidification.

Although, a particular feature of both methods is their extraordinary accuracy for relatively large time-steps, modelling the wide mushy with the two discontinuities the temperature error norm is slightly improved over the narrow mushy shown in Figure 5-40 and Table 5.5. This results because both methods maintain consistency between temperature and energy change, i.e. the energy lost from an element corresponds exactly with the temperature change unlike traditional capacitance and source-based methods. It is clear that the behaviour of  $\hat{c}^e$  is reasonably invariant as consequence of the ability of the NEM to annihilate both discontinuities in the heat flux at the phase front however is raised smoothly for the narrow or wide mushy solidification shown in the non-physical variable comparison Figure 5-41. Also highlighted is the non-physical nature of  $\hat{c}_{\text{cvcm}}^e$ , whose behaviour varies in a non-physical manner changing demonstrably with time-step.

Temperature histories at specified points along the diagonal of the cube on a fine mesh ( $\Delta x = 0.50\text{ mm}$ ) and relatively small time-step ( $\Delta t = 0.005\text{ s}$ ) are presented for the two discontinuities with narrow and wide mushy solidification in Figure 5-42 and Figure 5-44 respectively. A similar temperature profile is exhibited for the two cases, narrow and wide mushy, as time progresses. It is evident from the numerical evidence and again demonstrated in Figure 5-43 and Figure 5-45 for various points along the diagonal of the

cube, that the NEM removes the discontinuous behaviour regardless the number of discontinuities or the type of the transition zone present in the solidification process.

## **5.5 Conclusions**

From the extensive tests presented it is possible to conclude from the single-discontinuity results that despite the NEM and the CVCM reporting similar levels of accuracy for temperature and energy balance on a fine mesh, for medium and coarse meshes the NEM slightly outperforms the CVCM. However, consistency is the important feature from the results, which confirms the ability of the NEM to isolate and annihilate the source term from the solidification process regardless of the magnitude of latent heat release involved.

The comparison made between single-mushy and multidiscontinuous-mushy solidifications has provided information on the magnitude of errors involved. Energy and temperature errors are greater in the case where mushy solidification is used to approximate single-discontinuity solidification rather than multidiscontinuous solidification. Although, the temperature-error norm increases as the evaluation point moves along the principal diagonal, the maximum energy-error norm occurs at the start point when mesh is fine, however, this pattern is not repeated for the cases with medium and coarse meshes.

Transition zone size, narrow and wide, combined with two discontinuities has proved a stern example for the NEM, which independently from the size of the transition (mushy) zone identify and annihilate the discontinuities present in the solidification process.

Table 5.1 Performance data for Isothermal solidification

<b>MATERIAL PROPERTIES ZINC</b>					
Time step $\Delta t = 0.005s$					
	3-D cube modelled with a fine mesh				
	Points along the principal diagonal				
	x = 0.0 mm	x = 0.5 mm	x = 1.0 mm	x = 1.5 mm	x = 2.0 mm
	Test (L1) with L = 130 kJ/kg and N = 200 steps				
	Temperature error norm (°C)	0.07	0.08	0.09	0.12
	Energy loss error norm (%)	0.037	0.078	0.130	0.180
					0.055
	Test (L2) with L = 260 kJ/kg and N = 400 steps				
	Temperature error norm (°C)	0.14	0.11	0.20	0.19
	Energy loss error norm (%)	0.023	0.143	0.001	0.137
					0.005
	3-D cube modelled with a medium mesh				
	Points along the principal diagonal				
	x = 0.0 mm	x = 1.0 mm	x = 2.0 mm		
	Test (L1) with L = 130 kJ/kg and N = 200 steps				
	Temperature error norm (°C)	0.12	0.12	0.13	
	Energy loss error norm (%)	0.05	0.33	0.44	
	Test (L2) with L = 260 kJ/kg and N = 400 steps				
	Temperature error norm (°C)	0.23	0.51	0.18	
	Energy loss error norm (%)	0.05	1.32	0.6	
	3-D cube modelled with a coarse mesh				
	Points along the principal diagonal				
	x = 0.0 mm	x = 2.0 mm			
	Test (L1) with L = 130 kJ/kg and N = 200 steps				
	Temperature error norm (°C)	0.07	0.13		
	Energy loss error norm (%)	0.014	0.09		
	Test (L2) with L = 260 kJ/kg and N = 400 steps				
	Temperature error norm (°C)	0.87	0.77		
	Energy loss error norm (%)	0.17	1.57		

Note x means  $x = y = z$  for the co-ordinates along the principal diagonal on each cube

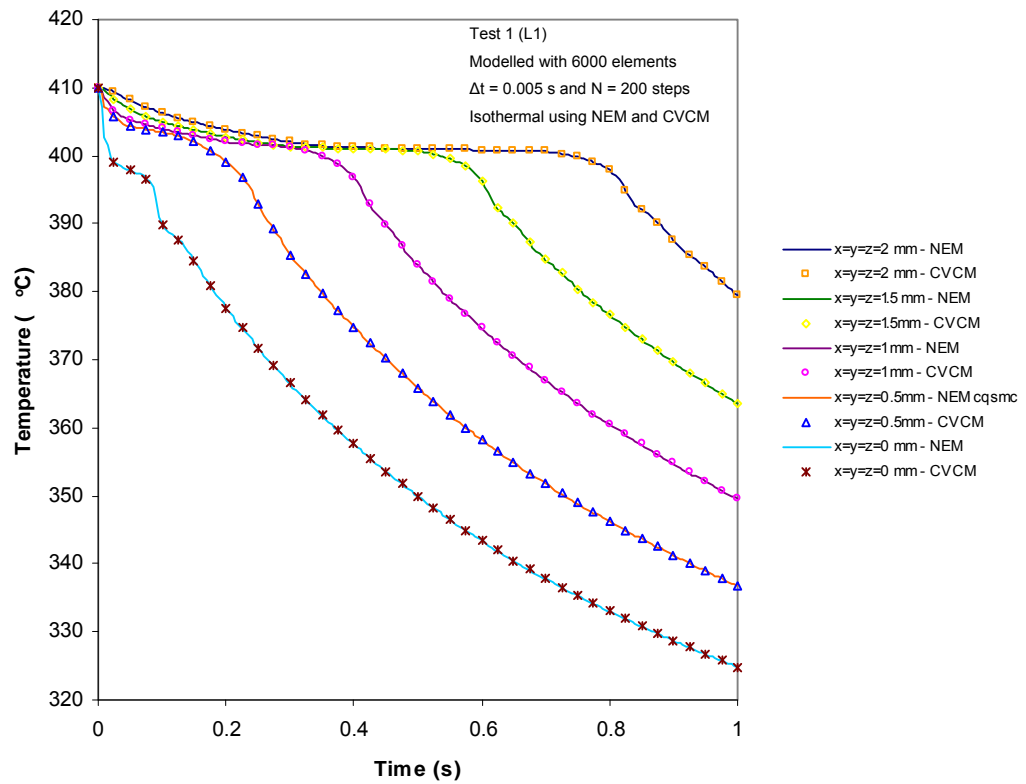


**Figure 5-1 Temperature history for isothermal solidification at different points along the diagonal of the cube for a fine mesh**

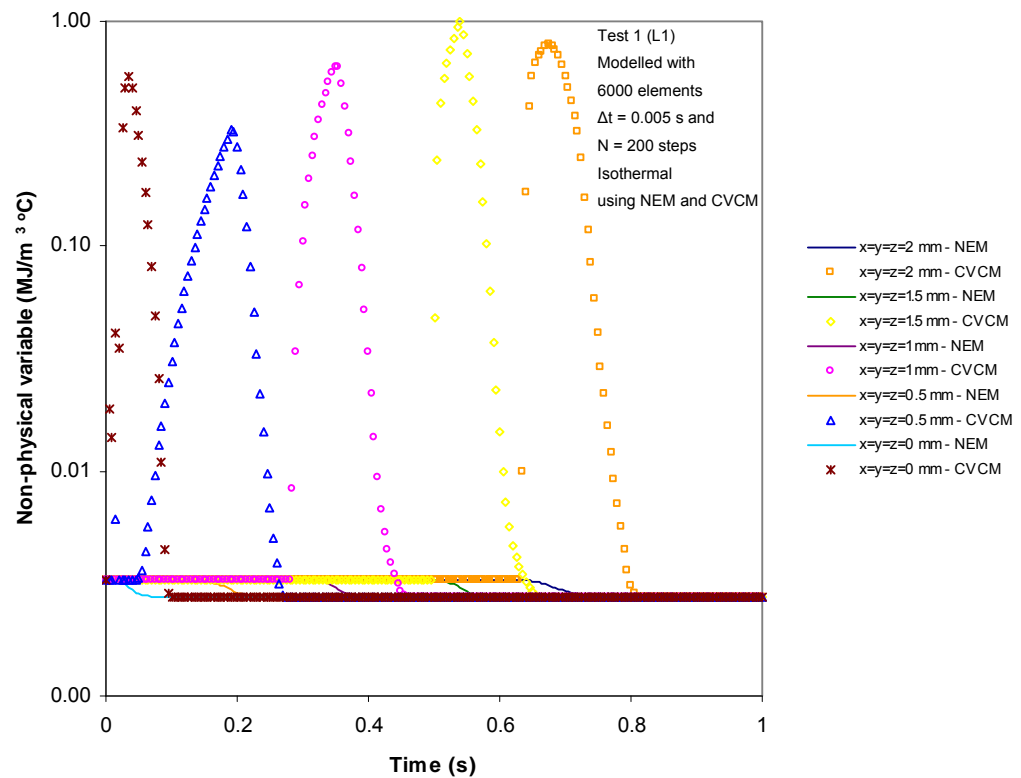


**Figure 5-2 Non-physical variable comparison for isothermal solidification along the diagonal of the cube for a fine mesh**

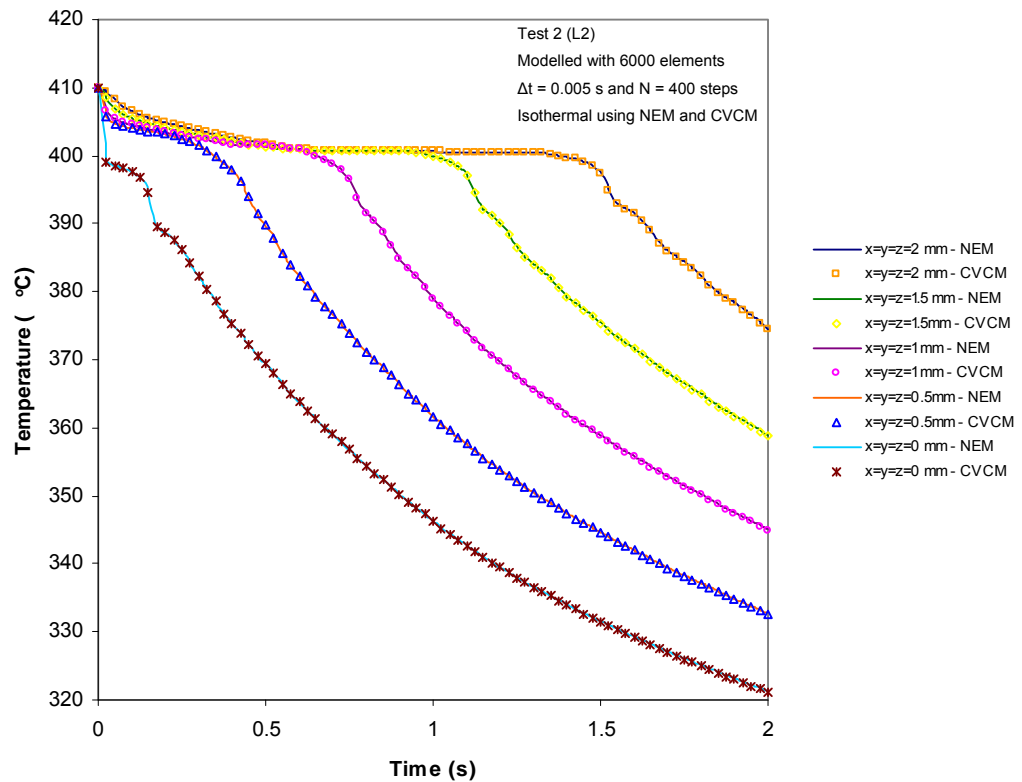


**Figure 5-3 Temperature history for isothermal solidification at different points along the diagonal of the cube for a fine mesh**

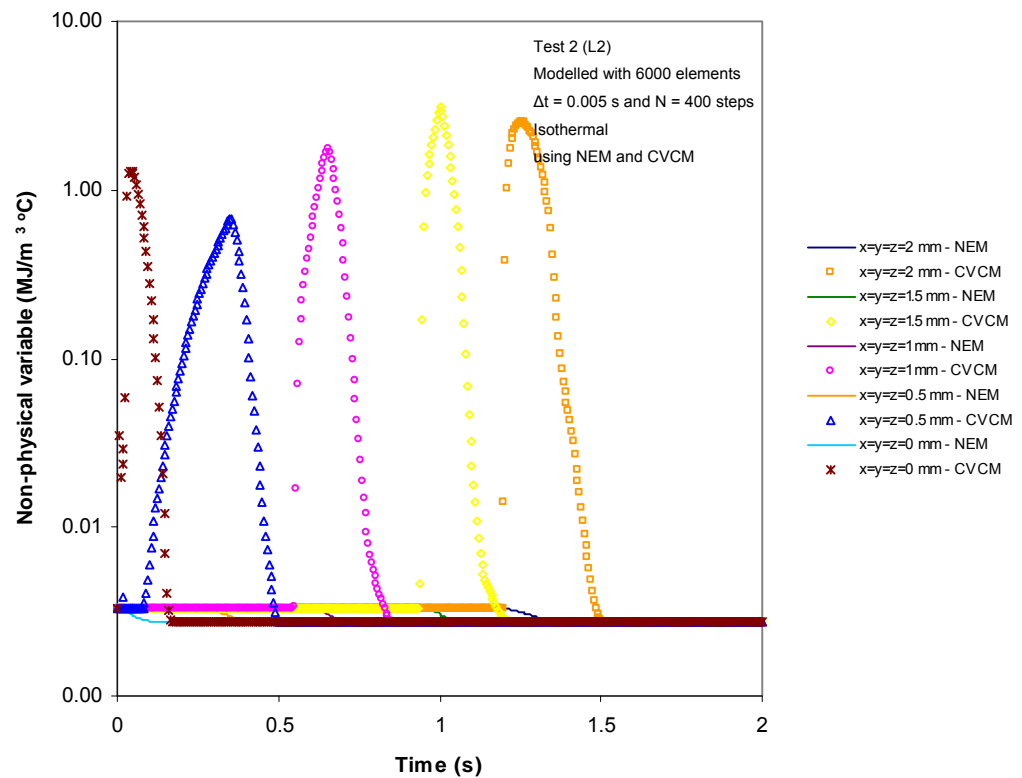


**Figure 5-4 Non-physical variable comparison for isothermal solidification along the diagonal of the cube for a fine mesh**



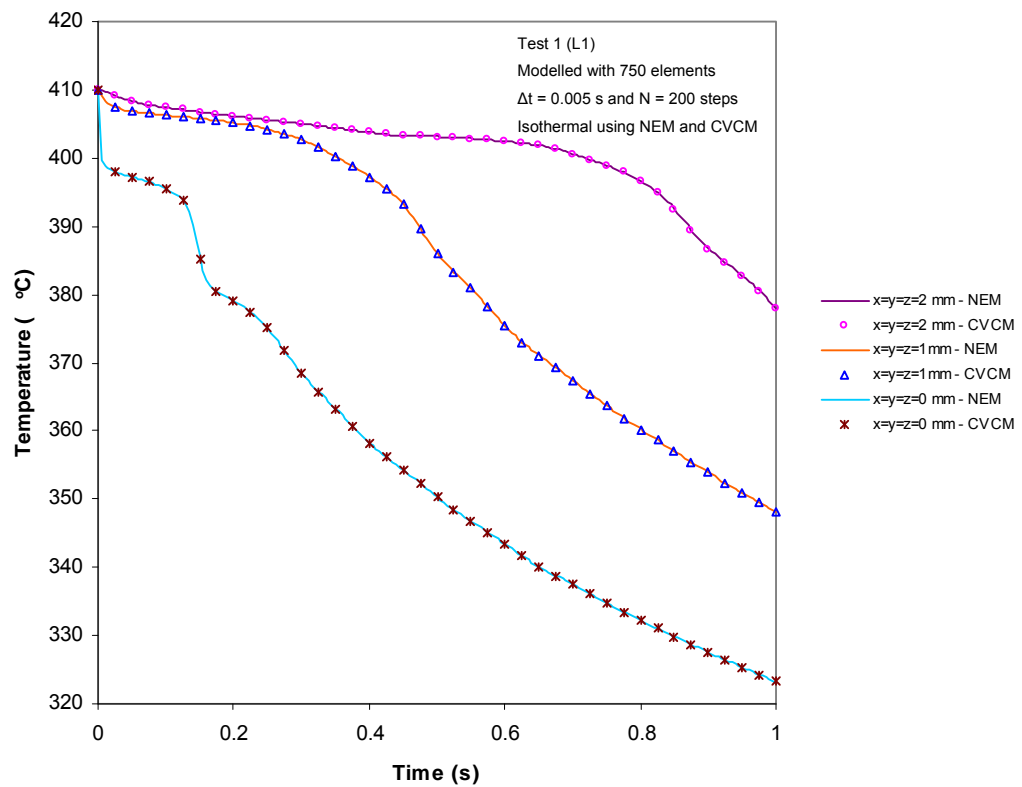


**Figure 5-5 Temperature history for isothermal solidification at different points along the diagonal of the cube for a medium mesh**

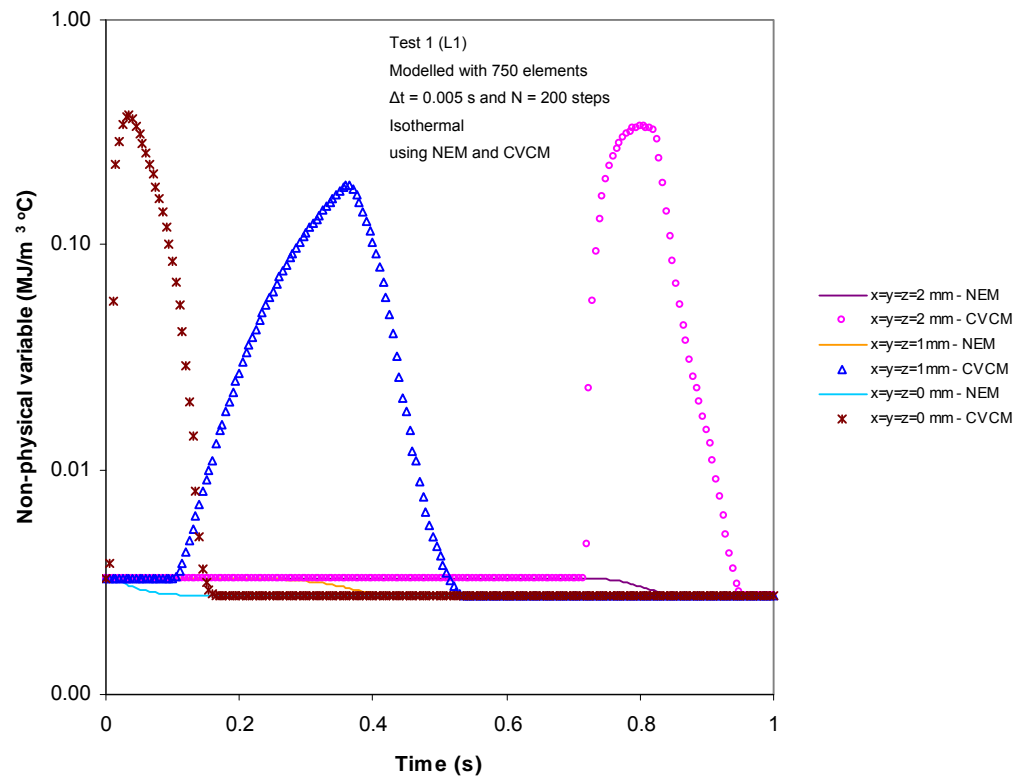


**Figure 5-6 Non-physical variable comparison for isothermal solidification along the diagonal of the cube for a medium mesh**

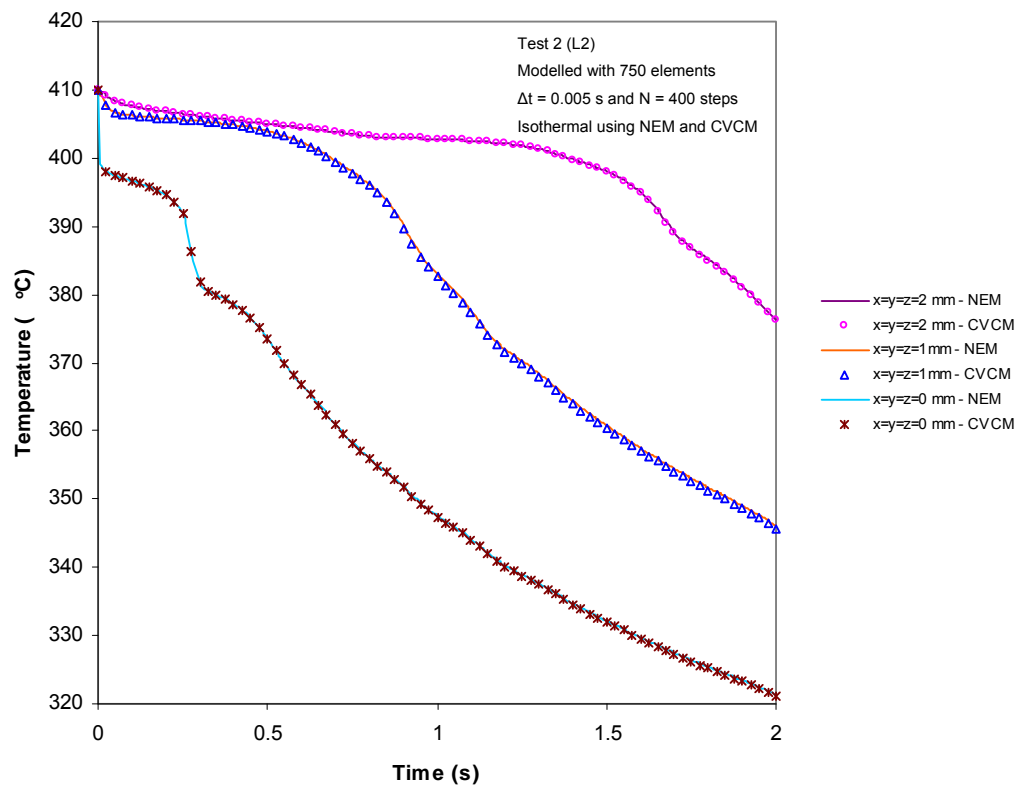


**Figure 5-7 Temperature history for isothermal solidification at different points along the diagonal of the cube for a medium mesh**

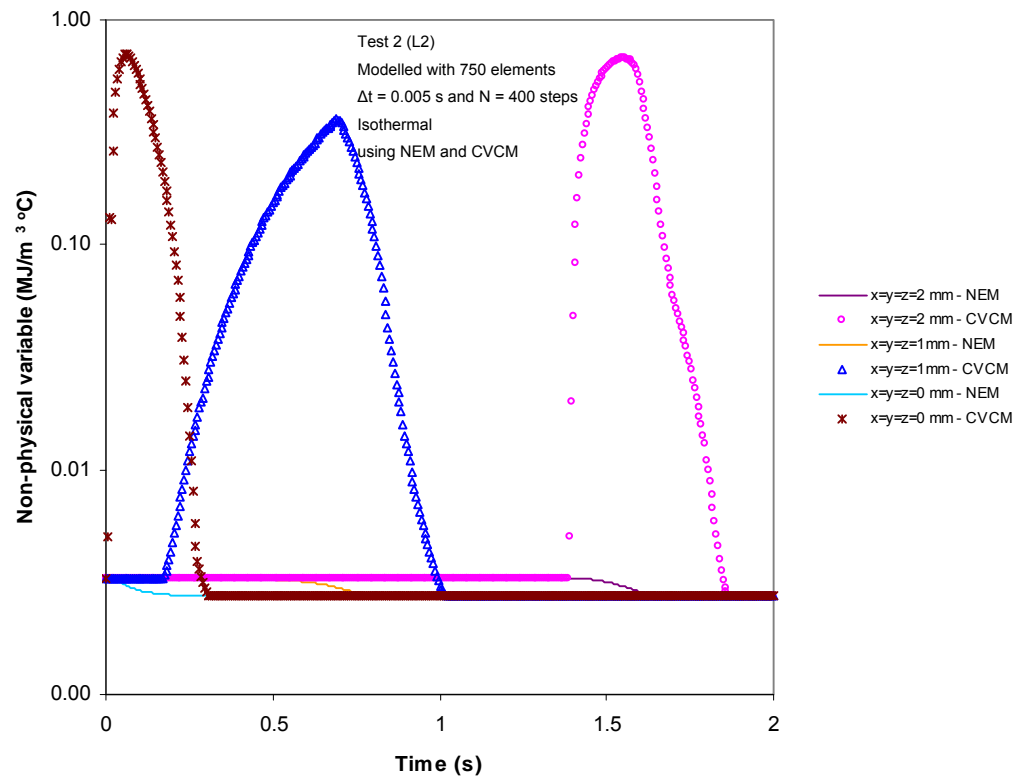


**Figure 5-8 Non-physical variable comparison for isothermal solidification along the diagonal of the cube for a medium mesh**

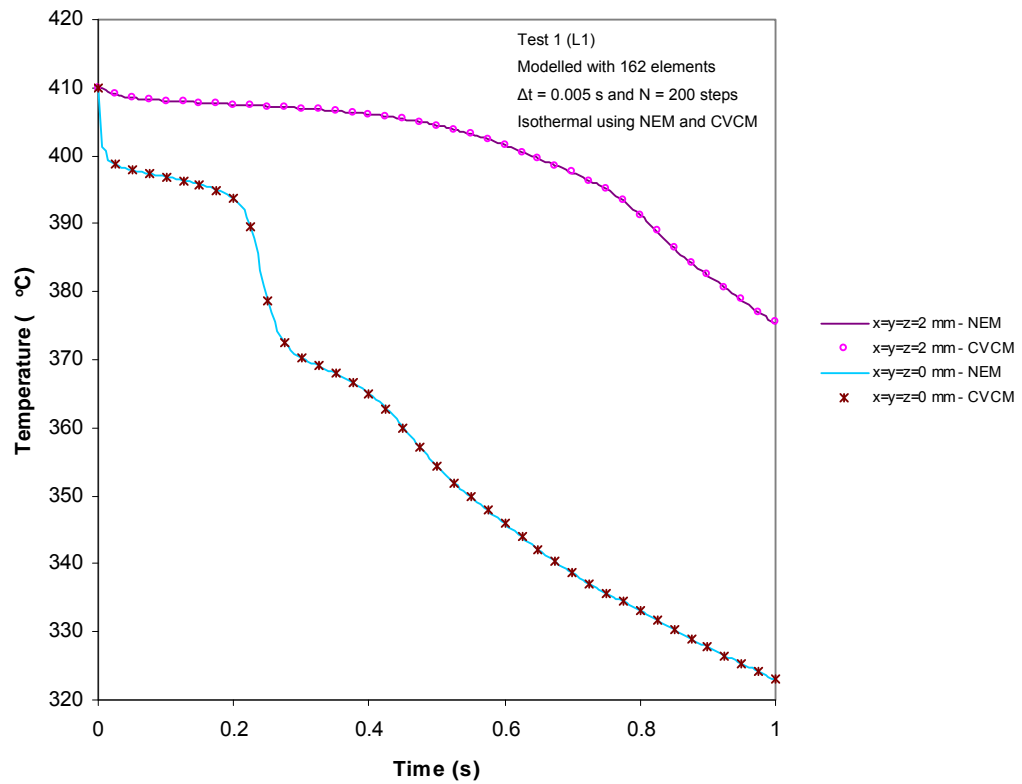


**Figure 5-9 Temperature history for isothermal solidification at different points along the diagonal of the cube for a coarse mesh**

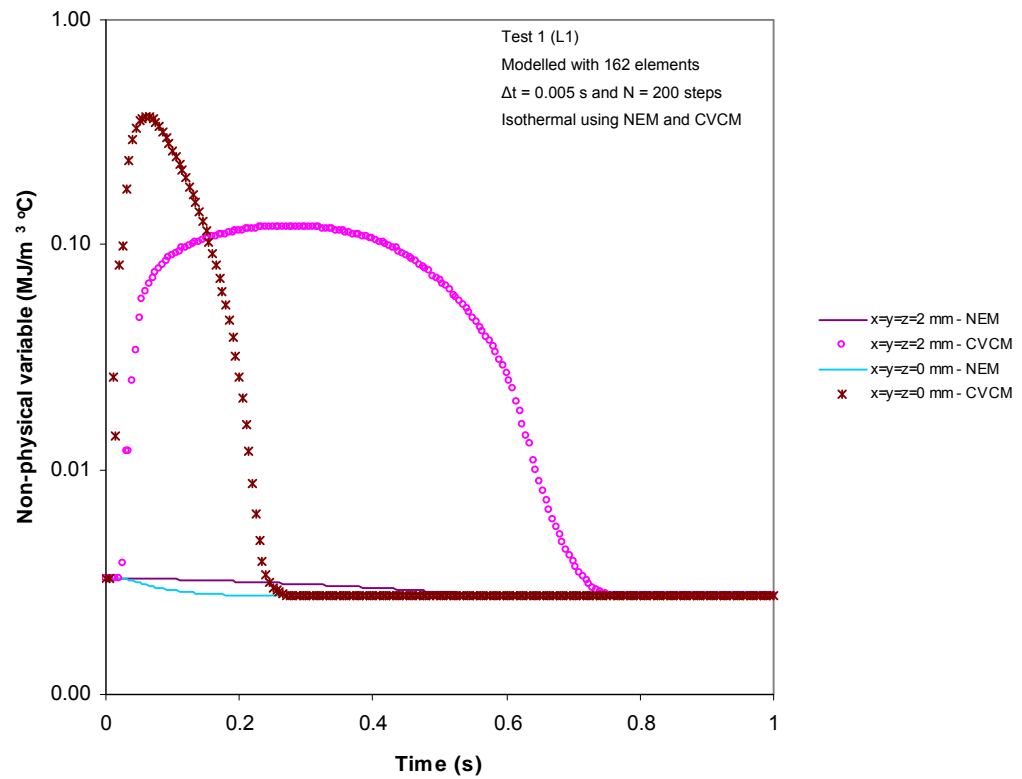


**Figure 5-10 Non-physical variable comparison for isothermal solidification along the diagonal of the cube for a coarse mesh**

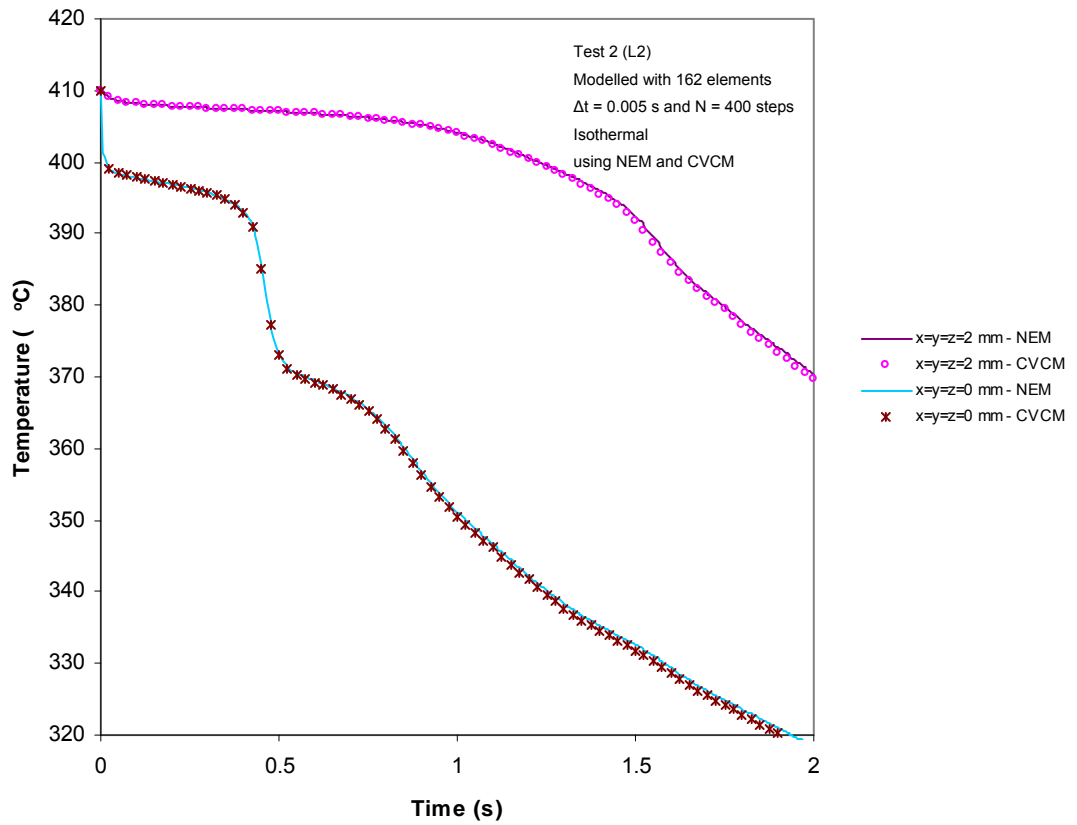


**Figure 5-11 Temperature history for isothermal solidification at different points along the diagonal of the cube for a coarse mesh**

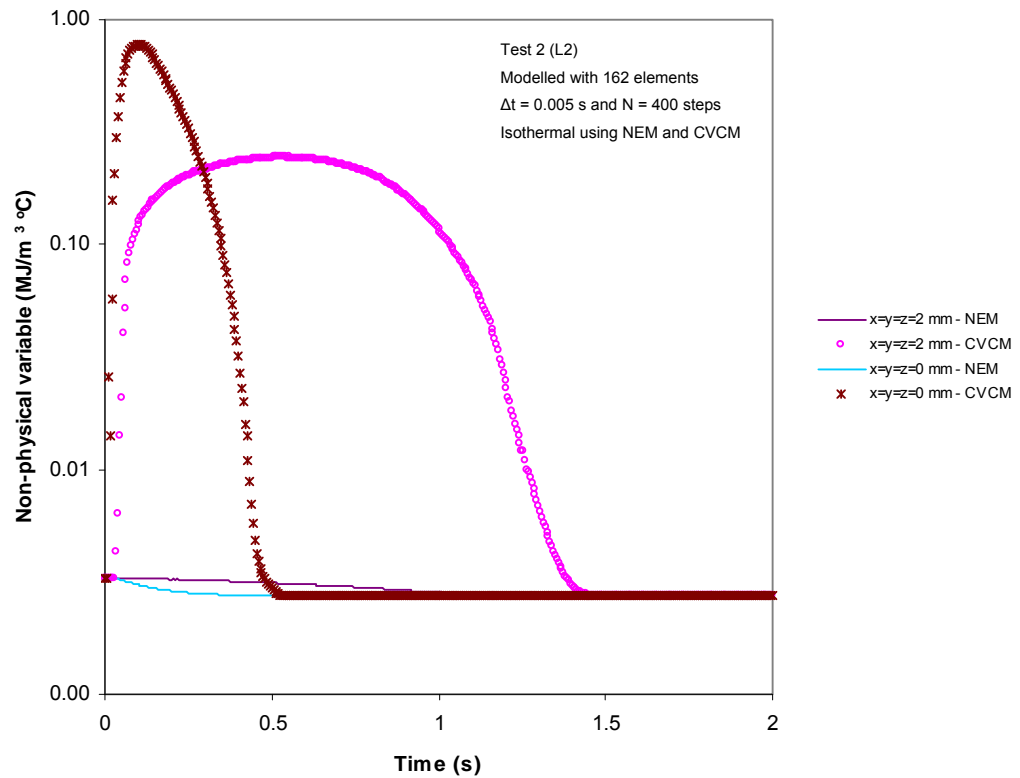


**Figure 5-12 Non-physical variable comparison for isothermal solidification along the diagonal of the cube for a coarse mesh**

Table 5.2 Performance data for Isothermal, Multi-discontinuous and Mushy solidification

MATERIAL PROPERTIES ZAMAK-5					
Time step $\Delta t = 0.005s$ and $N = 300$ steps					
	3-D cube modelled with a fine mesh				
	Points along the principal diagonal				
	x = 0.0 mm	x = 0.5 mm	x = 1.0 mm	x = 1.5 mm	x = 2.0 mm
	Isothermal (NEM) against Mushy (CVCM)				
Temperature error norm (°C)	4.25	4.90	5.66	6.58	7.64
Energy loss error norm (%)	23.29	11.67	11.51	14.49	8.03
	Multi-discontinuities (NEM) against Mushy (CVCM)				
Temperature error norm (°C)	1.08	1.24	1.52	1.33	1.70
Energy loss error norm (%)	24.12	8.47	9.92	7.11	0.98
	3-D cube modelled with a medium mesh				
	Points along the principal diagonal				
	x = 0.0 mm	x = 1.0 mm	x = 2.0 mm		
	Isothermal (NEM) against Mushy (CVCM)				
Temperature error norm (°C)	3.72	3.08	3.41		
Energy loss error norm (%)	1.17	9.31	6.30		
	Multi-discontinuities (NEM) against Mushy (CVCM)				
Temperature error norm (°C)	0.98	1.07	1.18		
Energy loss error norm (%)	2.65	4.51	5.13		
	3-D cube modelled with a coarse mesh				
	Points along the principal diagonal				
	x = 0.0 mm	x = 2.0 mm			
	Isothermal (NEM) against Mushy (CVCM)				
Temperature error norm (°C)	3.79	2.81			
Energy loss error norm (%)	0.0	5.08			
	Multi-discontinuities (NEM) against Mushy (CVCM)				
Temperature error norm (°C)	1.32	0.72			
Energy loss error norm (%)	2.86	4.01			

Note x means  $x = y = z$  for the co-ordinates along the principal diagonal on each cube

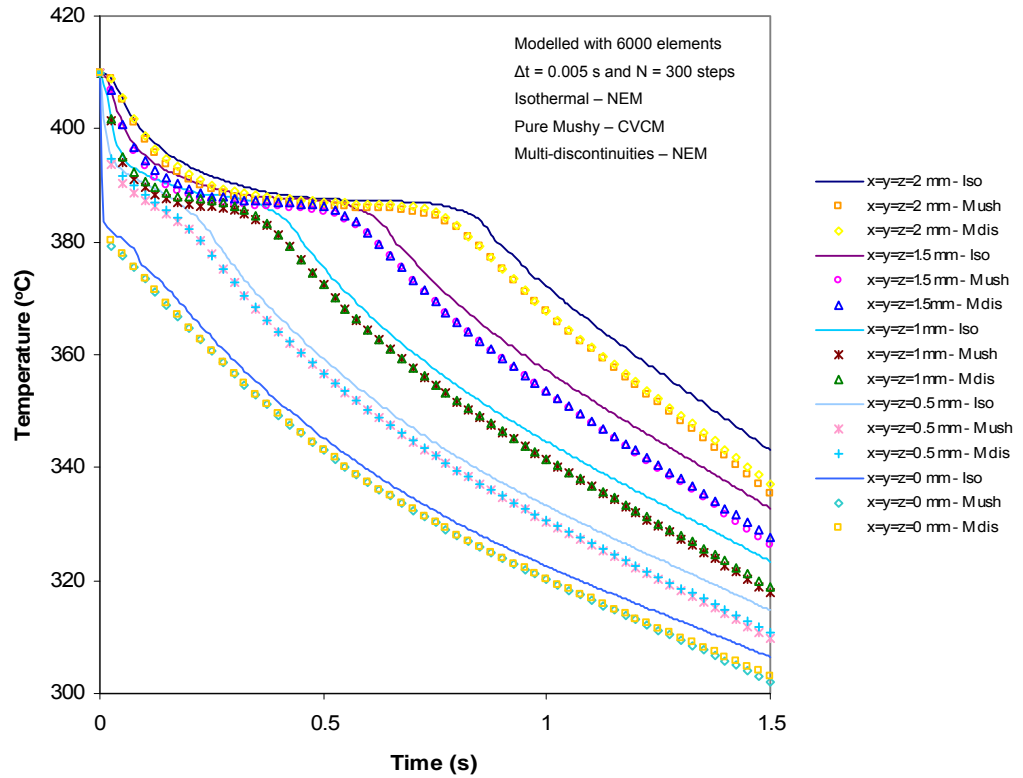


**Figure 5-13 Temperature history for Isothermal, Pure Mushy and Multi-discontinuities solidification along the diagonal of the cube for a fine mesh**

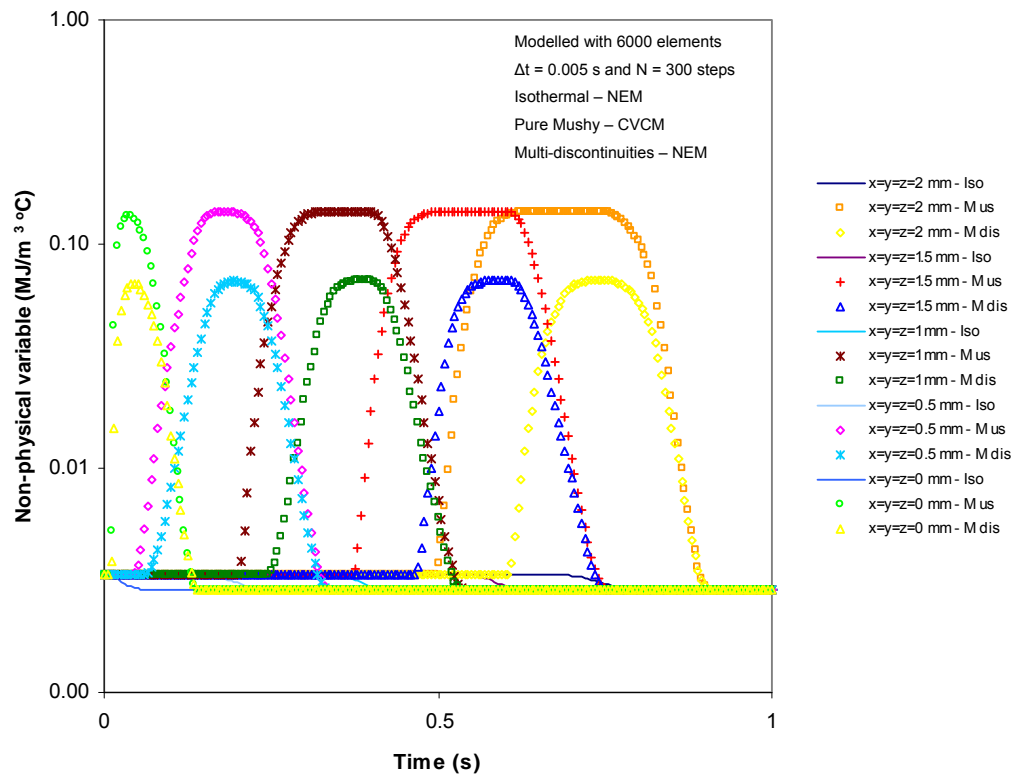


**Figure 5-14 Non-physical variable comparison for Isothermal, Pure Mushy and Multi-discontinuities solidification along the diagonal of the cube for a fine mesh**

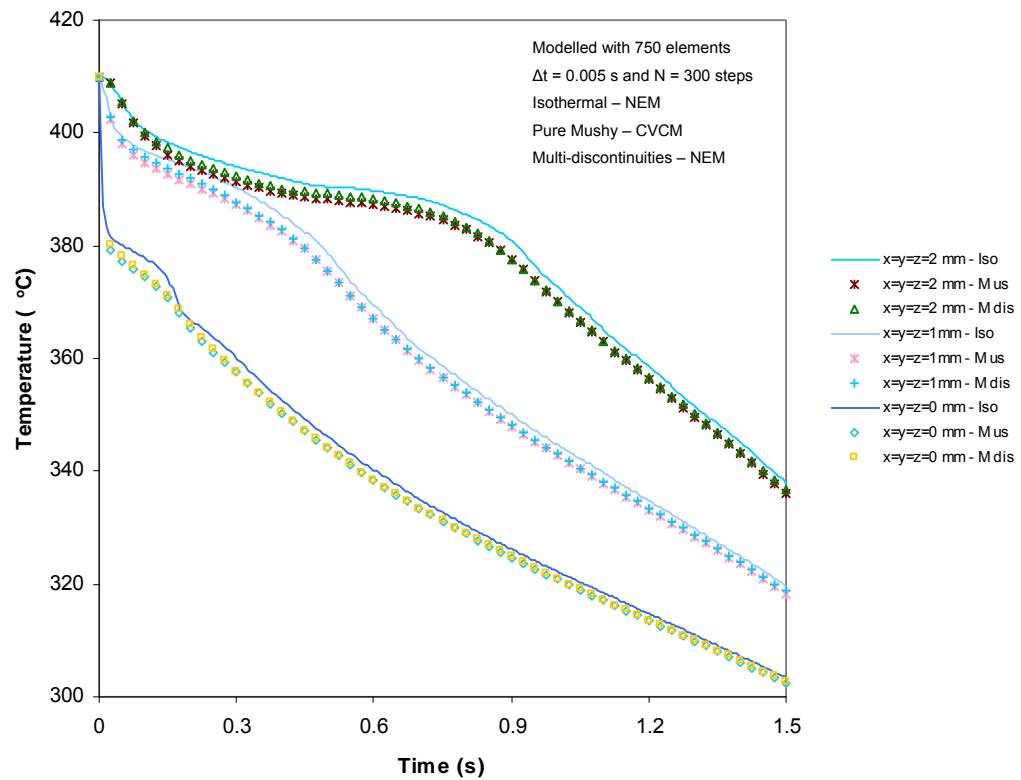


**Figure 5-15 Temperature history for Isothermal, Pure Mushy and Multi-discontinuities solidification along the diagonal of the cube for a medium mesh**

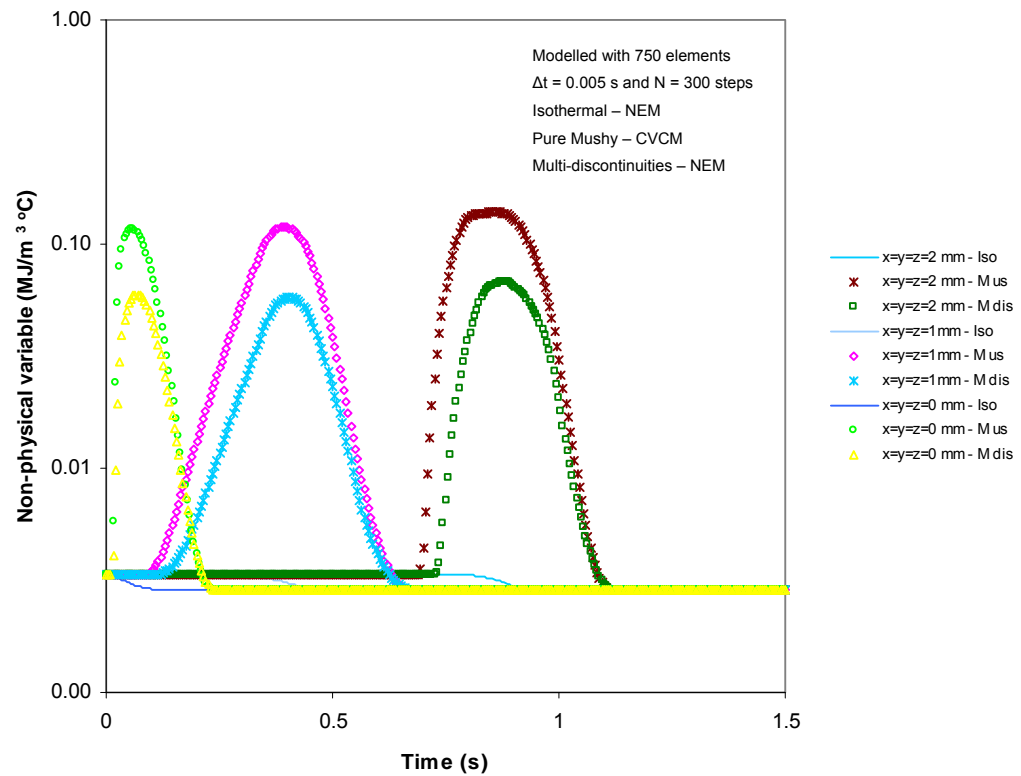


**Figure 5-16 Non-physical variable comparison for Isothermal, Pure Mushy and Multi-discontinuities solidification along the diagonal of the cube for a medium mesh**

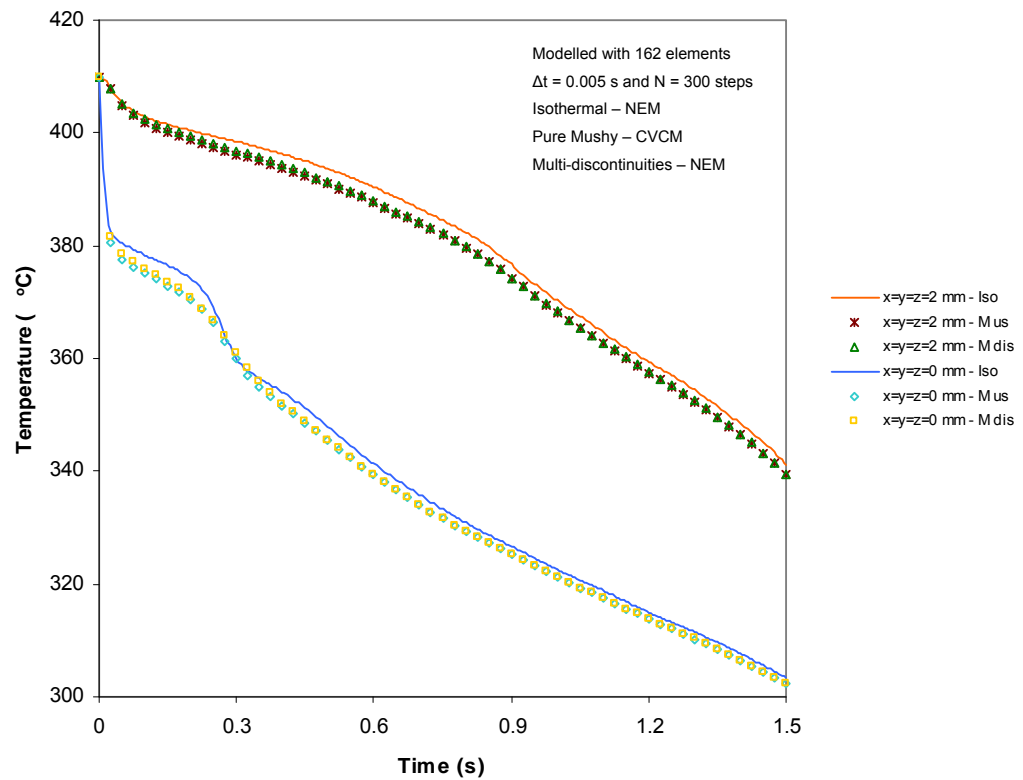


**Figure 5-17 Temperature history for Isothermal, Pure Mushy and Multi-discontinuities solidification along the diagonal of the cube for a coarse mesh**

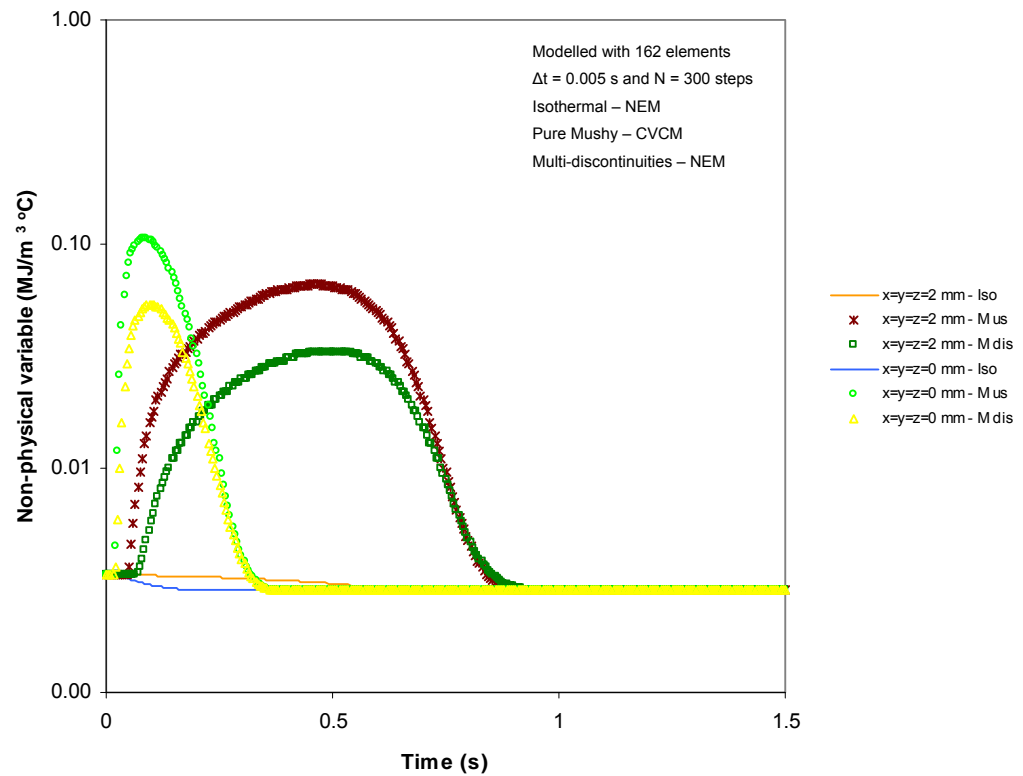


**Figure 5-18 Non-physical variable comparison for Isothermal, Pure Mushy and Multi-discontinuities solidification along the diagonal of the cube for a coarse mesh**



Table 5.3 Material properties for numerical test

Material Properties	units	Material 1 (Al-4.5%Cu)	Material 2 (Zamak-5)
Thermal conductivity – solid	$\frac{\text{W}}{\text{m}^\circ\text{C}}$	200	108
Thermal conductivity – liquid		90	50
Heat capacitance – solid	$\frac{\text{J}}{\text{kg}^\circ\text{C}}$	900	419
Heat capacitance – liquid		1100	505
Density – solid	$\frac{\text{kg}}{\text{m}^3}$	2800	6600
Density – liquid		2500	6800
Latent heat	$\frac{\text{kJ}}{\text{kg}}$	390	126
Solidus	$^\circ\text{C}$	548	380
Liquidus		646	386

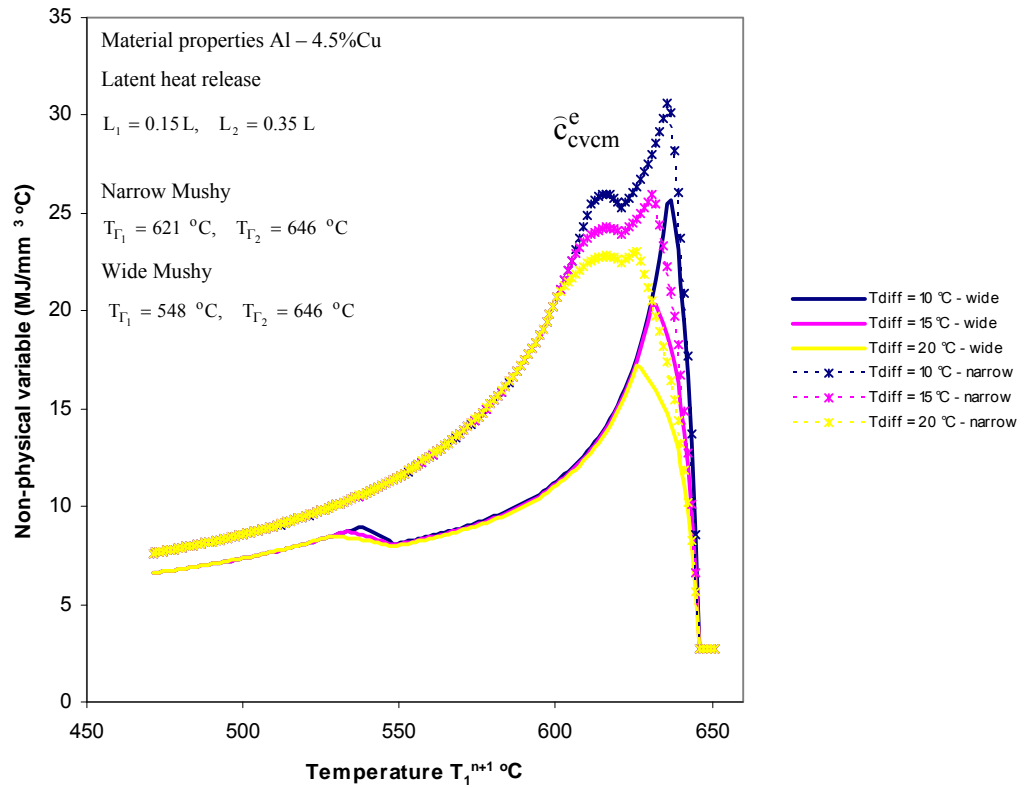
Table 5.4 Performance data for various mesh densities

<b>MATERIAL PROPERTIES ZAMAK-5</b>						
Time step $\Delta t = 0.005s$ and $N = 300$ steps						
	Two discontinuities with narrow mushy solidification; for latent heat release $L_1 = 0.15L$ and $L_2 = 0.35L$ and for temperatures at the phase-change $T_{\Gamma_1} = 380^\circ C$ and $T_{\Gamma_2} = 386^\circ C$					
	<b>CVCM</b>			<b>NEM</b>		
	$\Delta x = 0.50mm$	$\Delta x = 1.0mm$	$\Delta x = 1.67mm$	$\Delta x = 0.50mm$	$\Delta x = 1.0mm$	$\Delta x = 1.67mm$
Nodes in solid phase	1225	196	58	1225	196	58
Program execution time (s)	36.67	5.031	2.22	34.33	4.875	2.03
Temperature error norm (oC)	0.45	3.49	8.15	benchmark	3.48	8.13
Energy loss error norm (%)	0.408	1.063	2.535	benchmark	1.063	2.289
	Two discontinuities with wide mushy solidification; for latent heat release $L_1 = 0.15L$ and $L_2 = 0.35L$ and for the temperatures at the phase-change $T_{\Gamma_1} = 340^\circ C$ and $T_{\Gamma_2} = 386^\circ C$					
	<b>CVCM</b>			<b>NEM</b>		
	$\Delta x = 0.50mm$	$\Delta x = 1.0mm$	$\Delta x = 1.67mm$	$\Delta x = 0.50mm$	$\Delta x = 1.0mm$	$\Delta x = 1.67mm$
Nodes in solid phase	939	156	47	945	156	47
Program execution time (s)	39.37	5.141	1.984	36.81	4.922	2.0
Temperature error norm (oC)	0.35	2.86	6.25	benchmark	2.86	6.25
Energy loss error norm (%)	0.540	0	0.630	benchmark	0.09	0.630

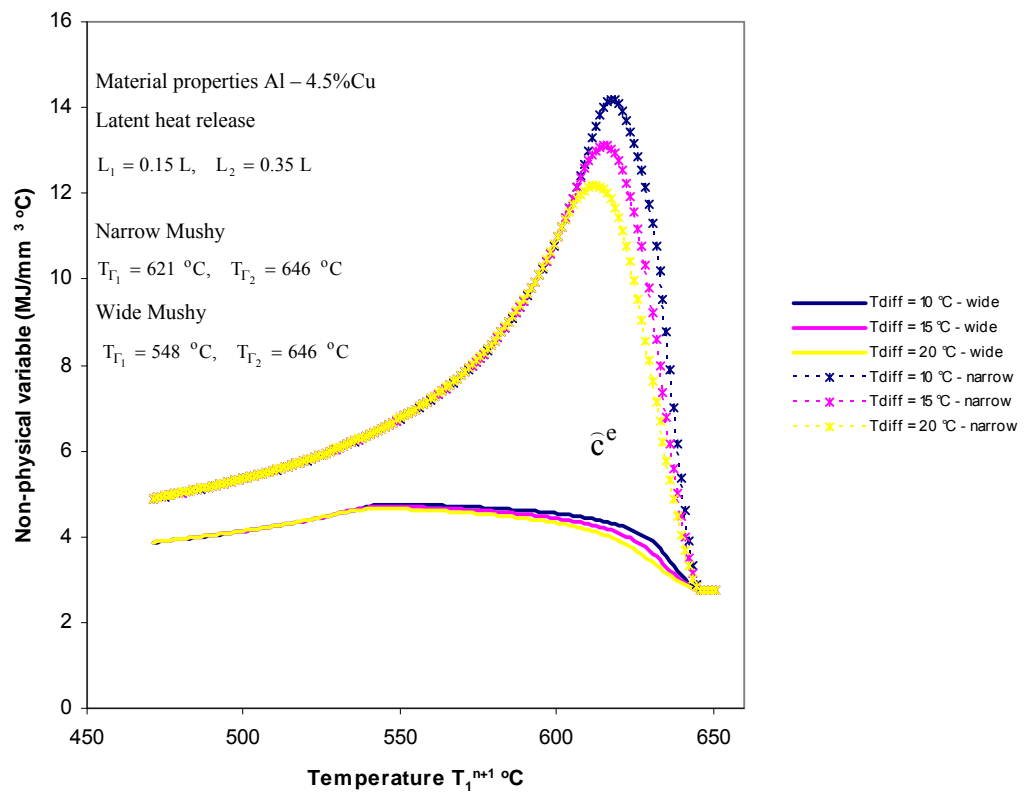
Note  $\Delta x$  means  $\Delta x = \Delta y = \Delta z$  for the mesh density on each cube

Table 5.5 Performance data for various time-steps

<b>MATERIAL PROPERTIES ZAMAK-5</b>					
Benchmark cube modelled with tetrahedron $\Delta x = \Delta y = \Delta z = 0.50\text{mm}$ with 6000 elements using time step $\Delta t = 0.005\text{s}$ and $N = 300$ steps for two discontinuities with narrow and wide mushy solidification					
	Cube modelled with tetrahedron $\Delta x = \Delta y = \Delta z = 1.00\text{mm}$ with 750 elements Two discontinuities with narrow mushy solidification; for latent heat release $L_1 = 0.15L$ and $L_2 = 0.35L$ and for temperatures at the phase-change $T_{R_1} = 380^\circ\text{C}$ and $T_{R_2} = 386^\circ\text{C}$				
		$\Delta t = 0.005\text{s}$ $N = 300$ steps	$\Delta t = 0.25\text{s}$ $N = 60$ steps	$\Delta t = 0.1\text{s}$ $N = 15$ steps	$\Delta t = 0.5\text{s}$ $N = 3$ steps
CVCN	Nodes in solid phase	196	193	177	129
	Program execution time (s)	5.031	0.625	0.3438	0.4531
	Temperature error norm (oC)	3.49	3.87	7.62	11.38
	Energy loss error norm (%)	1.063	1.390	3.598	1.798
NEM	Nodes in solid phase	196	193	177	129
	Program execution time (s)	4.875	0.6175	0.4062	0.4688
	Temperature error norm (oC)	3.48	3.87	7.62	11.39
	Energy loss error norm (%)	1.063	1.390	3.598	1.798
	Cube modelled with tetrahedron $\Delta x = \Delta y = \Delta z = 1.00\text{mm}$ with 750 elements Two discontinuities with wide mushy solidification; for latent heat release $L_1 = 0.15L$ and $L_2 = 0.35L$ and for temperatures at the phase-change $T_{R_1} = 340^\circ\text{C}$ and $T_{R_2} = 386^\circ\text{C}$				
		$\Delta t = 0.005\text{s}$ $N = 300$ steps	$\Delta t = 0.25\text{s}$ $N = 60$ steps	$\Delta t = 0.1\text{s}$ $N = 15$ steps	$\Delta t = 0.5\text{s}$ $N = 3$ steps
CVCN	Nodes in solid phase	156	150	129	38
	Program execution time (s)	5.141	2.828	0.3906	0.3125
	Temperature error norm (oC)	2.86	2.64	3.99	8.11
	Energy loss error norm (%)	0	0.180	2.160	4.95
NEM	Nodes in solid phase	156	150	129	38
	Program execution time (s)	4.922	2.438	0.4062	0.3594
	Temperature error norm (oC)	2.86	2.64	3.99	8.11
	Energy loss error norm (%)	0.09	0.180	2.160	4.95



**Figure 5-19 Non-physical variable (CVCM) comparison for multi-discontinuous narrow and wide mushy solidification for 1-D element**



**Figure 5-20 Non-physical variable (NEM) comparison for multi-discontinuous narrow and wide mushy solidification for 1-D element**

## 1-D SEMI-INFINITE SLAB PROBLEM

$$k \frac{\partial T}{\partial x}(0) = h(T_{\text{amb}} - T)$$

$$T_{\text{amb}} = 0^\circ\text{C}, T_{\text{init}} = 660^\circ\text{C}$$

$$h = 10^4 \text{ W/m}^2\text{C}$$

$$\frac{\partial T}{\partial x}(60) = 0$$

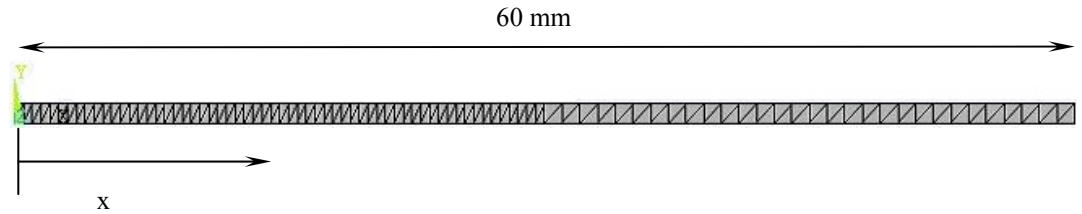


Figure 5-21 Mesh for 1-D semi-infinite slab problem

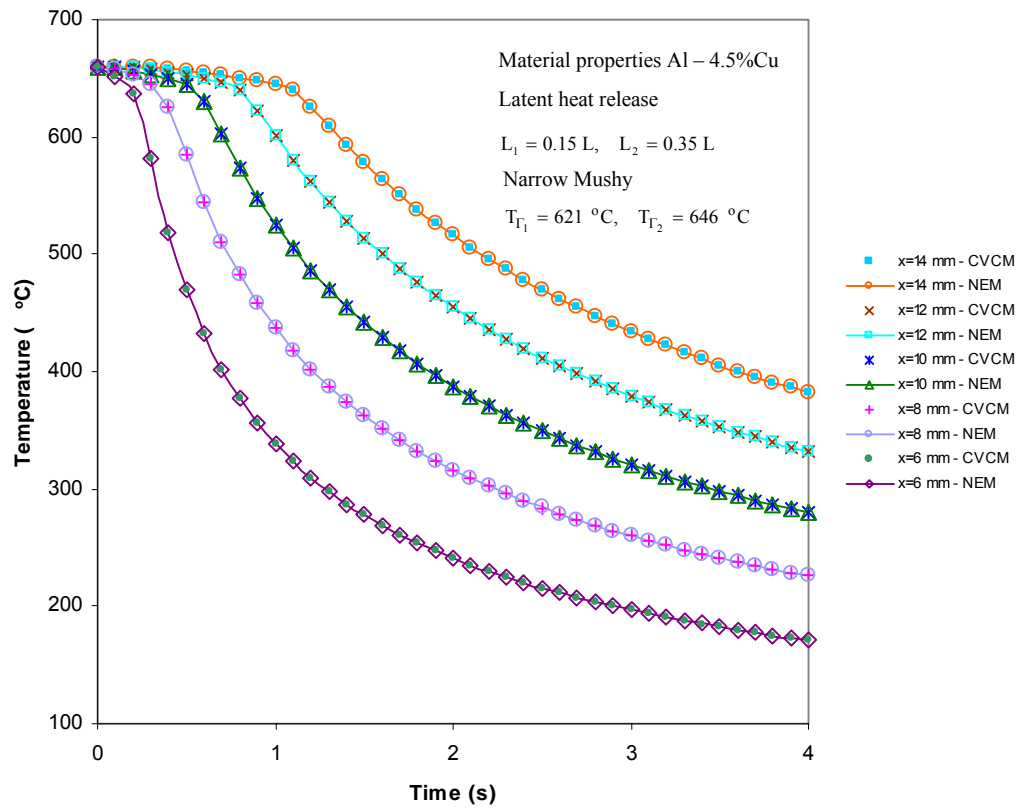
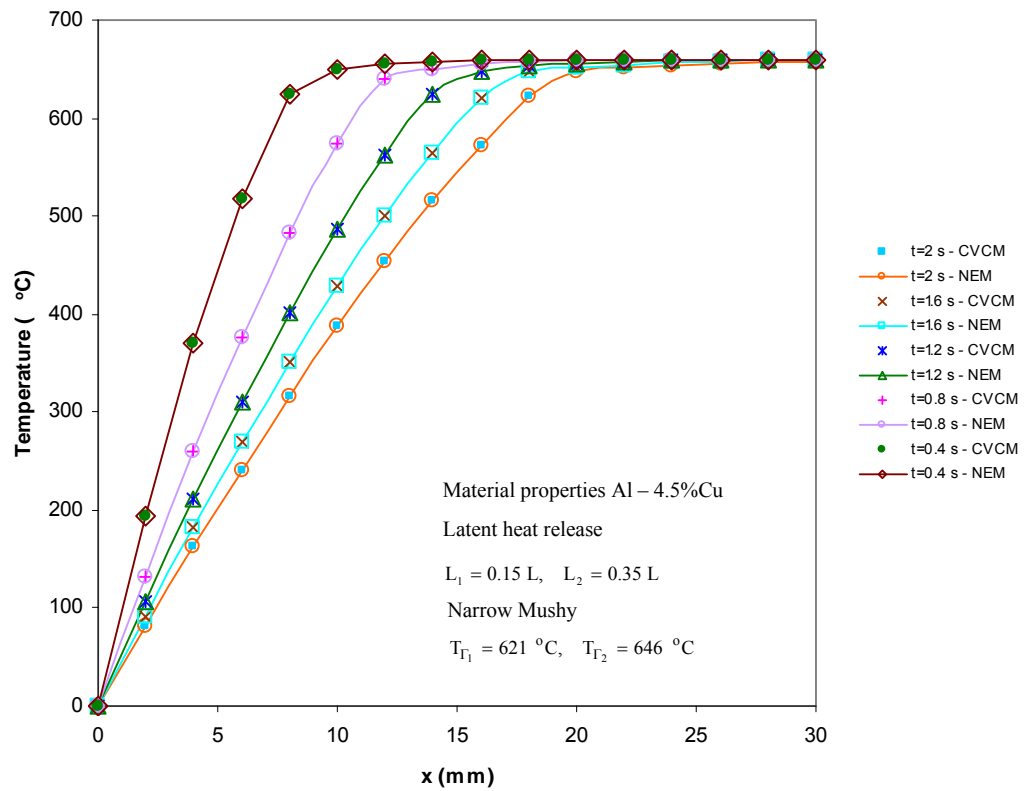
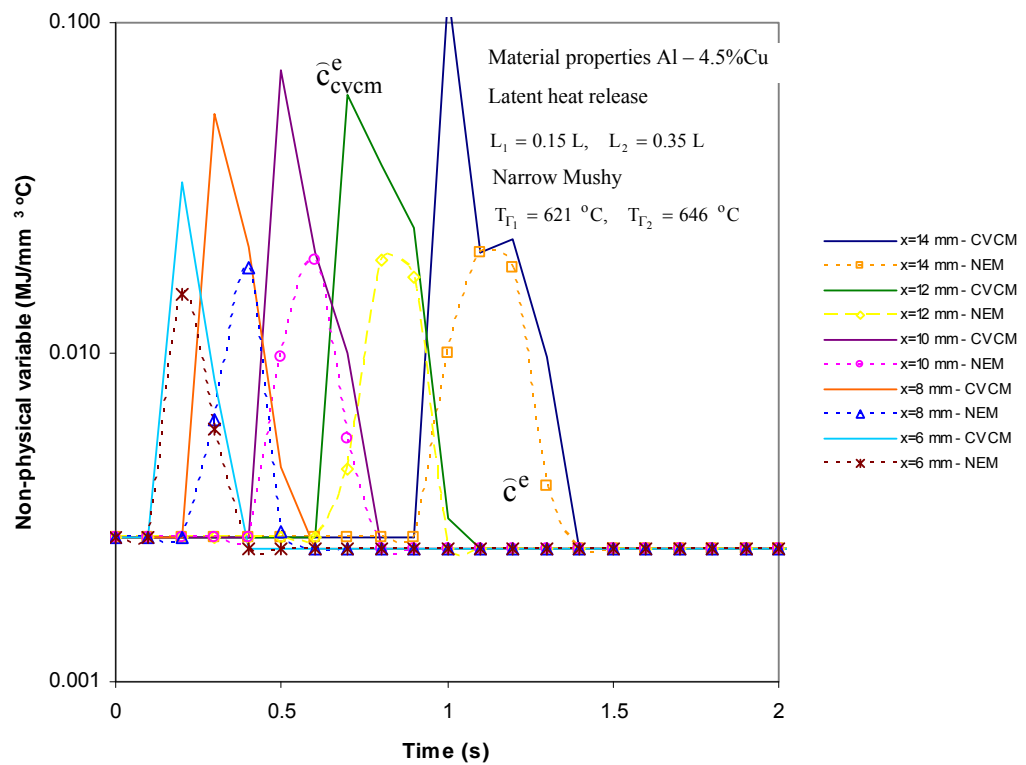


Figure 5-22 Temperature history for multi-discontinuous and narrow mushy solidification for 1-D semi-infinite slab



**Figure 5-23 Temperature profile for multi-discontinuous and narrow mushy solidification for 1-D semi-infinite slab**



**Figure 5-24 Non-physical variable comparison for multi-discontinuous and narrow mushy solidification for 1-D semi-infinite slab**

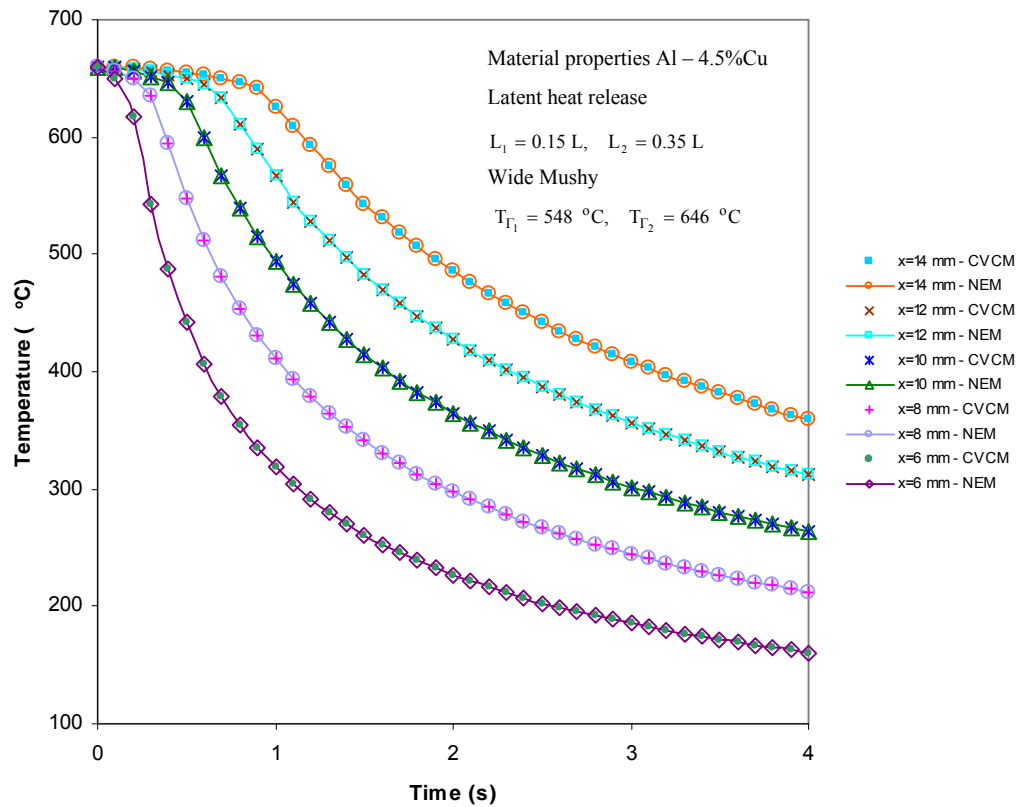


**Figure 5-25 Temperature history for multi-discontinuous and wide mushy solidification for 1-D semi-infinite slab**

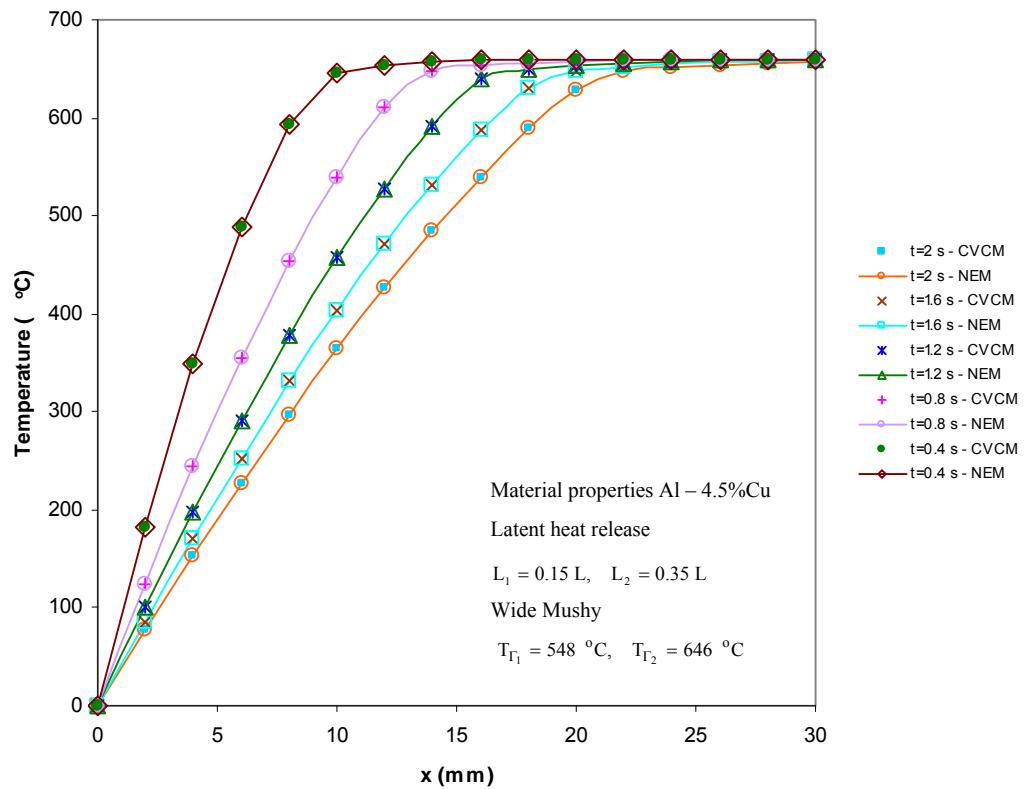


**Figure 5-26 Temperature profile for multi-discontinuous and wide mushy solidification for 1-D semi-infinite slab**

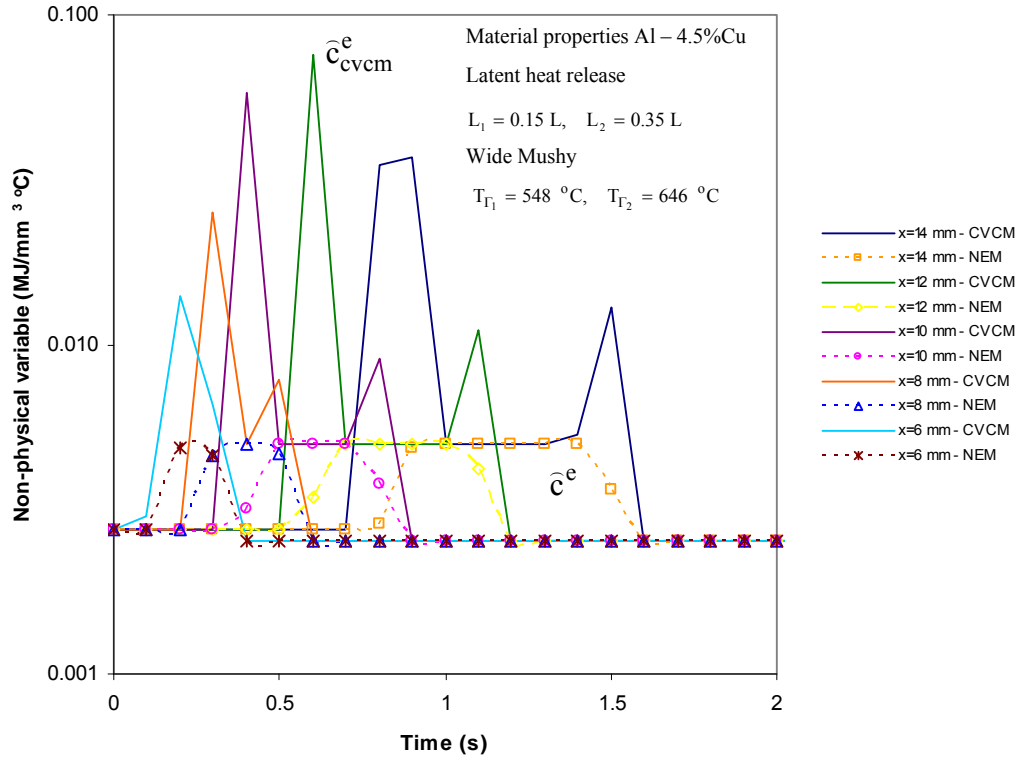


**Figure 5-27 Non-physical variable comparison for multi-discontinuous and wide mushy solidification for 1-D semi-infinite slab**

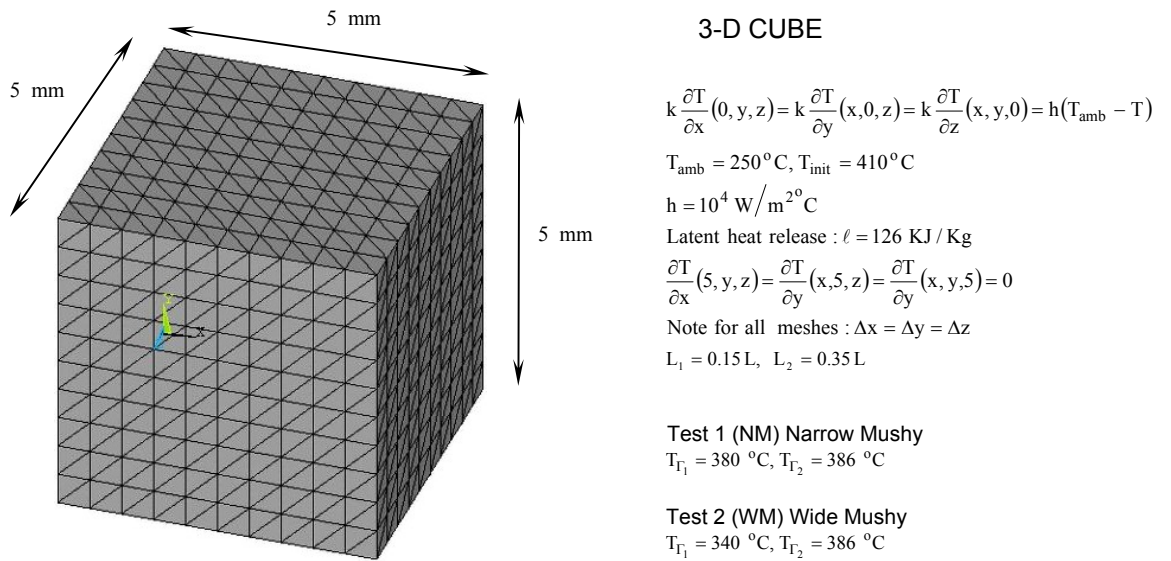


**Figure 5-28 Mesh for 3-D cube problem**



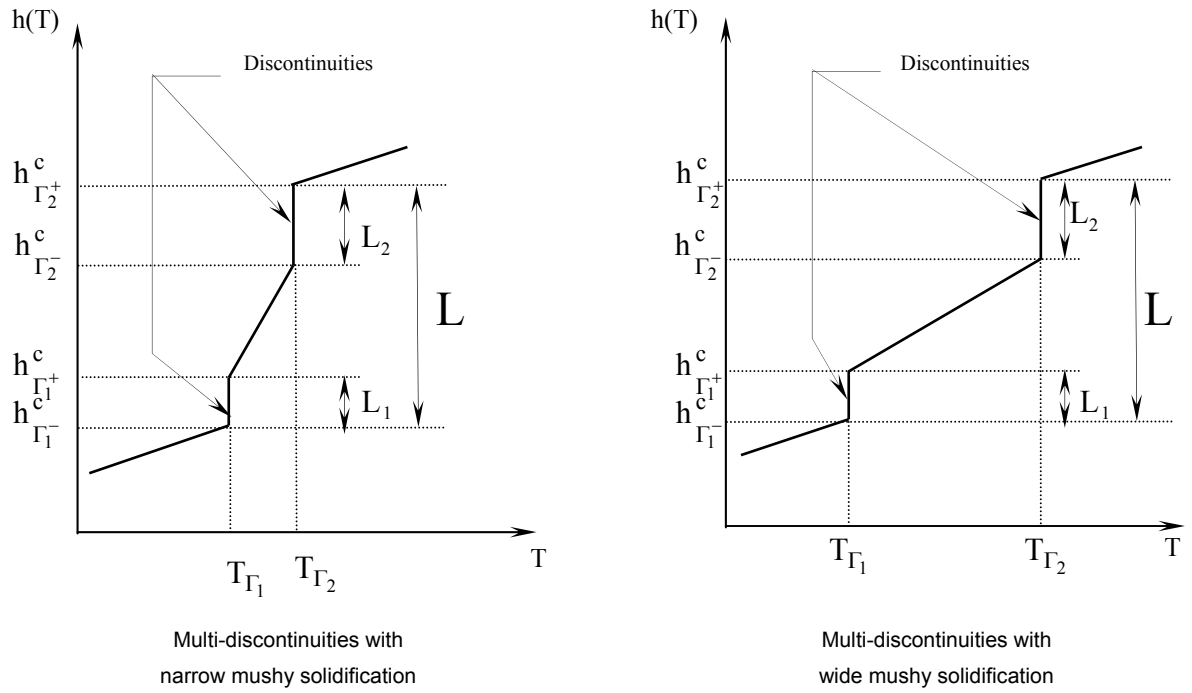


**Figure 5-29 Latent heat release involving multi-discontinuities with narrow and wide mushy solidification**

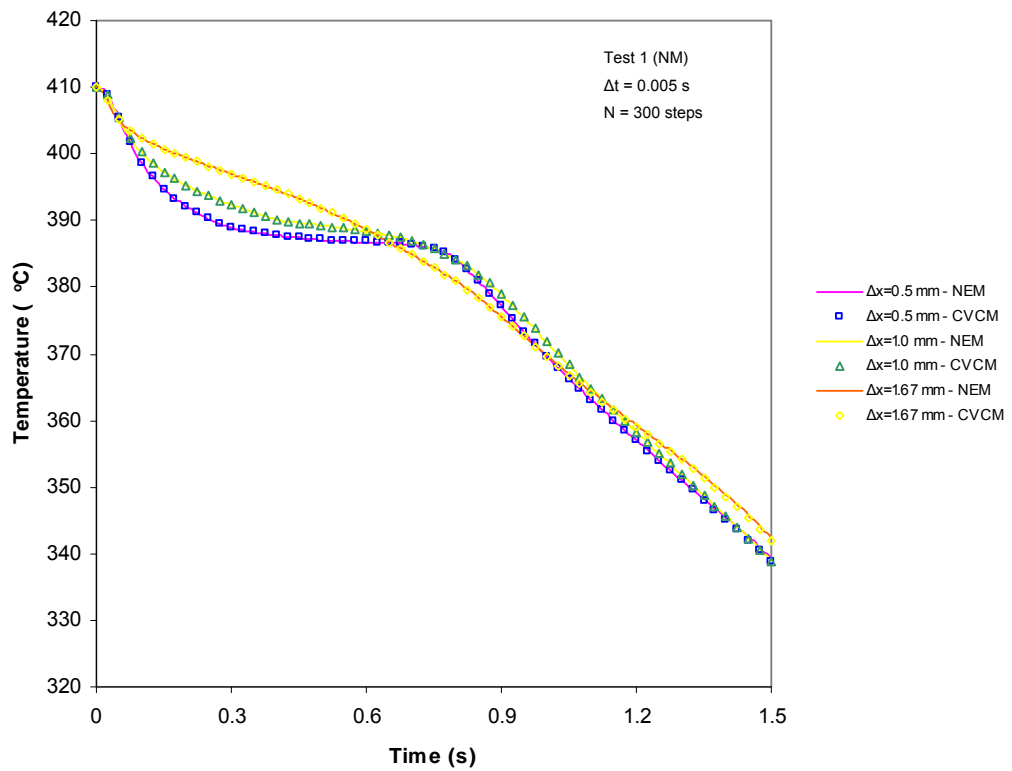


**Figure 5-30 Multi-discontinuous and narrow mushy solidification on a point  $x=y=z=2$  mm for different meshes**

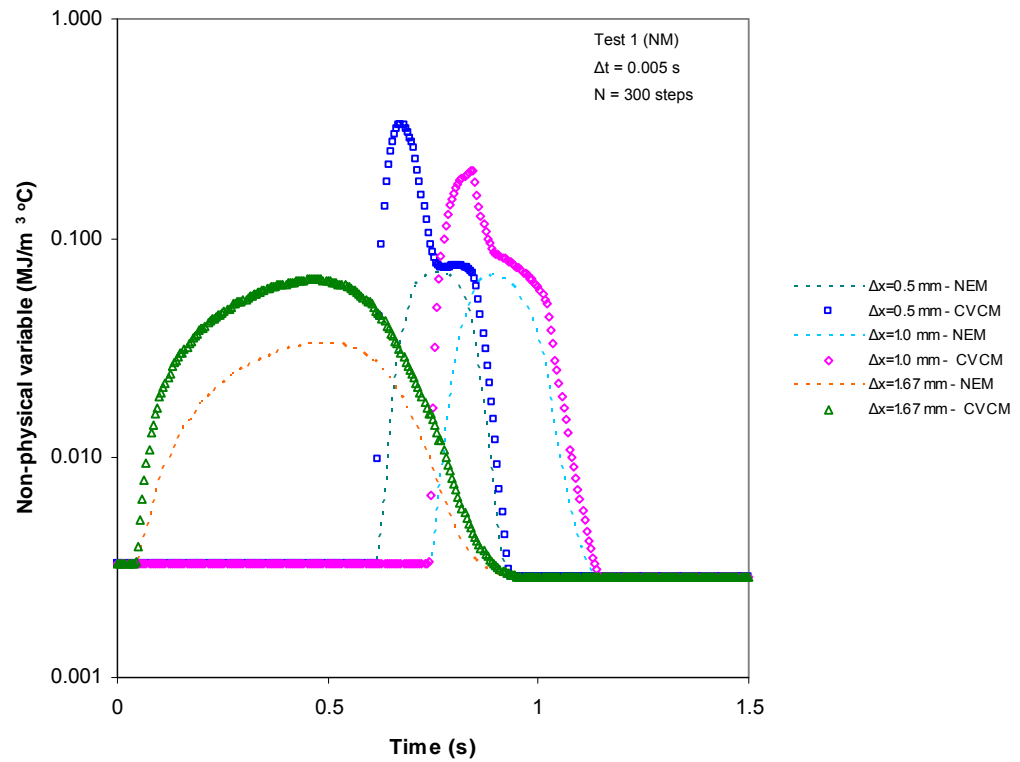


**Figure 5-31 Non-physical variable behaviour for Multi-discontinuous and narrow mushy solidification on a point  $x=y=z=2$  mm**

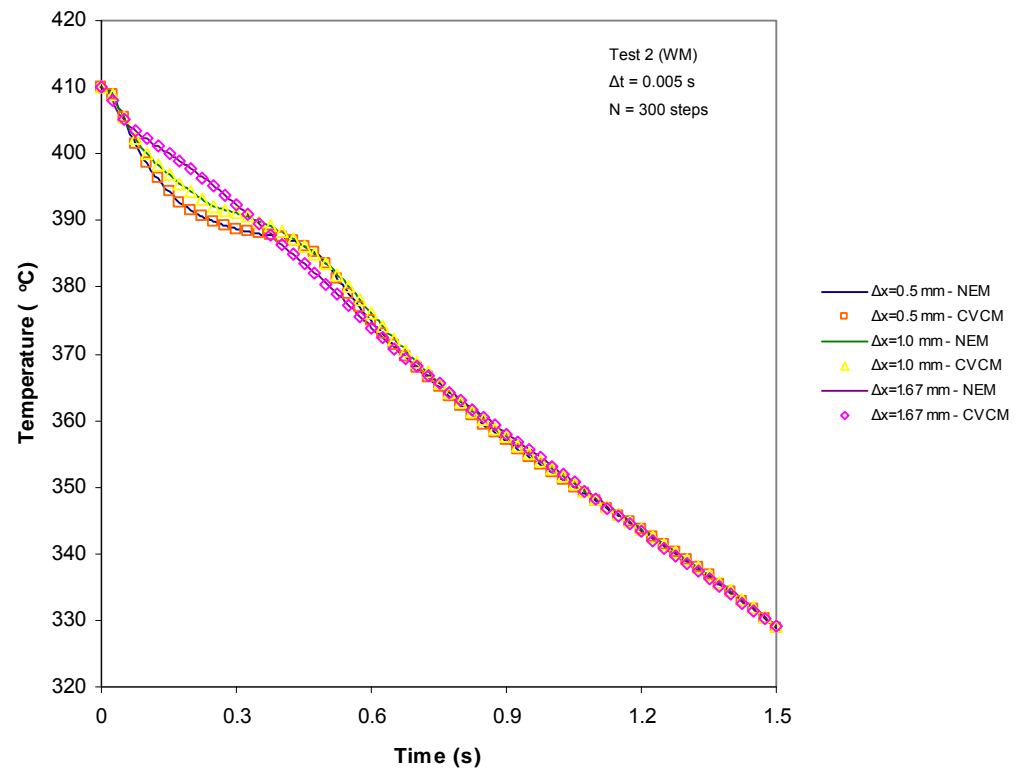


**Figure 5-32 Multi-discontinuous and wide mushy solidification on a point  $x=y=z=2$  mm for different meshes**

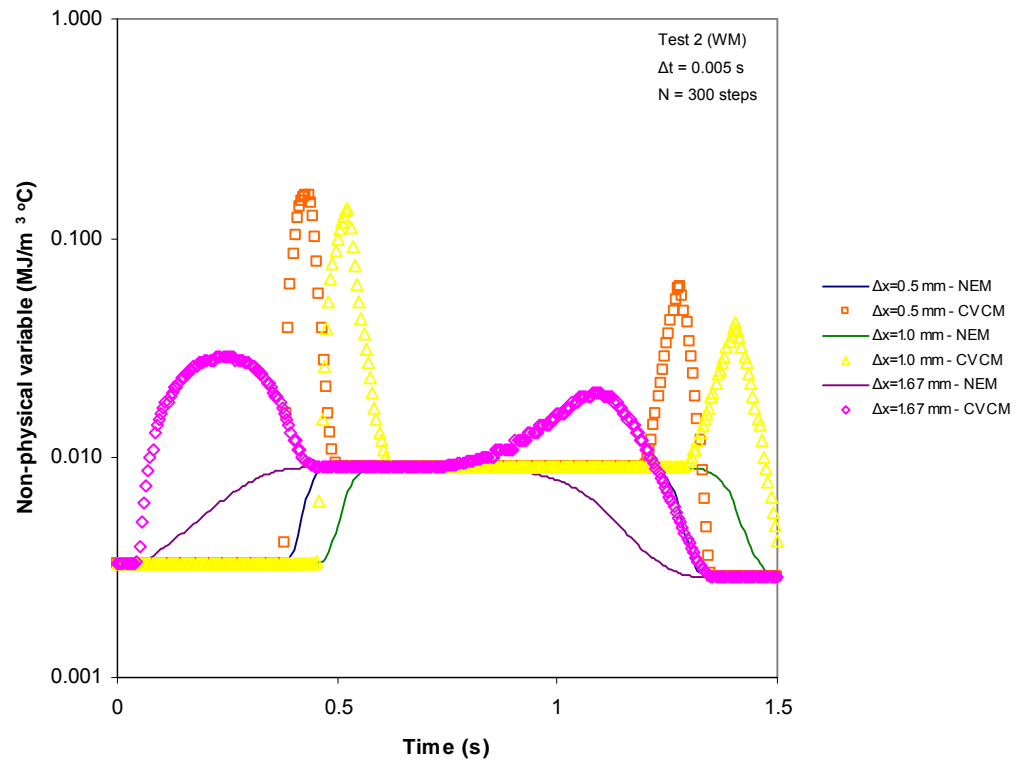


**Figure 5-33 Non-physical variable behaviour for Multi-discontinuous and wide mushy solidification on a point  $x=y=z=2$  mm**

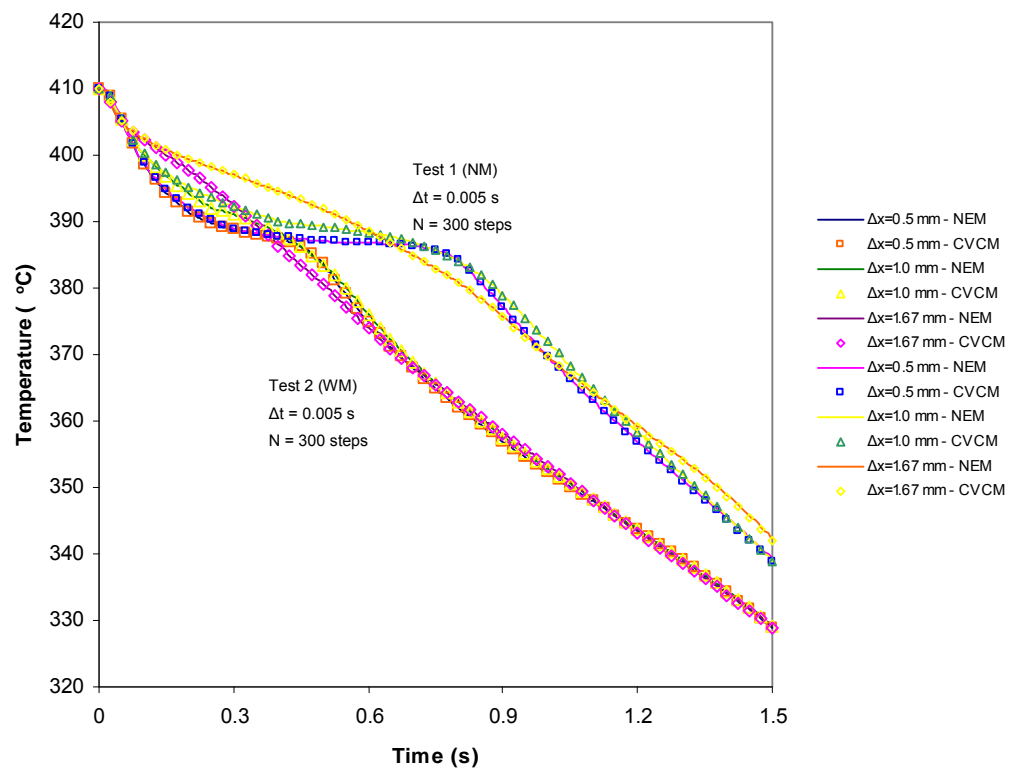


**Figure 5-34 Temperature history comparison for Multi-discontinuous narrow and wide mushy solidification on a point  $x=y=z=2$  mm for different meshes**

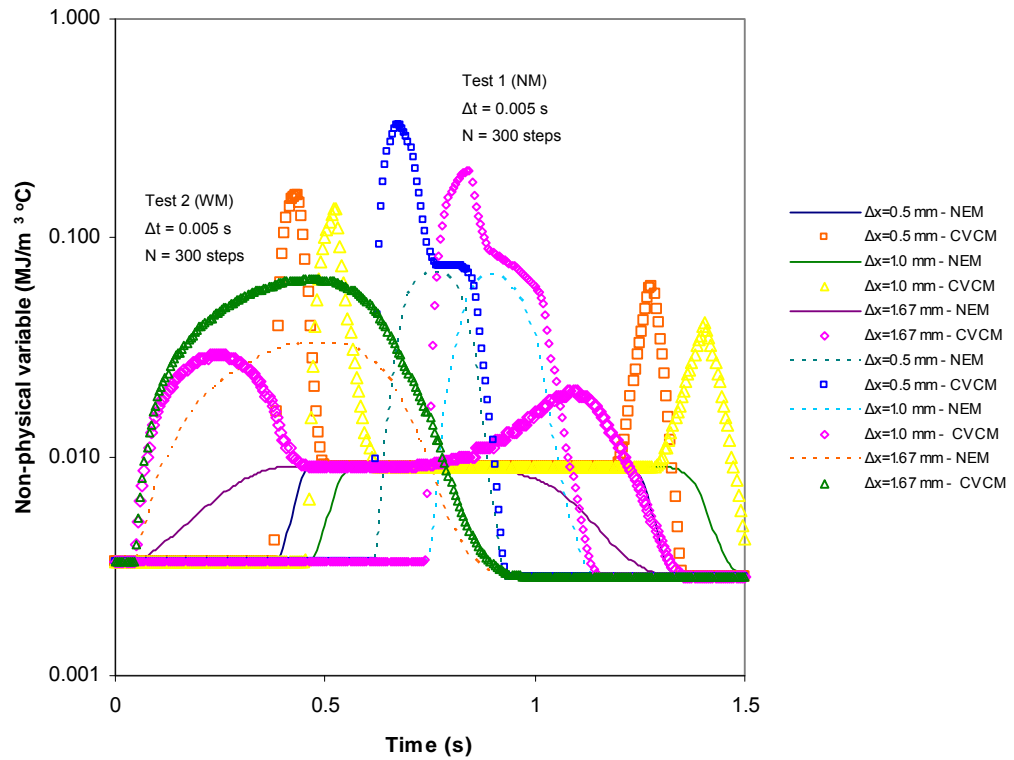


**Figure 5-35 Non-physical variable comparison for Multi-discontinuous narrow and mushy solidification on a point  $x=y=z=2$  mm for different meshes**

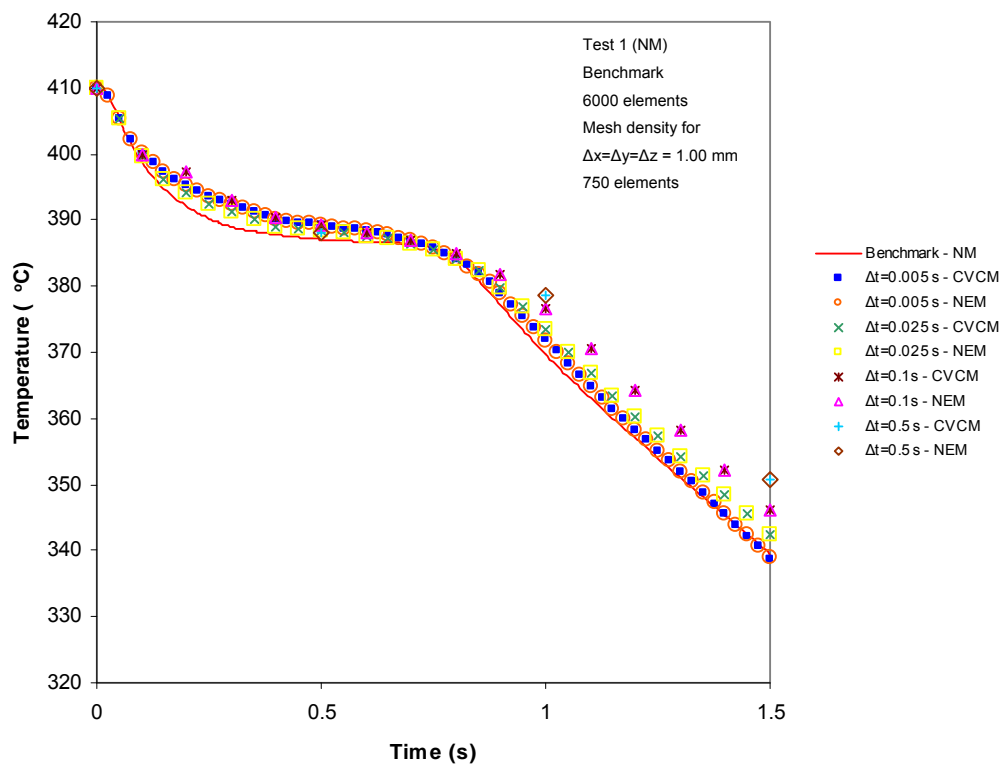


**Figure 5-36 Multi-discontinuous with narrow mushy solidification for different time steps on a coarse mesh contrasted to a fine mesh at a point  $x=y=z=2$  mm**

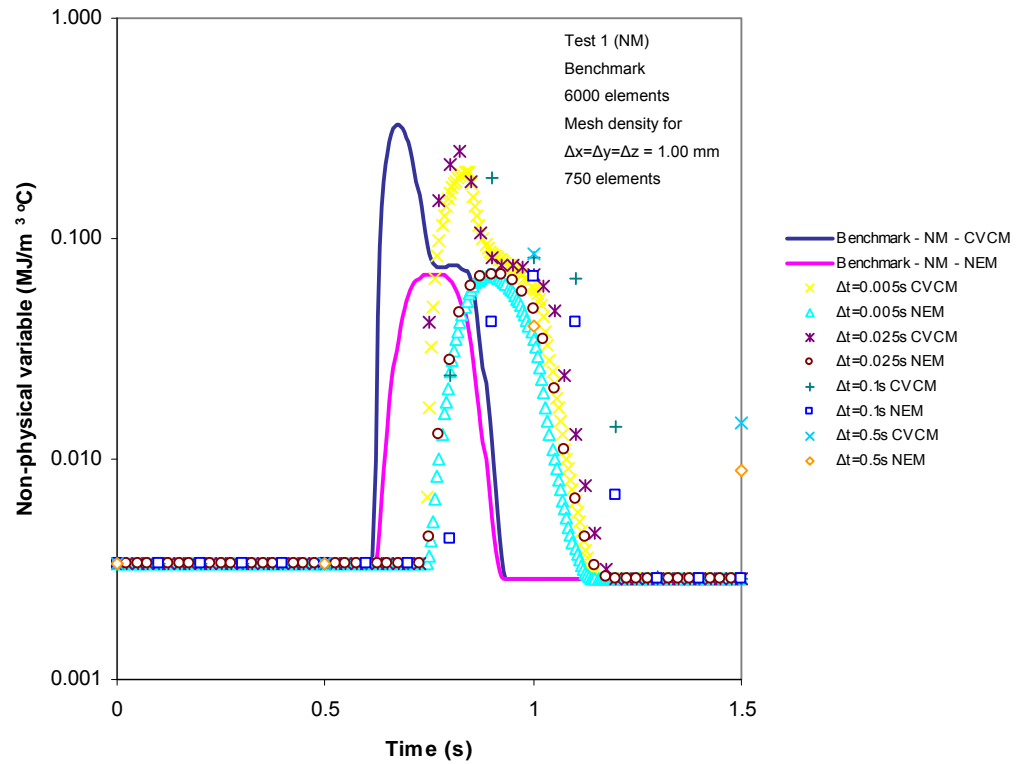


**Figure 5-37 Non-physical variable comparison for Multi-discontinuous and narrow mushy solidification for different time steps on a coarse and fine mesh at a point  $x=y=z=2$  mm**

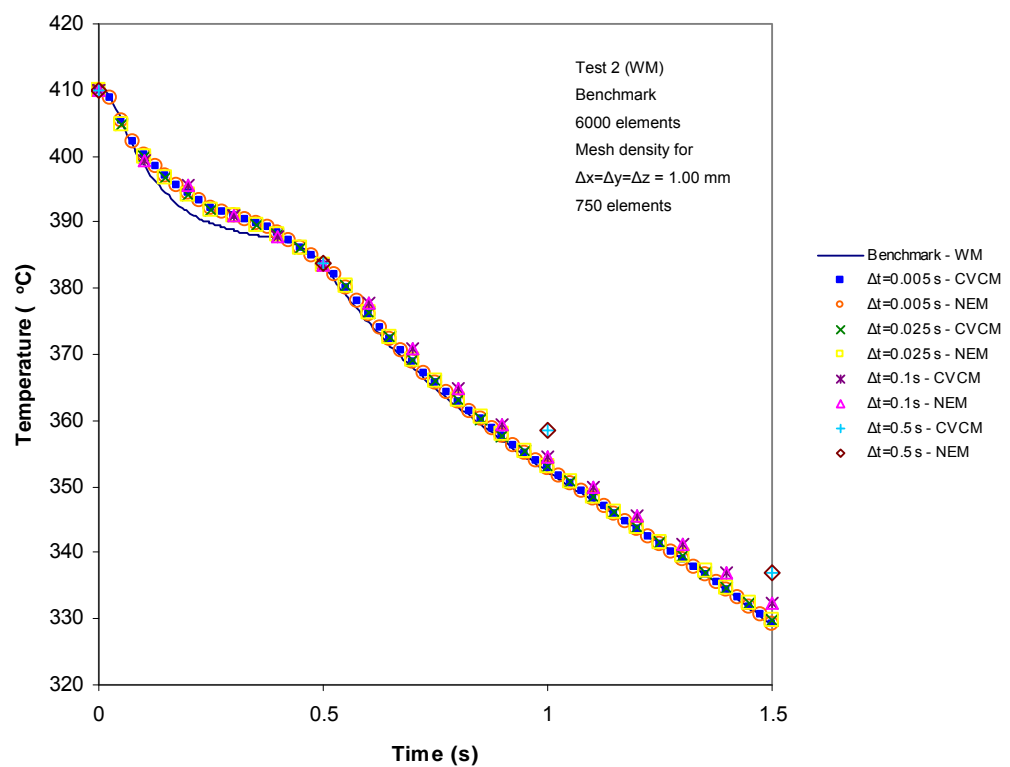


**Figure 5-38 Multi-discontinuous with wide mushy solidification for different time steps on a coarse mesh contrasted to a fine mesh at a point  $x=y=z=2$  mm**

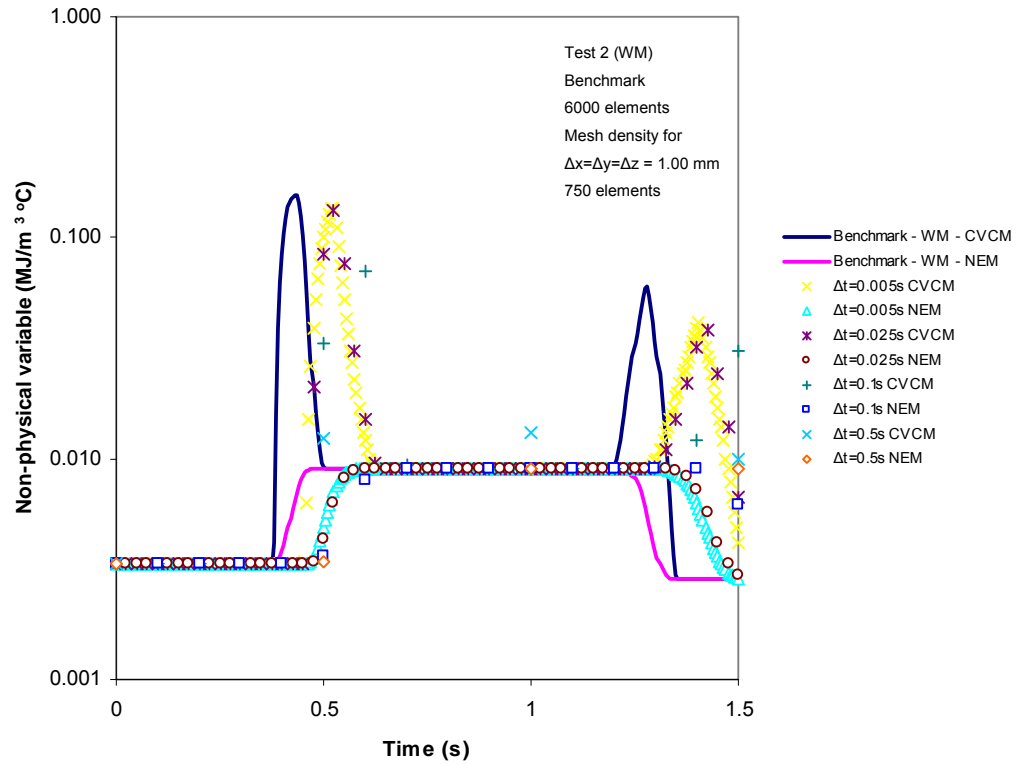


**Figure 5-39 Non-physical variable comparison for Multi-discontinuous and wide mushy solidification for different time steps on a coarse and fine mesh at a point  $x=y=z=2$  mm**

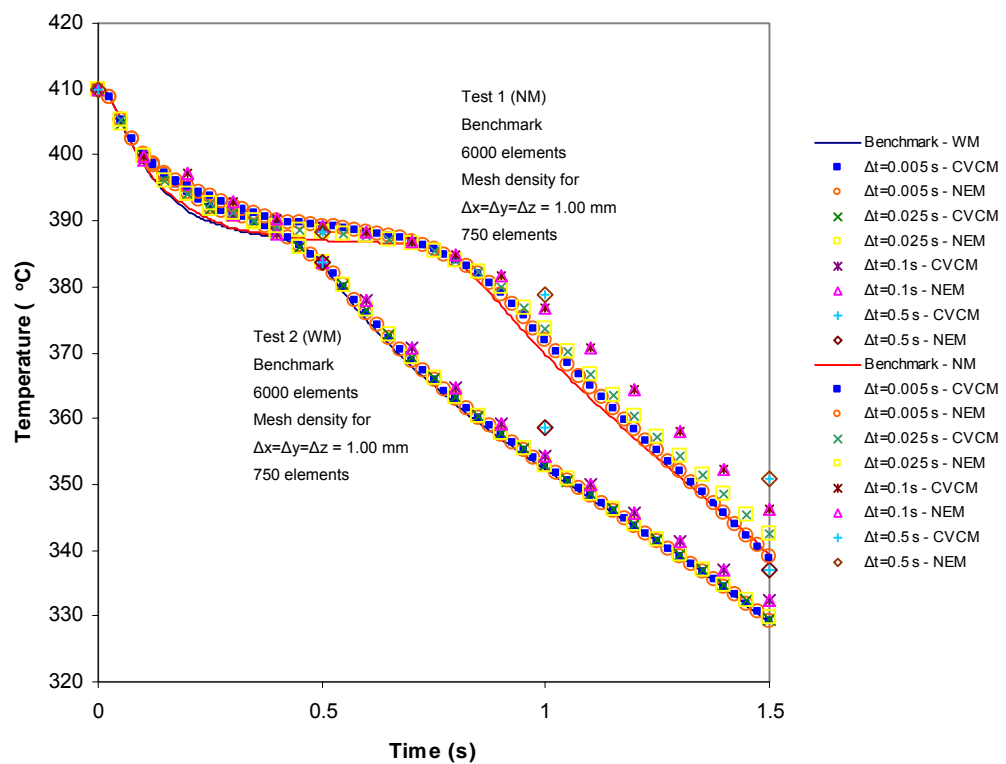


**Figure 5-40 Temperature history for Multi-discontinuous narrow and wide mushy solidification for different time steps at a point  $x=y=z=2$  mm**

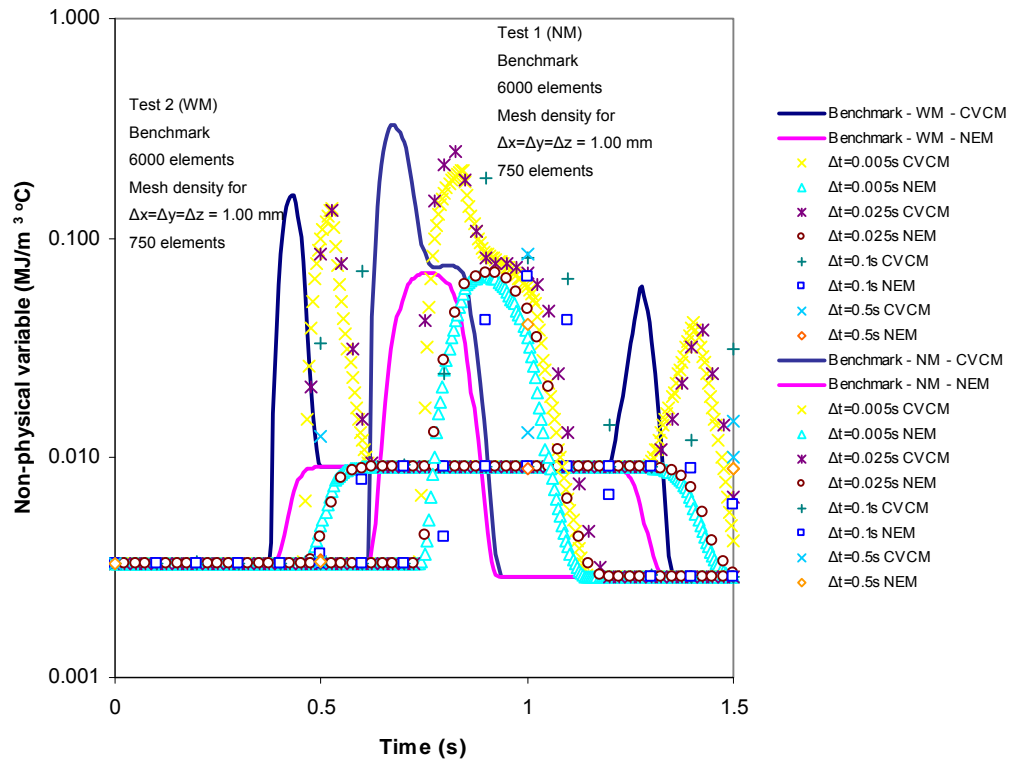


**Figure 5-41 Non-physical variable comparison for Multi-discontinuous narrow and wide mushy solidification for different time steps at a point  $x=y=z= 2$  mm**

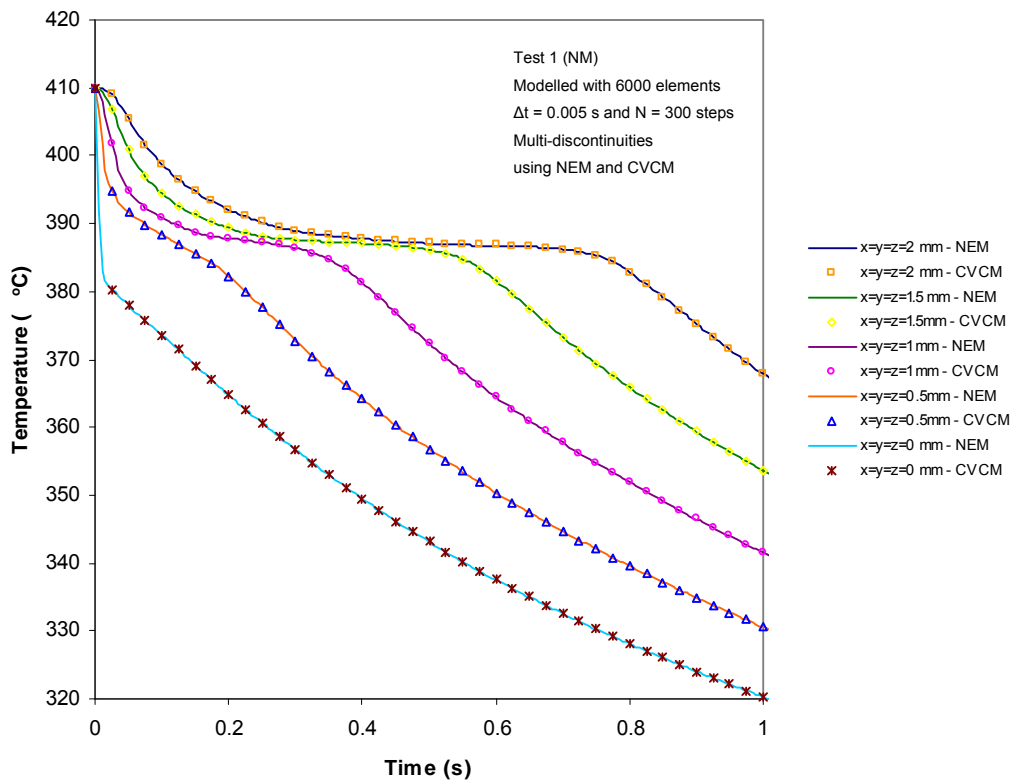


**Figure 5-42 Multi-discontinuous and narrow mushy solidification at different points along the diagonal of the cube for a fine mesh**

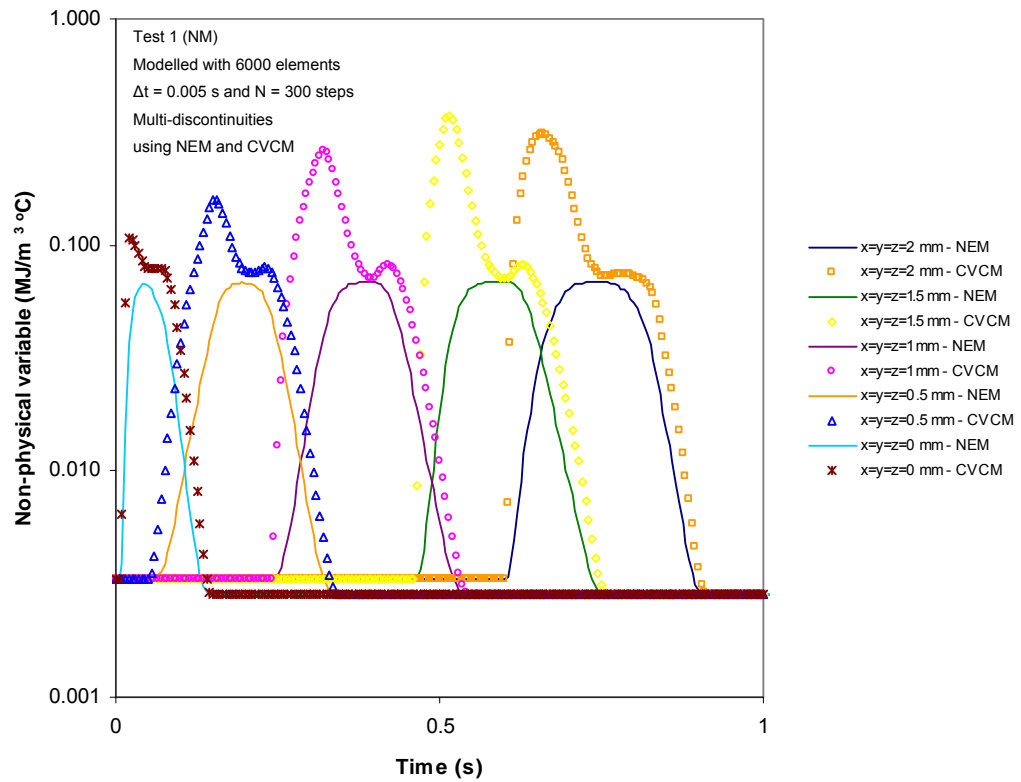


**Figure 5-43 Non-physical variable comparison for Multi-discontinuous and narrow mushy solidification along the diagonal of the cube for a fine mesh**

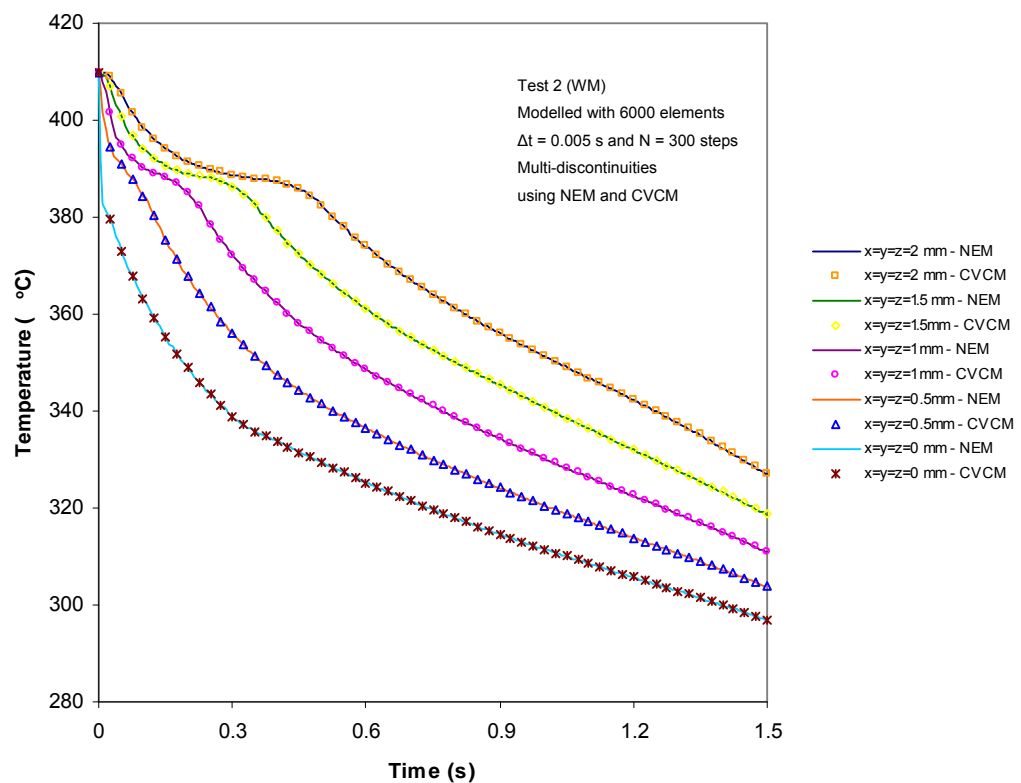


**Figure 5-44 Multi-discontinuous and wide mushy solidification at different points along the diagonal of the cube for a fine mesh**



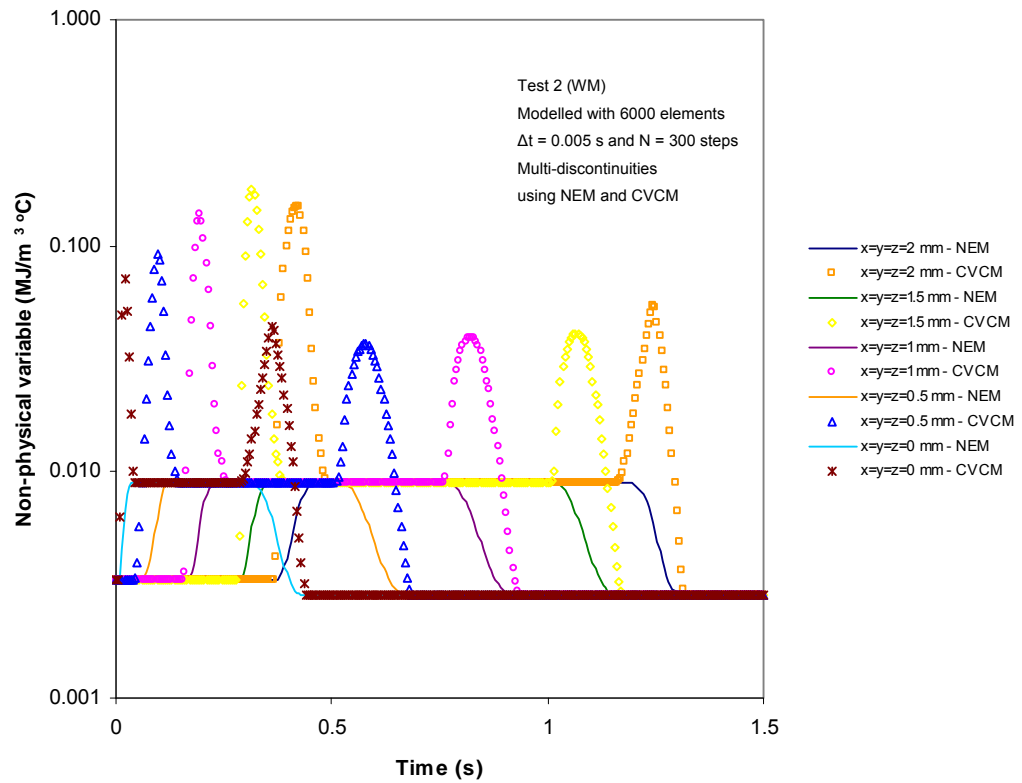


**Figure 5-45 Non-physical variable comparison for Multi-discontinuous and wide mushy solidification along the diagonal of the cube for a fine mesh**

## 6 CONCLUSIONS

---

The fundamental contribution of this thesis has evolved around the non-physical enthalpy method NEM for solidification with single discontinuity or multi-discontinuities. The conventional heat differential parabolic governing equation has been replaced and solved using the governing enthalpy-transport equation, which accounts essentially for the discontinuous physics avoiding the approximation and the arbitrariness common to the classical approaches. Understanding the remarkable source distribution like property at a discontinuity that the non-physical enthalpy method had, highlights an important feature for the precise removal of weak discontinuities, which is a common enthalpy-temperature response in solidification at the solidus and liquidus temperatures as a consequence of the phase-change and latent heat release. A range of simple problems have been used to provide an in-depth treatment and ease understanding of this novel methodology.

## **6.1 Solidification processes and modelling techniques**

Significant progress has been made in the solidification process although, conventional and special processes still depend on precise modelling starting from the liquid state to any phase transition during the solidification process. In sand casting, the liquid metal is poured into a die made of sand. Although, this process is relative easy to implement, the products have large dimensional tolerance, due to porosity caused by gas entrapment, which require machining. In pressure die-casting, the main concern is due to the existence of porosity because two events occurring at the same time as the mould is filled. The first is the formation of voids when the liquid solidifies; the second is the existence of whirl of liquid metal behind obstacles always present in industrial moulds, during pressure die-casting filling.

High pressure in the die-casting process decreases considerably the porosity, which allows both thinner and thicker parts, however ductility decreases and blistering appears as a consequence of entrapped gases in the final product. The other limitation is that no thermal treatment is feasible after casting because blistering defects appear. Recent die-casting process technologies have been developed to reduce the porosity and improve the mechanical properties in the final product, which generally are based on the semi-solid state however; economical factors constrain the application of this technique.

The selection of the numerical method to solve the phase-change problem depends not only on the nature of the problem but also on the priorities set by the user for accuracy, computational efficiency and ease of programming. For pure substances, the variable grid methods often yield more accurate results than those based on the fixed grid method. However, the fixed grid method is an easier program to implement. Moreover, the fixed grid method incorporated with the enthalpy technique can easily be extended to multidimensional problems for both pure and binary materials.

Due to the importance of convection in a large number of phase-change problems, wide experience has been accumulated in the numerical simulation of convection/diffusion processes coupled with phase-change. Numerical techniques for such complex phenomena are now being developed by scientists and engineers in different disciplines. The popularity of formulations capable of tackling three-dimensional problems is increasing, which are common in the industrial field. On the basis of experience gained so far, numerical methods based on the weak solution in conjunction with the control volume scheme in the fixed domain can be highly recommended for multidimensional melting and solidification problems.

With increasing interest in modelling of microstructure evolution occurring during solidification, a new generation of solidification models is rising. However, their accuracy in predicting the peculiar characteristics of microstructure is constantly focused on improving their performance.

## **6.2 Reflexions about NEM**

Discontinuities in the solidification process represented an important challenge for the numerical methods to cater for, although many numerical approaches have approximated a discontinuous solidification by using a continuous narrow temperature function. Although existing methods in terms of temperature field, provide a good approximation but in terms of energy prediction can give rise to large errors particularly related when a rapid energy change is present in the process. Scale level macro-micro solidification is considered another important constraint in terms of modelling, which has a direct influence in the selection of set of equations used to describe the physical phenomenon that correlated directly with the computer power capabilities to solve the equation system.

Even though, discontinuities have always been present and identified in the solidification process it is only recently that different techniques have appeared to deal with them. Non-physical enthalpy method (NEM) is providing a novel technique, which primarily identifies, tracks and annihilates the discontinuity present in the solidification process. Despite its relative complexity the method is founded on well-founded mathematical theory concerned with moving control volumes and adapted to embrace the novelty of non-physical variables to establish an alternative set of governing equations. Fundamentally, these equations are the product of applying the transport equation concept over a control volume (CV), which enables to track implicitly the discontinuity in the element by defining the correct velocity field. The governing FE transport equations have showed their real ability to isolating and accurately annihilating the discontinuity in the element furthermore, they have provided the linkage between the physical and non-physical variable, which acted as a constraint in the equation system.

Single discontinuity, multi-discontinuities and multi-discontinuities with linear transition zone (narrow and wide) have been the solidification types analysed in this research. Although, the problem selection is based on simple geometries, 1-D element, 1-D semi-infinite, 2-D semi-infinite corner and 3-D cube, the aim relies on the information available from the analytical and the CVCM cases, which represents the main method selected to compare against to NEM. Therefore, results showed in chapters 3 to 5 that temperature field and program time execution have a slightly improvement, which is linked with the

proper identification of the source term used in the scheme as a convergence factor. However, the validation and proving of the theory that are represented in the results involving the non-physical capacitance were the principal objectives in this research.

### **6.3 Future work**

The next stage for the non-physical enthalpy method (NEM) would include the momentum conservation equation, apart from the mass and energy conservation equations that have been successfully replaced and solved, which would definitely lead into two important fields for the solidification process. Firstly, it would allow the introduction of advection terms on the macroscopic scale and secondly, microstructure solidification describing grain structure formation and other micro structural features (e.g. secondary arm spacing, micro segregation model, etc.). The morphology, size, distribution, crystal orientation, correlation (texture) and number of phases define a microstructure. Phase and microstructure selection describes the variety of phases and microstructures that develop under given growth conditions and growth geometries, in which weak discontinuities are likely to appear

The non-physical enthalpy method (NEM) has been developed to annihilate discontinuous solidification regardless of the number of phase-changes present or the size of the transition (mushy) zone in the process. The NEM would be perfectly adaptable for other applications where physical phenomenon have discontinuities present, i.e. in the geological field, molten lava under the sea (constant pressure) or environmental change, melting ice in the North Pole, etc.

# REFERENCE

1. J. M. Camp and C. B. Francis, *The making, shaping and treating of steel*, Carnegie Steel Company, Pittsburgh, 1920.
2. R. F. Tylecote, *A history of metallurgy*, Institute of Materials, London, 1992.
3. M. Blair and T. L. Stevens, *Steel casting handbook*, ASM International, 1995.
4. D. M. Stefanescu, *Science and engineering of casting solidification*, Springer, New York, N. Y., 2008.
5. E. P. Degarmo, J. T. Black and R. A. Kohser, *Materials and processes in manufacturing*, Wiley, 2003.
6. J. Ni and C. Beckermann, *A volume-averaged two-phase model for transport phenomena during solidification*, Metallurgical Transactions B **22** (1991), no. 3, 349-361.
7. W. J. Boettinger, S. R. Coriell, A. L. Greer, A. Karma, W. Kurz, M. Rappaz and R. Trivedi, *Solidification microstructures: Recent developments, future directions*, Acta Materialia **48** (2000), no. 1, 43-70.
8. L. Gaston, A. Kamara and M. Bellet, *An arbitrary lagrangian-eulerian finite element approach to non-steady state turbulent fluid flow with application to mould filling in casting*, International Journal for Numerical Methods in Fluids **34** (2000), no. 4, 341-369.
9. F. P. Schleg, F. H. Kohloff and J. G. Sylvia, *Technology of metalcasting*, American Foundry Society, 2003.
10. S. Kalpakjian and S. R. Schmid, *Manufacturing engineering and technology*, Prentice Hall, 2006.
11. B. Cantor and K. O'Reilly, *Solidification and casting*, CRC press, 2003.
12. W. Kurz and D. J. Fisher, *Fundamentals of solidification*, Trans-Tech, Switzerland, 1986.
13. M. C. Flemings, *Solidification processing*, Mc-Graw Hill, New York, N.Y., 1974.
14. R. W. Lewis and K. Ravindran, *Finite element simulation of metal casting*, International Journal for Numerical Methods in Engineering **47** (2000), no. 1-3, 29-59.
15. R. W. Hamilton, D. See, S. Butler and P. D. Lee, *Multiscale modeling for the prediction of casting defects in investment cast aluminum alloys*, Materials Science and Engineering A **343** (2003), no. 1-2, 290-300.
16. C. H. Caceres, C. J. Davidson, J. R. Griffiths and C. L. Newton, *Effects of solidification rate and ageing on the microstructure and mechanical properties of az91 alloy*, Materials Science and Engineering A **325** (2002), no. 1-2, 344-355.
17. R. Mehrabian, D. R. Geiger and M. C. Flemings, *Refining by partial solidification*, Metall Trans **5** (1974), no. 3, 785-787.
18. R. Mehrabian, R. G. Riek and M. C. Flemings, *Preparation and casting of metal-particulate non-metal composites*, Metall Trans **5** (1974), no. 8, 1899-1905.
19. Y. M. Youssef, A. Chaijaruwanich, R. W. Hamilton, H. Nagaumi, R. J. Dashwood and P. D. Lee, *X-ray microtomographic characterisation of pore evolution during homogenisation and rolling of al-6mg*, Materials Science and Technology **22** (2006), no. 9, 1087-1093.
20. M. C. Flemings, *Behavior of metal alloys in the semisolid state*, Metallurgical Transactions A **22** (1991), no. 5, 957-981.

21. M. C. Flemings, R. G. Riek and K. P. Young, *Rheocasting*, Materials Science and Engineering **25** (1976), no. C, 103-117.
22. D. Brabazon, D. J. Browne and A. J. Carr, *Mechanical stir casting of aluminium alloys from the mushy state: Process, microstructure and mechanical properties*, Materials Science and Engineering A **326** (2002), no. 2, 370-381.
23. J. Collot, *Review of new process technologies in the aluminum die-casting industry*, Materials and Manufacturing Processes **16** (2001), no. 5, 595-617.
24. X. Li, Y. Yang and X. Cheng, *Ultrasonic-assisted fabrication of metal matrix nanocomposites*, Journal of Materials Science **39** (2004), no. 9, 3211-3212.
25. F. R. Giordano, W. P. Fox, S. B. Horton and M. D. Weir, *First course in mathematical modeling*, Cengage Learning, Belmont, C. A., 2008.
26. E. A. Bender, *An introduction to mathematical modeling*, Courier Dover Publications, New York, N. Y., 2000.
27. R. McHaney, *Computer simulation: A practical perspective*, Elsevier Academic Press, San Diego, California, 1991.
28. M. M. Meerschaert, *Mathematical modeling*, Elsevier Academic Press, San Diego, California, 2007.
29. B. P. Zeigler, H. Praehofer and T. G. Kim, *Theory of modeling and simulation: Integrating discrete event and continuous complex dynamic systems*, Elsevier Academic Press, San Diego, California, 2000.
30. N. M. H. Lightfoot, *The solidification molten steel*, **31** (1929), no. 1750, 97-116.
31. H. Carslaw and J. C. Jaeger, *Conduction of heat in solids*, University of Oxford and Clarendon Press, London, 1959.
32. L. M. Jiji, K. A. Rathjen and T. Drzewiecki, *Two-dimensional solidification in a corner*, International Journal of Heat and Mass Transfer **13** (1970), no. 1, 215-218.
33. A. Lazaridis, *A numerical solution of the multidimensional solidification (or melting) problem*, International Journal of Heat and Mass Transfer **13** (1970), no. 9, 1459-1477.
34. J. Crank and R. S. Gupta, *Isotherm migration method in two dimensions*, International Journal of Heat and Mass Transfer **18** (1975), no. 9, 1101-1107.
35. J. Donea, P. Fasoli Stella and S. Guiliani, "Lagrangian and eulerian finite element techniques for transient fluid structure interaction problems," *Transactions Fourth SMIRT*, vol. paper B 1/2, San Francisco, 1977, pp. 1-12.
36. R. W. Lewis, K. Morgan and R. H. Gallagher, "Finite element analysis of solidification and welding processes.," *Numerical Model of Manufacturing Processes, Winter Annual Meeting of ASME*, ASME (PVP-PB-025), Atlanta Ga, 1977, pp. 67-80.
37. K. Morgan, R. W. Lewis and O. C. Zienkiewicz, *An improved algorithm for heat conduction problems with phase change.*, **12** (1978), no. 7, 1191-1195.
38. K. Morgan, *A numerical analysis of freezing and melting with convection*, Computer Methods in Applied Mechanics and Engineering **28** (1981), no. 3, 275-284.
39. V. R. Voller and M. Cross, *Accurate solutions of moving boundary problems using the enthalpy method*, International Journal of Heat and Mass Transfer **24** (1981), 545-556.
40. W. D. Rolph III and K. J. Bathe, *An efficient algorithm for analysis of nonlinear heat transfer with phase changes.*, International Journal for Numerical Methods in Engineering **18** (1982), no. 1, 119-134.
41. L. Demkowicz, J. T. Oden and T. Strouboulis, *Adaptive finite elements for flow problems with moving boundaries. Part i: Variational principles and a posteriori estimates*, Computer Methods in Applied Mechanics and Engineering **46** (1984), no. 2, 217-251.

42. R. W. Lewis, H. C. Huang, A. S. Usmani and J. T. Cross, *Finite element analysis of heat transfer and flow problems using adaptive remeshing including application to solidification problems*, International Journal for Numerical Methods in Engineering **32** (1991), no. 4, 767-781.
43. J. Berntsen, R. Cools and T. O. Espelid, *Algorithm 720: An algorithm for adaptive cubature over a collection of 3-dimensional simplices*, ACM Transactions on Mathematical Software **19** (1993), no. 3, 320-332.
44. V. R. Voller and C. Prakash, *A fixed grid numerical modelling methodology for convection-diffusion mushy region phase-change problems*, International Journal of Heat and Mass Transfer **30** (1987), no. 8, 1709-1719.
45. E. Pardo and D. C. Weckman, *Fixed grid finite element technique for modelling phase change in steady-state conduction-advection problems*, International Journal for Numerical Methods in Engineering **29** (1990), no. 5, 969-984.
46. V. R. Voller, C. R. Swaminathan and B. G. Thomas, *Fixed grid techniques for phase change problems. A review*, International Journal for Numerical Methods in Engineering **30** (1990), no. 4, 875-898.
47. H. S. Udaykumar, R. Mittal and P. Rampunggoon, *Interface tracking finite volume method for complex solid-fluid interactions on fixed meshes*, Communications in Numerical Methods in Engineering **18** (2002), no. 2, 89-97.
48. D. J. Browne and J. D. Hunt, *A fixed grid front-tracking model of the growth of a columnar front and an equiaxed grain during solidification of an alloy*, Numerical Heat Transfer, Part B: Fundamentals **45** (2004), no. 5, 395 - 419.
49. P. Zhao, J. C. Heinrich and D. R. Poirier, *Fixed mesh front-tracking methodology for finite element simulations*, International Journal for Numerical Methods in Engineering **61** (2004), no. 6, 928-948.
50. C. Charbon, A. Jacot and M. Rappaz, *3d stochastic modelling of equiaxed solidification in the presence of grain movement*, Acta Metallurgica Et Materialia **42** (1994), no. 12, 3953-3966.
51. C.-A. Gandin, C. Charbon and M. Rappaz, *Stochastic modelling of solidification grain structures*, ISIJ International **35** (1995), no. 6, 651-657.
52. M. K. Deb, I. M. Babuska and J. T. Oden, *Solution of stochastic partial differential equations using galerkin finite element techniques*, Computer Methods in Applied Mechanics and Engineering **190** (2001), no. 48, 6359-6372.
53. I. Babuska, R. Temponet and G. E. Zouraris, *Galerkin finite element approximations of stochastic elliptic partial differential equations*, SIAM Journal on Numerical Analysis **42** (2004), no. 2, 800-825.
54. C. Beckermann, H.-J. Diepers, I. Steinbach, A. Karma and X. Tong, *Modeling melt convection in phase-field simulations of solidification*, Journal of Computational Physics **154** (1999), no. 2, 468-496.
55. W. J. Boettinger, J. A. Warren, C. Beckermann and A. Karma, *Phase-field simulation of solidification*, Annual Review of Materials Science **32** (2002), 163-194.
56. A. Jacot and M. Rappaz, *A pseudo-front tracking technique for the modelling of solidification microstructures in multi-component alloys*, Acta Materialia **50** (2002), no. 8, 1909-1926.
57. A. Badillo and C. Beckermann, *Phase-field simulation of the columnar-to-equiaxed transition in alloy solidification*, Acta Materialia **54** (2006), no. 8, 2015-2026.
58. E. L. Kotzin, "Timeline of casting technology," Michael J. Lessiter, 2002.
59. S. Sundarraj and V. R. Voller, *Effect of macro scale phenomena on microsegregation*, International Communications in Heat and Mass Transfer **21** (1994), no. 2, 189-197.



60. C. A. Santos, J. A. Spim Jr., M. C. F. Ierardi and A. Garcia, *The use of artificial intelligence technique for the optimisation of process parameters used in the continuous casting of steel*, Applied Mathematical Modelling **26** (2002), no. 10, 1077-1092.
61. G. Lame and C. B. P. E., *Memoire sur la solidification par refroidissement d' un globe solid*, Ann. Chem. Phys. **47** (1831), 250-260.
62. J. Stefan, *Über einige probleme der theorie der wärmeleitung*, Sitzungsberichte der Österreichischen Akademie der Wessenschaften Mathematisch-Naturwissenschaftliche **98** (1889), 473-484.
63. ---, *Über die theorie der eisbildung, insbesondere über die eisbildung im polameere*, Annalen der Physik und Chemie **42** (1891), 269-286.
64. S. Paterson, *Propagation of a boundary of fusion*, Proc. Glasgow Math. Assoc. **1** (1952-1953), 42-47.
65. T. R. Goodman, *The heat-balance integral and its application to problems involving a change of phase*, Trans. ASME **80** (1958), 335-342.
66. S. C. Gupta, *Two-dimensional heat conduction with phase change in a semi-infinite mould*, International Journal of Engineering Science **19** (1981), no. 1, 137-146.
67. M. Ciment and R. A. Sweet, *Mesh refinements for parabolic equations*, Journal of Computational Physics **12** (1973), no. 4, 513-525.
68. A. J. Dalhuijsen and A. Segal, *Comparison of finite element techniques for solidification problems.*, International Journal for Numerical Methods in Engineering **23** (1986), no. 10, 1807-1829.
69. S. C. Gupta, E. Laitinen and T. Valtteri, *Moving grid scheme for multiple moving boundaries*, Computer Methods in Applied Mechanics and Engineering **167** (1998), no. 3-4, 345-353.
70. S. C. Gupta, *A moving grid numerical scheme for multi-dimensional solidification with transition temperature range*, Computer Methods in Applied Mechanics and Engineering **189** (2000), no. 2, 525-544.
71. V. R. Voller and L. Shadabi, *Enthalpy methods for tracking a phase change boundary in two dimensions*, International Communications in Heat and Mass Transfer **11** (1984), no. 3, 239-249.
72. G. Comini, S. Del Guidice, R. W. Lewis and O. C. Zienkiewicz, *Finite element solution of non-linear heat conduction problems with special reference to phase change.*, International Journal for Numerical Methods in Engineering **8** (1974), no. 3, 613-624.
73. M. Salcudean and Z. Abdullah, *On the numerical modelling of heat transfer during solidification processes*, International Journal for Numerical Methods in Engineering **25** (1988), no. 2, 445-473.
74. H. Hu and S. A. Argyropoulos, *Mathematical modelling of solidification and melting: A review*, Modelling and Simulation in Materials Science and Engineering **4** (1996), no. 4, 371-396.
75. J. Roose and O. Storrer, *Modelization of phase changes by fictitious heat flow*, International Journal for Numerical Methods in Engineering **20** (1984), 217-225.
76. V. R. Voller and C. R. Swaminathan, *General source-based method for solidification phase change*, Numerical Heat Transfer, Part B: Fundamentals **19** (1991), no. 2, 175-189.
77. C. R. Swaminathan and V. R. Voller, *A general enthalpy method for modeling solidification processes*, Metallurgical Transactions B **23** (1992), no. 5, 651-664.
78. ---, *On the enthalpy method*, International Journal of Numerical Methods for Heat and Fluid Flow **3** (1993), no. 3, 233-244.
79. V. R. Voller, *An enthalpy method for modeling dendritic growth in a binary alloy*, International Journal of Heat and Mass Transfer **51** (2008), no. 3-4, 823-834.

80. C. Beckermann and R. Viskanta, *Double-diffusive convection due to melting*, International Journal of Heat and Mass Transfer **31** (1988), no. 10, 2077-2089.
81. A. D. Brent, V. R. Voller and K. J. Reid, *Enthalpy-porosity technique for modeling convection-diffusion phase change: Application to the melting of a pure metal.*, Numerical heat transfer **13** (1988), no. 3, 297-318.
82. D. T. Gethin, R. W. Lewis and M. R. Tadayan, *Finite element approach for modelling metal flow and pressurized solidification in the squeeze casting process*, International Journal for Numerical Methods in Engineering **35** (1992), no. 4, 939-950.
83. S. C. Huang, *Analytical solution for the buoyancy flow during the melting of a vertical semi-infinite region*, International Journal of Heat and Mass Transfer **28** (1985), no. 6, 1231-1233.
84. N. Ramachandran, J. P. Gupta and Y. Jaluria, *Thermal and fluid flow effects during solidification in a rectangular enclosure*, International Journal of Heat and Mass Transfer **25** (1982), no. 2, 187-194.
85. C. R. Swaminathan and V. R. Voller, *A time-implicit filling algorithm*, Applied Mathematical Modelling **18** (1994), no. 2, 101-108.
86. K. Ravindran and R. W. Lewis, *Finite element modelling of solidification effects in mould filling*, Finite Elements in Analysis and Design **31** (1998), no. 2, 99-116.
87. S. M. H. Mirbagheri, N. Varahram and P. Davami, *3d computer simulation of melt flow and heat transfer in the lost foam casting process*, International Journal for Numerical Methods in Engineering **58** (2003), no. 5, 723-748.
88. C. Beckermann, R. Viskanta and S. Ramadhyani, *Numerical study of non-darcian natural convection in a vertical enclosure filled with a porous medium.*, Numerical heat transfer **10** (1986), no. 6, 557-570.
89. H. Hu and S. A. Argyropoulos, *Modelling of stefan problems in complex configurations involving two different metals using the enthalpy method*, Modelling and Simulation in Materials Science and Engineering **3** (1995), no. 1, 53-64.
90. ---, *Mathematical modeling and experimental measurements of moving boundary problems associated with exothermic heat of mixing*, International Journal of Heat and Mass Transfer **39** (1996), no. 5, 1005-1021.
91. M. C. Schneider and C. Beckermann, *Simulation of micro-/macrosegregation during the solidification of a low-alloy steel*, ISIJ International **35** (1995), no. 6, 665-672.
92. S. Chakraborty and P. Dutta, *Effects of dendritic arm coarsening on macroscopic modelling of solidification of binary alloys*, Materials Science and Technology **17** (2001), no. 12, 1531-1538.
93. C. Charbon, A. Jacot and M. Rappaz, *Three-dimensional probabilistic modelling of equiaxed eutectic solidification in the presence of convection*, Materials Science and Engineering A **173** (1993), no. 1-2, 143-148.
94. M. Rappaz and C.-A. Gandin, *Process modelling and microstructure*, (The Royal Society) Philosophical Transactions: Physical Sciences and Engineering **351** (1995), 563-577.
95. C. Y. Wang and C. Beckermann, *Equiaxed dendritic solidification with convection: Part i. Multiscale/multiphase modeling*, Metallurgical and Materials Transactions A: Physical Metallurgy and Materials Science **27** (1996), no. 9, 2754-2764.
96. ---, *A unified solute diffusion model for columnar and equiaxed dendritic alloy solidification*, Materials Science and Engineering A **171** (1993), no. 1-2, 199-211.
97. ---, *Prediction of columnar to equiaxed transition during diffusion-controlled dendritic alloy solidification*, Metallurgical and Materials Transactions A **25** (1994), no. 5, 1081-1093.

98. N. Ahmad, H. Combeau, J.-L. Desbiolles, T. Jalanti, G. Lesoult, J. Rappaz, M. Rappaz and C. Stomp, *Numerical simulation of macrosegregation: A comparison between finite volume method and finite element method predictions and a confrontation with experiments*, Metallurgical and Materials Transactions A: Physical Metallurgy and Materials Science **29** (1998), no. 2, 617-630.
99. W. R. Osorio and A. Garcia, *Modeling dendritic structure and mechanical properties of zn-al alloys as a function of solidification conditions*, Materials Science and Engineering A **325** (2002), no. 1-2, 103-111.
100. J. Crank, *Free and moving boundary problems*, Clarendon Press, Oxford, UK, 1984.
101. R. W. Lewis and P. M. Roberts, *Finite element simulation of solidification problems*, Applied Scientific Research **44** (1987), no. 1-2, 61-92.
102. J. Wanqi, *Further discussions on the solute redistribution during dendritic solidification of binary alloys*, Metallurgical and Materials Transactions B **25** (1994), no. 5, 731-739.
103. I. H. Katzarov and J. R. Popov, *Pore formation in hot spots*, International Journal of Heat and Mass Transfer **39** (1996), no. 14, 2861-2867.
104. R. T. Tenchev, J. A. Mackenzie, T. J. Scanlon and M. T. Stickland, *Finite element moving mesh analysis of phase change problems with natural convection*, International Journal of Heat and Fluid Flow **26** (2005), no. 4 SPEC. ISS., 597-612.
105. K. K. Tamma and R. R. Namburu, *Recent advances, trends and new perspectives via enthalpy-based finite element formulations for applications to solidification problems*, International Journal for Numerical Methods in Engineering **30** (1990), no. 4, 803-820.
106. C. G. Makridakis and I. Babuska, *On the stability of the discontinuous galerkin method for the heat equation*, SIAM Journal on Numerical Analysis **34** (1997), no. 1, 389-401.
107. T. Strouboulis, I. Babuska and K. Copps, *The design and analysis of the generalized finite element method*, Computer Methods in Applied Mechanics and Engineering **181** (2000), no. 1-3, 43-69.
108. J. Chessa, H. Wang and T. Belytschko, *On the construction of blending elements for local partition of unity enriched finite elements*, International Journal for Numerical Methods in Engineering **57** (2003), no. 7, 1015-1038.
109. V. R. Voller, *Fast implicit finite-difference method for the analysis of phase change problems*, Numerical Heat Transfer, Part B: Fundamentals **17** (1990), no. 2, 155-169.
110. V. R. Voller and M. Cross, *An explicit numerical method to track a moving phase front*, International Journal of Heat and Mass Transfer **30** (1983), 147-150.
111. W. Bushko and I. R. Groose, *New finite element method for multidimensional phase change heat transfer problems*, Numerical Heat Transfer B **19** (1991), 31-48.
112. S. R. Runnels and G. F. Carey, *Finite element simulation of phase change using capacitance methods*, Numerical Heat Transfer B **19** (1991), 13-30.
113. Y. Chen, Y.-T. Im and Z.-H. Lee, *Three dimensional finite element analysis with phase change by temperature recovery method*, International Journal of Machine Tools and Manufacture **31** (1991), no. 1, 1-7.
114. S. Bounds, K. Davey and S. Hinduja, *A modified effective capacitance method for solidification modelling using linear tetrahedral finite elements*, International Journal for Numerical Methods in Engineering **39** (1996), no. 18, 3195-3215.
115. K. Davey and I. Rosindale, *Control volume capacitance method for solidification modelling*, International Journal for Numerical Methods in Engineering **46** (1999), no. 3, 315-340.

116. K. Davey and N. J. Rodriguez, *A control volume capacitance method for solidification modelling with mass transport*, International Journal for Numerical Methods in Engineering **53** (2002), no. 12, 2643-2671.
117. ---, *Solidification modelling with a control volume method on domains subjected to viscoplastic deformation*, Applied Mathematical Modelling **26** (2002), no. 3, 421-447.
118. W. K. Liu, T. Belytschko and H. Chang, *An arbitrary lagrangian-eulerian finite element method for path dependent materials*, Comp. Meth. App. Mech. and Engineering **58** (1986), 227-245.
119. K. Davey and L. D. Clark, *Sensitivity and optimization for shape and non-linear boundary conditions in thermal boundary elements*, International Journal for Numerical Methods in Engineering **56** (2003), no. 4, 553-587.
120. G. H. Golub and C. F. Van Loan, *Matrix computations*, John Hopkins University Press, London, 1991.
121. K. Davey and R. Mondragon, *A non-physical enthalpy method for the numerical solution of isothermal solidification*, International Journal for Numerical Methods in Engineering **84** (2010), no. 2, 214-252.
122. J. Chessa, P. Smolinski and T. Belytschko, *The extended finite element method (xfem) for solidification problems*, International Journal for Numerical Methods in Engineering **53** (2002), no. 8, 1959-1977.
123. D. R. Noble, P. R. Schunk, E. D. Wilkes, T. A. Baer, R. R. Rao and P. K. Notz, "Large deformation solid-fluid interaction via a level set approach," Sandia National Laboratories, Albuquerque, New Mexico, USA, 2003.

# APPENDIX A

Validation of transport equation (3.41), which is of a form that requires some justification as it includes a term unseen in transport equation in Sections 3.4 to 3.8, i.e.  $\int_{\Gamma_i^e} \hat{h}(\underline{v}_N^* - \underline{v}_N^\times) \cdot \nabla N_i d\Gamma$ . Application of Reynolds Transport equation and Stokes Theorem to equation (3.41) gives

$$\begin{aligned} \int_{\Gamma_i^e} \frac{D^\times N_i \hat{h}'}{D^\times t} + N_i \hat{h}' \operatorname{div}_{\Gamma_i} \underline{v}^\times d\Gamma + \int_{\Gamma_i^e} \operatorname{div}_{\Gamma_i} N_i \hat{h}' (\underline{v}_T^* - \underline{v}_T^\times) d\Gamma + \int_{\Gamma_i^e} \hat{h}' (\underline{v}_N^* - \underline{v}_N^\times) \cdot \nabla N_i d\Gamma = \\ = \int_{\Gamma_i^e} N_i \left[ \rho (\underline{v} - \underline{v}^\times) \cdot \underline{n} \right] d\Gamma = - \int_{\Gamma_i^e} N_i \left[ \underline{q} \cdot \underline{n} \right] d\Gamma \end{aligned} \quad (A 1)$$

where subscripts T and N refer to tangential and normal components, respectively.

Since equation (A 1) applies equally to any portion of  $\Gamma_i^e$  the equivalent partial differential equation can be deduced and is of the form

$$\begin{aligned} \frac{D^\times N_i \hat{h}'}{D^\times t} + N_i \hat{h}' \operatorname{div}_{\Gamma_i} \underline{v}^\times + \operatorname{div}_{\Gamma_i} N_i \hat{h}' (\underline{v}_T^* - \underline{v}_T^\times) + \hat{h}' (\underline{v}_N^* - \underline{v}_N^\times) \cdot \nabla N_i = \\ = N_i \left[ \rho (\underline{v} - \underline{v}^\times) \cdot \underline{n} \right] = -N_i \left[ \underline{q} \cdot \underline{n} \right] \end{aligned} \quad (A 2)$$

Application Leibniz law to the derivatives and on rearrangement equation (A 2) reduces to

$$\begin{aligned} \hat{h}' \left[ \frac{D^\times N_i}{D^\times t} + (\underline{v}_T^* - \underline{v}_T^\times) \cdot \nabla_{\Gamma_i} N_i + (\underline{v}_N^* - \underline{v}_N^\times) \cdot \nabla N_i \right] + \\ + N_i \left[ \frac{D^\times \hat{h}'}{D^\times t} + \hat{h}' \operatorname{div}_{\Gamma_i} \underline{v}^\times + \operatorname{div}_{\Gamma_i} \hat{h}' (\underline{v}_T^* - \underline{v}_T^\times) \right] = N_i \left[ \rho (\underline{v} - \underline{v}^\times) \cdot \underline{n} \right] = -N_i \left[ \underline{q} \cdot \underline{n} \right] \end{aligned} \quad (A 3)$$

which in turn implies

$$\frac{D^\times \widehat{h}'}{D^\times t} + \widehat{h}' \operatorname{div}_{\Gamma_i} \underline{v}^\times + \operatorname{div}_{\Gamma_i} \widehat{h}' (\underline{v}_T^* - \underline{v}_T^\times) = \rho (\underline{v} - \underline{v}^\times) \cdot \underline{n} \Big|_{\Gamma_i} = -\underline{q} \cdot \underline{n} \Big|_{\Gamma_i} \quad (\text{A } 4)$$

and

$$\frac{D^\times N_i}{D^\times t} + (\underline{v}_T^* - \underline{v}_T^\times) \cdot \nabla_{\Gamma_i} N_i + (\underline{v}_N^* - \underline{v}_N^\times) \cdot \nabla N_i = \frac{D^\times N_i}{D^\times t} + (\underline{v}^* - \underline{v}^\times) \cdot \nabla N_i = \frac{D^* N_i}{D^* t} = 0 \quad (\text{A } 5)$$

where equation (A 5) confirms equation (3.43)

It is important to appreciate that

$$\frac{D^\times N_i}{D^\times t} + (\underline{v}^* - \underline{v}^\times) \cdot \nabla N_i = \frac{D^* N_i}{D^* t} \quad (\text{A } 6)$$

but

$$\frac{D^\times \widehat{h}'}{D^\times t} + (\underline{v}^* - \underline{v}^\times) \cdot \nabla \widehat{h}' \neq \frac{D^* \widehat{h}'}{D^* t} \quad (\text{A } 7)$$

since  $\nabla \widehat{h}'$  is not defined and neither is  $D^* \widehat{h}' / D^* t$  as the domain of definition for  $\widehat{h}'$  is  $\Gamma_i^e$  and not  $\Omega_e$ .

## APPENDIX B

Solidification with two discontinuities and linear transition zone depicted in Figure B-1 has been analysed in chapter 5 with special interest in the effect of the transition zone size has in order to define accurately the temperature field and non-physical variable using NEM. Firstly, the energy balance equation that captures sensible and latent heat and secondly the identification of the source terms, which are annihilated

### *Integral evaluation*

The evaluation of the integrals in equations (4.51) and (4.52) requires the establishment of relationship between specific enthalpy and temperature. Therefore, assuming specific heat capacitance approach  $c_k^c = dh_k^c/dT$ , which is spatially and temporally invariant in  $\Omega_k^e$  see section 4.10. For this case, two discontinuities with linear mushy solidification is depicted in Figure B-2 for 1-D solidification moving in an Eulerian frame and in Figure B-3 for various linear elements and represented in general with equation (4.59) for time  $t_n$ , which is

$$\int_{\Omega_c} \rho^n h^n dV = \sum_{k=k_s^n}^{k_f^n} M_k^n L_{k-1} + \sum_{k=k_s^n}^{k_f^n} M_k^n h_{\Gamma_{k-1}}^c + \sum_{k=k_s^n}^{k_f^n} \rho_k c_k^c \int_{\Omega_k^n} (T - T_{\Gamma_{k-1}}) dV \quad (4.59)$$

For this case, when  $k = k_s^n = 1$  and recalling that the terms  $h_{\Gamma_{k-1}}^c$  and  $T_{\Gamma_{k-1}}$  are replaced by  $h_{ref}^c$  and  $T_{ref}$  respectively,  $L_{k-1}$  is undefined and set to zero and  $k_f^n = 3$  gives

$$\begin{aligned} \int_{\Omega_c} \rho^n h^n dV = & M_1^n h_{\Gamma_{ref}}^c + \rho_1 c_1^c \int_{\Omega_1^n} (T - T_{\Gamma_{ref}}) dV + M_2^n L_1 + M_2^n h_{\Gamma_1^-}^c + \rho_2 c_2^c \int_{\Omega_2^n} (T - T_{\Gamma_1}) dV + \\ & + M_3^n L_2 + M_3^n h_{\Gamma_2^-}^c + \rho_3 c_3^c \int_{\Omega_3^n} (T - T_{\Gamma_2}) dV \end{aligned} \quad (B-1)$$

which capture the specific heat distribution for the two discontinuities with a linear mushy solidification see Figure B-3, only if  $c_2^c = h_{\Gamma_2^-}^c - h_{\Gamma_1^+}^c / T_{\Gamma_2} - T_{\Gamma_1}$ , similar expression can be obtained for  $t_{n+1}$

### Jump term evaluation

Accurate evaluation of the integral  $\int_{t_n}^{t_{n+1}} \sum_{k \in K_e} \int_{\Gamma_k^e(t)} \rho h \underline{v}_k^\times \cdot \underline{n} d\Gamma dt$  has been achieved and discussed on detail in Section 4.10.1, where a constant mass element is considered thus  $\rho h \underline{v}_k^\times \cdot \underline{n}$  is replaced by  $-\rho_{k+1} L_k \underline{v}_k^\times \cdot \underline{n}_k$ . Consider the integral from chapter 4

$$\begin{aligned} \sum_{k=k_s}^{k_f} \int_{t_n}^{t_{n+1}} \int_{\Gamma_{k-1}^e(t)} \rho h \underline{v}_{k-1}^\times \cdot \underline{n} d\Gamma dt &= - \sum_{k=k_s}^{k_f} \rho_k L_{k-1} \int_{t_n}^{t_{n+1}} \int_{\Gamma_{k-1}^e(t)} \underline{v}_{k-1}^\times \cdot \underline{n} d\Gamma dt = \\ &= - \sum_{k=k_s}^{k_f} \rho_k L_{k-1} V_k^{\text{swept}} = - \sum_{k=k_s}^{k_f} L_{k-1} (M_k^{n+1} - M_k^n) \end{aligned} \quad (4.61)$$

In this case, for two discontinuities and a mushy linear solidification the above equation gives

$$\sum_{k=1}^3 \int_{t_n}^{t_{n+1}} \int_{\Gamma_{k-1}^e(t)} \rho h \underline{v}_{k-1}^\times \cdot \underline{n} d\Gamma dt = - \sum_{k=1}^3 L_{k-1} (M_k^{n+1} - M_k^n) = - [L_1 (M_2^{n+1} - M_2^n) + L_2 (M_3^{n+1} - M_3^n)] \quad (B-2)$$

recall that  $L_{k-1}$  is undefined and set to zero when  $k = k_s^n = 1$

Combining equation (B-1) for  $t_{n+1}$  and  $t_n$  and equation (B-2) gives

$$\begin{aligned} \int_{\Omega_e} \rho^{n+1} h^{n+1} dV - \int_{\Omega_e} \rho^n h^n dV + \sum_{k=k_s}^{k_f} \int_{t_n}^{t_{n+1}} \int_{\Gamma_{k-1}^e(t)} \rho h \underline{v}_{k-1}^\times \cdot \underline{n} d\Gamma dt &= \left[ M_1^{n+1} h_{\Gamma_{\text{ref}}}^c + \rho_1 c_1^c \int_{\Omega_1^{e^{n+1}}} (T - T_{\Gamma_{\text{ref}}}) dV + \right. \\ &+ M_2^{n+1} L_1 + M_2^{n+1} h_{\Gamma_1^-}^c + \rho_2 c_2^c \int_{\Omega_2^{e^{n+1}}} (T - T_{\Gamma_1}) dV + M_3^{n+1} L_2 + M_3^{n+1} h_{\Gamma_2^-}^c + \rho_3 c_3^c \int_{\Omega_2^{e^{n+1}}} (T - T_{\Gamma_2}) dV \Big] - \\ &- \left[ M_1^n h_{\Gamma_{\text{ref}}}^c + \rho_1 c_1^c \int_{\Omega_1^{e^n}} (T - T_{\Gamma_{\text{ref}}}) dV + M_2^n L_1 + M_2^n h_{\Gamma_1^-}^c + \rho_2 c_2^c \int_{\Omega_2^{e^n}} (T - T_{\Gamma_1}) dV + M_3^n L_2 + \right. \\ &\quad \left. + M_3^n h_{\Gamma_2^-}^c + \rho_3 c_3^c \int_{\Omega_2^{e^n}} (T - T_{\Gamma_2}) dV \right] - [L_1 (M_2^{n+1} - M_2^n) + L_2 (M_3^{n+1} - M_3^n)] \end{aligned} \quad (B-3)$$

which reduces to



$$\begin{aligned}
& \int_{\Omega_e} \rho^{n+1} h^{n+1} dV - \int_{\Omega_e} \rho^n h^n dV + \sum_{k_s} \int_{t_n}^{t_{n+1}} \int_{\Gamma_k^c(t)} \rho h \underline{v}_k^\times \cdot \underline{n} d\Gamma dt = \left[ (M_1^{n+1} - M_1^n) h_{\Gamma_{\text{ref}}}^c + (M_2^{n+1} - M_2^n) h_{\Gamma_1^-}^c + \right. \\
& \left. + (M_3^{n+1} - M_3^n) h_{\Gamma_2^-}^c \right] + \left[ \rho_1 c_1^c \int_{\Omega_1^{c^{n+1}}} (T - T_{\Gamma_{\text{ref}}}) dV + \rho_2 c_2^c \int_{\Omega_2^{c^{n+1}}} (T - T_{\Gamma_1}) dV + \rho_3 c_3^c \int_{\Omega_3^{c^{n+1}}} (T - T_{\Gamma_2}) dV \right] - \\
& - \left[ \rho_1 c_1^c \int_{\Omega_1^{c^n}} (T - T_{\Gamma_{\text{ref}}}) dV + \rho_2 c_2^c \int_{\Omega_2^{c^n}} (T - T_{\Gamma_1}) dV + \rho_3 c_3^c \int_{\Omega_3^{c^n}} (T - T_{\Gamma_2}) dV \right] \quad (\text{B-4})
\end{aligned}$$

where it is apparent that latent energy terms are annihilated in equation (B-3) to give equation (B-4) as predicted by the annihilation theory.

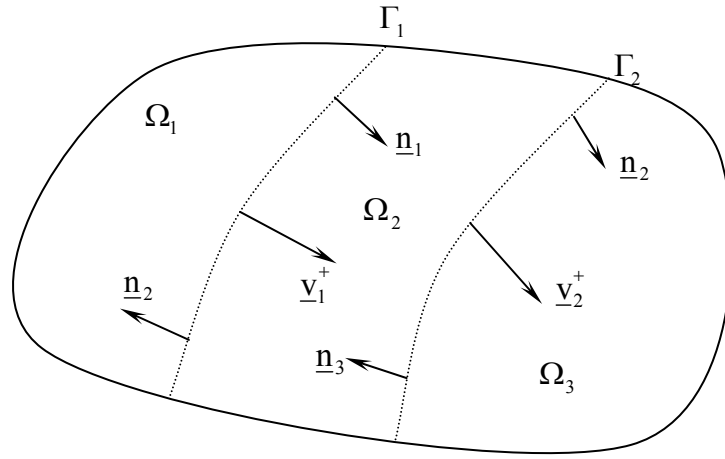


**Figure B-1 Partition domain  $\Omega$  with non-overlapping open domains and two discontinuities**

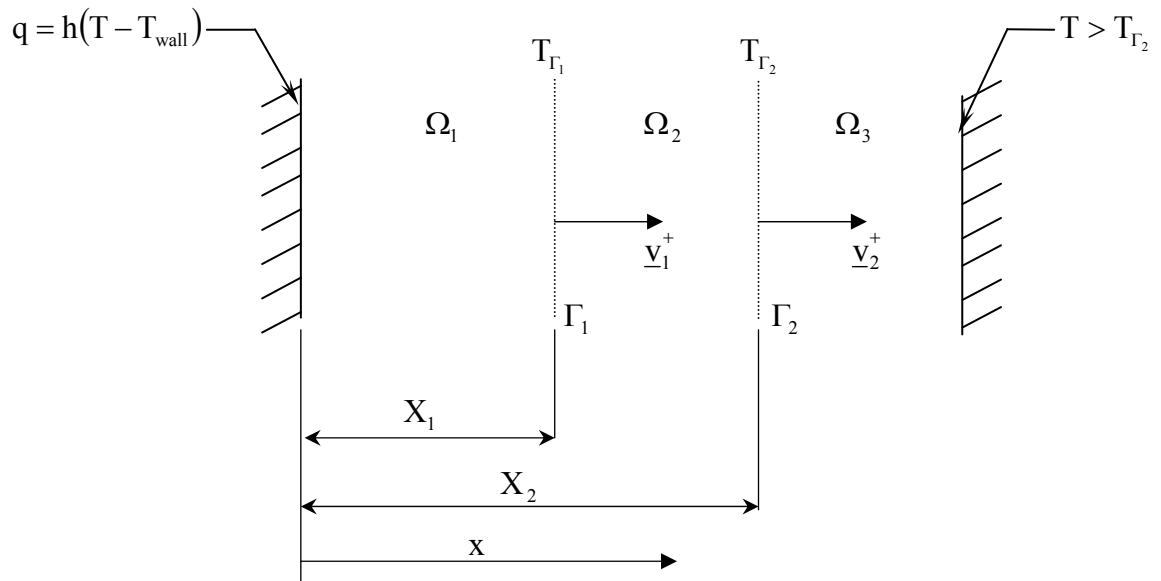


Figure B-2 1-D solidification problem with two fronts on an Eulerian frame

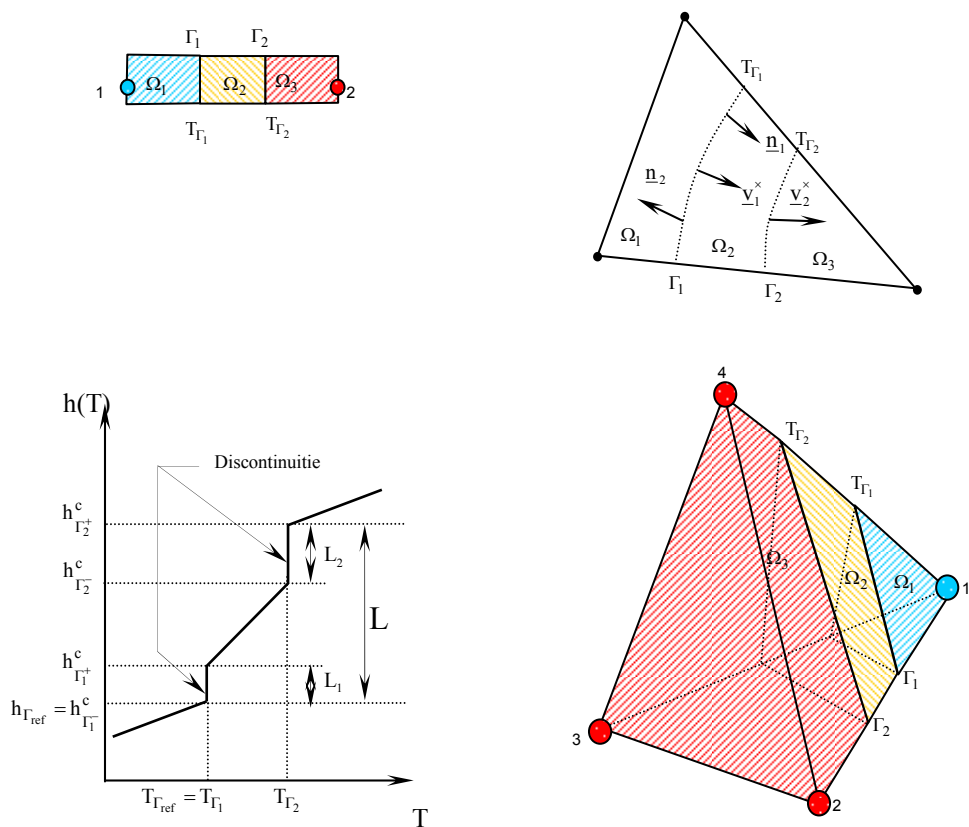


Figure B-3 Solidification with phase discontinuities and associated regions in a linear element